

Heterogeneous Chemistry of Reactive Species on Aerosol Surfaces

Joanna Elizabeth Dyson

Submitted in accordance with the requirements
for the degree of Doctor of Philosophy

The University of Leeds
School of Chemistry

March 2022

The candidate confirms that the work submitted is her own, except where work which has formed part of a jointly authored publications has been included. The contribution of the candidate and the other authors to this work has been explicitly indicated below. The candidate confirms that appropriate credit has been given within the thesis where reference has been made to the work of others.

Details of the experimental methods in *Chapter 3: Photo-Fragmentation Laser Induced Fluorescence Technique for Measuring HONO Production from Aerosols* and the results in *Chapter 4: HONO Production from Illuminated TiO₂ and Mixed TiO₂/Ammonium Nitrate Aerosol Surfaces* have appeared in the publication below:

Dyson, J. E., Boustead, G. A., Fleming, L. T., Blitz, M., Stone, D., Arnold, S. R., Whalley, L. K., and Heard, D. E.: Production of HONO from NO₂ uptake on illuminated TiO₂ aerosol particles and following the illumination of mixed TiO₂/ammonium nitrate particles, *Atmos. Chem. Phys.*, 21, 5755–5775, <https://doi.org/10.5194/acp-21-5755-2021>, 2021.

Within this publication, I was responsible of the measurements of HONO production from aerosol surfaces with assistance from Graham A. Boustead, Lauren T. Fleming, Lisa K. Whalley and Mark Blitz. I was also responsible for developing and running the model, with assistance from Lisa K. Whalley. The manuscript was prepared by myself, Lisa K. Whalley and Dwayne E. Heard with contributions from all co-authors.

This copy has been supplied on the understanding that it is copyright material and that no quotation from the thesis may be published without proper acknowledgment.

Acknowledgments

I would like to thank my supervisors; Dwayne, Lisa and Steve for all their help and support throughout the last 3.5 years, in particular Lisa who was always around to help with anything from experimental or modelling queries to existential crises.

Special thanks to Graham for being such a calming presence and for patiently listening to my waffling for the last 4.5 years.

Lastly, I would like to thank the B36 office group for supporting me, emotionally and academically throughout the entire process.

Abstract

A photo-fragmentation laser induced fluorescence instrument coupled to an aerosol flow-tube was validated and calibrated for the measurement of HONO from sub-micron aerosol surfaces. The production of HONO from illuminated TiO₂ aerosol surfaces in the presence of NO₂ was investigated and the reactive uptake coefficient of NO₂ to form HONO for NO₂ mixing ratios of 34 – 400 ppb was found to be in the range of $\gamma_{NO_2 \rightarrow HONO} = (9.97 \pm 3.51) \times 10^{-6}$ at 286 ppb to a maximum of $\gamma_{NO_2 \rightarrow HONO} = (1.26 \pm 0.17) \times 10^{-4}$ at 51 ppb NO₂ for a lamp photon flux of $(1.65 \pm 0.02) \times 10^{16}$ photons cm⁻² s⁻¹. The reactive uptake of NO₂ to form HONO on TiO₂ was found to increase with NO₂ mixing ratio to ~ 51 ppb NO₂, followed by a decrease with further increase in NO₂. Box modelling studies supported a mechanism involving two NO₂ molecules per HONO molecule formed, suggesting the formation of an NO₂ dimer intermediate on the surface of the aerosol.

Using the maximum experimental value of $\gamma_{NO_2 \rightarrow HONO}$, a production rate of HONO for Beijing Summertime was estimated to be 1.70×10^5 molecules cm⁻³ s⁻¹ (~24.8 ppt hr⁻¹). From the calculated net gas phase production of HONO for the same conditions (~3.8 ppt hr⁻¹) it was concluded that production of HONO from TiO₂ aerosol surfaces in the presence of NO₂ would have little effect on the overall HONO budget for Summertime in Beijing.

In the absence of NO₂, the production of HONO from ammonium nitrate aerosols was investigated due to recent studies proposing particulate nitrate photolysis as an important source of HONO and hence NO_x following photolysis (renoxification) in the marine boundary layer. Significant production of HONO from pure ammonium nitrate aerosols was not seen. However, with the addition of TiO₂ in a 1:1 mixture with ammonium nitrate, the production of HONO observed *was* significant. Using experimental results for mixed TiO₂/ammonium nitrate aerosol experiment, a rate of HONO production from nitrate photolysis for ambient marine conditions was calculated to be 68 ppt hr⁻¹, taking Cape Verde in the tropical Atlantic Ocean as an example of such environments. This is a significant rate of production of HONO, with a magnitude similar to the missing HONO production rate calculated in the RHAMBLE campaign which took place at Cape Verde in 2007.

A Potential Aerosol Mass chamber was built and characterised for the production of secondary organic aerosols (SOA) from oxidation of volatile organic compounds (VOC). The effect of changing the concentrations of limonene and O₃ on the size distributions of SOA was investigated, with size distributions for SOAs derived from α -pinene and limonene with both O₃ and OH as the oxidants compared.

The PAM chamber was coupled to an aerosol flow tube system and was validated against previous observations for the measurement of HO₂ uptake onto aerosol surfaces. The uptake of HO₂ onto limonene-derived SOA was measured with an interference observed, postulated to be due to RO₂ species coming off the SOA surface after the charcoal denuders. Trace amounts of limonene after the denuders and OH from the sliding injector (formed as a bi-product of water photolysis for the generation of HO₂) were also found to be present within the flow tube leading to a production of peroxy radicals as the injector was pulled back due to VOC + OH reactions. With the addition of a Gas Chromatography (GC) trap after the denuders which significantly reduced any interference seen, though to an unknown extent, a decay of HO₂ in the presence of limonene-derived SOA was observed and uptake coefficients of $\gamma_{HO_2} = 0.10 \pm 0.03$ and $\gamma_{HO_2} = 0.15 \pm 0.03$ were measured for 22 % and 58 % RH respectively at atmospheric pressure and 298 K.

Using a novel parameterisation by Song et al., 2020, the uptake coefficient of HO₂, γ_{HO_2} , was calculated using measured values of temperature, RH, aerosol pH, aerosol liquid water content (ALWC), particulate matter concentration ([PM]) and $[Cu^{2+}]_{eff}$ for Beijing Summer AIRPRO campaign in 2017. For the entire campaign, the average HO₂ uptake coefficient calculated was 0.070 ± 0.035 (1 σ) with values ranging from as low as 0.002 to as high as 0.15, though still significantly lower than the value of $\gamma_{HO_2} = 0.2$, commonly used in modelling studies. Using the calculated values of γ_{HO_2} for the Summer AIRPRO campaign, the OH, HO₂ and RO₂ radical concentrations were calculated using a box-model incorporating the Master Chemical Mechanism (v. 3.3.1), with and without the addition of aerosol uptake, and compared to the measured concentrations. The effect of HO₂ uptake onto aerosols was investigated using 2 models: MCM_ α pinene_SA with γ_{HO_2} fixed at 0.2, and MCM_ α pinene_gamma with the values of γ_{HO_2} calculated by the Song parametrization. A rate of destruction analysis showed the dominant loss pathway for

HO₂ to be HO₂ + NO for all NO concentrations across the campaign with HO₂ uptake contributing < 0.3 % to the total loss of HO₂, as expected for a polluted urban location. However, at low NO r, i.e. < 0.1 ppb NO, up to 78 % of HO₂ loss was due to HO₂ uptake within MCM_αpinene_SA (γ_{HO_2} = 0.2) and up to 28 % of HO₂ loss was due to HO₂ uptake within MCM_αpinene_gamma, despite the much lower γ_{HO_2} values compared to γ_{HO_2} of 0.2. From this, it can be concluded that in cleaner environments away from urban centres with high concentrations of NO but where aerosol surface area is high still, values of γ_{HO_2} of less than 0.2 could still have a significant effect on the overall HO₂ concentration.

Reference:

Song, H., Chen, X., Lu, K., Zou, Q., Tan, Z., Fuchs, H., Wiedensohler, A., Moon, D. R., Heard, D. E., Baeza-Romero, M. T., Zheng, M., Wahner, A., Kiendler-Scharr, A., and Zhang, Y.: Influence of aerosol copper on HO₂ uptake: a novel parameterized equation, *Atmos. Chem. Phys.*, 20, 15835-15850, <https://doi.org/10.5194/acp-20-15835-2020>, 2020.

Table of Contents

Table of Figures	XII
Table of Tables.....	XXIX
List of Abbreviations.....	XXXII
1 Introduction	1
1.1 Atmospheric Warming and Air Quality	1
1.2 Tropospheric Oxidation Chemistry	4
1.2.1 The HO _x Cycle	4
1.2.2 The Role of Nitrous Acid.....	7
1.2.3 The Importance of Atmospheric Models	9
1.2.4 Short Introduction to the Thesis.....	9
1.3 The Sources and Properties of Atmospheric Aerosols	10
1.4 Heterogeneous Production of HONO from Aerosol Surfaces	14
1.4.1 Humic acid	15
1.4.2 Titanium Dioxide	17
1.4.3 Particulate Nitrate Photolysis.....	18
1.5 Effect of Relative Humidity on the Production of HONO from Aerosol Surfaces	19
1.6 Mechanism of Heterogeneous Uptake of HO ₂ onto Aqueous Phase Aerosols	21
1.6.1 Resistor Model	21
1.6.2 Self-Reaction.....	25
1.6.3 Reaction with Transition Metals	26
1.7 Mechanism of Heterogeneous Uptake of HO ₂ onto Solid Aerosols	28
1.8 Factors Affecting the Uptake of HO ₂ onto Aerosol Surfaces.....	30
1.8.1 Aerosol pH	30

1.8.2	Temperature	31
1.8.3	Relative Humidity	31
1.8.4	Concentration of HO ₂	35
1.8.5	Exposure Time	36
1.9	Global Distribution of HO ₂ and HO ₂ uptake.....	37
1.10	Atmospheric Modelling	40
1.10.1	Zero Dimensional Modelling and the Master Chemical Mechanism ..	40
1.10.2	Global and Regional Modelling	41
1.10.3	HO ₂ Uptake in Previous Modelling Studies	41
1.10.4	Model-Measurement Comparison of Atmospheric Radicals.....	46
1.11	Project Outline	49
2	Experimental Methods for HO ₂ Uptake from Aerosol Surfaces	50
2.1	Overview of Experimental Set-up.....	50
2.2	HO ₂ generation	52
2.2.1	The Sliding Injector	52
2.3	Aerosol Flow Tube.....	53
2.4	Aerosol Generation using a Potential Aerosol Mass Chamber	54
2.5	The FAGE Instrument	56
2.5.1	FAGE Principle of Operation	56
2.5.2	FAGE Cell and the Detection of HO ₂	60
2.5.3	Reference Cell.....	63
2.5.4	Data Acquisition Cycle	64
2.6	FAGE Calibration	66
2.7	Experimental Procedure and Data Analysis.....	69
2.7.1	Background Signal measurement	69
2.7.2	Moving Injector Experiment.....	70

2.7.3	Error Analysis	74
2.8	Summary	75
3	Photo-Fragmentation Laser Induced Fluorescence Technique for Measuring HONO Production from Aerosols.....	76
3.1	Previous Instrumentation for the measurement of HONO	76
3.1.1	DOAS	76
3.1.2	LOPAP	77
3.2	Overview of Experimental Set-up	80
3.3	Aerosol Generation and Characterisation.....	81
3.3.1	Generating Aerosols and Neutralising Charge.....	81
3.3.2	Controlling Relative Humidity (RH)	83
3.3.3	Controlling Aerosol Concentration	83
3.3.4	Characterisation of Aerosols Using a Scanning Mobility Particle Sizer (SMPS)	84
3.3.5	SMPS Calibration	86
3.4	Description of the HONO Instrument	87
3.4.1	Fragmentation of HONO.....	87
3.4.2	Detection of OH	89
3.4.3	Detection Cell.....	90
3.4.4	Data Acquisition.....	92
3.4.5	Measuring a Background Signal	95
3.5	Calibration	97
3.5.1	OH Calibration	97
3.5.2	HONO Calibration	100
3.5.3	O ₃ actinometry	102
3.6	Using NO ₂ Actinometry to Measure the Photolysis Rate of NO ₂	105
3.7	Calculating a Limit of Detection	109

3.8	Summary	109
4	HONO Production from Illuminated TiO ₂ and mixed TiO ₂ /Ammonium Nitrate Aerosol Surfaces	111
4.1	Results of TiO ₂ Aerosol experiments.....	111
4.1.1	Production of HONO from TiO ₂ Aerosol Surfaces	111
4.1.2	Relative Humidity Dependence of HONO Production from TiO ₂ Aerosol Surfaces	112
4.1.3	NO ₂ Uptake Coefficient Calculations	116
4.1.4	Effect of Light Intensity on the Production of HONO from TiO ₂ Aerosol Surfaces	124
4.2	Modelling HONO Production from NO ₂ Adsorption on Illuminated TiO ₂ Aerosol Surfaces	125
4.2.1	Box Model Description and Results	125
4.3	HONO Production from TiO ₂ and Ammonium Nitrate Aerosol Mixture	138
4.3.2	Atmospheric Implications of HONO production Experiments	143
4.3.3	Experimental Summary: HONO Production from Aerosol Surfaces	146
5	Characterisation of Secondary Organic Aerosol Formation using a Potential Aerosol Mass Chamber.....	148
5.1	The Importance of SOAs.....	148
5.2	An Introduction to PAM Chambers as a Type of Oxidation Flow Reactor....	149
5.3	Monoterpene Oxidation by Ozone	151
5.4	Characterising α -pinene-derived Secondary Organic Aerosols Using an SMPS	153
5.5	Characterising Limonene-derived Secondary Organic Aerosols Using an SMPS	157
5.5.1	SOA Formed From the Reaction of Limonene With Ozone	157
5.5.2	SOA Formed from the Reaction of Limonene and the OH radical ...	161

5.6	Summary	167
6	Measurements of HO ₂ Uptake Coefficient onto Secondary Organic Aerosols Generated using A Potential Aerosol Mass Chamber.....	170
6.1	Measurements of HO ₂ Uptake Coefficient onto Secondary Organic Aerosols	170
6.1.1	Validating HO ₂ Uptake Apparatus.....	170
6.1.2	Uptake of HO ₂ onto Limonene-derived Secondary Organic Aerosols	173
6.1.3	Using a GC Trap to Remove Interference.....	185
6.2	Summary	187
7	Modelling the impact of HO ₂ Uptake onto Aerosols During Summertime in Beijing with the Master Chemical Mechanism.....	189
7.1	Introduction to the Summer AIRPRO Campaign.....	189
7.2	Model Description	193
7.3	Modelling Results.....	195
7.3.1	MCM-base vs MCM_αpinene model	195
7.3.2	Impact of HO ₂ uptake to Aerosols	203
7.3.3	Testing a Novel Parameterisation for the Influence of Aerosol Copper Concentration on HO ₂ Uptake	215
7.4	Modelling Summary	231
8	Conclusions and Future Work.....	233
8.1	Overview	233
8.2	Production of HONO from Illuminated TiO ₂ aerosols surfaces	233
8.2.1	Future Work	236
8.3	Uptake of HO ₂ onto Limonene-derived Secondary Organic Aerosols	236
8.3.1	Future Work	237

8.4 Modelling the Effect of HO ₂ Uptake onto Aerosols Surfaces During AIRPRO Summer Campaign.....	237
8.4.1 Future Work.....	239
Bibliography	240

Table of Figures

Figure 1.1. Relationship between observations of land and ocean surface temperature, greenhouse gas concentrations and sea level and the anthropogenic CO ₂ emissions. a) Globally averaged combined land and ocean surface temperature anomalies relative to the average over the period of 1986-2005. b) Globally averaged sea level change relative to the same period. c) Atmospheric concentrations of greenhouse gases CO ₂ (green), methane (orange) and nitrous oxide (red) determined from ice core data (dots) and direct atmospheric measurements (lines). d) Global anthropogenic CO ₂ emissions from forestry and land use in addition to fossil fuel combustion. Image taken from IPCC 2014 synthesis report (IPCC, 2014).	1
Figure 1.2. Global mean radiative forcing taken from 2013 IPCC report. The effective radiative forcing (defined by the IPCC as the change in the net top of the atmosphere downward flux after allowing for atmospheric temperatures, water vapour and clouds) is shown as solid bars whereas the radiative forcing is shown as hatched bars for the period 1750-2011 (Myhre et al., 2013).	2
Figure 1.3. Schematic of the HO _x cycle showing the major production and destruction pathways of tropospheric oxidants, OH and HO ₂	5
Figure 1.4. Typical number and volume distributions of atmospheric particles within different aerosol modes. Image taken from (Seinfeld and Pandis, 2006).	11
Figure 1.5. Aerosol size distributions for TiO ₂ aerosols generated during the HONO production experiment showing aerosol surface area (black) and aerosol particle number (green) between diameters of 14 and 661 nm (sheath flow: 3 lpm).	11
Figure 1.6. Deliquescence curve for NaCl showing the hygroscopic growth factor, g_e versus RH at a dry diameter of 100 nm for NaCl from a nebulizer or sea spray chamber. Image taken from Zieger et al., 2017.	14
Figure 1.7. Dependence of HONO formation on NO ₂ concentration on humic acid aerosol (filled circles, 26 % RH) and humic acid coatings (empty circles, 21 % RH). The inset shows the dependence of the reactive uptake coefficient on NO ₂ concentration. Image taken from Stemmler et al., 2007.	16

Figure 1.8. Uptake coefficient of $\text{NO}_2 \rightarrow \text{HONO}$ on Arizona test dust as a function of NO_2 initial concentration for coated flow tube (CFT, black) and aerosol flow tube (AFT, red) experiments. Figure taken from Dupart et al., 2014. 18

Figure 1.9. Dependence of reactive uptake coefficient of $\text{NO}_2 \rightarrow \text{HONO}$ on the relative humidity on humic acid aerosol (left axis) and humic acid coated walls (right axis). Filled circles represent the uptake coefficient measured on humic acid aerosols at 25 ppb NO_2 whereas the empty circles represent the uptake coefficient on humic acid coatings at 20 ppb NO_2 . Image taken from Stemmler et al., 2007. 20

Figure 1.10. Dependence of the uptake coefficient of $\text{NO}_2 \rightarrow \text{HONO}$ from TiO_2 aerosols on RH. Image taken from Gustafsson et al., 2007. 21

Figure 1.11. Processes involved in the uptake, reaction and desorption of a gas phase molecule by a liquid droplet. Image reproduced from Holloway and Wayne, 2010. 22

Figure 1.12. Dependence of HO_2 uptake coefficient on relative humidity for a) dry and aqueous $\text{NH}_4(\text{SO}_4)_2$ aerosols and b) dry and aqueous NaCl aerosols as a function of RH. Uptake coefficient values taken from Thornton and Abbatt, 2005; Taketani et al., 2008 and George et al., 2013. 33

Figure 1.13. HO_2 uptake coefficient onto copper (II)-doped sucrose aerosol particles as a function of (a) relative humidity and (b) aerosol particle viscosity. The fits represent the expected HO_2 uptake coefficient calculated using the KM-SUB model with the Price et al., 2014 (red) and Zobrist et al., 2011 (blue) diffusion parameterisations Zobrist et al., 2011; Price et al., 2014. Image taken from Lakey et al., (2016). 34

Figure 1.14. Dependence of HO_2 uptake coefficient on initial HO_2 concentration for aqueous $(\text{NH}_4)_2\text{SO}_4$ aerosol for 54 % RH (black), 65 % RH (red) and 75 % RH (green). Image taken from George et al., 2013. 35

Figure 1.15. Dependence of HO_2 uptake coefficients for aqueous NaCl aerosols as a function of reaction time for two initial HO_2 concentrations. RH kept constant at 60 %. Error bars are 1σ of average values. Image taken from George et al., 2013. 36

Figure 1.16. a) Global OH distribution in 10^6 molecules cm^{-3} . b) Global HO_2 distribution in 10^8 molecules cm^{-3} . In both cases the left panel shows the annual tropospheric mean while the right panel shows annual zonal mean up to 10 hPa. The

solid black line on the right panel indicates the average boundary layer height while the upper dashed line represents the tropopause mean height with the surrounding solid lines the maximum and minimum mean tropopause height. Figure taken from Lelieveld et al., 2016.....38

Figure 1.17. Surface and zonal mean γHO_2 for January and July calculated using GEOS-Chem using a new parameterisation by MacIntrye and Evans, 2011. Image taken from MacIntrye and Evans, 2011.40

Figure 2.1. Schematic diagram of the aerosol flow tube system used to study the uptake of HO_2 onto aerosol surfaces. CPM: Channel Photomultiplier, HEPA: High Efficiency Particulate Air filter, FAGE: Fluorescence Assay by Gas Expansion, RH: Relative Humidity, T: Temperature, MFC: Mass Flow Controller. Image taken from George et al., 2013.50

Figure 2.2. Gas purification system TSI model 3074B. Used for removal of contaminants from the departmental nitrogen supply TSI, 2008b.....51

Figure 2.3. Sliding injector used for the addition of HO_2 radicals into the flow tube during HO_2 uptake experiments. Image taken from Moon, 2018.....53

Figure 2.4. Aerosol flow tube setup showing connection to the FAGE cell of the right. Sliding injector is shown on the left.....54

Figure 2.5. Leeds SOA generation setup. MFC: Mass Flow Controller, PAM: Potential Aerosol Mass, SMPS: Scanning Mobility Particle Sizer, VOC: Volatile Organic Compound.55

Figure 2.6. Leeds PAM chamber with 4 UV lights.....56

Figure 2.7. Schematic of the potential energy curves of OH. Excitation from ground electronic state to first excited electronic state shown in black. Emission via fluorescence shown in navy and collisional quenching shown in teal. M is a bath gas such as O_2 or N_2 . Image reproduced from Heard, 2006a.57

Figure 2.8. Off-resonance fluorescence detection of OH radicals. Q represents quenching. Figure adapted from Heard, 2006b.....58

Figure 2.9. Energy level diagram showing the excitation and fluorescence of OH in the FAGE technique. R represents changes in rotational energy levels. Q represents quenching. Figure adapted from Heard, 2006b.....59

Figure 2.10. Schematic of the FAGE cell used to measure HO₂ (not to scale). Top panel shows cross-section of cell taken from the side, as if looking down the baffled arms of the cell with the laser path going through the image. Bottom panel shows a cross-section of the same cell from the front, showing the path of the laser from left to right through the arms. 61

Figure 2.11. Schematic of the 308 nm pulsed dye laser and reference cell showing one beam splitter. Up to three beam splitters can be used to divide the light into up to 3 fibre launchers while still delivering 5% of laser light to the reference cell. 62

Figure 2.12. An example scan of the reference cell showing the initial scan across the peak, the online measurement and the offline measurement. 64

Figure 2.13. Schematic showing the data acquisition cycle for the FAGE instrument measuring HO₂ uptake. MCP: multi-channel plate. PCC: photon counting card. Image is not to scale. Gate A is 1 μs in length and measures the OH present and any background signal while Gate B is 20 μs in length and measures the solar background signal (which is not relevant for these experiments). 65

Figure 2.14. Schematic of FAGE calibration set up. MFC: Mass Flow Controller. FAGE: Fluorescence Assay by Gas Expansion. 68

Figure 2.15. HO₂ (purple) and OH (black) calibration curves. Error bars represent ±1σ with the linear least squares fit shown in black (OH) and purple (HO₂). The gradient (i.e. the calibration factor) is in units of counts s⁻¹ mW⁻¹ molecule⁻¹ cm³ and the intercept is in units of counts s⁻¹ mW⁻¹. 69

Figure 2.16. Example of ln(HO₂) vs t / s for a wall loss experiment i.e. without the presence of aerosols for a relative humidity of 65 %. The error bars represent 1 σ. The gradient of the wall loss (k_{wall}) was -0.02 ± 0.001 71

Figure 2.17. An example showing difference between Brown corrected k' values and $k_{obs}-k_{wall}$ values for an experiment with limonene-derived SOA aerosols. The gradient is 1.054, giving an increase of 5.4 % in k' compared to $k_{obs}-k_{wall}$ 72

Figure 2.18. First order rate coefficient, k' (s⁻¹), after brown correction, plotted against aerosol surface area (m² m⁻³) for ammonium sulphate aerosols. RH = 65 ± 2%. Uptake coefficient of HO₂ of 0.04 ± 0.01 calculated from the gradient. Error bars represent 1 σ. 73

Figure 3.1. Schematic of the Leeds aerosol flow tube system coupled to a photo-fragmentation laser-induced fluorescence detector for HONO. CPC: condensation particle counter; DMA: differential mobility analyser; HEPA: high efficiency particle air filter; FAGE: fluorescence assay by gas expansion; MCP: microchannel plate photomultiplier; MFC: mass flow controller; RH/T: relative humidity/ temperature probe; SMPS: scanning mobility particle sizer.....	80
Figure 3.2 Cross section of the mounted TSI 3076 atomiser. Image taken from TSI, 2005.....	82
Figure 3.3. Schematic of aerosol removal processes present within a HEPA filter. Black circles represent glass fibres and the beige circles represent aerosol particles.	83
Figure 3.4. Vertical cross-section of SMPS instrument. Image taken from TSI, 2008a	84
Figure 3.5. Cross-sectional schematic of an inertial impactor. Image recreated from reference TSI, 2008a.	86
Figure 3.6. Average particle number size distributions for latex calibration beads of known diameters 100 nm (black), 300 nm (red), 400 nm (blue) and 600 nm (green).	87
Figure 3.7. UV absorption spectrum of HONO at 0.5 nm optical resolution. Image taken Brust et al., 2000.....	88
Figure 3.8. Schematic of the Spectron Laser Systems Nd:YAG 1064 nm laser and optics used for the generation and delivery of 355 nm light to the OH detection cell.	89
Figure 3.9. Schematic of the detection cell and the aerosol flow tube. The gas expansion through the pinhole into the central axis of the cell is shown. The photolysis laser (blue) and the probe laser (light blue) are fired perpendicular to each other but also perpendicular to the collection optics and detector. Image adapted from Boustead, 2019.....	91
Figure 3.10. Schematic showing the data acquisition cycle for the PF-LIF instrument measuring HONO after fragmentation to OH. PCC: photon counting card, MCP: multi-channel plate. Shaded regions show when MCP and PCC are both on and data	

is being collected. The photolysis laser pulse is shown in blue and OH signal following the probe laser firing is shown in purple (OH fluorescence signal) and red (laser scatter signal)..... 94

Figure 3.11. Example data acquisition cycle with OH background not subtracted. All counts before photolysis laser trigger (shaded orange) at $\sim 160 \mu\text{s}$ can be treated as a background signal in the cell from either laser scatter from the 308 nm probe laser, residual OH plasma from the previous 355 nm laser fire in the previous run or any HONO impurities present in the cell. The dip in the OH background at $\sim 80 \mu\text{s}$ (shaded purple) is an artefact of the photon counting card (PCC) which was always present and was ignored during analysis. The peak after the photolysis laser fire (shaded blue) was due to OH formed from fragmentation of HONO, either from production on aerosols, impurities in the nitrogen or NO_2 cylinders or from formation on the walls of the cell or in the Teflon tubing. This signal then dropped off rapidly. Immediately following the peak at $\sim 160 \mu\text{s}$ a broad peak due to OH plasma formed in the cell can be seen (shaded green). This peak changed as a function of RH. The signal then returned to the OH background level (shaded orange)..... 96

Figure 3.12. Schematic of the OH calibration set-up using the OH calibration wand. Humidified air at 40 lpm is flown down the calibration wand past a collimated light source towards the pinhole of the FAGE cell. Exhaust tube is used to take excess flow to a fumehood. 98

Figure 3.13. Dependence of OH signal normalised to laser power on [OH]. Error bars represent $\pm 1\sigma$ with the linear least squares fit shown in red. The gradient (i.e. the calibration factor) is in units of $\text{counts s}^{-1} \text{mW}^{-1} \text{molecule}^{-1} \text{cm}^3$ and the intercept is in units of $\text{counts s}^{-1} \text{mW}^{-1}$ 100

Figure 3.14. HONO calibration set up using a non-collimated light source. Humidified nitrogen flow containing NO, 20 lpm, was flown into a glass wand and past non-collimated mercury lamp to generate HONO in large concentrations which flows over the pinhole. Exhaust tube used to remove toxic NO excess flow. 101

Figure 3.15. Example of O_3 actinometry showing the linear relationship between $[\text{O}_3]$ / ppb and lamp current / mA. Error bars show 1σ . Value at 2 mA is a slight outlier due to flickering of the lamp at low current. 102

Figure 3.16. Example of HONO calibration using O₃ actinometry showing the relationship between the HONO counts and the [HO_x] / molecules cm⁻³. C_{HONO} for this calibration was $(3.63 \pm 0.51) \times 10^{-9}$ counts mW⁻¹ molecule⁻¹ cm³. Linear least squares fit shown in red with the dashed lines showing the 68 % confidence limits. The intercept is in units of counts mW⁻¹ and the gradient of the slopes are in counts mW⁻¹ molecule⁻¹ cm³. The errors are 1 σ 104

Figure 3.17. NO_x profile with time during NO₂ actinometry. The illuminated periods are shaded in pink, with NO₂ (red) decreasing during these periods due to photolysis and NO (black) increasing. As the experiment progressed increasing known concentrations of NO₂ were added in a stepwise manner. 107

Figure 3.18 UVA emission spectrum for the 15 W bench lamp used in these experiments between 290-400 nm. The integrated photon flux over this wavelength range is $(1.65 \pm 0.02) \times 10^{16}$ photons cm⁻² s⁻¹ determined from the measured $j(\text{NO}_2)$ of $(6.43 \pm 0.30) \times 10^{-3}$ s⁻¹. 108

Figure 4.1. Dependence of HONO production on TiO₂ aerosol surface area. [NO₂] = 200 ppb, RH = 15 ± 1 %, illumination time = 52 s, photon flux = $(1.63 \pm 0.09) \times 10^{16}$ photons cm⁻² s⁻¹, in N₂ at 295 ± 3 K. Errors ± 1 σ showing variation in HONO signal. The non-zero intercept was due to HONO produced from the walls of the system without the presence of an aerosol surface 111

Figure 4.2. HONO concentration measured at the end of the flow tube as a function of the initial NO₂ concentration, for the aerosol surface area density of $(1.6 \pm 0.8) \times 10^{-2}$ m²m⁻³, relative humidity 15 ± 1 %, photon flux $(1.63 \pm 0.09) \times 10^{16}$ photons cm⁻² s⁻¹ (290-400 nm wavelength range), reaction time of 52 seconds and N₂ carrier gas. Each point is an average of up to 20 measurements at the same aerosol surface area and NO₂ concentration. The highest average concentration of HONO measured for the aerosol surface area density in this plot was 0.90 ± 0.12 ppb at [NO₂] = 54 ± 5 ppb. The x error bars represent the sum in quadrature of the errors in the N₂ and NO₂ gas flows and the NO₂ dilution. The y error bars represent 1 σ . The SA varied over the experiments at different NO₂ concentrations leading to a larger error in the quoted SA. 112

Figure 4.3. RH dependence of HONO production from illuminated TiO₂ aerosol surfaces at 298 K in N₂ at 71 (black) and 170 (red) ppb initial NO₂ concentration.

Aerosol surface area density was kept constant at $(1.59 \pm 0.16) \times 10^{-2} \text{ m}^2\text{m}^{-3}$. Photon flux = $(1.63 \pm 0.09) \times 10^{16} \text{ photons cm}^{-2} \text{ s}^{-1}$, illumination time = 52 ± 2 secs. The error bars represent 1σ 113

Figure 4.4. Monolayers of water on the surface of TiO_2 at 298 K as a function of % RH calculated using parameterisation by Goodman et al., 2001. 114

Figure 4.5. Typical aerosol surface area distribution for single component TiO_2 aerosols (RH = 15 ± 1 %) measured after the flow tube. Total surface area is $0.018 \text{ m}^2 \text{ m}^{-3}$ 116

Figure 4.6. Pseudo-first-order rate coefficient for HONO production, k (open circles) as a function of aerosol surface area for $[\text{NO}_2]=200 \text{ ppb}$ and RH= 15 ± 1 %, T = $293 \pm 3 \text{ K}$ and a photolysis time of 52 ± 2 seconds. The red line is a linear-least squared fit including 1σ confidence bands (dashed lines) weighted to both x and y errors (1σ), the gradient of which yields $\gamma_{\text{NO}_2 \rightarrow \text{HONO}} = (2.17 \pm 0.09) \times 10^{-5}$, with the uncertainty representing (1σ). The total photon flux of the lamp = $(1.63 \pm 0.09) \times 10^{16} \text{ photons cm}^{-2} \text{ s}^{-1}$ 118

Figure 4.7. Experimental results for the reactive uptake coefficient of NO_2 to form HONO on TiO_2 aerosol surfaces, $\gamma_{\text{NO}_2 \rightarrow \text{HONO}}$, as a function of initial NO_2 concentration. All experiments conducted in N_2 at 15 ± 1 % RH and 295 K. Photon flux = $(1.63 \pm 0.09) \times 10^{16} \text{ photons cm}^{-2} \text{ s}^{-1}$, illumination time = 52 ± 2 seconds. The uptake coefficient was determined from the gradient of the pseudo-first order rate coefficient, k , versus aerosol surface area density varied from 0- $\sim 0.04 \text{ m}^2\text{m}^{-3}$, using equation Eq 4.5. 119

Figure 4.8. Time series of HONO / counts throughout an experimental day with HONO produced with UV lamps on (black circles) i.e. production from illuminated TiO_2 surfaces, and with UV lamps off (red circles) i.e. HONO background in the lines/reacting off the walls of either the cell or the flow-tube. The gradient and intercept of the lamp off HONO dark trend was removed from the illuminated HONO data values to offset any varying background. 123

Figure 4.9. Model 1 calculations for (a) the concentration of HONO and (b) the reactive uptake coefficient to form HONO, $\gamma_{\text{NO}_2 \rightarrow \text{HONO}}$, as a function of NO_2 mixing ratio for a model run time of 52 s. The estimated rate coefficients used in this model are shown in Table 4.3. 127

Figure 4.10. Schematic diagram of proposed light-driven mechanism of HONO formation via the adsorption of NO₂ and subsequent dimerization on an aerosol surface in the presence of water. Loss reactions of HONO dependent and independent of NO₂ are also shown. Both Eley Rideal, Model 2, and Langmuir Hinshelwood, Model 3, mechanisms are shown with relevant estimated and calculated rate coefficients used also shown, detailed fully below. Nitrogen shown in black, oxygen shown in red and hydrogen shown in blue. * denotes intermediate steps of the isomerisation of symmetric N₂O₄ to *trans*-ONO-NO₂ which is then predicted to form HONO. Image taken from Dyson et al., 2021. 130

Figure 4.11. Experimental values (open circles with 1σ error bars), Model 2 (green line) and Model 3 (pink line) calculations for (a) HONO concentration after 52 s illumination and (b) NO₂ reactive uptake coefficient, $\gamma_{NO_2 \rightarrow HONO}$, as a function of the initial NO₂ mixing ratio. The mechanisms used for these model runs included a 2:1 stoichiometric relationship between the NO₂ adsorbed on the TiO₂ aerosol surface and the HONO produced, as well as additional HONO loss reactions which are dependent on NO₂, see Table 1 for details. Models 2 and use an Eley-Rideal and Langmuir-Hinshelwood mechanisms, respectively, for the formation of the NO₂ dimer on the aerosol surface. 135

Figure 4.12. Dependence of the HONO concentration generated as a function of aerosol surface area density for pure NH₄NO₃ aerosol (black open squares, error bars represent 1σ) and 1:1 TiO₂/NH₄NO₃ mixed aerosol (red open circles, error bars represent 1σ). Both experiments were performed in N₂ at 295 K, an illuminated residence time of 30 s, and a lamp photon flux of $(8.29 \pm 2.39) \times 10^{16}$ photons cm⁻² s⁻¹. The NH₄NO₃ only experiment was performed at $\sim 50 \pm 5$ % RH while the TiO₂/NH₄NO₃ mix experiment was performed at 20 ± 2 % RH. For all points, the background HONO seen observed without illumination has been subtracted. At zero aerosol surface area density there is no HONO generated from the walls of the flow tube. The variation in HONO produced for the mixed nitrate dust aerosol was thought to be due to the difficulties that arose from TiO₂ and ammonium nitrate not being completely miscible with TiO₂ tending to precipitate out of solution. 140

Figure 4.13. Dependence of [HONO] on the nitrate content within the aerosol phase, calculated using the AIM model for the mixed nitrate/TiO₂ experiment. From the gradient of this plot, $j(pNO_3)$ was calculated to be $(3.29 \pm 0.89) \times 10^{-4}$ s⁻¹. Experiment

performed at 15 ± 1 % RH, in N_2 at 295 K with a lamp photon flux of $(8.29 \pm 2.39) \times 10^{16}$ photons $cm^{-2} s^{-1}$. For all points, the background HONO seen observed without illumination has been subtracted..... 142

Figure 5.1. First steps in the ozonolysis of α -pinene. The addition of ozone across the double bond of α -pinene creates a primary ozonide which breaks apart to a Criegee intermediate (CI). The Criegee intermediate can then undergo a 1,4 H-shift to form a vinyl hydroperoxide (VHP). VHP can then rapidly lose an OH radical to form the vinyloxy radical (radical centre indicated by the black dot) which forms an RO_2 radical when O_2 is present. Figure reproduced from Iyer et al., 2021. 152

Figure 5.2. a) average particle number size distributions (cm^{-3}), b) average aerosol surface area size distributions ($m^2 m^{-3}$) and c) average volume size distribution ($nm^3 cm^{-3}$) of α -pinene-derived SOAs averaged over 5-10 runs for each initial α -pinene concentration of 4.5 ppm (green), 9 ppm (blue), 22 ppb (red) and 44 ppm (black) for an ozone concentration of 8 ppm. Experiment done in air. Temperature = 24 ± 2 °C, Pressure = 760 Torr..... 154

Figure 5.3. a) average particle number size distributions (cm^{-3}), b) average aerosol surface area size distributions ($m^2 m^{-3}$) and c) volume size distribution ($nm^3 cm^{-3}$) on 2 different experimental days (purple circles represent day 1 and green circles represent day 2), averaged over 5-10 runs, showing that reproducible size distributions can be generated using the PAM chamber. Initial α -pinene concentration = 9 ppm, O_3 concentration = 8 ppm. Total particle number was $(5.07 \pm 0.02) \times 10^6 cm^{-3}$ and $(4.58 \pm 0.03) \times 10^6 cm^{-3}$, for day 1 (pink) and day 2 (turquoise) respectively. Total aerosol surface area was $(5.94 \pm 0.04) \times 10^{-1} m^2 m^{-3}$ and $(5.68 \pm 0.06) \times 10^{-1} m^2 m^{-3}$, for day 1 (purple) and day 2 (green) respectively. All experimental conditions kept the same. Temperature = 24 ± 2 °C, Pressure = 760 Torr. Errors shown are 1σ 156

Figure 5.4. a) average particle number size distributions (cm^{-3}), b) average aerosol surface area size distributions ($m^2 m^{-3}$) and c) volume size distribution ($nm^3 cm^{-3}$) of limonene-derived SOAs, averaged over 5-10 SMPS runs, for fixed initial limonene concentrations of 1.7 ppm, ozone concentrations of 0.5 ppm (dark blue), 1.35 ppm (light blue), 2.21 ppm (light purple) and 2.85 ppm (purple). RH = 14 ± 4 %, pressure = 760 Torr, temperature = 24 ± 2 °C. Errors represent 1σ 158

Figure 5.5. a) average particle number size distributions (cm^{-3}), b) average aerosol surface area size distributions ($\text{m}^2 \text{m}^{-3}$) and c) volume size distributions ($\text{nm}^3 \text{cm}^{-3}$) of limonene-derived SOAs, averaged over 5-10 SMPS runs, for fixed O_3 limonene concentrations of 1.35 ppm, initial limonene concentrations of 0.43 ppm (red), 0.86 ppm (pink), 1.71 ppm (orange) and 3.85 ppm (yellow). $\text{RH} = 14 \pm 4 \%$ RH, pressure = 760 Torr, temperature = $24 \pm 2 \text{ }^\circ\text{C}$, flow rate = 4 lpm. Errors represent 1σ 160

Figure 5.6. a) average particle number size distributions (cm^{-3}), b) average aerosol surface area size distributions ($\text{m}^2 \text{m}^{-3}$) and c) volume size distribution ($\text{nm}^3 \text{cm}^{-3}$) of OH-initiated limonene-derived SOAs, averaged over 5-10 SMPS runs, for fixed initial limonene concentration of 1.71 ppm, with one 254 nm lamp (light green), two lamps (dark green), three lamps (grey) and four lamps (black). O_3 concentration = 1.35 ppm, $\text{RH} = 14 \pm 4 \%$. Temperature of the chamber increased from $24 \pm 2 \text{ }^\circ\text{C}$ to $60 \pm 5 \text{ }^\circ\text{C}$ during the experiment. Pressure = 760 Torr, flow rate = 4 lpm. Errors represent 1σ 162

Figure 5.7. a) average particle number size distributions (cm^{-3}), b) average aerosol surface area size distributions ($\text{m}^2 \text{m}^{-3}$) and c) volume size distributions ($\text{nm}^3 \text{cm}^{-3}$) of OH-initiated limonene-derived SOAs, averaged over 5-10 SMPS runs, for two 254 nm lamps, with 0.43 ppm (pink), 0.86 ppm (purple), 1.71 ppm (blue) and 3.85 ppm (orange) initial limonene concentration. $\text{RH} = 14 \pm 4 \%$ RH. Pressure = 760 Torr, temperature of PAM chamber = $60 \pm 5 \text{ }^\circ\text{C}$, flow rate = 4 lpm. Errors represent 1σ 166

Figure 5.8. Comparison of a) particle number size distribution (cm^{-3}), b) aerosol surface area size distributions ($\text{m}^2 \text{m}^{-3}$) and c) volume size distributions ($\text{nm}^3 \text{cm}^{-3}$) for O_3 -initiated (black circles, left axis) and OH-initiated (red circles, right axis) limonene SOA formation. Limonene concentration = 1.71 ppm, O_3 concentration = 1.35 ppm. $\text{RH} = 14 \pm 4 \%$. Note the right axes for particle number and surface area are 1 and 2 orders of magnitude larger than the respective left axes due to more aerosols in the case of OH initiated oxidation. Errors shown are 1σ 168

Figure 6.1. HO_2 signal decay with injector distance, k_{wall} , due to loss to the surface of $(\text{NH}_4)_2\text{SO}_4$ aerosols in the flow tube. Aerosol surface area = $0.006 \pm 0.0002 \text{ m}^2 \text{m}^{-3}$. By plotting $\ln\text{HO}_2$ vs t (calculated from injector distance and flow rate), a k_{obs} value of 0.11 s^{-1} can be calculated. 171

Figure 6.2. First order rate coefficient, $k'(s^{-1})$ following Brown correction, as a function of aerosol surface area (m^2m^{-3}) for $(NH_4)_2SO_4$ aerosols at 65 % RH (red circles) and 73 % RH (black circles). Error bars represent 1σ . Gradients give γ_{HO_2} of 0.037 ± 0.008 for 65 % RH and 0.010 ± 0.002 for 73 % RH. 172

Figure 6.3. Comparison of FAGE signals with and without aerosols present. a) shows the HO_2 decay signal as injector is pulled back from 30 -70 cm due to wall loss (blue). b) shows the equivalent with the presence of limonene-derived secondary organic aerosols formed via ozonolysis. Shaded orange regions show the OH background signal when NO flow and HO_2 injector lamp is off. Any signal here is dark counts and laser scatter from 308 nm laser. Shaded red regions show the NO background when HO_2 injector lamp is off but NO flow is on at 50 sccm. This is the signal from any interfering species in the NO gas cylinder, potentially HONO. Ideally this should be as close to OH background as possible. Blue shaded region shows the laser online signal with NO flow and HO_2 generation on. The slight dips in signal when the injector is moved are assumed to be due to a small quantity of lab air (and therefore trace amounts of NO) being introduced via the injector inlet and decreasing the HO_2 concentration within the flow tube. 174

Figure 6.4. FAGE OH signal ($counts\ s^{-1}$) at different injector positions (cm). No NO was present for this experiment but the injector lamp was on and as such OH but not HO_2 was measured by the FAGE cell. Error bars represent 1σ 176

Figure 6.5. Signal time series showing the effect of adding denuder in the series to remove limonene. Condition 1: No limonene added to flow, the HO_2 signal, i.e. wall loss decay, decays from $\sim 450 - 420$ counts when the injector is pulled back from 30 - 70 cm. Condition 2: limonene added to the flow with no denuder in place. Signal increases to ~ 720 counts. Production of radicals (interference A) seen when injector pulled back from 30 - 70 cm in comparison to condition 1. Slight increase in NO background in comparison to condition 1. Condition 3: Limonene added to the flow, one charcoal denuder in place. Signal decreases back to approximately counts seen in condition 1. NO background is the same for condition 2 and 3. Shaded orange regions show OH background when NO flow and HO_2 injector lamp was off. Shaded red regions show the NO background when HO_2 injector lamp is off but NO flow is on at 50 sccm. Blue shaded region shows the online signal with NO flow and HO_2

generation on. Shaded grey region shows laser offline. No O₃ was present for this experiment..... 178

Figure 6.6. Comparison of FAGE signal without aerosols present, with SOA removed and with SOA present. a) shows the HO₂ wall loss decay signal as injector was pulled back from 30 – 70 cm. b) shows FAGE signal with SOA removed by HEPA filters vs when SOA is not removed. It is possible that denuders do not fully remove any gas phase RO₂ species or other highly oxygenated molecules and that these could be causing an interference. The shaded orange region shows OH background when NO flow and HO₂ injector lamp was off. Shaded red regions show the NO background when HO₂ injector lamp is off but NO flow is on at 50 sccm. This is the signal from any contaminants in the NO lines or cylinder. Ideally this should be as close to OH background as possible. An interference in NO background is seen however when SOAs are present. Blue shaded region shows the online signal with NO flow and HO₂ generation on. Shaded grey region shows laser offline..... 179

Figure 6.7. Top panel shows the NO dependence of HO₂ signal (purple circles) and interference B signal when SOAs are present (red circles) and the NO flow is on but HO₂ injector lamp is off i.e. no HO₂ generation, between 0-65 sccm. Bottom panel shows the dependence between 0-10 sccm. Typical experimental NO flow used to convert HO₂ to OH in detection cell for the uptake of HO₂ onto SOA experiments was 50 sccm, cell pressure was 1.3 Torr. Error bars represent 1σ. 181

Figure 6.8. Comparison of FAGE signal a) before “cleaning” PAM chamber and b) after “cleaning” PAM chamber. Blue shaded regions show the online signal with NO flow and HO₂ generation on with injector pulled back from 30 – 70 cm. In both a) and b) a production signal is seen where a decay would be expected (interference A). Shaded red regions show the NO background when HO₂ injector lamp is off but NO flow is on at 50 sccm (interference B). This signal is should be ~5-10 counts mW⁻¹ s⁻¹ however interference B, present only when SOAs are present, is artificially increasing this background. This interference is lower in b) after the PAM chamber was cleaned. Interference A (shaded in blue) with NO and injector lamp on was also lower in counts after the PAM chamber was cleaned. 184

Figure 6.9. Increase in interference B signal throughout an experimental day providing strong evidence that interference is due to a build up/aging of products in the PAM chamber.	185
Figure 6.10. Example of HO ₂ decay with injector distance for wall loss experiment (grey circles) and with the presence of limonene-derived SOAs (red circles, aerosol surface area of 2.64 ± 0.05 m ² m ⁻³). Experiment done at 22 ± 2 % RH.	186
Figure 6.11. First order rate coefficient, <i>k'</i> (s ⁻¹), after the Brown correction, plotted against aerosol surface area (m ² m ⁻³) for limonene-derived secondary organic aerosols formed by reaction with O ₃ . RH = 58%. Uptake coefficient of HO ₂ of 0.15 ± 0.03 calculated from the gradient. Error bars represent 1 σ.....	186
Figure 7.1. Average median diurnal profile for measurements of <i>j</i> (O ¹ D) (s ⁻¹), O ₃ (ppbv), HONO (ppbv), NO (ppbv), NO ₂ (ppbv) and CO (ppbv) for the Summer AIRPRO campaign. The dashed lines represent the 25/75 th percentiles. Diurnals show 60 minute averages, taken over the entire measurement period.	193
Figure 7.2. Average median diurnal for (a) measured (black) and modelled (blue) OH radical concentrations, (b) measured (black) and modelled (red) HO ₂ radical concentrations, and (c) measured (black) and modelled (green) total RO ₂ radical concentrations. All model outputs shown are for MCM-base runs. 25 th /75 th percentiles in measured concentrations shown as shaded regions. Diurnals show 60 minute averages, taken over the entire measurement period.	196
Figure 7.3. The ratio of measured/modelled for MCM_base for a) OH (blue), b) HO ₂ (red) and c) RO ₂ (green) binned over the range of NO concentrations for the Summer AIRPRO campaign. Solid lines show the median average radical concentrations while dashed lines show the 25 th /75 th percentile.....	198
Figure 7.4. Simplified mechanism of the oxidation of VOCs. Figure reproduced from Kroll and Seinfeld, 2008.	200
Figure 7.5. Average diurnal comparison of measured and modelled (a) OH, (b) HO ₂ and (c) RO ₂ values from both the MCM_base (light blue) and MCM_αpinene (dark blue) models. The diurnals show 60 minute averages, taken over the entire measurement period.	201

Figure 7.6. The ratio of measured/modelled a) OH, b) HO₂ and c) RO₂ for MCM-base (light blue) and MCM- α pinene (dark blue) models binned over the range of NO concentrations for the Summer AIRPRO campaign. Solid lines show the median average radical concentrations while dashed lines show the 25th/75th percentile. ...202

Figure 7.7. Average median diurnal of aerosol surface area (cm³ cm⁻³) for summer AIRPRO campaign. Averaged up to 15 mins.204

Figure 7.8. Average median diurnal comparison between measured and modelled OH, HO₂ and RO₂ values from both the MCM- α pinene (blue) and MCM- α pinene_SA (orange). All diurnals averaged at a time resolution of 60 minutes. 25th/75th percentile shown as dashed lines.205

Figure 7.9. The ratio of measured/modelled a) OH, b) HO₂ and c) RO₂ for MCM- α pinene (blue) and MCM- α pinene_SA (orange) models binned over the range of NO concentrations for the Summer AIRPRO campaign. Solid lines show the median average radical concentrations while dashed lines show the 25th/75th percentile.206

Figure 7.10. Rate of destruction analysis (RODA) showing the dominant loss pathways of HO₂ within MCM- α pinene shown as a) a diurnal variation and b) as a function of NO concentration (as a log plot) for the whole 24 hours a day.....208

Figure 7.11. Correlation plot of aerosol surface area (cm² cm⁻³) against NO₂ (orange) and NO (red) for the Summer Beijing Campaign.210

Figure 7.12. Rate of destruction analysis (RODA) showing the dominant loss pathways of HO₂ within MCM- α pinene_SA shown as a) a diurnal variation and b) as a function of NO concentration (as a log plot) for the whole 24 hours a day. Median removal of HO₂ by uptake (%) as a function of NO / ppb is also shown as solid black line, with 25th/75th percentile shown as the black dashed lines. Maximum percentage removal by uptake is shown as an orange dashed line.....211

Figure 7.13. Contribution of HO₂ + NO (orange), HO₂ + RO₂ (green) and HO₂ uptake (teal) loss pathways to total HO₂ removal in the MCM- α pinene_SA model as a function of NO mixing ratio (log), calculated using rate of destruction analysis. 25th/75th percentile are shown as dashed lines.213

Figure 7.14. Time series of measured parameters from Beijing AIRPRO Summer campaign used to calculate HO₂ uptake coefficient using the new parameterisation (Song et al., 2020). Each parameter has been averaged up to a 1 day time resolution to calculate the uptake coefficient due to measured [Cu²⁺]_{eff} and [PM] being at this resolution. The calculated γ_{HO_2} is shown in the bottom panel, for conditions where measured ALWC was used in the calculation (dashed grey line, right hand axis) in comparison to when a fixed [ALWC] = 14 $\mu\text{g m}^{-3}$ was used (solid black line, left hand axis)..... 219

Figure 7.15. Relationship between the calculated [ALWC] / $\mu\text{g m}^{-3}$ and the measured relative humidity (RH) / % for Beijing Summer Campaign. [ALWC] calculated using ISOPROPRIA model. RH measured with a dewpoint hygrometer. 223

Figure 7.16. Dependence of uptake coefficient on aerosol copper concentration, [Cu]²⁺_{eff}, focusing on the effect of varying [PM] with fixed [ALWC] and vice versa. Pink lines show the effect on uptake coefficient of varying [PM] from 5-50 $\mu\text{g m}^{-3}$ with a fixed [ALWC] of 10 $\mu\text{g cm}^{-3}$. Blue lines show the effect on uptake coefficient of varying [ALWC] from 10-500 $\mu\text{g m}^{-3}$ with a fixed [PM] of 5 $\mu\text{g m}^{-3}$. The copper concentration range of 10⁻⁴-10⁻³ M is relevant for the Summer AIRPRO campaign. The yellow line shows the effect on the calculated uptake coefficient of varying Cu, with [ALWC] and [PM] taken as the averages from the Beijing campaign, i.e. [ALWC] = 14 $\mu\text{g m}^{-3}$ (fixed in parameterisation as such) and [PM] = 38.8 $\mu\text{g m}^{-3}$. Dashed black line indicates the average [Cu]²⁺_{eff} for Beijing summer campaign while the dashed red line indicates the average [Cu]²⁺_{eff} for the Wangdu campaign. Note that the [PM] and [ALWC] are both higher for Wangdu campaign compared to the Beijing campaign. 225

Figure 7.17. Average median diurnal comparison for modelled a) OH, b) HO₂ and c) RO₂ radicals from MCM_αpinene (blue), MCM_αpinene_SA (orange) and MCM_αpinene_SA (lilac) models. All diurnals are averaged at a time resolution of 60 minutes. 25th/75th percentile shown as dashed lines. 226

Figure 7.18. The ratio of measured/modelled OH, HO₂ and RO₂ for MCM_αpinene (blue) and MCM_αpinene_gamma (lilac) models binned over the range of NO concentrations for the Summer AIRPRO campaign for day-time values only

($j(\text{O}^1\text{D}) > 1 \times 10^6 \text{ s}^{-1}$). Solid lines show the median average radical concentrations while dashed lines show the 25th/75th percentile.....227

Figure 7.19. Rate of destruction analysis (RODA) showing the dominant loss pathways of HO₂ within MCM_αpinene_γ shown as a) a diurnal variation and b) as a function of NO concentration. Median removal of HO₂ by uptake (%) as a function of NO / ppb is shown as solid black line, with 25th/75th percentile shown as the black dashed lines. Maximum percentage removal by uptake for a given NO mixing ratio is shown as a lilac dashed line.228

Figure 7.20. Percentage contribution of HO₂ uptake to HO₂ removal as seen in MCM_αpinene_SA model (blue line, $\gamma_{\text{HO}_2} = 0.2$) and MCM_αpinene_γ model (purple line, $\gamma_{\text{HO}_2} = 0.070 \pm 0.035$) for Summer AIRPRO Beijing campaign plotted as a function of NO concentration / ppb. Dashed lines represent the 25th/75th percentiles.230

Figure 7.21. Time series of calculated HO₂ uptake coefficient (black line and markers), measured aerosol surface area/ m² m⁻³ (red line) and measured NO/ ppb (purple line) for the Summer AIRPRO campaign. Time resolution for uptake coefficient is 1 day while the time resolution for NO mixing ratio and aerosol surface area is 15 minutes.....231

Table of Tables

Table 1.1. Uptake coefficients for HO ₂ onto inorganic salt aerosols from previous work. This table has been updated from George et al., 2013.....	45
Table 1.2 Model-measurement comparisons of HO ₂ from campaigns worldwide. Table has been modified from the thesis of Slater et al., 2020.....	48
Table 2.1. Description of background measurements for FAGE instrument measuring HO ₂ uptake from aerosol surfaces.	70
Table 3.1. Summary of different HONO measurement instrumentation.	79
Table 3.2. Vibrational modes of HONO (Shan et al., 1989).....	88
Table 3.3. Uncertainty in calibration parameters.	105
Table 3.4. jNO ₂ , j(HONO) and flux values calculated through NO ₂ actinometry with 1, 2 and 4 bench lamps used.	108
Table 4.1 Percentage of NO ₂ converted through photolysis of UV lamps to NO...	121
Table 4.2. Full reaction mechanism included in Model 1 used to model the uptake of NO ₂ to form HONO on TiO ₂ aerosol surfaces. All rate coefficients are estimated, as described below,	127
Table 4.3. Full reaction mechanism included in models 1-3 used to model the uptake of NO ₂ to form HONO on TiO ₂ aerosol surfaces. All rate coefficients are estimated with the exception of the NO ₂ and HONO photolysis rate coefficient. ^a Measured using chemical actinometry with the knowledge of the experimentally determined spectral output of the lamp and the cross-sections and quantum yields of NO ₂ and HONO, see Section 3.6 for more detail. ^b Calculated using a photon flux of $(1.63 \pm 0.09) \times 10^{16}$ photons cm ⁻² s ⁻¹ . ^c Sander et al., 2003. Rate coefficients are in the units of s ⁻¹ or cm ³ molecule ⁻¹ s ⁻¹	132
Table 5.1. Average total particle number (cm ⁻³) and average total aerosol surface area (m ² m ⁻³) for increasing the number of 254 nm lamps inside the PAM chamber with O ₃ concentration fixed at 1.35 ppm. RH = 14 ± 4 %. It is worth noting that the size distributions measured were truncated at ~ 700 nm and so these total particle number and surface areas, more importantly for surface area, are underestimated due to the maximum particle size the SMPS can measure with the current DMA.	164

Table 6.1. Comparison of uptake coefficients of HO ₂ measured on dry and aqueous (NH ₄) ₂ SO ₄ salt aerosols at 293 ± 2 K.....	173
Table 7.1. Measurements taken by different universities during the Beijing Summer AIRPRO campaign. These species are directly referred to in this chapter: full description of every instrument and measurement taken can be found in Slater, 2020. IAP: Institute of Atmospheric Physics, Beijing. ICP-MS: Inductively Coupled Plasma Mass Spectrometry. Time resolution of all instruments was averaged up to or interpolated to 15 minutes for modelling purposes with the exception of the PM _{2.5} filter samples, of which there was only 1 sample taken a day.....	191
Table 7.2. Full description of measured species for Summer AIRPRO campaign, added to constrain the model.....	194
Table 7.3. Average fractional contribution (%) of individual HO ₂ loss pathways to total HO ₂ loss in MCM_αpinene.....	209
Table 7.4. Average contribution (%) of individual HO ₂ loss pathways to total HO ₂ loss in MCM_αpinene_SA. ^a The percentage change is normalised to the original MCM_αpinene model contribution for each pathway. Above 10 ppb NO, HO ₂ + NO loss pathway dominates and so the addition of HO ₂ uptake is not significant.	212
Table 7.5. Average parameter values for the Summer AIRPRO campaign in Beijing 2017. ^a This is the minimum required ALWC for which the parameterisation can be used. For most of the campaign the ALWC was below 14 μg m ⁻³ . Copper (II) ion concentration is given in both mol L ⁻¹ and ng m ⁻³ due to mol L ⁻¹ being the unit used in the parameterisation but ng m ⁻³ being a more atmospherically relevant unit.	218
Table 7.6. Sensitivity analysis showing effect of changing the mass accommodation coefficient, <i>a</i> HO ₂ , on the calculated average γHO ₂ for the Summer AIRPRO campaign in Beijing, 2017.	220
Table 7.7. Average measured parameters in new parameterisation for the Wangdu 2014 campaign (Song et al., 2020). Copper (II) ion concentration given in both mol L ⁻¹ and ng m ⁻³ due to mol L ⁻¹ being the unit used in the parameterisation but ng m ⁻³ being a more atmospherically relevant unit.	221

Table 7.8. Comparison of measured parameters in new parameterisation for the Summer AIRPRO Beijing 2017 Campaign and the Wangdu 2014 campaign (Wangdu campaign values from Song et al., 2020)..... 223

Table 7.9. Average contribution (%) of individual HO₂ loss pathways to total HO₂ loss in MCM_αpinene (shaded blue), MCM_αpinene_gamma (shaded lilac) and MCM_αpinene_SA (shaded orange) for <0.1 ppb NO..... 229

List of Abbreviations

AIM	Aerosol Inorganic Model
AIRLESS	effects of AIR pollution on cardiopulmonary disease in urban and peri-urban residents in Beijing
AIRPOLL	sources and emissions of AIR POLLutant in Beijing
AIRPRO	An integrated study of AIR pollution PROCesses in Beijing
APHH	Air Pollution and Human Health
APIC-ESTEE	Air Pollution Impacts of Cardiopulmonary disease in Beijing: an integrated study of Exposure Science, Toxicogenomics and Environmental Epidemiology
BBO	β -Barium Borate
BC	Black Carbon
BNC	Berkeley Nucleonics Corporation
BrC	Brown Carbon
BVOC	Biogenic Volatile Organic Compound
CCN	Cloud Condensation Nuclei
CH ₄	Methane
CI	Criegee Intermediate
CIMS	Chemical Ionisation Mass Spectrometry
ClearfLo	Clean air for London
CO	Carbon Monoxide
CO ₂	Carbon Dioxide
CPC	Condensation Particle Counter
CPM	Channel Photomultiplier
CRDS	Cavity Ring Down Spectroscopy
DMA	Differential Mobility Analyser

DOAS	Direct Optical Absorption Spectroscopy
ELVOC	Extremely Low Volatility Organic Compounds
FAGE	Fluorescence Assay by Gas Expansion
GC	Gas Chromatography
GEOS-CHEM	Goddard Earth Observing System (chemical transport model)
H ₂ SO ₄	Sulphuric acid
HEPA	High Efficiency Particle Air
HNO ₃	Nitric acid
HO ₂	Hydroperoxy Radical
HOM	Highly Oxygenated Molecule
HONO	Nitrous Acid
HO _x	Hydroxyl and Hydroperoxy radicals
IAP	Institute of Atmospheric Physics
INHANCE	Integrated assessment of the emission-health-socioeconomic nexus and air pollution mitigation solutions and interventions in Beijing
ID	Internal Diameter
IPCC	Intergovernmental Panel on Climate Change
IR	Infra-Red radiation
k(OH)	OH reactivity
LIF	Laser Induced Fluorescence
LOD	Limit of Detection
LOPAP	Long Path Absorption Photometer
lpm	litres per minute
LP-DOAS	Long Path Differential Optical Absorption Spectroscopy
MCM	Master Chemical Mechanism
MCP	Micro Channel Plate

MFC	Mass Flow Controller
MRC	Medical Research Council
N ₂	Nitrogen
NAMBLEX	North Atlantic Marine Boundary Layer Experiment
NCP	North China Plain
Nd:YAG	Neodymium doped Yttrium Aluminium Garnet
NERC	Natural Environmental Research Council
NO	Nitric Oxide
NO ₂	Nitrogen Dioxide
NO _x	Nitrous Oxides
NSFC	National Natural Science Foundation of China
O ₂	Oxygen
O ₃	Ozone
OA	Organic Aerosol
OC	Organic Carbon
OD	Outer Diameter
OH	Hydroxyl Radical
OVOC	Oxygenated Volatile Organic Compound
PAM	Potential Aerosol Mass
PF-LIF	Photo-Fragmentation Laser Induced Fluorescence
ROS	Reactive Oxygenated Species
RO ₂	Peroxy Radical
PM	Particulate Matter
PM _{2.5}	Particulate Matter below 2.5 μm in size
PM ₁₀	Particulate Matter below 10 μm in size
PMT	Photo-Multiplier Tube

ppb	Parts Per Billion
ppm	Parts Per Million
ppt	Parts Per Trillion
PSL	Polystyrene Latex
RH	Relative Humidity
RHaMBLe	Reactive Halogens in the Marine Boundary Layer
SA	Surface Area
SOA	Secondary Organic Aerosol
Slm	Standard litres per minute
SMPS	Scanning Mobility Particle Sizer
SNR	Signal to Noise Ratio
SVOC	Semi-Volatile Organic Compound
TiO ₂	Titanium dioxide
TMI	Transition Metal Ion
UM-UKCA	Unified Model - United Kingdom Chemistry and Aerosol
UV	Ultra Violet
VOC	Volatile Organic Compound
W.H.O.	World Health Organisation
WRF-Chem	Weather Research and Forecasting model coupled with Chemistry

1 Introduction

1.1 Atmospheric Warming and Air Quality

Two major concerns facing society in the 21st century are climate change and air pollution. Since the industrial revolution, anthropogenic emissions of species such as carbon dioxide (CO₂), nitrogen oxides (NO_x) and methane (CH₄) have been increasing. CO₂, CH₄ and water vapour are greenhouse gases which contribute to global warming through their positive radiative effect, with water vapour being the largest contributor to the natural greenhouse effect (Myhre et al., 2013). The relationship between greenhouse gas concentrations and surface temperature since 1850 is shown in Figure 1.1.

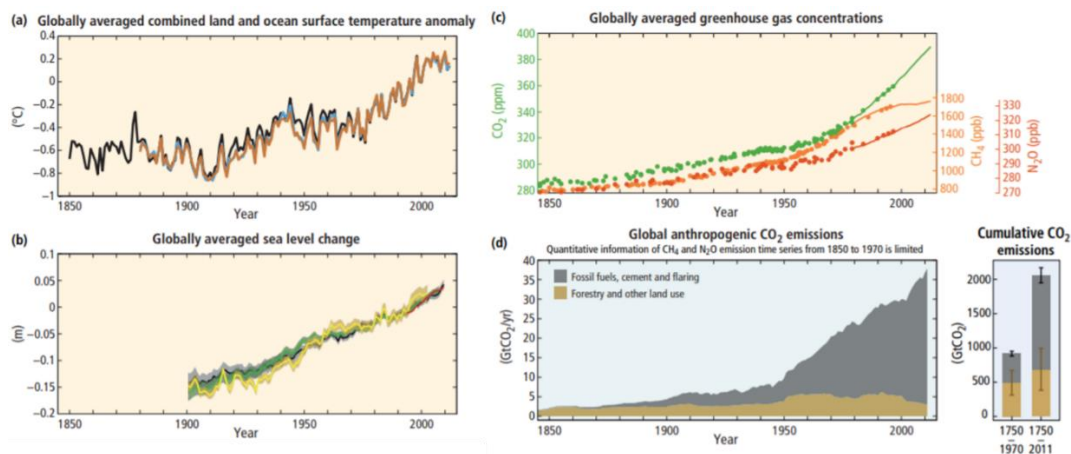


Figure 1.1. Relationship between observations of land and ocean surface temperature, greenhouse gas concentrations and sea level and the anthropogenic CO₂ emissions. a) Globally averaged combined land and ocean surface temperature anomalies relative to the average over the period of 1986-2005. b) Globally averaged sea level change relative to the same period. c) Atmospheric concentrations of greenhouse gases CO₂ (green), methane (orange) and nitrous oxide (red) determined from ice core data (dots) and direct atmospheric measurements (lines). d) Global anthropogenic CO₂ emissions from forestry and land use in addition to fossil fuel combustion. Image taken from IPCC 2014 synthesis report (IPCC, 2014).

Radiative forcing is a measure of the net change in the energy balance of the Earth system due to an imposed perturbation, usually presented as changes between pre-industrial and present day, and is one of the more widely employed metrics used to examine how anthropogenic drivers contribute to climate change (Myhre et al., 2013). An increase in greenhouse gases in the atmosphere, whether due to increased anthropogenic emission or as a bi-product of increased temperature (for example,

increased water vapour concentrations with increasing atmospheric temperature), hinders the loss of infra-red radiation from the Earth's surface to space, skewing the balance of incoming and outgoing radiation and leading to a warming effect; the effects of which can be seen in the melting of the polar ice caps, extreme weather, the acidifying of oceans, the expansion of subtropical deserts and species extinction (Forster et al., 2007). One of the main reasons for striving to understand atmospheric chemistry is to be able to predict climate change and contain future warming of the atmosphere. The radiative forcing effect of various pollutants and aerosols are shown in Figure 1.2.

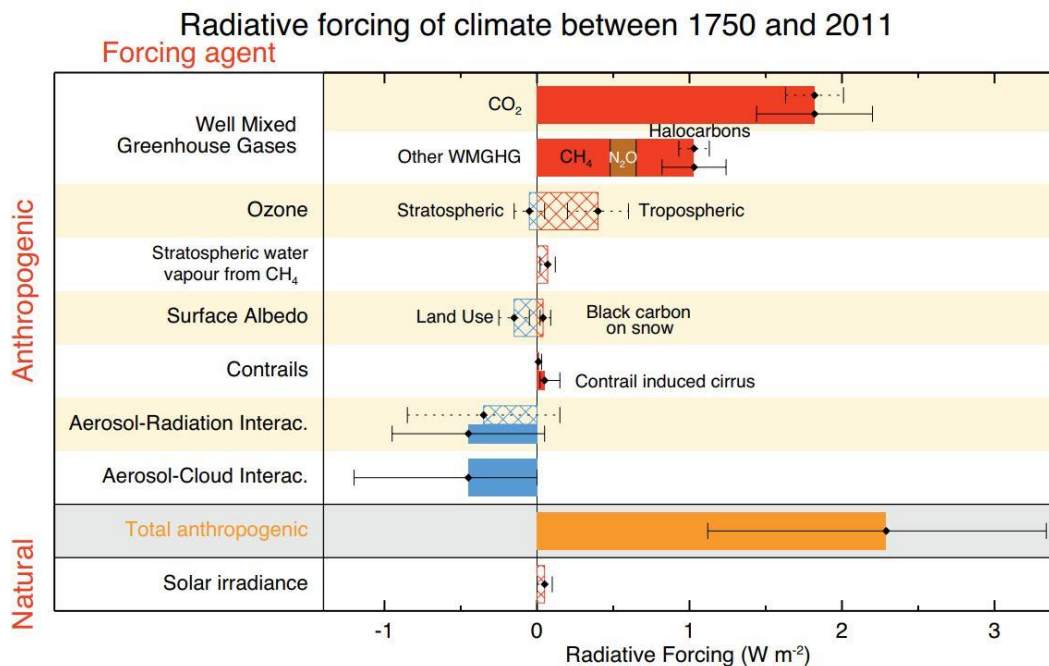


Figure 1.2. Global mean radiative forcing taken from 2013 IPCC report. The effective radiative forcing (defined by the IPCC as the change in the net top of the atmosphere downward flux after allowing for atmospheric temperatures, water vapour and clouds) is shown as solid bars whereas the radiative forcing is shown as hatched bars for the period 1750-2011 (Myhre et al., 2013).

In addition to the warming of the atmosphere, increased anthropogenic emissions have led to a deterioration in air quality: a concern due to the serious long term negative health effects seen as a product of poor air quality and the other main reason for having a thorough understanding of atmospheric chemistry. Exposure to high levels of pollution can lead to premature death from respiratory diseases, cardiovascular diseases and cancer (Brauer et al., 2016;Gakidou et al., 2017). As well as having a negative effect on human health, a decreased standard of air quality can have undesirable effects on the environment, such as an increase in acid rain leading to an

increase in acidic species in soil which leads to damaged vegetation and a reduction in crop yield (Forster et al., 2007).

In many regions the three most important pollutants in terms of human health are ground level ozone, NO_x and particulate matter. NO_x (NO₂ and NO) is released into the atmosphere as a product of combustion and is a major pollutant leading to poor air quality and the formation of photochemical smog. Nitrogen dioxide (NO₂) is formed by the reaction of nitrogen monoxide (NO) with an oxidising species in the troposphere, such as HO₂, leading to the formation of the hydroxyl radical (OH) (Ye et al., 2017a). NO₂ can also be directly emitted from high temperature combustion engines. An increase NO₂ in the atmosphere and therefore in photochemical smog has led to an increase in respiratory problems such as asthma (IPCC, 2014). In the troposphere, the dominant oxidising species involved in the formation of NO₂ is ozone (O₃). While stratospheric ozone provides a protective blanket for the earth against harmful UV radiation and excessive planetary heating, ground level ozone is toxic to both humans and plant life. Tropospheric ozone causes damage at a cellular level, impairing cellular function. Additionally ozone reduces the carbon assimilation of trees leading to deforestation and the potential for future food shortage (Kinney, 2008). In the short term, these pollutants can all cause shortness of breath and pain breathing, coughing, throat irritation and inflamed respiratory tracts as well as increased risk of complications for pre-existing respiratory conditions (Kinney, 2008).

Aerosols and particulate matter are also major contributors to poor urban air quality. Aerosols are liquid or solid particles suspended in a gas and have both natural and anthropogenic sources with particles below 10 µm in size, known as PM₁₀, being hazardous to human health. PM₁₀ can travel into the bronchi and cause lasting damage to the inside of the lungs. However, particles below 2.5 µm in diameter, PM_{2.5}, can get into the bloodstream and cause damage on a cellular level (IPCC, 2014). In 2016, the WHO stated that indoor and outdoor air pollution was responsible for an estimated 7 million deaths globally, with 91% of the world's population living in places where the air quality exceeds the WHO guideline limits (GBD 2015 Risk Factors Collaborators, 2016). Aerosols also play a role in the warming and cooling of the atmosphere due to their ability to act to both absorb and scatter IR radiation, meaning they have both a positive and a negative radiative forcing effect.

1.2 Tropospheric Oxidation Chemistry

1.2.1 The HO_x Cycle

The hydroxyl radical (OH) and the closely coupled hydroperoxyl radical (HO₂), known collectively as HO_x radicals, are known for their role in the chemical oxidation processes in the atmosphere therefore making them vital species when considering climate change and air pollution. The OH radical is the main daytime tropospheric oxidant, with a major role as a source of tropospheric ozone (O₃) (Levy, 1971) and as a sink for atmospheric pollutants and radical species, making OH radical concentration critical in determining the oxidation capacity of the atmosphere. Trace gases, of which methane is a prime example, are removed from the atmosphere by OH, giving it the name of the “atmospheric detergent”. However, the OH radical also has a role in the formation of secondary pollutants such as tropospheric ozone and secondary organic aerosols (SOAs), formed via the oxidation of volatile organic compounds (VOCs). Understanding the sources and sinks of OH, and HO₂, within the atmosphere is therefore crucial in order to fully understand the concentration and distribution of trace atmospheric species associated with climate change and poor air quality. The HO_x cycle showing the main production, loss and regeneration of OH is shown in Figure 1.3. Note the role of nitrogen oxides (NO_x) within the HO_x cycle. These pathways will dominate in urban, high NO_x environments.

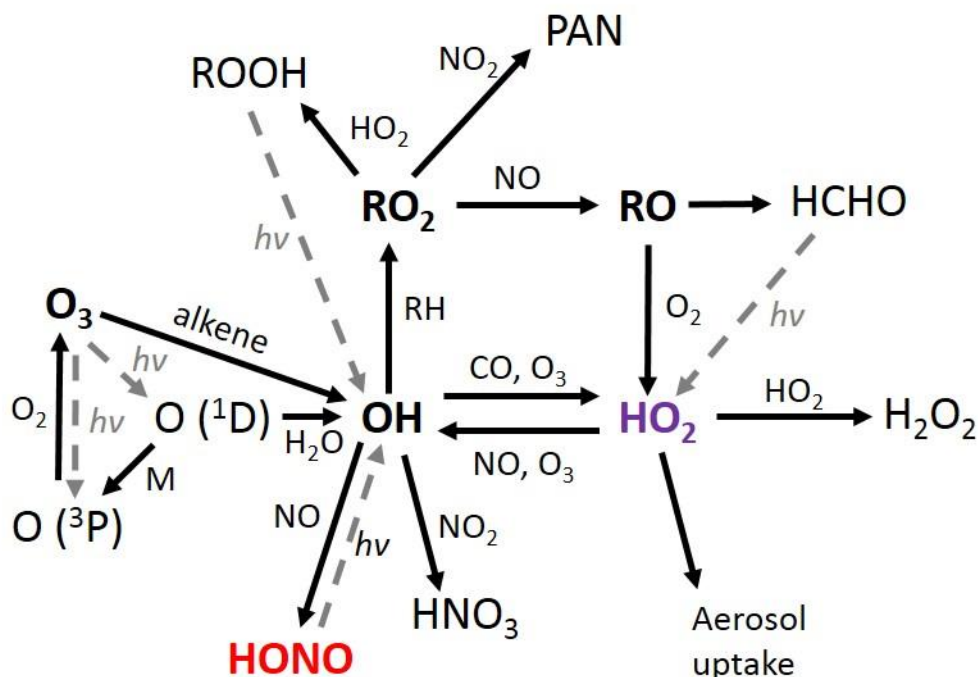
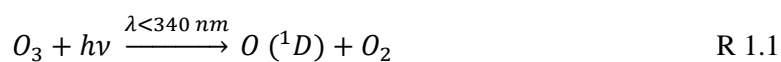
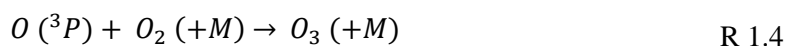


Figure 1.3. Schematic of the HO_x cycle showing the major production and destruction pathways of tropospheric oxidants, OH and HO₂.

The OH radical is formed primarily from the photolysis of O₃ at $\lambda < 340$ nm followed by the reaction of O (¹D) with H₂O_(v):



The majority of the excited O (¹D) state formed will be quenched back to its ground O (³P) state, by an inert gas (M) e.g. nitrogen, due to water vapour only being present in trace amounts in the atmosphere. This ground state of atomic oxygen can then react to reform O₃ via the reaction with diatomic oxygen:



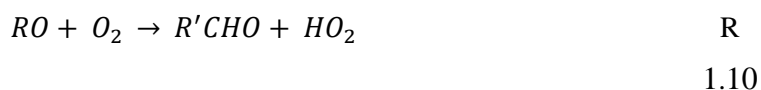
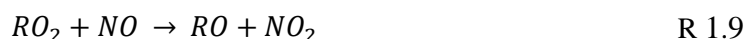
The OH radicals formed can then react with carbon monoxide (CO) to give HO₂. In low NO_x and VOC environments, around 70 % of OH formed will undergo this reaction to form HO₂ (Holloway and Wayne, 2010).



OH can then be reformed by the reaction of HO₂ with O₃:



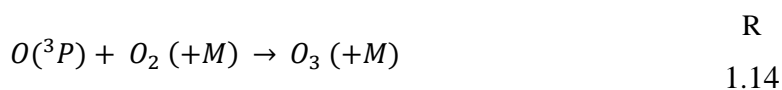
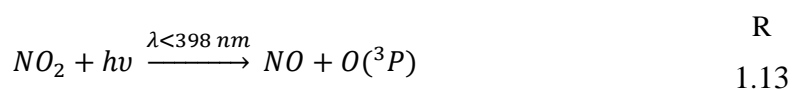
In high NO_x and VOC environments, OH is lost via the reaction with methane or a combination of VOCs to form peroxy radicals (RO₂). The formed RO₂ radicals can then react with NO to form RO radicals which then further react with O₂ to form HO₂.



Under high NO_x conditions, HO₂ is lost by the reaction with NO to regenerate the OH radical, which can be lost through reaction with NO₂ to form HNO₃.



The NO₂ formed via the reaction of HO₂ or RO₂ with NO, can then be photolysed to form O (³P) which then reacts with O₂ to reform the polluting tropospheric O₃. The reactions of HO₂ and RO₂ with NO are the only pathways for net O₃ production in the troposphere.



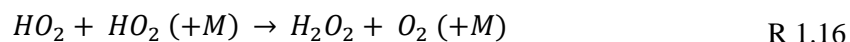
In low NO_x conditions, i.e. remote or rural environments however, RO₂ radicals can react via a self or cross reaction, eventually leading to the formation of HO₂.



In addition to bimolecular self or cross-reaction, RO₂ radicals can undergo an inter- or intramolecular H-abstraction leading to autoxidation on the addition of O₂, following a H-shift. Alkoxy, RO radicals, can also undergo a H-shift followed by O₂ addition, to

form a new RO₂ with one more oxygen than the previous RO₂. In this way, highly oxygenated molecules (HOMs) are formed.

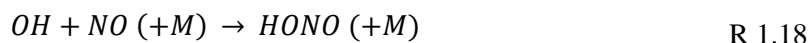
The loss process of HO₂ in low NO_x conditions is governed by the self-reaction and the reaction with RO₂, though the uptake of HO₂ onto aerosol surfaces could also be important in environments with high aerosol loadings:



1.2.2 The Role of Nitrous Acid

A major source of OH in polluted environments is the photolysis of nitrous acid (HONO) at $\lambda < 400$ nm. Previous studies have shown HONO to be a dominating source of OH in the early morning especially due to longer wavelength light being prevalent (Ren et al., 2006; Dusanter et al., 2009; Michoud et al., 2014). During a recent study in Beijing Wintertime, HONO photolysis accounted for over 90 % of the primary production of OH averaged over the day (Slater et al., 2020; Dyson et al., 2021). As such, understanding the formation of HONO in highly polluted environments is crucial to understanding the concentration and distribution of OH and other key atmospheric radical species, as well as secondary gas or aerosol phase products associated with climate change and air quality.

Concentrations of HONO in the atmosphere can range from a few pptv in remote clean environments (Reed et al., 2017) to over 10 ppbv in more polluted areas such as Beijing (Crilley et al., 2019). The main gas phase source of HONO in the troposphere is through the reaction of NO with the OH radical, with the loss process being via photolysis to reform OH making HONO both a source and a sink of OH radicals, as shown below:



HONO has also been shown to be directly emitted by vehicles (Kurtenbach et al., 2001; Li et al., 2008), the rate of emission of which is generally estimated as a fraction of known NO_x (NO₂+NO) emissions. Current atmospheric chemistry models underestimate the concentration of HONO indicating a potential missing tropospheric source of HONO. Many studies have postulated reactions to account for the missing

source, with these most commonly being heterogeneous in nature, either on aerosol or ground surfaces. Direct flux measurements, tower and aircraft observations demonstrate the existence of HONO sources from ground or canopy surfaces (Vogel et al., 2003; Zhang et al., 2009; Ren et al., 2011; Sörgel et al., 2011a; Wong et al., 2012; Young et al., 2012; Zhang et al., 2012; Oswald et al., 2015; Sörgel et al., 2015). These sources could involve photo-enhanced conversion of HNO₃ to HONO on ground surfaces (Zhou et al., 2003; George et al., 2005), bacterial production from nitrate sources found in soil (Su et al., 2011; Oswald et al., 2013), HONO formation from the photolysis of particulate nitrate, postulated to be important in marine environments (George et al., 2005; Oswald et al., 2013; Ye et al., 2016b; Reed et al., 2017; Ye et al., 2017a; Ye et al., 2017b), photolysis of ortho-substituted nitrophenols (Bejan et al., 2006) and photo-sensitized reduction of NO₂ on humic surfaces (Stemmler et al., 2007; Zhou et al. 2011). Rapid cycling of gas-phase nitric acid to nitrous acid via particulate nitrate photolysis in the clean marine boundary layer was experimentally measured from aerosol filter samples collected during the 2013 NOMADSS aircraft measurements campaign over the North Atlantic Ocean (Ye et al., 2016b). In addition to this ground-based measurements of HONO made at Cape Verde in the tropical Atlantic Ocean (Reed et al., 2017) provided evidence that a mechanism for renoxification in low NO_x areas is required (Reed et al., 2017; Ye et al., 2017a).

Recent model calculations depict a missing daytime source of HONO, not consistent with known gas-phase production mechanisms, direct HONO emissions or dark heterogeneous formation i.e. prevalent night-time sources. A detailed HONO budget analysis was completed following the ClearfLo project in London in the summer of 2012 which compared the measured average daytime concentration of HONO, 0.4 ppbV, to the output of a zero-dimensional model using the Master Chemical Mechanism (MCMv3.2) including the following HONO sources: direct emission, photolysis of ortho-substituted nitro-phenols, the proposed reaction of HO₂×H₂O with NO₂, photolysis of adsorbed HNO₃ on ground and aerosol surfaces and the photosensitized conversion of NO₂ to HONO (Lee et al., 2016). The addition of sources only increased the average daytime modelled HONO concentration to 0.1 ppbV leaving a significant missing source of 0.3 ppbV suggesting a current lack of understanding in additional heterogenous sources of HONO production. Correlation

studies showed, as has been suggested previously, that the missing source is both light-driven and dependant on the NO_2 concentration (Kleffmann, 2007; Michoud et al., 2014; Spataro and Ianniello, 2014; Lee et al., 2016). This project will investigate the production of HONO from aerosol surfaces in further detail.

1.2.3 The Importance of Atmospheric Models

In a world where approximately 7 million people die a year due to indoor and outdoor air pollution it is imperative to understand the effect pollutants have on the atmosphere in order to accurately predict the lifetime of the longer lived pollutants which impact climate and air quality (GBD 2015 Risk Factors Collaborators, 2016). Atmospheric models can therefore be utilised in a predictive capacity to mitigate anthropogenic effects on the environment. Comparing field data to model outputs allows the study of atmospheric systems and specific atmospherically relevant compounds. Any missing sources or sinks in proposed mechanisms can then be identified and examined through further experimental and modelling studies.

As stated above, recent model calculations under-predict the concentration of HONO suggesting a missing daytime source of HONO. Numerical chemistry models also have a tendency to over predict HO_2 especially in low NO_x conditions due perhaps to lack of understanding of heterogenous uptake of HO_2 onto aerosol surfaces.

1.2.4 Short Introduction to the Thesis

This thesis will address the role of aerosols in the gas-phase composition of the troposphere through the experimental study of the uptake and production of HONO, HO_2 and RO_2 onto atmospherically relevant submicron aerosols as a function of temperature and relative humidity.

Specifically, the production of HONO from TiO_2 single-component and mixed aerosol surfaces will be investigated and the mechanism of formation modelled using a kinetic box model. The uptake of HO_2 onto limonene-derived secondary organic aerosols, formed via both ozonolysis and OH oxidation with an oxidation flow reactor, will be also reported. Lastly, HO_2 uptake modelled using a new parameterisation will be presented and compared to measured radical concentrations from the Beijing Summer AIRPRO campaign.

1.3 The Sources and Properties of Atmospheric Aerosols

As mentioned in Section 1.1, aerosols act as both absorbers and emitters of IR radiation meaning they have both a positive and negative radiative forcing effect and so play a role in both the warming and cooling of the atmosphere. An increase in aerosols in the atmosphere will also have an indirect effect on climate and global warming: aerosols can act as cloud condensation and ice nuclei leading to a change in the single scattering albedo. Aerosols can also affect the abundance and spread of trace gases by both heterogeneous and multiphase processes. They also have a role in the spread of pathogens and other biological organisms.

Aerosols are suspended particles, typically between 1 nm and 100 μm in diameter which can be classed into different modes depending on their size, shown in Figure 1.4. The most abundant aerosol mode in the atmosphere is known as the Aitken mode consisting of aerosols below 0.1 μm in diameter. Between 0.1 and 5 μm , aerosols are known as the accumulation mode, with any aerosols between 1 – 100 μm being known as the coarse mode. Accumulation mode aerosols are generally formed from the growth via coagulation or condensation of ultrafine particles whereas coarse mode aerosols are formed from mechanical generation processes at the Earth's surface such as erosion (Pöschl, 2005). Example aerosol surface area and particle number size distributions typically measured during the TiO₂ HONO experiment are shown in Figure 1.5.

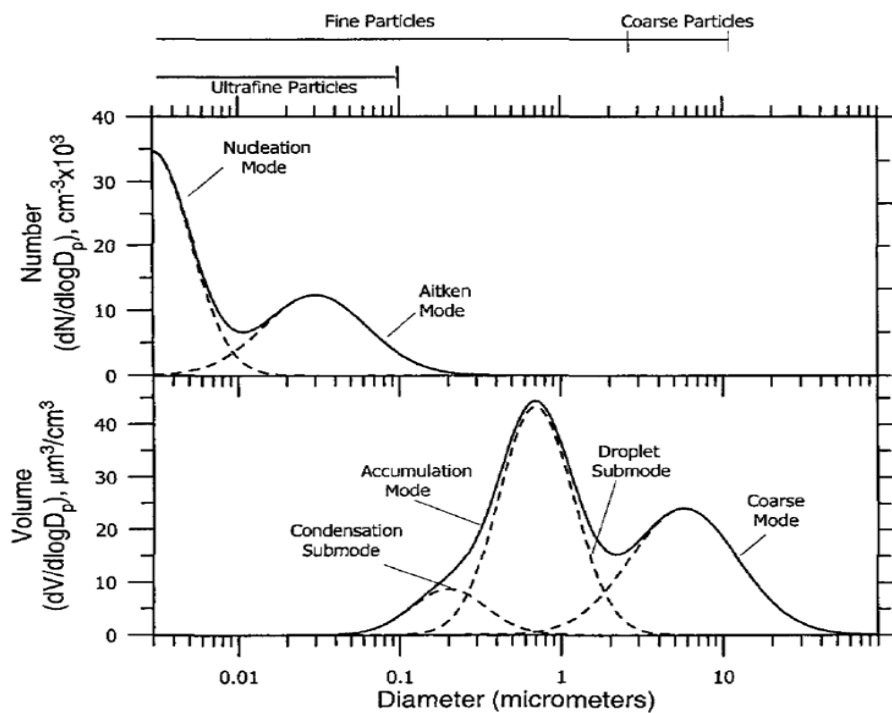


Figure 1.4. Typical number and volume distributions of atmospheric particles within different aerosol modes. Image taken from (Seinfeld and Pandis, 2006).

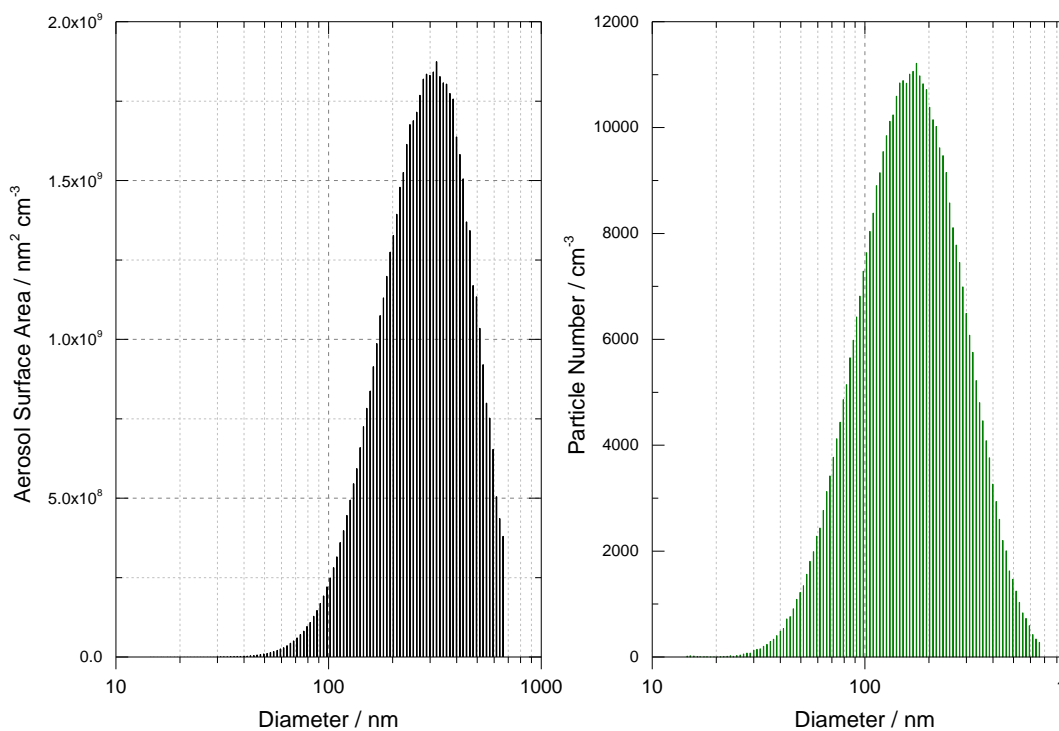


Figure 1.5. Aerosol size distributions for TiO_2 aerosols generated during the HONO production experiment showing aerosol surface area (black) and aerosol particle number (green) between diameters of 14 and 661 nm (sheath flow: 3 lpm).

Aerosols are also categorised as either primary or secondary. Primary aerosols are emitted directly into the atmosphere while secondary aerosols are produced by gas-to-particle conversion. Examples of primary aerosols include sea salt, biogenic aerosols, carbonaceous aerosols and mineral dust. Secondary aerosols include sulphate aerosols, secondary organic aerosols formed from the oxidation of volatile organic compounds and nitrate aerosols (Boucher et al., 2013). Aerosols can be further categorised into biogenic and anthropogenic aerosols. Anthropogenic aerosols are mainly produced by fuel combustion and account for ~20% of all solid particles in the atmosphere (Wayne, 2000). Due to a large proportion of the world's industry being located in the northern hemisphere, aerosols formed from combustion products, such as black carbon and sulphate aerosols, are prevalent there. Primary organic aerosols can be produced by wildfires or biomass burning, a phenomena prevalent in Africa and South East Asia. In comparison, biogenic production of aerosols occurs as a result of natural phenomena such as sandstorms, volcanos and sea spray. A large component of atmospheric biogenic aerosols is mineral dust especially around the equatorial Atlantic where a large component of aerosols is Saharan dust (Pöschl, 2005).

In the atmosphere, gas phase chemistry can lead to the formation of oxygenated volatile organic compounds (VOCs), which then condense to the aerosol phase. Aerosols formed in this way are known as Secondary Organic Aerosols (SOAs), and can be formed via several different pathways: firstly, new particle formation where semi-volatile organic compounds (SVOCs) are formed and go on to allow nucleation and growth of new aerosol particles; secondly, the formation of SVOCs by either gas-phase reaction or uptake onto existing aerosol or cloud particle surfaces and lastly, by heterogeneous reactions forming low or non-volatile compounds by chemical reaction with VOCs or SVOCs at the surface or inside the bulk of existing cloud or aerosol particles (Pöschl, 2005).

Aerosol loadings in the troposphere can typically vary between $\sim 1 \mu\text{g m}^{-3}$ and $100 \mu\text{g m}^{-3}$ though higher loadings have been observed during pollution events in megacities (Seinfeld and Pandis, 2006). During a measurement period in Beijing in January 2013, Zhang et al., 2014 reported concentrations of submicron aerosols of up to $423 \mu\text{g m}^{-3}$ comprised of organic aerosols (50 %), sulfates (22 %), nitrates (14 %), ammonium (10 %) and chloride (4 %). In comparison, during the ClearfLo campaign in London in 2012, SOA levels peaked at $\sim 15 \mu\text{g m}^{-3}$ (Ots et al., 2016).

The chemistry involving aerosols depends on the composition of the aerosol. Some aerosols, such as inorganic salt aerosols, can exist as either solid or aqueous aerosols, depending on the relative humidity. Aqueous salts in the atmosphere cycle between liquid and crystalline phases depending on the available gas-phase water, due to the hygroscopicity of the aerosol. Hygroscopicity is typically defined as the ability of a substance, such as an aerosol particle, to *adsorb* or *absorb* water as a function of relative humidity (RH) (Xu et al., 2020). Interactions with water vapour in the atmosphere largely changes the roles of aerosol particles in the earth system as well as the size. When water vapour is supersaturated, meaning $RH > 100\%$ aerosol particles can act as cloud condensation nuclei (CCN) leading to the formation of cloud droplets. Aerosols can also act as ice nucleating particles (INP) leading to the formation of ice crystals (Tang et al., 2014b). When water vapour is not supersaturated however, i.e. $RH < 100\%$ the aerosol particles in the surrounding environment exist in an equilibrium containing a certain amount of adsorbed or absorbed water. A RH of 0% correlates to a totally dry atmosphere, such as over a dry desert. The amount of water that an aerosol particle can contain depends on the RH, temperature, chemical composition and size of the particle (Moon et al., 2018; Xu et al., 2020).

The water content of aqueous aerosols is controlled largely by the RH of the atmosphere. The RH dictates the proportion and the size of condensed aqueous aerosols in the atmosphere. RH is defined as the ratio of the partial pressure of gaseous water to the saturation vapour pressure of pure water at a fixed temperature (Lin and Tabazadch, 2002). As the RH increases a point is reached where, depending on aerosol composition, a solid particle will spontaneously absorb water and become aqueous. This is known as the deliquescence point. Past this point, the aerosol will continue to take up water, thereby growing in size. However, a decrease in humidity back towards the deliquescence point will not necessarily lead to re-crystallisation of the aerosol. This is due to hysteresis. The point at which a condensed aerosol returns to a solid particle form due to a decreasing RH is known as the efflorescence point. At this point a solid core will reform inside the aerosol. Above the efflorescence point the aerosol can become supersaturated and form a metastable solution due to the energy barriers of crystallisation. Because of this phenomenon it is important to know the composition and solubility of aerosols as the size and the phase of the aerosols is often dependant

on the RH and can change rapidly with changing RH. Figure 1.6 shows an example of a sea salt aerosol deliquescence curve.

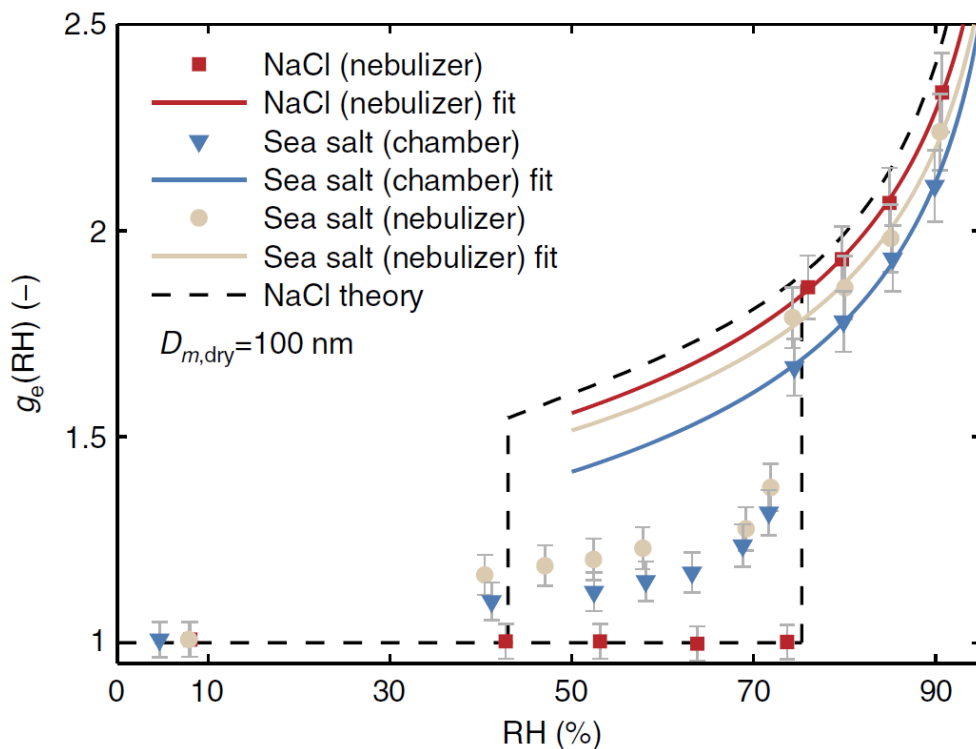


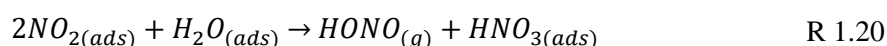
Figure 1.6. Deliquescence curve for NaCl showing the hygroscopic growth factor, g_e versus RH at a dry diameter of 100 nm for NaCl from a nebulizer or sea spray chamber. Image taken from Zieger et al., 2017.

1.4 Heterogeneous Production of HONO from Aerosol Surfaces

Previously, ambient aerosols have been considered an unimportant heterogeneous reaction media in comparison to ground or canopy surfaces which have a larger surface area. In urban areas however, like London or Beijing, aerosols could still be a significant source of HONO. The importance of aerosol surface area is still debated with respect to the heterogeneous formation of HONO. The dependence of HONO formation on light and aerosol surface area is often expressed by calculating the NO_2 reactive uptake coefficient, γ_{NO_2} .

The dark heterogeneous formation of HONO is known to occur via the uptake of NO_2 on aerosol, ground or canopy surfaces. The main source of HONO in dark periods is the hydrolysis of NO_2 to produce gaseous HONO, leaving HNO_3 adsorbed to the surface, shown in R 1.20. This reaction is seen experimentally under dark conditions

and is also observed during field campaigns as an accumulation of HONO throughout the night (Finlayson-Pitts et al., 2003; Ramazan et al., 2004b; Gustafsson et al., 2006).



Heterogeneous production of HONO from surfaces and coated wall experiments have been more thoroughly studied, especially relating to the hydrolysis reaction of NO₂ on surfaces coated with HNO₃ in the dark. Heterogeneous production from aerosol surfaces under illuminated conditions are less well studied however. Several studies have been conducted on a range of atmospherically relevant aerosols such as secondary organic aerosols, humic acid and TiO₂ (Bröske et al., 2003; Gustafsson et al., 2006; Stemmler et al., 2007; Dupart et al., 2014).

1.4.1 Humic acid

Humic compounds are formed from the degradation of biological matter and are the most abundant organic species on the Earth's surface (Stemmler et al., 2007). Due to soil abrasion and biomass burning, humic matter is likely to exist on airborne surfaces. Aromatic compounds found in biomass burning aerosol may undergo oxidation processes that lead to humic-like substances (HULIS). HULIS are high molecular weight organic compounds found in atmospheric particles, fog and cloud water and are known as "humic-like" due to the similarity to ground/marine humic substances (Zheng et al., 2013). HULIS are of interest due to their surface activity and light absorbing capability and photochemical activity. HULIS can have an effect on aerosol hygroscopicity, cloud condensation nuclei formation, aerosol surface tension and aerosol optical properties (Kiss et al., 2005; Dinar et al., 2007; Fan et al., 2012). Possible sources of HULIS include soil (Simoneit, 1980, plants Salma et al., 2010), ocean (Krivácsy et al., 2008), biomass burning (Salma et al., 2010; Kuang et al., 2015), coal combustion (Tan et al., 2016), oil burning in shipping (Kuang et al., 2015), vehicular emissions (Yamanokoshi et al., 2014) and secondary formation (Krivácsy et al., 2008; Kuang et al., 2015).

A study by Stemmler et al., 2007 investigated the interactions of humic acid aerosols with NO₂ under illuminated conditions reporting relatively low uptake coefficients in the range of 10⁻⁷ (dark) – 6 × 10⁻⁶ (illuminated). The dependence of the uptake coefficient on NO₂ concentration in this study is shown in the inset of Figure 1.7.

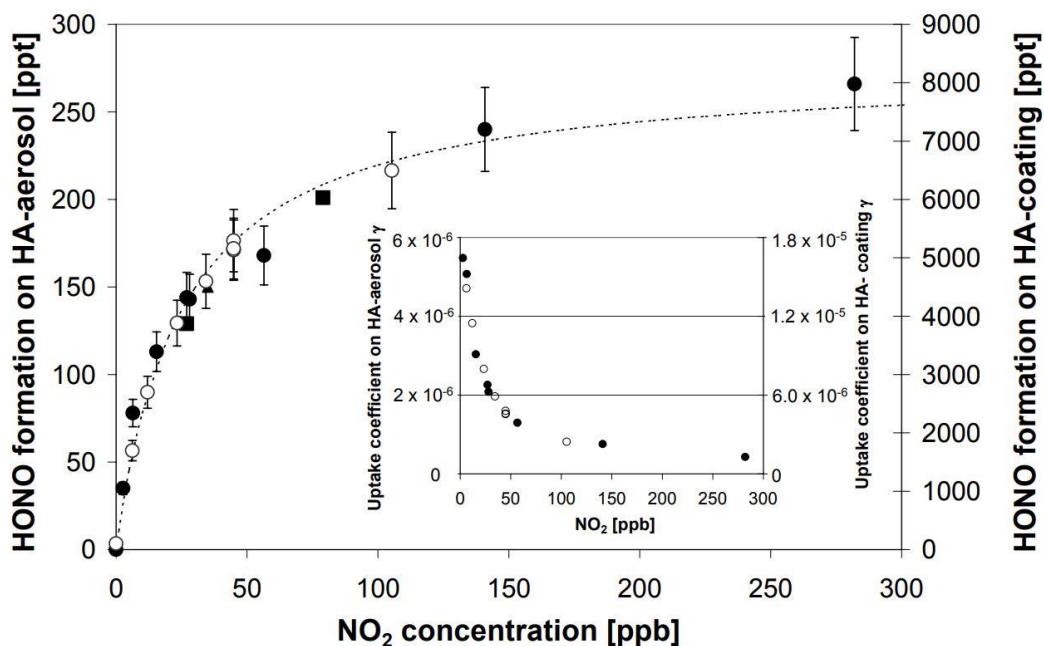


Figure 1.7. Dependence of HONO formation on NO_2 concentration on humic acid aerosol (filled circles, 26 % RH) and humic acid coatings (empty circles, 21 % RH). The inset shows the dependence of the reactive uptake coefficient on NO_2 concentration. Image taken from Stemmler et al., 2007.

The HONO production from humic acid aerosols increases rapidly with NO_2 concentration until a plateau is reached. This is typical of a Langmuir-Hinshelwood type process where a reactant saturates the surface fully leading to a levelling off of product production with increasing reactant concentration. For Langmuir-Hinshelwood processes the higher the concentration of the gas phase species, the more rapidly saturation coverage of the surface is reached and the faster the uptake coefficient of the gas phase species will decrease with time (Ammann et al., 2003).

The production of HONO was observed not to increase linearly with lamp flux potentially indicating that any photo-reduced species formed on the surface may deactivate via the reaction with photo-oxidants, this reaction being in competition with the reaction of NO_2 . The lifetime of the reduced species must then be decreasing with an increase in lamp flux, as shown by R 1.21-R 1.23.



1.4.2 Titanium Dioxide

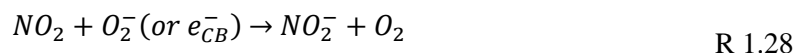
It is estimated that 1604-1960 Tg yr⁻¹ of dust particles are emitted into the atmosphere (Ginoux et al., 2001). Titanium dioxide is a photocatalytic compound found in dust particles at mass mixing ratios from 0.1-10 % depending on the location of particle suspension (Hanisch and Crowley, 2003). Under UV irradiation ($\lambda < 390$ nm) TiO₂ promotes an electron (e_{CB}^-) from the conduction band to the valence band leaving behind a positively charged hole (h_{VB}^+) in the valence band (Chen et al., 2012):



which can lead to reduction and oxidation reactions of any surface adsorbed gas-phase species, such as NO₂, potentially leading to the formation of HONO.

In previous studies HONO has been observed as a major gas-phase product of the reaction of NO₂ on TiO₂ aerosol surfaces (Gustafsson et al., 2006; Dupart et al., 2014). Gustafsson et al., 2006 found that upon irradiation of TiO₂ aerosols, significant HONO production and subsequent NO₂ depletion occurred. In this study, the rate of photo-induced HONO production was ~ 75 % of the total NO₂ consumption, leading to the conclusion that photo induced production of HONO via the reaction of NO₂ + H₂O (R 1.20) was not being observed; based on the stoichiometry of the reaction, half the HONO to the rate of NO₂ consumption should be produced. Gustafsson et al., 2006 showed the rate of the light induced reaction of NO₂ on pure TiO₂ aerosols depended on relative humidity, emphasizing super-hydrophilic nature of TiO₂ surfaces under UV irradiation. Dupart et al., 2014 also observed a dependence of uptake of NO₂ on relative humidity onto TiO₂ containing aerosols, however the reported HONO yield in this study was lower at 30 %, with the main gas phase-products measured being NO and HONO for experiments with 110 ppb NO₂ due perhaps to TiO₂ only being a small percentage of the mineral dust aerosols this study focused on in comparison to single component TiO₂ aerosols used in Gustafsson et al., 2006. Dupart et al., 2014 postulated the following mechanism of HONO production, which is consistent with the formation of the NO₂⁻ anion seen in a previous study on TiO₂ surfaces (Nakamura et al., 2000):





In the study by Dupart et al., 2014 the reactive uptake coefficients of NO_2 were found to be strongly dependent on NO_2 concentration showing, as with the production from humic acid aerosols, a Langmuir-Hinshelwood type behaviour characterised by the adsorption of NO_2 onto the surface followed by chemical reaction, seen as a decrease in uptake coefficient with increasing NO_2 as the surface becomes saturated. The dependence of the uptake coefficient on the NO_2 concentration reported by Dupart et al., 2014 is shown in Figure 1.8 for both coated flow tube (CFT) experiments and aerosol flow tube (AFT) experiments.

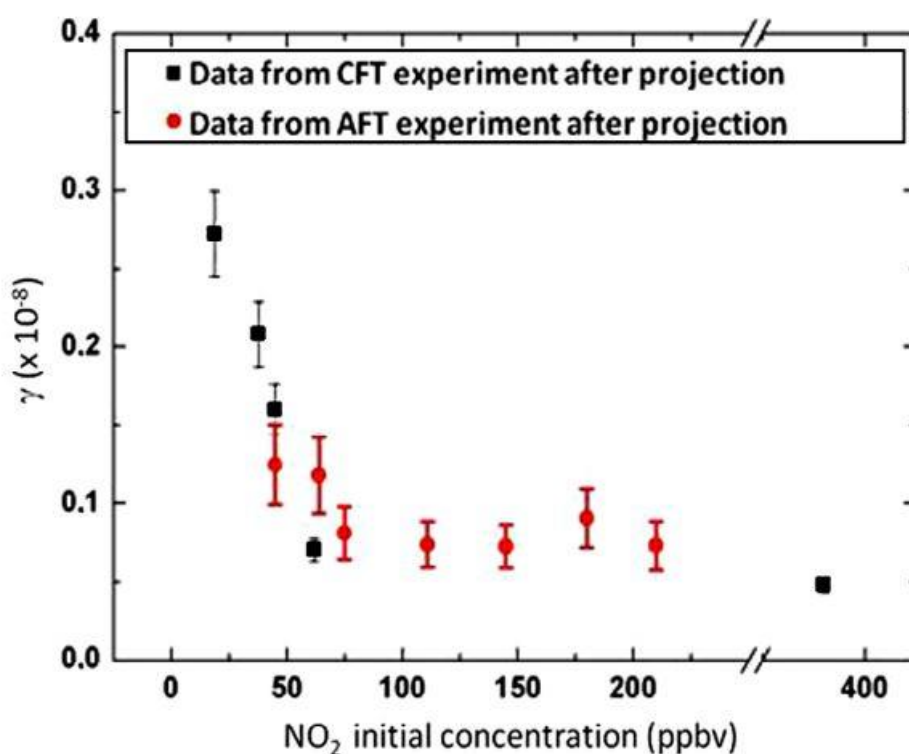


Figure 1.8. Uptake coefficient of $\text{NO}_2 \rightarrow \text{HONO}$ on Arizona test dust as a function of NO_2 initial concentration for coated flow tube (CFT, black) and aerosol flow tube (AFT, red) experiments. Figure taken from Dupart et al., 2014.

1.4.3 Particulate Nitrate Photolysis

Photolysis of gaseous HNO_3 is known to be a relatively slow process, with a rate coefficient of $\sim 7 \times 10^{-7} \text{ s}^{-1}$ under tropical midday conditions (Finlayson-Pitts and Pitts, 2000). Since HNO_3 is efficiently lost by wet removal in the lower atmosphere,

formation of HNO₃ is considered to be a termination step of reactive nitrogen in the troposphere. However, photolysis of surface adsorbed HNO₃ has been found to be much faster, with rate constants from $1 \times 10^{-5} - 3 \times 10^{-3} \text{ s}^{-1}$ reported for both natural and artificial surfaces (Zhou et al., 2003; Zhou et al., 2011; Ye et al., 2016a). Photolysis of particulate nitrate, pNO₃⁻, has recently been postulated to be a source of gas-phase HONO in the atmosphere (Zhang et al., 2009; Reed et al., 2017; Ye et al., 2017a; Ye et al., 2017b). Several studies have reported much faster photolysis of nitrate within or on aerosol surfaces compared to gas phase nitric acid, with particulate nitrate photolysis rates being up to ~3 orders of magnitude greater than gas phase HNO₃ photolysis in marine boundary layer conditions (Ye et al., 2016b).



Rapid cycling of gas-phase nitric acid to gas-phase nitrous acid via particulate nitrate photolysis in the clean marine boundary layer was proposed as a source of HONO during the 2013 NOMADSS aircraft measurements campaign over the North Atlantic Ocean (Ye et al., 2016b) where offline aerosol filter samples were taken and pNO₃ photolysis rate was determined using laboratory experiments offline. Ground-based measurements of HONO made at Cape Verde in the tropical Atlantic Ocean provided evidence that a mechanism for re-nitrosation in low NO_x areas is required (Reed et al., 2017; Ye et al., 2017a).

1.5 Effect of Relative Humidity on the Production of HONO from Aerosol Surfaces

Relative humidity affects the composition of atmospheric aerosols leading to a change in their adsorption properties. As explained in Section 1.3, as the RH increases the aerosol particles will reach a point, the deliquescence point, where the aerosol will spontaneously absorb water to become aqueous. Different aerosols react differently to an increase in RH.

It is thought that an increase in surface water can lead to inhibition of surface reactions. In a study by Stemmler et al., 2007, the HONO production from humic acid aerosol surfaces was investigated up to 88 % RH. In the humidity range of 20-60 % the uptake of NO₂ onto the humic acid aerosols was constant, appearing to drop off after 60 %, shown in Figure 1.9.

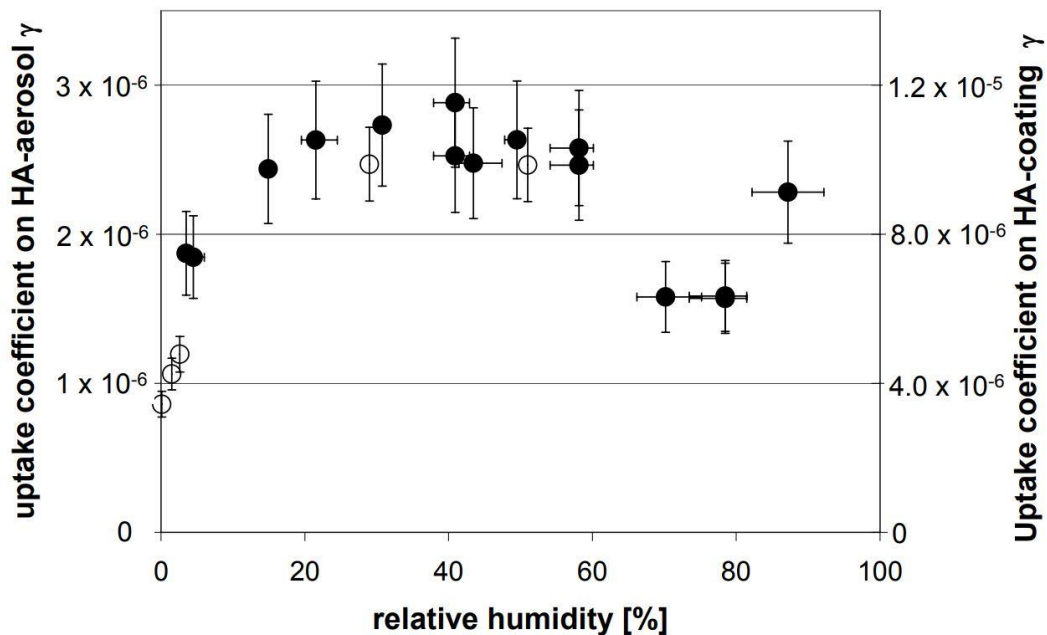


Figure 1.9. Dependence of reactive uptake coefficient of $\text{NO}_2 \rightarrow \text{HONO}$ on the relative humidity on humic acid aerosol (left axis) and humic acid coated walls (right axis). Filled circles represent the uptake coefficient measured on humic acid aerosols at 25 ppb NO_2 whereas the empty circles represent the uptake coefficient on humic acid coatings at 20 ppb NO_2 . Image taken from Stemmler et al., 2007.

The increase in water adsorbed to the surface and in the aqueous phase with increasing RH could counteract the reaction of NO_2 in several ways leading to a decreased production of HONO: firstly, NO_2 may be more soluble in the presence of dry humic acid meaning an increase in RH leads to a decrease in NO_2 in the particle phase; secondly, Gysel et al., 2004 observed a decrease in the aerodynamic diameter of humic acid after 60 % RH which would lead to a decrease in surface area and therefore a reduction in the uptake of NO_2 to form HONO; and lastly, an increase in the surface concentration of water could inhibit the reaction between electron donor and acceptor and therefore the formation of HONO (Gysel et al., 2004; Stemmler et al., 2007).

In comparison, production of HONO from TiO_2 aerosol particles has a much lower peak in uptake of NO_2 as function of RH. A study by Gustafsson et al., 2006 showed a negative correlation between HONO formation rate coefficient and the relative humidity which was explained by the increase water adsorption inhibiting NO_2 adsorption and/or electron/hole transfer processes at the TiO_2 /gas interface. This could also be exacerbated by the super-hydrophilic properties of TiO_2 surfaces under UV radiation (Gustafsson et al., 2006). The uptake coefficient as a function of RH

observed in this study is shown in Figure 1.10. This thesis also covers the RH dependence of HONO production from NO_2 on TiO_2 surfaces, the results of which are described in detail in Section 4.1.2.

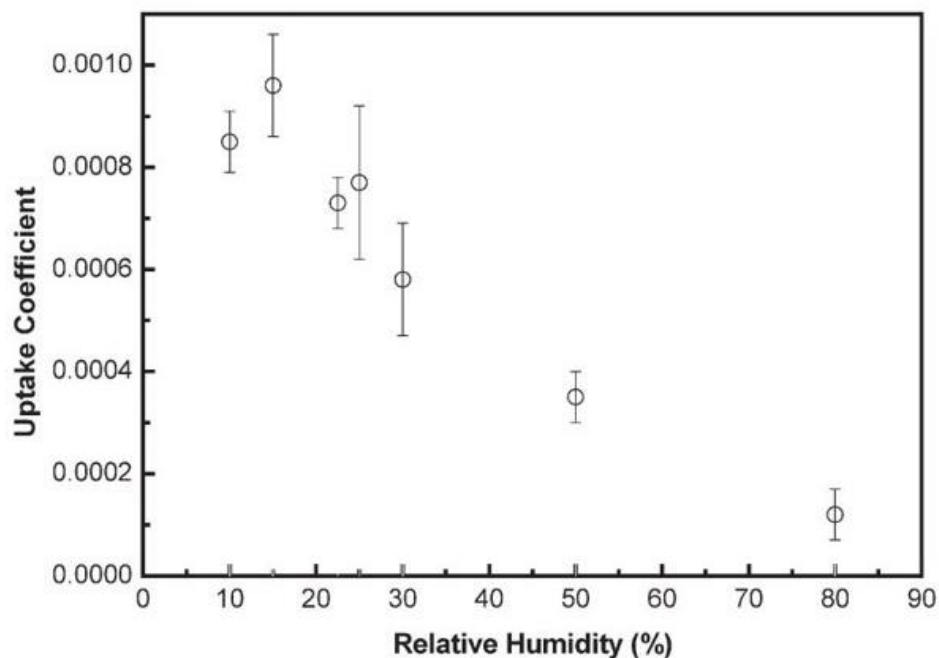


Figure 1.10. Dependence of the uptake coefficient of $\text{NO}_2 \rightarrow \text{HONO}$ from TiO_2 aerosols on RH. Image taken from Gustafsson et al., 2007.

1.6 Mechanism of Heterogeneous Uptake of HO_2 onto Aqueous Phase Aerosols

1.6.1 Resistor Model

The steps involved in what is known as the resistor model are:

- i) Gas-phase transport of a reactant to the surface of the droplet
- ii) Accommodation by the droplet at its surface
- iii) Diffusion of the reactant into the droplet
- iv) Chemical reaction with a species dissolved in the droplet
- v) Diffusion of the unreacted molecules and any products to the surface of the droplet
- vi) Desorption of the species from the liquid-solid interface

This mechanism is depicted in Figure 1.11.

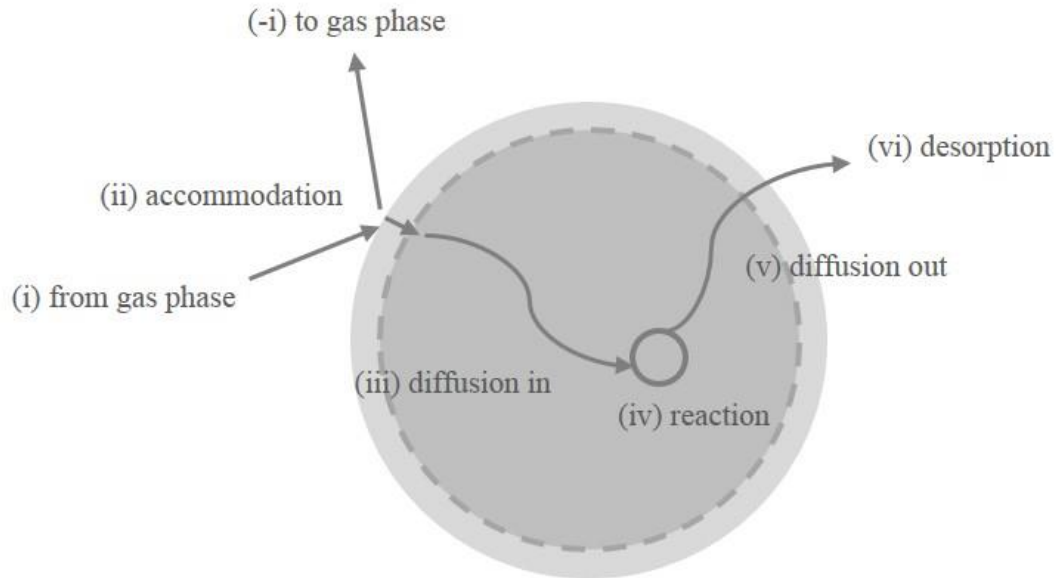


Figure 1.11. Processes involved in the uptake, reaction and desorption of a gas phase molecule by a liquid droplet. Image reproduced from Holloway and Wayne, 2010.

The resistor model gets its name from the analogy of resistance in an electrical circuit. The essentials of the resistor model can be described by Eq 1.1 where each step in the process is treated in terms of conductance, normalised to the rate of gas phase collisions. Note that resistance is equal to the reciprocal of conductance (Finlayson-Pitts and Pitts, 2000).

$$\frac{1}{\gamma_{HO_2}} = \frac{1}{\Gamma_{gas\ diff}} + \frac{1}{\alpha} + \frac{1}{\Gamma_{sol} + \Gamma_{rxn}} \quad \text{Eq 1.1}$$

where $\Gamma_{gas\ diff}$ is the conductance associated with the gas-phase diffusion to the aerosol surface, Γ_{sol} is the conductance associated with the solubility, Γ_{rxn} is the conductance associated with the reaction in aqueous bulk of the aerosol, γ_{HO_2} is the uptake coefficient of HO_2 and α is the mass accommodation coefficient (Finlayson-Pitts and Pitts, 2000).

The first step of the process involves the diffusion of the gas reactant to the surface which is dependent on the gas phase diffusion coefficient (D_g) and the gas-surface collision frequency. It can be assumed that the collision frequency is determined by the ambient pressure surrounding the droplet. However, as the gas phase molecules are accommodated by the aerosol, the concentration of the gas species surrounding the droplet surface will decrease. This causes additional diffusion to the interface by Ficks

law (the diffusive flux goes from regions of high concentration to regions of low concentration). Therefore, the rate of accommodation is limited by the diffusive flux towards the aerosols as gas-phase diffusion may provide resistance to the uptake process if the transfer across the interface is favourable. If the diffusive flux is slow then the concentration of gas phase molecules surrounding the surface of the aerosol are not replaced sufficiently (Moon, 2018). For large particles or very rapid uptake processes the gas diffusion process can be the limiting factor to overall uptake (Tang et al., 2014a) though for atmospheric aerosols with a diameter of $\sim 0.2 \mu\text{m}$ gas phase uptake tends to be limited mostly by the free molecular collision rate (Jacob, 2000). The conductance associated with the gas phase diffusion of mono-disperse spherical particles can be calculated using the Fuchs-Sutugin relation (Eq 1.2) (Fuchs and Sutugin, 1970; Hanson et al., 1996).

$$\frac{1}{\Gamma_{gas\ diff}} = \frac{0.75 + 0.238K_n}{K_n(1 + K_n)} \quad \text{Eq 1.2}$$

where Knudsen number, K_n , is defined as

$$K_n = \frac{3D_c}{\omega r} \quad \text{Eq 1.3}$$

where D_c is the gas phase diffusion coefficient ($\text{m}^2 \text{s}^{-1}$), ω is the mean molecular speed (m s^{-1}) and r is the surface area weighted radius (m). A method for calculating gas-phase diffusion of poly-dispersed aerosol particles has also been developed in recent years (Tang et al., 2012).

The fraction of gas molecules that are accommodated into the aerosol against the number of collisions with the aerosol surface is defined as the mass accommodation coefficient, α . Therefore $1/\alpha$ is the interfacial resistance (Finlayson-Pitts and Pitts, 2000). After uptake at the interface, diffusion into the bulk of the aerosol occurs. Diffusion in the liquid bulk of the aerosol is characterised in the resistance model by Γ_{sol} , the liquid phase saturation limitation. This is governed by the diffusion coefficient within the liquid, D_l . Γ_{sol} can also be written in terms of the diffusion coefficient:

$$\frac{1}{\Gamma_{sol}} = \frac{\omega}{4HRT} \sqrt{\frac{\pi t}{D_l}} \quad \text{Eq 1.4}$$

where ω is the average molecular speed (m s^{-1}), H is the Henry's law constant (M atm^{-1}), R is the gas constant ($\text{mol}^{-1} \text{L atm K}^{-1}$), T is the temperature (K), t is the gas-aerosol interaction time (s) and D_l is the liquid phase diffusion coefficient ($\text{m}^2 \text{s}^{-1}$) (Finlayson-Pitts and Pitts, 2000; Matthews, 2014);.

For volatile solutes, the amount of gas that dissolves in the condensed phase aerosol is directly proportional to the partial pressure of the gas in equilibrium with the aerosol. This is known as Henry's law and is commonly expressed as shown in Eq 1.5.

$$[X] = H_X p_X \quad \text{Eq 1.5}$$

where $[X]$ is the concentration of gas (mol dm^{-3}) X , H_X is the Henry's law coefficient ($\text{m}^3 \text{mol}^{-1} \text{atm}^{-1}$) for the gas and p_X is the partial pressure of the gas (atm).

After a certain amount of time the partitioning between gas and liquid phases will reach equilibrium. The solubility decreases as the concentration of gas within the interface rapidly increases preventing further accommodation.

Finally, reactive uptake occurs once the rate of reaction of the reactant and the aqueous reagent held within the aqueous aerosol bulk is greater than the rate of uptake and diffusion. If the rate of reaction is very fast, the reaction will occur within the interfacial layer but if it is slower then the reaction will occur following diffusion into the bulk of the aerosol. A measure of the distance from the interface in which the reaction occurs is known as the reacto-diffusive length and is defined in Eq 1.6. The conductance of the reaction in the bulk is expressed in Eq 1.7 (Finlayson-Pitts and Pitts, 2000; Moon, 2018)

$$l = \sqrt{\frac{D_l}{k_{rxn}}} \quad \text{Eq 1.6}$$

$$\frac{1}{\Gamma_{rxn}} = \frac{\omega}{4HRT} \sqrt{\frac{1}{D_l k_{rxn}}} \quad \text{Eq 1.7}$$

where ω is the average molecular speed (m s^{-1}), D_l is the diffusion coefficient in the aqueous phase ($\text{m}^2 \text{s}^{-1}$) and k_{rxn} is the rate constant for the reaction (s^{-1}).

If the species in question is not reactive with itself or with the species within the aerosol then only diffusion of species to the aerosol surface, adsorption and diffusion in the bulk need to be considered in the uptake. As such the uptake coefficient can be written as:

$$\frac{1}{\gamma} = \frac{1}{\Gamma_{gas\ diff}} + \frac{1}{\alpha} + \frac{1}{\Gamma_{sol}} \quad \text{Eq 1.8}$$

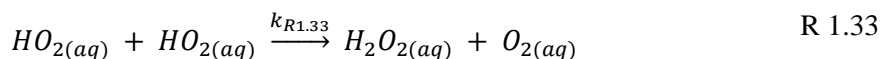
As such the uptake of a species, into the aerosol will be controlled by the mass accommodation, α , the gas phase diffusion to the aerosol surface and the solubility of the species within the aerosol. As the aerosol becomes saturated with an unreactive species the uptake coefficient will tend to zero.

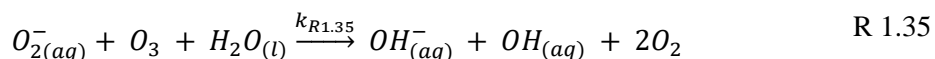
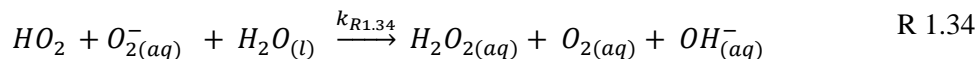
If the species is reactive, such as HO₂, as shown in Eq 1.1, the uptake coefficient can be limited by the mass accommodation or by the gas phase diffusion of the species if the species is highly soluble and reactive. In this case the uptake coefficient can also be limited by the solubility of the species or the rate of reaction within the bulk of the aerosol. If Γ_{sol} is much faster than Γ_{rxn} then Γ_{rxn} can be removed from the equation for simplification. Conversely if the solubility is much slower than the reaction in the bulk then Eq 1.1 can be written as:

$$\frac{1}{\gamma} = \frac{1}{\Gamma_{gas\ diff}} + \frac{1}{\alpha} + \frac{1}{\Gamma_{rxn}} \quad \text{Eq 1.9}$$

1.6.2 Self-Reaction

On entering the aqueous phase within a condensed aerosol without the presence of transition metal ions, a given HO₂ molecule is most likely to react with another HO₂ molecule or with its conjugate base, O₂⁻ (Thornton and Abbatt, 2005; Thornton et al., 2008). Hanson et al., 1994 proposed that the formation of H₂O₂ via the self-reaction was relatively slow meaning that it is only favoured at higher concentrations of HO₂. The following mechanism, shown in R 1.31 - R 1.35, was proposed to explain the mechanism of HO₂ self-reaction (Jacob, 2000).





where $k_{R1.33}$ is $8.6 \times 10^5 \text{ M}^{-1} \text{ s}^{-1}$, $k_{R1.34}$ is $1.0 \times 10^8 \text{ M}^{-1} \text{ s}^{-1}$ and $k_{R1.35}$ is $1.5 \times 10^9 \text{ M}^{-1} \text{ s}^{-1}$ (Thornton and Abbatt, 2005).

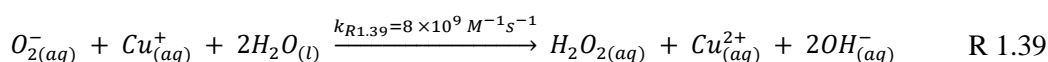
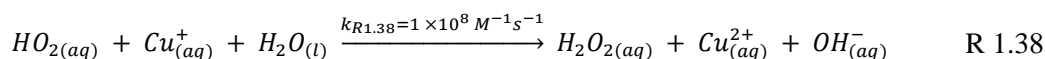
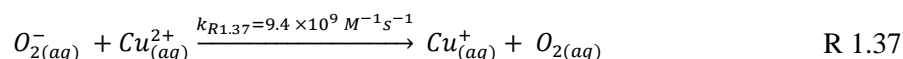
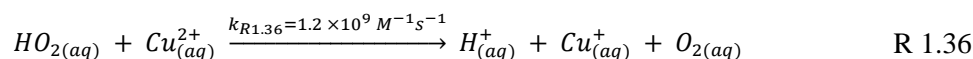
The mechanism of self-reaction proposes that mass accommodation of gaseous HO_2 into the aerosol is then followed by the pH dependent partitioning of $HO_{2(aq)}$ into $H^+_{(aq)}$ and the conjugate base of HO_2 , $O_{2(aq)}^-$. H_2O_2 has been observed as a product of the HO_2 self-reaction on sea salt aerosols (Loukhovitskaya et al., 2009). In a study by Thornton and Abbatt (2008) the known pathways for HO_2 loss were studied and the uptake coefficient of HO_2 was found to be strongly dependent on particle phase, size, temperature and pH for the HO_2 self-reaction loss pathway, further discussed in Section 1.8.

The mass accommodation coefficient or the sticking coefficient, α_{HO_2} , is the probability that gaseous HO_2 will be taken into a surface layer of the aqueous bulk aerosol upon collision. The mass accommodation coefficient has been measured over a range of acidic and neutral pHs with values of α_{HO_2} ranging from 0.1 – 1.0. Mozurkewich et al., 1987 was the first to measure the mass accommodation coefficient for the loss of HO_2 on deliquesced copper doped aerosols, proposing a minimum value of 0.2. Cooper and Abbatt also measured a minimum value of 0.2 for deliquesced copper doped aerosols 10 years later (Cooper and Abbatt 1996). George et al., 2013 reported a measured α_{HO_2} of 0.4 ± 0.3 on Cu(II)-doped $(NH_4)_2(SO_4)$ aerosols. A study the same year reviewed the kinetic data for heterogeneous reactions in the atmosphere suggesting α_{HO_2} should be >0.5 (Ammann et al., 2013). Due to the varied nature of experimentally determined values of α_{HO_2} , the mass accommodation coefficients used with models also varies widely.

1.6.3 Reaction with Transition Metals

When aqueous aerosols are doped with transition metal ions (TMI), such as Cu (II) or Fe (II), a different mechanism, compared to the self-reaction, is in operation. Mozurkewich et al., 1987 were the first to conduct experiments designed to measure the mass accommodation coefficient, α_{HO_2} in the presence of Cu (II) ions. Copper

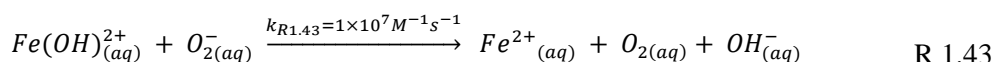
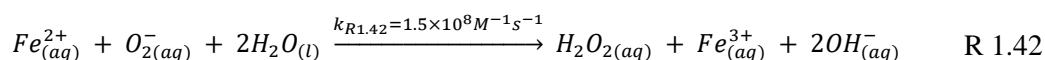
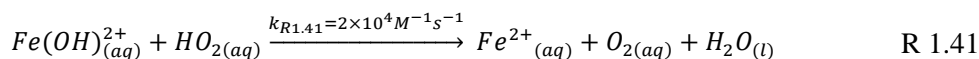
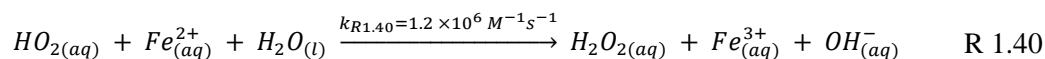
acts as a catalyst to speed up the reaction of HO₂ to give H₂O₂ and O₂, shown below in R 1.36 - R 1.39 (Thornton and Abbatt, 2005).



The reaction of HO₂ with Cu_(aq)²⁺, R 1.36, can be rate limiting under acidic conditions with $k_{R1.37}=1.2 \times 10^9 M^{-1} s^{-1}$. The reaction of the conjugate base, O_{2(aq)}⁻ with Cu_(aq)⁺ however, R 1.37 and R 1.39, is rapid in comparison with $k > 1 \times 10^9 M^{-1} s^{-1}$ (Thornton and Abbatt, 2005).

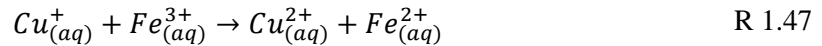
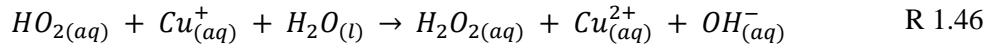
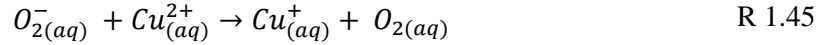
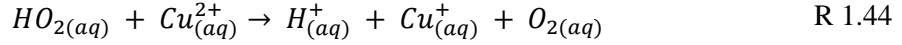
At high concentrations of copper, the overall rate of HO₂ uptake will be controlled by the mass accommodation coefficient due to transport processes rather than limiting factors such as solubility (George et al., 2013). However, concentrations of Cu (II) are not typically high enough in the troposphere for this loss mechanism to be significant, aside from regions where mineral dust is prevalent (Thornton and Abbatt, 2005). The studies of Mao et al., 2013 and Thornton et al., 2008 were both in agreement that the uptake coefficient of HO₂ via transition metal ion (TMI) catalysis becomes insignificant for copper concentrations $< 1 \times 10^{-4} M$ (Thornton et al., 2008; Mao et al., 2013).

In comparison, the uptake of HO₂ in the presence of Fe (II) is believed to proceed via a mechanism shown in R 1.40 - R 1.43 (Jacob, 2000).

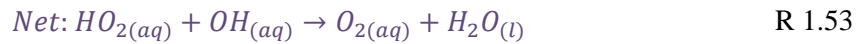
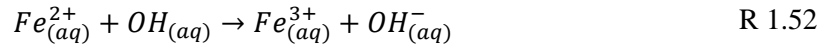
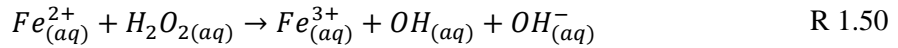
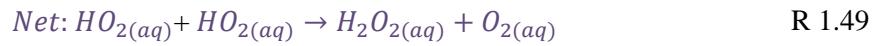
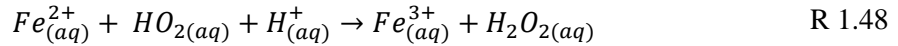


It is worth noting that the rate coefficients for the destruction of HO₂ in the presence of Fe (II) are significantly slower than those in the presence of Cu (II). Several studies have shown that including H₂O₂ as the major product of HO₂ uptake onto aerosols

leads to an over-prediction of H₂O₂ compared to field observations (de Reus et al., 2005; Mao et al., 2010a). More recently a catalytic redox coupling mechanism has been proposed by Mao et al., 2013 suggesting that aerosols containing both Cu (II) and Fe (II) could lead to the production of H₂O as a product of HO₂ uptake rather than H₂O₂.



Following the formation of Fe (II), Mao et al., 2013 proposed 3 possible reaction steps leading to the formation of water *or* H₂O₂:



Mao et al., 2013 proposed a new pathway initiated by the uptake of gas phase HO₂ onto aerosols followed by the Cu-Fe redox mechanism described above, leading to the sustaining of [Fe (II)] overnight over the open ocean. This can also dominate Fe (III) reduction at lower concentrations of Fe (III)-oxalate complexes. This enhances OH production via the Fenton reaction which is sustained by the influx of HO₂ from the gas phase (Mao et al., 2017).

1.7 Mechanism of Heterogeneous Uptake of HO₂ onto Solid Aerosols

Previous studies have shown γ_{HO_2} values to be lower on dry aerosol surfaces. In a study by Taketani et al., 2008 the uptake coefficient of HO₂ onto dry NaCl aerosol surface at 20% RH was seen as to be < 0.01. When the RH of the system was increased to 75 %, and therefore pushed past the deliquescence point of NaCl, the uptake

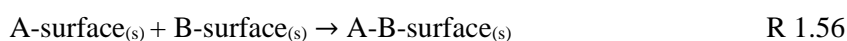
coefficient increased to 0.1 (Taketani et al., 2008). Similarly in a study by George et al., 2013 the uptake coefficient of HO₂ onto dry NaCl at 33% RH was <0.004 compared to the uptake coefficient of 0.01 for RH between 67-76 % RH. Despite this, uptake of HO₂ onto dry aerosols could be important in arid regions such as the Sahara where a large percentage of the aerosol phase is composed of dry mineral dust.

There are two mechanisms by which heterogeneous reactions of HO₂ on dry aerosol surfaces can occur: the Eley-Rideal and the Langmuir-Hinshelwood mechanisms. In the Eley-Rideal mechanism a molecule in the gas phase collides with another molecule which is already adsorbed onto a surface. The two molecules then react. In comparison the Langmuir-Hinshelwood mechanism involves the encounter of adsorbed molecular fragments or atoms colliding on a surface whereupon a reaction can occur and the products then desorb off the surface (Baxter and Hu, 2002). It is accepted that the majority of surface catalysed reactions, the Langmuir-Hinshelwood mechanism is preferred with there being very few systems where it can be conclusively shown that the Eley-Rideal mechanism is operating (Atkins and Paula, 2005). The two mechanisms are represented in R 1.54 to R 1.57.

Eley-Rideal



Langmuir-Hinshelwood



It is not known which mechanism the HO₂ self-reaction occurs via as neither has been confirmed through kinetic observations. It is difficult to test which of these mechanisms is occurring as they are usually differentiated by changing the concentration of either A or B. For the Langmuir-Hinshelwood mechanism it would be expected that increasing the concentration of A so that [A] >> [B], would decrease the rate of the reaction whereas it would not affect the rate of reaction if the Eley-Rideal mechanism was occurring. However, HO₂ uptake results in H₂O₂ as the product suggesting that both A and B are HO₂ making distinguishing which mechanism is at play very difficult (Matthews, 2014).

The surface coverage (Θ) of an aerosol can be given by the Langmuir isotherm. The rate of change of surface coverage (Θ) due to gas phase adsorption to the surface is proportional to the partial pressure of $A_{(g)}$ and the number of vacant sites on the surface, $N(1 - \Theta)$, where N is the total number of sites:

$$\frac{d\Theta}{dt} = k_{adsorption}p_A N(1 - \Theta) \quad \text{Eq 1.10}$$

The rate of change of surface coverage due to desorption of a surface adsorbed species from the surface is proportional to the number of adsorbed species:

$$\frac{d\Theta}{dt} = -k_{desorption}N\Theta \quad \text{Eq 1.11}$$

Assuming equilibrium, i.e. rate of surface coverage due to adsorption and desorption are equal, gives the Langmuir isotherm:

$$\Theta = \frac{Kp}{1 + Kp} \quad \text{Eq 1.12}$$

where K is the equilibrium constant for the adsorption/desorption reaction of A with a surface and has a negative dependence on temperature and binding energy of adsorption and p is either the gas phase pressure or, alternatively, the concentration of species A (Atkins and Paula, 2005). Therefore, from Eq 1.12, as the concentration of the gas phase species decreases, the surface coverage will also decrease.

1.8 Factors Affecting the Uptake of HO_2 onto Aerosol Surfaces

Previous parameterisation has led to an understanding of the dependence of the uptake of HO_2 on environmental and chemical parameters, allowing a more accurate representation of heterogeneous processes including HO_2 in numerical models. Better understanding the factors affecting the uptake and production of HO_2 on aerosol surfaces will allow more accurate model predictive capacity and therefore better comparison with field measurements.

1.8.1 Aerosol pH

HO_2 is a weak acid at room temperature with a pK_a of ~ 4.7 meaning that the solubility and reactivity of HO_2 is dependent on pH (Thornton et al., 2008). Due to the effect pH would have on the equilibrium of the dissociation reaction of HO_2 to its conjugate base, O_2^- , both the HO_2 self-reaction and the reactions catalysed by TMI are dependent

on pH. When the aerosol is more acidic, less HO₂ will enter the aqueous aerosol phase due to Le Chatelier's principle thereby forcing the equilibrium back towards HO₂. Above a pH of 4, the solubility of HO₂ is higher which leads to a decrease in the evaporative flux of HO₂ out of solution. An effective Henry's law constant can be defined to account for increased solubility (Thornton and Abbatt, 2005; Thornton et al., 2008). Note that it is not directly possible to measure the pH of an aerosol.

$$H_{eff} = H_{HO_2} \left(1 + \frac{K_{eq}}{[H^+]} \right) \quad \text{Eq 1.13}$$

where K_{eq} is the equilibrium constant, H_{HO_2} is the physical Henry's law constant and H_{eff} is the effective Henry's law constant. H_{eff} increases exponentially with decreasing temperature.

1.8.2 Temperature

The acid-base dissociation of HO₂, specifically the solvation reaction of HO_{2(g)} to HO_{2(aq)}, is highly temperature dependent (Macintyre and Evans, 2011). The solubility of HO₂ changes significantly with temperature meaning that temperature has an effect on the uptake of HO₂ onto aerosols. For a given aerosol pH, aqueous HO₂ chemistry is very sensitive to temperature fluctuations with γ_{HO_2} showing a strong inverse temperature dependence which can be explained by the variation with temperature of Henry's Law constant for a gas in a liquid. A gas has a higher entropy than a liquid meaning that as the gas dissolves into the liquid phase the entropy of the system decreases which is unfavourable to the system. During this process heat is released as the dissolution of a gas in a liquid is an exothermic process. Increasing the temperature therefore will lead to the system favouring the endothermic process, the return of the species to the gas phase, due to Le Chatelier's principle which states that a system will counteract a change in the system so as to bring the system back into equilibrium. Therefore with an increase in temperature there is a decrease in solubility as the system moves to correct the increase in temperature leading to less collisions of HO₂ with aerosol surfaces and therefore a decrease in γ_{HO_2} (Thornton et al., 2008).

1.8.3 Relative Humidity

The effect of RH on the uptake of HO₂ depends on the composition and phase of the aerosol in question. Salt aerosols, for example, should have a higher γ_{HO_2} when in a deliquesced state in comparison to those which remain in the effloresced state. As the

RH increases past the deliquescence point of a salt aerosol, the aerosol will take up more water and will rapidly increase in size. This will decrease the aerosol acidity and increase the aerosol surface area thereby increasing the solubility of the HO₂ and the potential for collisional reactions.

Some studies however have shown that an increase in water content of the aerosol can have a detrimental effect on the uptake of HO₂. In a study by Remorov et al., 2002 an increase in relative humidity led to a decrease in radical uptake onto NaCl aerosols suggested to be due to water adsorption competing with HO₂ adsorption thereby decreasing the number of free sites available for radical adsorption and reaction. In opposition to this, a study by Taketani et al., 2008 showed an increase in γ_{HO_2} onto NaCl particles with an increase in relative humidity with a value of <0.01 at 20% RH increasing to 0.1 ± 0.02 at 75% RH. A similar study by George et al., 2013 on NH₄NO₃ aerosols showed no observable effect on γ_{HO_2} with an increase in relative humidity other than potentially increasing the loss rate of HO₂ to the walls. Observed uptake coefficients of HO₂ for NH₄(SO₄)₂ and NaCl in both dry and aqueous forms as reported by multiple studies are shown in Figure 1.12.

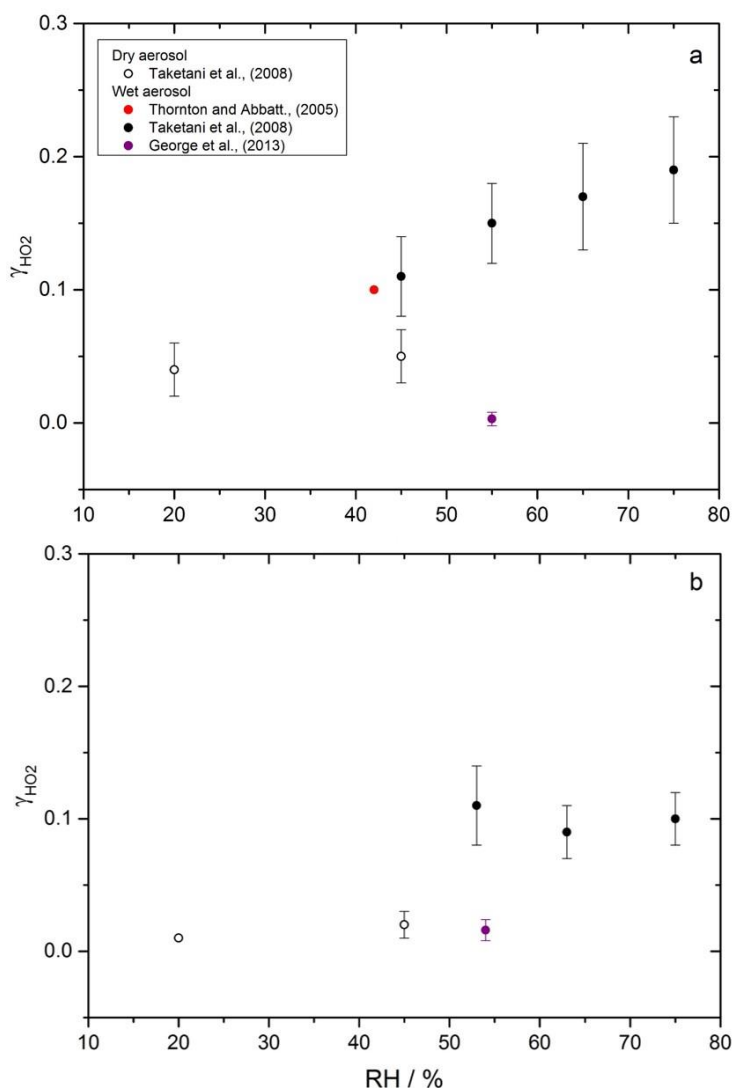


Figure 1.12. Dependence of HO₂ uptake coefficient on relative humidity for a) dry and aqueous NH₄(SO₄)₂ aerosols and b) dry and aqueous NaCl aerosols as a function of RH. Uptake coefficient values taken from Thornton and Abbatt, 2005; Taketani et al., 2008 and George et al., 2013.

A study conducted on polystyrene latex particles sought to investigate the relative humidity dependence by using a particle which would not change size with an increase in relative humidity, unlike salt aerosols, and as such the dependence on relative humidity would not be due to presence of water in the particle, and therefore not due to a change in phase (Taketani et al., 2010). The positive dependence on RH seen on PSL particles observed was speculated to be due to a HO₂-H₂O complex forming under high RH which could explain the dependence if uptake of HO₂-H₂O is more efficient (Taketani et al., 2010). The same study also saw a positive dependence of RH on levoglucosan particles which do show hygroscopic growth.

A variation in RH can also have an effect on the viscosity of certain aerosols. In a study by Lakey et al., 2016a, γ_{HO_2} for Cu(II) doped sucrose aerosols was equal to the mass accommodation coefficient, $\alpha = 0.22 \pm 0.06$, at 65% RH but decreased to $\gamma = 0.012 \pm 0.007$ upon decreasing the RH to 17%. At high surface water concentration total uptake is driven by reaction in the bulk aerosol near to the surface and is limited by mass accommodation. At low RH however, uptake is limited by surface reaction. At a lower RH the surface is very viscous meaning that the reacto-diffusive length is much lower stopping HO_2 uptake from occurring rapidly. With an increase in RH, once the viscosity is reduced and the reacto-diffusive length increases, uptake of HO_2 can occur readily at the surface and in the near-surface bulk of the aerosol.

In the Lakey et al., 2016 study, the reacto-diffusive lengths of HO_2 were seen to be between 4-7 nm at the highest RH of 65 % decreasing to between ~ 0.006 -0.05 nm at the lowest RH of 17 %, shown in Figure 1.13. These reacto-diffusive lengths are much smaller than the diameter of aerosol particles seen in this study showing that HO_2 radical reactions were limited to the outer molecular layers of the particle before fully reacting away (Lakey et al., 2016a).

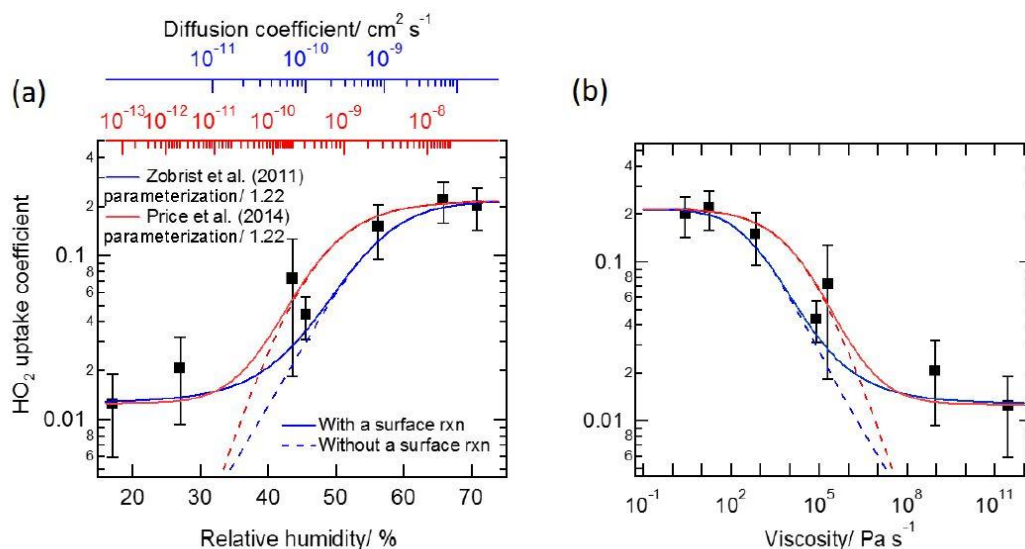


Figure 1.13. HO_2 uptake coefficient onto copper (II)-doped sucrose aerosol particles as a function of (a) relative humidity and (b) aerosol particle viscosity. The fits represent the expected HO_2 uptake coefficient calculated using the KM-SUB model with the Price et al., 2014 (red) and Zobrist et al., 2011 (blue) diffusion parameterisations Zobrist et al., 2011; Price et al., 2014. Image taken from Lakey et al., (2016).

1.8.4 Concentration of HO₂

As mentioned in section 1.6.2, the self-reaction of HO₂ on aqueous aerosol surfaces is second order with respect to aqueous HO₂ concentration. This means that an increase in HO₂ concentration should mean an increase in γ_{HO_2} . The inverse relationship however is seen experimentally. In a study by George et al., (2013), experiments on aqueous (NH₄)₂SO₄ aerosol observed larger values of γ_{HO_2} at lower HO₂ concentrations, most likely due to aerosol surface saturation effects leading to a reduction in the uptake capacity and therefore a decrease in uptake coefficient at high initial [HO₂] (George et al., 2013). This effect seems to be greater at higher RH, perhaps due to larger size of the aerosol (more water encasing the solid core of the aerosol). The experimental dependence of HO₂ uptake coefficient on initial HO₂ concentration for aqueous (NH₄)₂SO₄ aerosol is shown in Figure 1.14 (George et al., 2013).

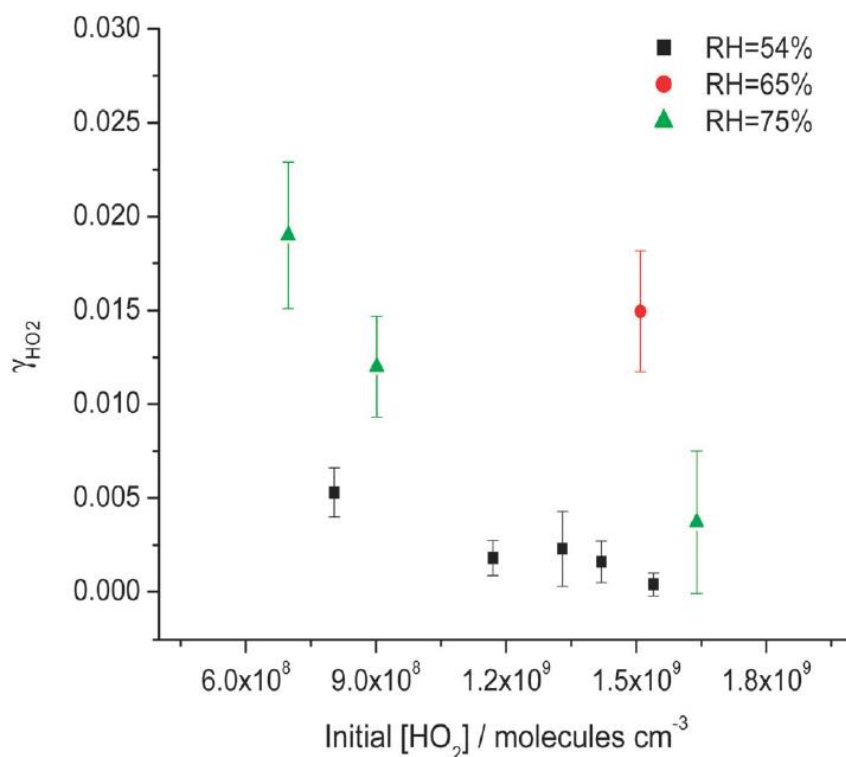


Figure 1.14. Dependence of HO₂ uptake coefficient on initial HO₂ concentration for aqueous (NH₄)₂SO₄ aerosol for 54 % RH (black), 65 % RH (red) and 75 % RH (green). Image taken from George et al., 2013.

1.8.5 Exposure Time

The uptake of HO₂ has a negative time dependence due most likely to aerosol surface saturation. It is possible that from an initial maximum of the mass accommodation, the uptake coefficient could slowly decrease to a stable value (Matthews, 2014). The surface and the bulk of the aerosol may become quickly saturated with HO₂ thereby reducing the uptake coefficient from its initial value. Conversely, a reactive component of the aerosol could be used up over time or the aerosol could become more viscous with aging leading to a decrease in HO₂ uptake. For flow tube experiments in particular longer exposure times could also lead to an increase in HO₂ wall loss. Figure 1.15 shows an example of the negative correlation between HO₂ uptake coefficient and exposure time for aqueous NaCl aerosols at 60 % RH (George et al., 2013).

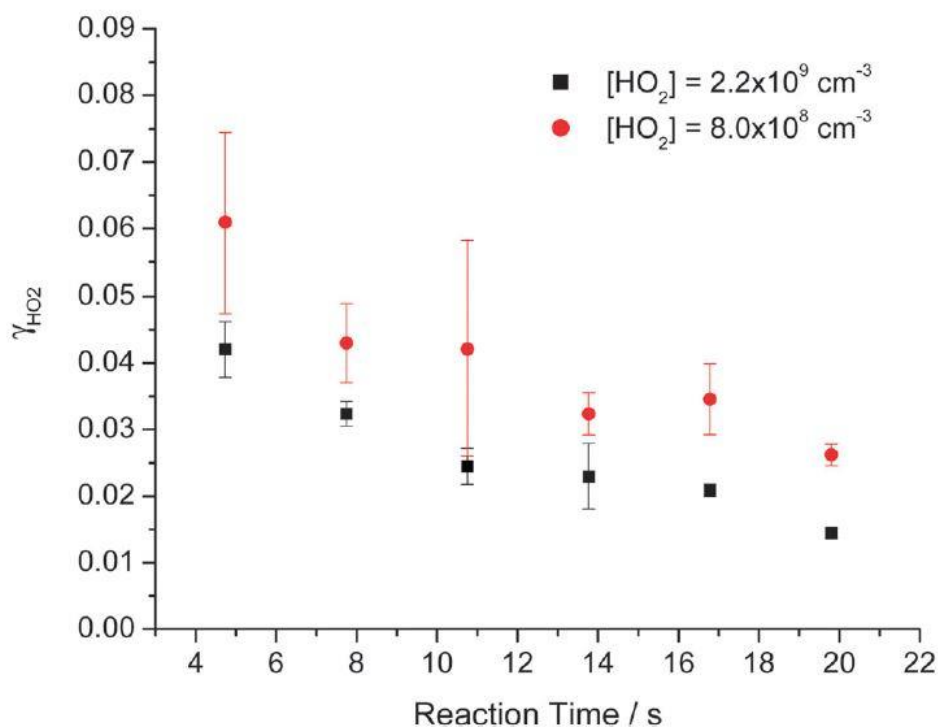


Figure 1.15. Dependence of HO₂ uptake coefficients for aqueous NaCl aerosols as a function of reaction time for two initial HO₂ concentrations. RH kept constant at 60 %. Error bars are 1σ of average values. Image taken from George et al., 2013.

1.9 Global Distribution of HO₂ and HO₂ uptake

An example of the annual global OH and HO₂ concentration distributions, as reported in Lelieveld et al., 2016, is shown in Figure 1.16. As expected given the higher concentrations of OH towards the equatorial region, HO₂ concentrations are also highest towards the equator, due to increase in photochemistry, with both OH and HO₂ concentrations being lowest globally in the Arctic/Antarctic regions. OH concentrations are highest in the tropics where both UV and water vapour concentrations are high. This means that the concentration of HO₂ is higher in these regions due to the recycling of OH into HO₂. However concentrations of HO₂ are also high in the mid-northern latitudes where CO and NO₂ concentrations are high due to increased levels of fuel combustion. Due to the abundance of NO₂ in the northern hemisphere, tropospheric O₃ is also higher. As such concentrations of OH tend to be higher in the northern hemisphere due to increased O₃. This is reduced in part by increased OH loss due to high CO concentrations (Jacob, 1999).

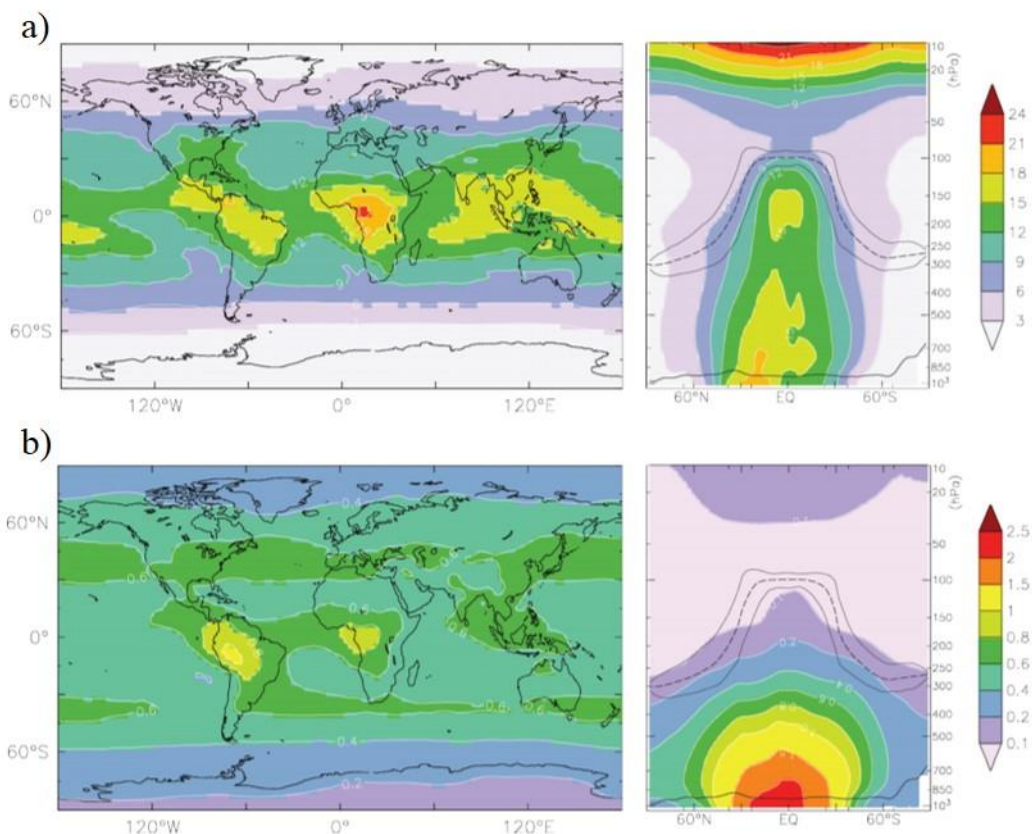


Figure 1.16. a) Global OH distribution in 10^6 molecules cm^{-3} . b) Global HO₂ distribution in 10^8 molecules cm^{-3} . In both cases the left panel shows the annual tropospheric mean while the right panel shows annual zonal mean up to 10 hPa. The solid black line on the right panel indicates the average boundary layer height while the upper dashed line represents the tropopause mean height with the surrounding solid lines the maximum and minimum mean tropopause height. Figure taken from Lelieveld et al., 2016.

By considering the effect of parameters such as temperature, relative humidity and aerosols pH, described earlier in Section 1.8, it is possible to model the distribution of both HO₂ and the uptake of HO₂ globally. From this, the potential loss of HO₂ to aerosols would be expected to be highest in low temperature regions due to the strong negative temperature dependence of γ_{HO_2} .

Macintyre and Evans, 2011 performed a study on the spatial distribution of γ_{HO_2} using the GEOS-Chem global chemical transport model. In this study a parameterisation for γ_{HO_2} was created based on the available laboratory studies including data for different particle compositions as well as temperature and RH dependences. GEOS-Chem model simulations were then run using γ_{HO_2} value of 0.2 as recommended by Jacob (2000), and then using the γ_{HO_2} values calculated by the parameterisation. While this

study neglected to consider the importance of TMI catalysis, and therefore most likely reported a γ_{HO_2} on the lower end of values reported in previous studies, it can however be used qualitatively to show the areas where heterogeneous uptake of HO_2 may be important globally. It is also important to note that where HO_2 concentration is lower, the HO_2 self-reaction will be less important and therefore HO_2 uptake will be relatively more important when considering all HO_2 loss pathways.

In this study a global mean average of 0.028 was reported for γ_{HO_2} , using the new parameterisation. Higher values were reported at higher latitudes as expected due to the negative temperature dependence and positive RH dependence of HO_2 uptake. High γ_{HO_2} values were also reported over the west coast of Africa due to high aerosol loading and higher RH, potentially even higher as TMI catalysis was not considered in the model. The presence of photo-catalytic substances in mineral dust could also lead to increased uptake in these regions. Over the Sahara itself the γ_{HO_2} values were lower however due to the high temperature in these regions. The results of the global model showing the mean γ_{HO_2} value for January and July are shown in Figure 1.17.

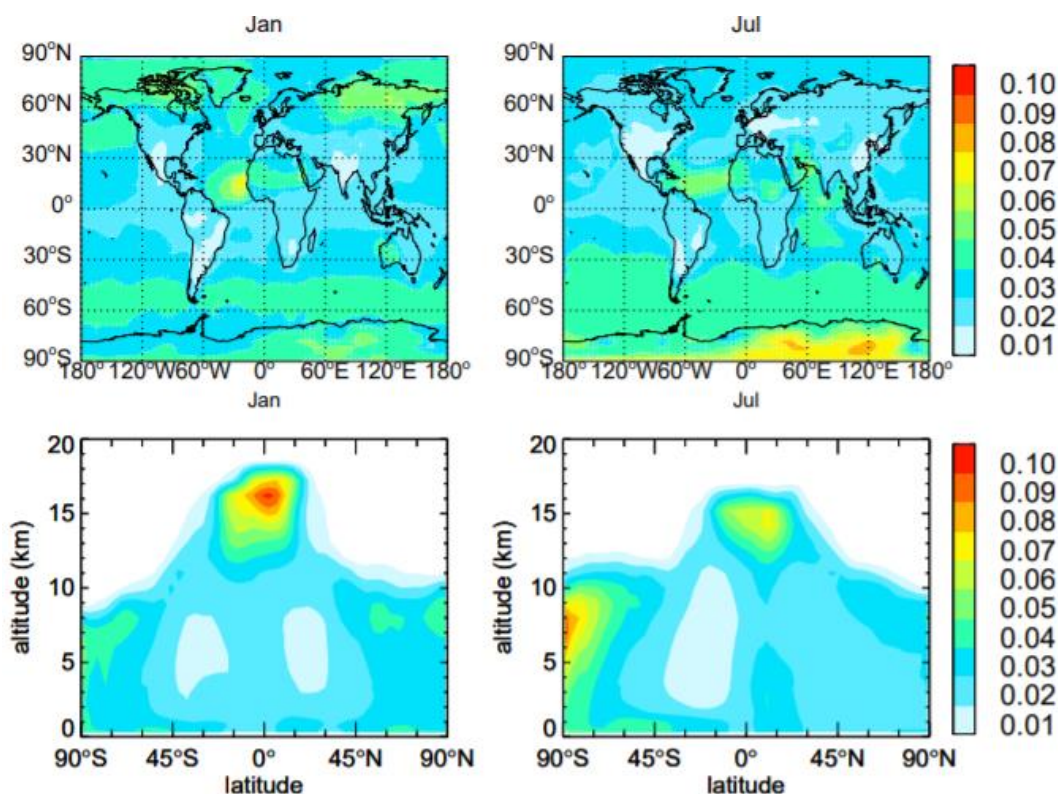


Figure 1.17. Surface and zonal mean γ_{HO_2} for January and July calculated using GEOS-Chem using a new parameterisation by MacIntrye and Evans, 2011. Image taken from MacIntrye and Evans, 2011.

1.10 Atmospheric Modelling

1.10.1 Zero Dimensional Modelling and the Master Chemical Mechanism

Zero-dimensional models pinpoint a single position in the atmosphere i.e. a box, and consider only the chemistry occurring within this space with no attention to the transport of species in or out of this box. For shorter lived species such as OH with reactive lifetimes of less than a second transport processes are not an important consideration. OH radical concentrations are therefore controlled by *in situ* chemistry making OH ideal for study in chemical mechanisms. However, for longer lived species such as O₃, transport can be important meaning regional, global or trajectory models which incorporate transport mechanisms are more appropriate prediction tools. Note that due to computational limitations, these larger scale models tend to run with simplified chemical schemes. This is combatted in part by constraining models to measured values of photolysis rates and concentrations of longer lived species.

The Master Chemical Mechanism (MCMv3.3.1) is a near-explicit mechanism which describes the gas-phase degradation of a series of primary emitted VOC's in the troposphere. The mechanism considers the degradation of 143 VOC's and contains ~17000 elementary reactions of 6700 species (Whalley et al., 2013). An advantage of the MCM is that it treats the oxidation of those that VOC's that have been thoroughly studied explicitly. Unfortunately, many VOC's within the mechanism have not been studied so the kinetics and branching ratios of the reactions of these VOCs are unknown. Assumptions based on structure-activity relationships are used to provide the necessary data to output radical concentrations.

1.10.2 Global and Regional Modelling

In contrast to zero-dimensional box models, 2D and 3D models do include transport processes. While these larger scale models have a more basic suite of reactions and species, they have the advantage of considering the global or regional effect of varying important reactive species through the inclusion of the global or regional distribution of radical species such as HO₂, and how these species change with wind and weather patterns. Zero-dimensional models, however, can be used in conjunction to identify which reactions within a particular environment are prevalent and this information can then be fed into a larger scale model. In this way models of different scales can be used to complement each other.

The Weather Research and Forecasting model coupled with Chemistry (WRF-Chem) is a fully online-coupled, regional, numerical weather prediction model (Conibear et al., 2018). The model includes modules for gas-phase chemistry and aerosol physiochemical processes and simulates emission, transport, mixing and chemical transformation of trace gases and aerosols simultaneously with the meteorology (Conibear et al., 2018). The United Kingdom Chemistry and Aerosols model (UKCA), however, is a chemistry and aerosol model coupled to the Met Office Unified Model capable of simulating composition and climate from the troposphere to the mesosphere (Morgenstern et al., 2009).

1.10.3 HO₂ Uptake in Previous Modelling Studies

Numerical chemistry models have a tendency to over predict HO₂ especially in low NO_x conditions. For example, during the ClearfLo campaign in London 2012 the model over predicted HO₂ by up to a factor of 10 in times of low NO_x which was

attributed to a missing peroxy radical sink (Whalley et al., 2018). Over-prediction of HO₂ could also be due to the absence or underestimation of the uptake coefficient of HO₂ onto aerosol surfaces.

HO₂ uptake has been studied both through modelling and experimentally for over 20 years. Jacob, 2000 recommended an uptake coefficient (γ_{HO_2}) of 0.2 for use within models. This value is high in comparison to those experimentally determined on a variety of atmospherically relevant aerosols which are often below 0.01 – this is the case when aerosols are not doped with transition metals (Jacob, 2000). Experimentally, when Cu (II) or Fe (II) catalysts are used γ_{HO_2} can be seen to be as high as 0.6 (Taketani et al., 2008).

A parameterisation for γ_{HO_2} based on an aqueous phase mechanism was suggested by Thornton et al., 2008. For all aerosol types, not including mineral dust within which catalytic TMIs are naturally abundant, an aqueous phase recombination mechanism based on the acid-base dissociations of HO₂ to produce H₂O₂ was used to calculate the uptake onto tropospheric aerosols. The assumption that transition metal ions were present in dust aerosols led to the uptake coefficient onto dust being taken as the constant value of 0.2. Thornton et al., 2008 found through modelling that low values for γ_{HO_2} , i.e. < 0.05, dominate the lower troposphere especially in tropical regions then increasing to values of >0.1 in the upper troposphere where it is colder. This relationship is chiefly because of the negative temperature dependence of the conversion of HO₂ (g) to HO₂ (aq) (Thornton et al., 2008). In arid regions such as the Sahara desert where dust is prevalent, the assumption was made of the presence of high concentrations of transition metal ions and therefore high γ_{HO_2} were seen in the outputs for lower tropospheric regions with high dust outflow. Other assumptions were also made involving pH, copper ion speciation and mass accommodation coefficient values making this parameterisation best considered as an upper limit resulting in higher values of γ_{HO_2} than those seen experimentally (Thornton et al., 2008).

Macintyre and Evans (2011) introduced a new parameterisation using the GEOS-Chem global chemical transport model run with five externally mixed aerosol types: black carbon; dust; sulphate; organic carbon and sea salt. The model simulations were run using both γ_{HO_2} of 0.2 as originally suggested in Jacob, 2000 and then with new parameterisations (Jacob, 2000; Macintyre and Evans, 2011). Due to the temperature

dependence of γ_{HO_2} , the highest values of ~ 0.1 were found at high latitudes i.e. γ_{HO_2} increases with a decrease in temperature and an increase in humidity. Warm tropical regions and regions where sulphate and organic aerosols dominate showed the lowest values of γ_{HO_2} at ~ 0.01 . The global mass-weighted annual average γ_{HO_2} was calculated to be ~ 0.028 , much lower than the value of 0.2 suggested in Jacob, 2000. In comparison, the global mean average of ~ 0.1 was given in Thornton et al., 2008. This difference may be due to no assumption being made of the presence of transition metal ions by Macintyre and Evans so the value of 0.028 is more likely a lower limit for the uptake coefficient. This study showed on a global scale, the impact of a lower γ_{HO_2} only had a small effect on the concentration of oxidants and sulphur species. This effect was more important regionally however with the conclusion being that tropospheric chemistry models which neglected to include HO_2 uptake processes will over predict sulphate formation in the lower troposphere while under-predicting it in the upper troposphere thereby potentially changing the transport and distribution of sulphur throughout the atmosphere (Macintyre and Evans, 2011).

In a study by Mao et al., 2013 the sensitivity of γ_{HO_2} to Cu ion concentrations was shown to be weak when the concentration of Cu ions were in excess of 5×10^{-4} M: consistent with Thornton et al., 2008. With a five-fold decrease in Cu concentration, the γ_{HO_2} value only decreased from 0.85 to 0.61. This was mainly attributed to the diffusion limitations of HO_2 uptake in the aqueous phase showing its rapid reaction with Cu (II). Box model simulations of aqueous aerosol chemistry were also conducted to investigate the effect of Cu-Fe- HO_x cycling on the HO_x budget. These simulations gave a range of pH dependant values for γ_{HO_2} from 0.4-1. These values were incorporated into the GEOS-Chem global model (Mao et al., 2013). However, values this high for the uptake coefficient are not representative of the global troposphere as Cu (II) ion concentrations are likely to be much lower than those assumed within the model in addition to the large uncertainties in aerosol phase and mixing state. The effect of applying an upper limit of $\gamma_{HO_2}=1$ for all aerosols on the oxidant chemistry was studied using GEOS-Chem by Mao et al., 2013. The yield of H_2O_2 was taken as zero with fast conversion of HO_2 into H_2O included instead which had the effect of bringing the global mean tropospheric OH concentration closer to the observational constraints, increasing the CO concentration in the model. The modelled effects of this were seen strongly in the extratropical northern hemisphere and over

the Southern Ocean where there was high aerosol loading. Modelled surface ozone concentrations also decreased over North America and Eurasia helping to correct mean model bias for ozone. Thus, the mechanism of fast HO₂ conversion to H₂O in aqueous aerosols improved the simulation of tropospheric oxidant chemistry in GEOS-Chem though not necessarily for the right reasons (Mao et al., 2013).

A more recent study by Li et al., 2018, suggested that the ~40 % decrease in fine particulate matter over the period of 2013-2017 in China was slowing down the aerosol sink of HO₂ radicals and thus leading to increased ozone production. It was found that changes in PM_{2.5} were more important in driving the ozone trends during this period than NO_x or VOC emissions. An uptake coefficient of 0.2 was used for HO₂ and the conversion to H₂O or H₂O₂ (Li et al., 2018). This value was chosen to be consistent with laboratory measurements made by Taketani et al., 2012 in which HO₂ uptake onto aerosol surfaces collected from 2 sites in eastern China were found to be as high as 0.23 ± 0.07 and 0.25 ± 0.09 (Taketani et al., 2012; Li et al., 2018). The reactive uptake of NO_x species with conversion to HNO₃ was also included with the uptake of HO₂ being by far the dominant effect, accounting for most of the sink of HO_x radicals in the model in eastern China. This effect is the most important in the North China Plain where PM_{2.5} concentrations are the highest. A sensitivity model simulation was run by Li et al., 2018 to give the product of the reaction of HO₂ with transition metal catalysis to be H₂O₂ instead of H₂O and this showed no significant difference. Table 1.1 summarises experimental uptake coefficients of HO₂ onto inorganic salt aerosols.

Salt Composition	RH / %	$\gamma(\text{HO}_2)$	Reference
Dry $(\text{NH}_4)_2\text{SO}_4$ aerosol	20	0.04 ± 0.02	Taketani et al., 2008
	45	0.05 ± 0.02	Taketani et al., 2008
	32-54	< 0.004	George et al., 2013
Dry NaCl aerosol	20	< 0.01	Taketani et al., 2008
	45	0.02 ± 0.01	Taketani et al., 2008
	33-54	< 0.004	George et al., 2013
Dry TiO_2 aerosol	11	0.021 ± 0.001	Moon et al., 2018
	66	0.036 ± 0.007	Moon et al., 2018
Aqueous $(\text{NH}_4)_2\text{SO}_4$ aerosol	42	~ 0.1	Thornton and Abbatt, 2005
	45	0.11 ± 0.03	Taketani et al., 2008
	55	0.15 ± 0.03	Taketani et al., 2008
	55	0.003 ± 0.005	George et al., 2013
	65	0.17 ± 0.04	Taketani et al., 2008
	65-75	0.01 ± 0.01	George et al., 2013
	75	0.19 ± 0.04	Taketani et al., 2008
Aqueous NaCl aerosol	53	0.11 ± 0.03	Taketani et al., 2008
	54	0.016 ± 0.008	George et al., 2013
	63	0.09 ± 0.02	Taketani et al., 2008
	67-76	0.01 ± 0.13	George et al., 2013
	75	0.10 ± 0.02	Taketani et al., 2008
Aqueous Cu(II)-doped $(\text{NH}_4)_2\text{SO}_4$ aerosol	42	0.5 ± 0.1	Thornton and Abbatt, 2005
	45	0.53 ± 0.13	Taketani et al., 2008
Aqueous Cu(II)-doped	53	0.65 ± 0.17	Taketani et al., 2008
Aqueous Cu(II)-doped NH_4HSO_4 aerosol	53-65	0.4 ± 0.3	Mozurkewich et al., 1987
	75	0.4 ± 0.08	George et al., 2013

Table 1.1. Uptake coefficients for HO_2 onto inorganic salt aerosols from previous work. This table has been updated from George et al., 2013.

1.10.4 Model-Measurement Comparison of Atmospheric Radicals

Testing current understanding of HO_x chemistry using box models often leads to a significant over-prediction in the concentration of HO₂ as well as an under-prediction in HONO suggesting a previously undetermined sink of HO₂ and a missing source of HONO. Heterogeneous uptake is often considered a plausible missing sink for HO₂ in models whereas heterogeneous production on aerosol or ground surfaces is a plausible source of HONO thereby providing motivation for the study of the heterogeneous chemistry of reactive species on aerosol surfaces as outlined in this project.

The over-prediction of HO₂ compared to observed concentrations during field campaigns has ranged from ~20-95% (Cantrell et al., 1996; Sommariva et al., 2004; de Reus et al., 2005; Sommariva et al., 2006; Kanaya et al., 2007; Stone et al., 2012) with many modelling studies estimating the uptake coefficient of HO₂ as 1, the maximum possible value (Kanaya et al., 2007; Mao et al., 2010). During the ARCTAS 2008 campaign, Mao et al., 2010a measured concentrations of HO₂ over a range of altitudes in the Arctic. Mao et al., 2010a showed that including a HO₂ uptake coefficient calculated by Thornton et al., 2008 parameterisation showed better agreement than a single value for the uptake coefficient. During the London campaign (ClearfLo) undertaken by the Leeds group in 2012, the detailed box model using the Master Chemical Mechanism (MCM v3.2) showed a missing peroxy radical sink at low NO_x conditions leading to an over-prediction of HO₂ by a factor of 10 under these conditions (Whalley et al., 2018). In this model, under high NO conditions, modelled and measured HO₂ concentrations were in agreement. Similarly, in an earlier campaign (NAMBLEX) in 2005 undertaken by the Leeds group at the Mace Head Atmospheric Research Station, there was an over-prediction of HO₂ from the models with the budget for HO₂ being closed by the introduction of a reaction with measured IO and BrO radicals and the uptake to aerosols of HO₂ (Smith et al., 2006). A more recent megacity study comparing the measured values of HO₂, observed during a summer campaign in Beijing (AIRPRO campaign 2017), also over-predicted HO₂. This was accounted for partly by a missing OH source in addition to a missing HO₂ destruction term (Whalley et al., 2021). This is considered further in Section 7.

During the ClearfLo campaign measurements of HONO were also carried out with the subsequent model runs under-predicting HONO concentration even with the addition of extra HONO sources including dark conversion of NO₂ on surfaces, direct emission

of HONO, photolysis of ortho-substituted nitrophenols, the reaction of $\text{HO}_2 \times \text{H}_2\text{O}$ with NO_2 , photolysis of adsorbed HNO_3 on ground and aerosol surfaces and photolytic conversion of NO_2 on surfaces. The ensuing study by Lee et al., 2016 concluded that the missing HONO source was in correlated to NO_2 and required sunlight. Increasing the photolytic conversion of NO_2 on surfaces by a factor of 10 served to close the HONO daytime budget at all times suggesting a source of HONO from the heterogeneous reaction of NO_2 on urban surfaces (Lee et al., 2016). Table 1.2 compares the measured and modelled values of OH and HO_2 for field campaigns in the last 2 decades.

Campaign, Location	Month, Year	OH measured (10⁶ cm⁻³)	OH measured/ modelled	HO₂ measured (10⁸ cm⁻³)	HO₂ measured / modelled	Notes	Reference
PMTACS-NY2001, New York, US	Jun - Aug, 2001	7	0.91	1	0.81	Midday av.	Ren et al., 2006
IMPACT, Tokyo Japan	Jan – Feb, 2004	1.5	0.93	0.27	0.88	Midday av.	Kanaya et al., 2007
IMPACT-L, Tokyo, Japan	Jul – Aug, 2004	6.3	0.86	2.31	1.29	Midday av.	Kanaya et al., 2007
PRIDE-PRD2006, China	July, 2006	12.3 ²	2.12	1.75 ²	0.94	Midday av.	Lu et al., 2012
TRAMP, Texas, 2006	Aug – Oct, 2006	15	1.6	1.2	1.37	Value at 12:20 pm	Chen et al., 2010
ClearFlo, London UK	Jul - Aug, 2012	2.1, 2.8	0.75, 0.67	1.5, 0.6	0.3, 0.31	Midday av. (SW, E)	Whalley et al., 2018
Wangdu, China	Jun – Jul, 2014	9	1.5	9	0.9	Midday av.	Tan et al., 2017
BEST-ONE, Beijing, China	Jan – Mar, 2016	2.2	2	0.5	2.5	Midday av.	Tan et al., 2018
PKU, Beijing, China	Nov – Dec, 2017	1.4	1.4	0.3	7.5	Midday av.	Ma et al., 2019

Table 1.2 Model-measurement comparisons of HO₂ from campaigns worldwide. Table has been modified from the thesis of Slater et al., 2020.

1.11 Project Outline

The overall aims of this project are to:

1. Improve understanding of the role that aerosols play in the change in gas-phase composition of the troposphere.
2. Improve understanding of uptake and production of reactive gas-phase species through heterogeneous chemistry on aerosol surfaces.

The objectives of this project are as follows:

1. To measure the production rate of HONO from illuminated TiO₂ aerosols as a function of NO₂ and use a kinetic box model to investigate the possible reaction mechanisms for the formation of HONO from NO₂ uptake on aerosol surfaces.
2. To investigate the production of HONO from particulate nitrate photolysis with and without TiO₂ present on ammonium nitrate aerosol surfaces.
3. To build and calibrate a potential aerosol mass chamber for the production of secondary organic aerosols from the oxidation of volatile organic compounds.
4. To measure HO₂ uptake coefficients on α -pinene and limonene-derived SOA surfaces.
5. To quantify the impacts of HO₂ uptake on aerosol surfaces using box modelling studies by means of the Master Chemical Mechanism.

2 Experimental Methods for HO₂ Uptake from Aerosol Surfaces

2.1 Overview of Experimental Set-up

The uptake of HO₂ radicals onto aerosol surfaces was studied using an aerosol flow tube coupled to a Fluorescence Assay by Gas Expansion (FAGE) cell which allowed the highly sensitive detection of HO₂ via the conversion to OH followed by Laser Induced Fluorescence (LIF) detection at low pressure. The system worked by flowing aerosols, either generated using an atomiser or by OH-initiated or O₃ chemistry within a Potential Aerosol Mass (PAM) chamber, through a laminar flow reactor with HO₂ added from a moving injector. The decay in HO₂ concentration was then determined as a function of exposure time. A Scanning Mobility Particle Sizer (SMPS) was used to characterise the aerosols leaving the flow tube reactor. A schematic of the aerosol flow tube system, coupled to the HO₂ detection cell is shown in Figure 2.1.

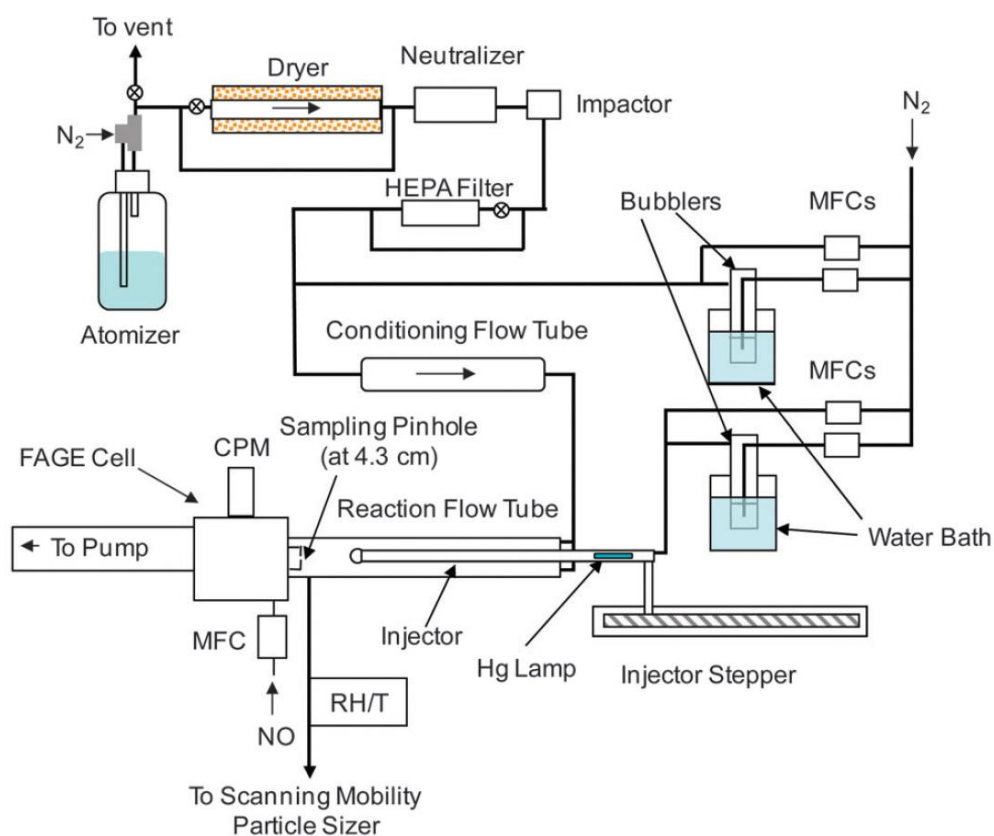


Figure 2.1. Schematic diagram of the aerosol flow tube system used to study the uptake of HO₂ onto aerosol surfaces. CPM: Channel Photomultiplier, HEPA: High Efficiency Particulate Air filter, FAGE: Fluorescence Assay by Gas Expansion, RH: Relative Humidity, T: Temperature, MFC: Mass Flow Controller. Image taken from George et al., 2013.

All aerosol experiments were conducted at room temperature (295 ± 3 K) using nitrogen as a carrier gas. Whenever departmental nitrogen was used as the carrier gas for the experiment, the flow was passed through a gas purification system (TSI 3074 B) which was comprised of two filters which remove water, oil droplets and particulates, a membrane dryer to remove excess moisture and finally a carbon filter to remove any lingering oil vapour. This filter purification system removes 99.99995 % of particles of 100 nm in diameter at a velocity of 10 cm s^{-1} . A schematic of the purification system is shown in Figure 2.2.

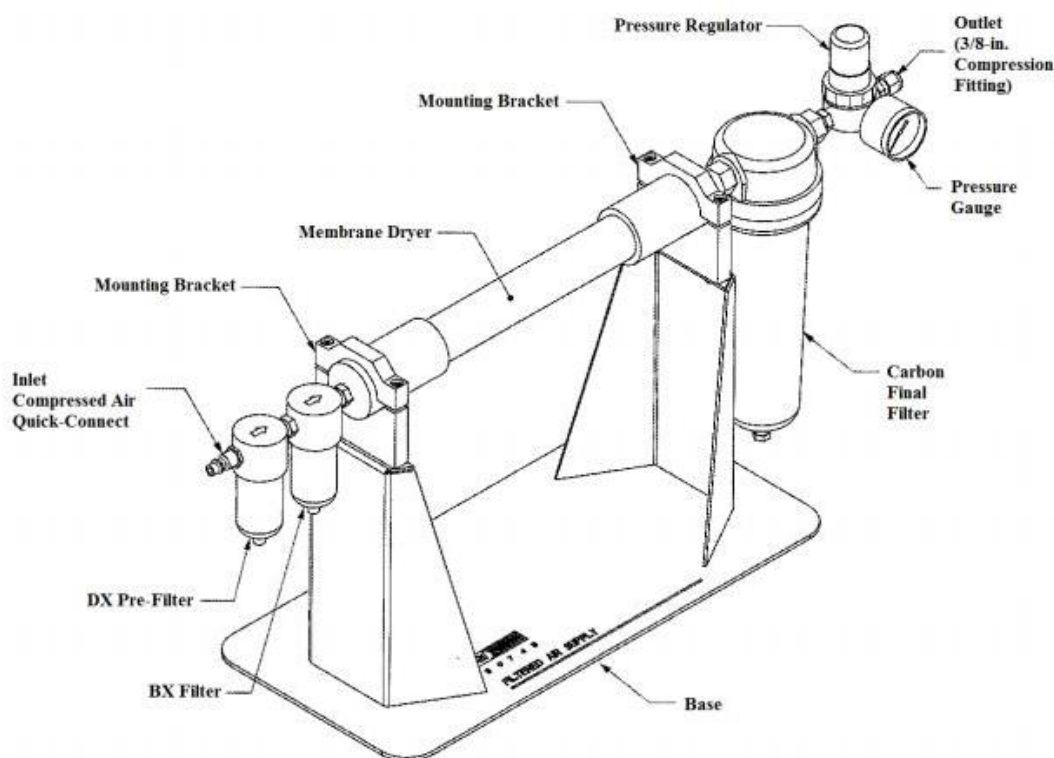


Figure 2.2. Gas purification system TSI model 3074B. Used for removal of contaminants from the departmental nitrogen supply TSI, 2008b.

The FAGE detection cell was kept at low pressure, 1.2-1.3 Torr, by using a rotary pump (Edwards, E1M80) and a roots blower (Edwards, EH1200) in combination. All gas flows were controlled using mass flow controllers (MKS and Brooks). The relative humidity (RH) and temperature of the gas flow leaving the flow tube was measured using a RH/T probe (Rotronics HC2-S, accuracy ± 1 % RH). A chilled mirror hygrometer (General Eastern Optica) was used to calibrate the RH/T probe.

2.2 HO₂ generation

The HO₂ radicals were generated within a sliding injector inside the aerosol flow tube by passing a flow of humidified nitrogen containing trace amounts of oxygen over a 185 nm mercury lamp. The subsequent photolysis of H₂O vapour produced H atoms that rapidly reacted with the O₂ in the nitrogen flow to give HO₂ radicals (George et al., 2013).



By keeping the flow through the sliding injector as well as the current of the mercury lamp constant it can be assumed that the initial concentration of HO₂ generated, [HO₂]₀, defined as the concentration at the first injector position within the flow tube, remained the same throughout the entirety of the experiment. As shown in R 2.1, OH is also produced by the photolysis of water. Any OH produced however was rapidly lost to the walls of the injector and so was not observed exiting the injector.

2.2.1 The Sliding Injector

The sliding injector, shown in Figure 2.3, was used to vary the exposure time of HO₂ to the aerosols contained in the flow tube reactor. The injector (110 cm length, 1.9 cm external diameter, 1.6 cm internal diameter) was made from stainless steel and contained a 185 nm mercury lamp at the inlet. This lamp was located at the furthest point from the detection cell, to allow for any heat created to dissipate before entering the flow tube. The inside of the injector housed a Teflon tube (1.5 cm external diameter, 0.8 cm internal diameter) used to reduce HO₂ wall loss down the length of the injector and to ensure all OH generated from R 2.1 was lost to the walls and did not enter the flow-tube. The tip of the injector was made from Teflon and drilled with 20 x 1 mm holes equally spaced around the circumference 0.5 cm from the tip to allow the injector flow entering the flow tube to be perpendicular to the aerosol flow. This ensured turbulent mixing (Moon, 2018).

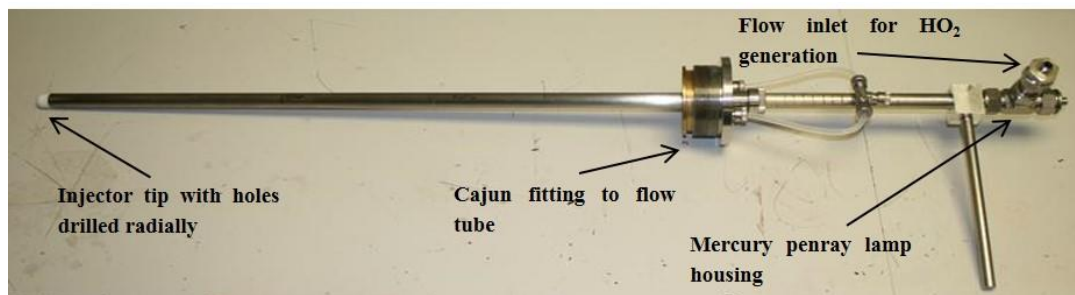


Figure 2.3. Sliding injector used for the addition of HO₂ radicals into the flow tube during HO₂ uptake experiments. Image taken from Moon, 2018.

2.3 Aerosol Flow Tube

A borosilicate glass flow tube reactor (100 cm L, 5.9 cm OD) was used to measure the kinetics of HO₂ uptake on aerosol surfaces. Glass was used due to the reactive uptake of HO₂ being sensitive to transition metal contamination; it was also useful to be able to see the position of the sliding injector within the flow-tube. The walls of the flow-tube were coated with Halocarbon wax to reduce the loss of HO₂ to the walls. This was done by dissolving the wax into a chlorinated solvent, usually dichloromethane, and pouring it into the flow-tube, turning it periodically to get an even coverage. The wax layer could then be removed for cleaning using large ovens. The end of the flow tube furthest from the injector port was connected to the FAGE cell with a compression fitting containing an O-ring (Moon, 2018). The temperature was taken using a calibrated probe (Rotronics HygroClip2, $\pm 0.1\text{K}$) located either by the injector port or at one of the ports closest to the FAGE cell. A Scanning Mobility Particle Sizer (SMPS), fully described in Section 3.3.4, was attached after the flow-tube to measure the aerosol particle number and surface area size distributions. An ozone analyser (Thermo Fischer, model 49i) was also connected to the exhaust of the flow-tube by the FAGE cell. Figure 2.4 shows the flow-tube attached to the FAGE cell.



Figure 2.4. Aerosol flow tube setup showing connection to the FAGE cell of the right. Sliding injector is shown on the left.

2.4 Aerosol Generation using a Potential Aerosol Mass Chamber

A Potential Aerosol Mass chamber provided a stable method for the generation of secondary organic aerosols. Potential Aerosol Mass (PAM) is defined as the maximum aerosol mass that can be produced by the oxidation of precursor gases. Within a PAM chamber, the precursor gas or gases were rapidly oxidized by excess concentrations of oxidant leading to the formation of low volatility compounds which partitioned to form SOA. The level of oxidant could be varied by changing the UV light intensity. For experiments where O_3 was the oxidant, a 185 nm mercury pen-ray lamp, housed before the chamber, was used to convert O_2 (in air flow) to O_3 , R 2.3 and R 2.4. For experiments where OH was the oxidant, 254 nm lamps housed inside the chamber were used to convert O_3 to OH, R 1.1 and R 1.2.



The Leeds PAM chamber is a 16.5 L pyrex cylinder (50 cm L and 20.5 cm ID) containing 4 quartz tubes which house 4, 254 nm UV lights used for the production of OH and flushed with N_2 to cool. A single ozone-producing 185 nm mercury lamp was placed in-line to the flow of air before the PAM chamber inlet. A bypass flow was used to control the ratio of air flowing past the 185 nm lamp, thereby controlling the O_3 production. VOC precursors were added into the chamber via a bubbler set up

which was used to vaporise the VOC e.g. limonene by flowing nitrogen gas through a dilution of VOC in milli-Q water, usually a 1/30 or 1/40 dilution, and then adding this flow into the larger inlet flow containing air and the chosen oxidant. Five MFCs were used: Two for air to control flow past the Hg lamp for O₃ generation, one humidified (10 slm, MKS) and one dry (1 slm, MKS); one for nitrogen 254 nm lamp flush (5 slm, MKS); one for nitrogen, to bubble the precursor VOC into the chamber (1 slm, MKS); and one for a makeup flow of air added after the PAM chamber to increase the flow if necessary (5 slm, Mykrolis). The flow through the chamber was kept low enough to ensure laminar flow, with a Reynolds number of ~42 for a flow rate of 6 lpm. Two charcoal denuders were added in series after the PAM chamber to remove residual VOC and O₃ from the flow before it passed into the flow tube. FAGE instruments have been shown to be sensitive to detection of certain RO₂ species in HO₂ detection mode. These RO₂ species derive from alkene or aromatic VOCs and so any residual monoterpene in the flow tube could lead to an RO₂ interference if VOC + OH reactions of VOC + O₃ reactions were permitted to occur within the flow tube. Any O₃ could react with HO₂ to artificially increase the loss of HO₂ within the flow tube as the injector is pulled back if allowed to pass into the flow tube. Figure 2.5 shows a schematic of the SOA generation system and Figure 2.6 shows the Leeds PAM chamber with the UV lights on.

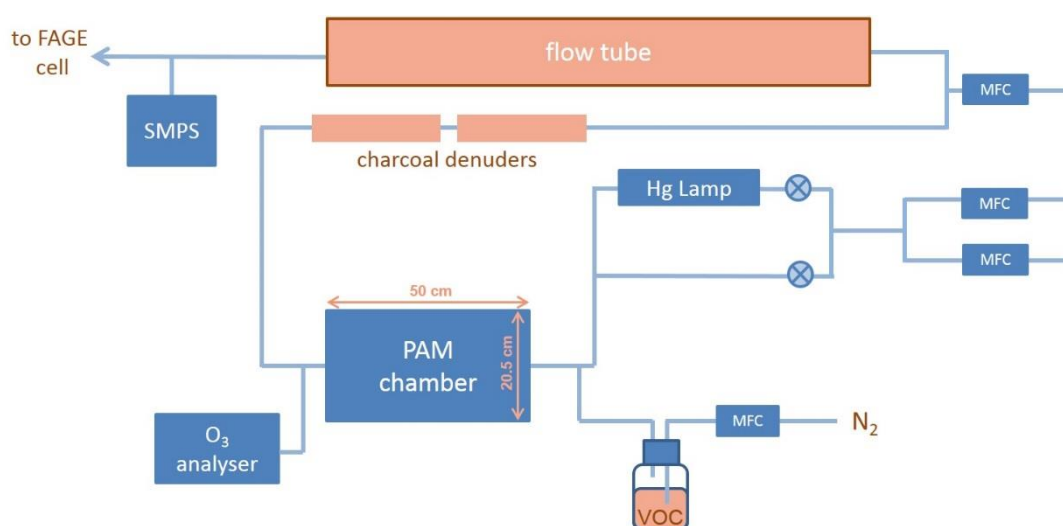


Figure 2.5. Leeds SOA generation setup. MFC: Mass Flow Controller, PAM: Potential Aerosol Mass, SMPS: Scanning Mobility Particle Sizer, VOC: Volatile Organic Compound.



Figure 2.6. Leeds PAM chamber with 4 UV lights.

2.5 The FAGE Instrument

2.5.1 FAGE Principle of Operation

The lifetime of the OH radical in the atmosphere is short, usually much less than 1 s. Its concentration, which is low making it difficult to measure, is controlled on a local scale by the variation of sunlight, O₃ levels, water vapour concentrations and concentrations of pollutants. Due to this, *in-situ* measurements of OH are extremely difficult. The three most commonly used methods which provide a high enough sensitivity are differential-optical absorption spectroscopy (DOAS), selected ion-chemical ionisation mass spectrometry (CIMS) and laser induced fluorescence spectroscopy (LIF) (Heard, 2006a).

Laser Induced Fluorescence was first proposed as a detection method for atmospheric OH radicals in 1972 (Baardsen and Terhune, 1972). Fluorescence spectroscopy is used to probe the electronic states of molecules such as OH, by excitation of electrons from the molecules ground electronic state to an electronically excited state. Electronic states are split into vibrational levels which are then split further into rotational levels. Vibrational levels result from the vibrational motion of the nuclei which occurs when there is a change in potential energy of the molecule i.e. when a bond is stretched or compressed. Rotational levels result from the overall rotational motion of a molecule.

During fluorescence spectroscopy, an electron will be excited from the ground electronic state usually to the first excited electronic state (to one of the ro-vibrational levels within this state) through the absorption of light with a wavelength corresponding to the energy gap between the two electronic states. The molecule can then lose this energy through several processes namely; fluorescence; quenching; inter-system crossing; internal conversion or vibrational energy transfer (Brown, 1998). When OH radicals are excited to the $v' = 0$ state, the only means of relaxation back to the ground $v'' = 0$ state is by giving out light in the form of fluorescence or through collisional quenching with another molecule, such as N_2 or O_2 (Heard, 2006b). Quenching through collision with a bath molecule removes the excess energy and converts it into thermal motion or internal excitation of the non-fluorescent species. This is shown schematically in Figure 2.7.

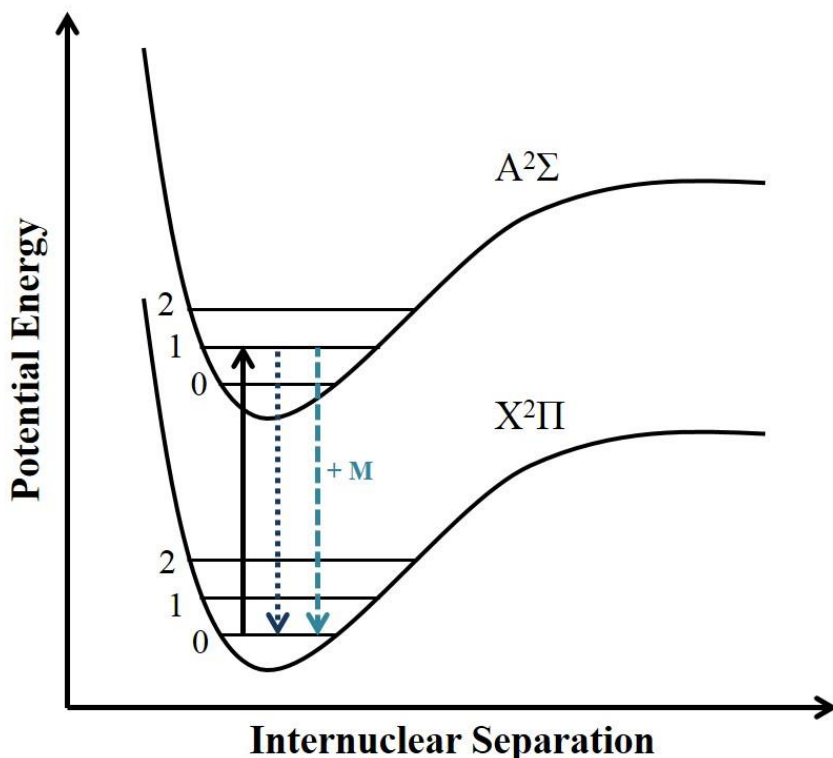


Figure 2.7. Schematic of the potential energy curves of OH. Excitation from ground electronic state to first excited electronic state shown in black. Emission via fluorescence shown in navy and collisional quenching shown in teal. M is a bath gas such as O_2 or N_2 . Image reproduced from Heard, 2006b.

On-resonance Laser Induced Fluorescence (LIF) works by exciting the OH radical and detecting the fluorescence that follows when it relaxes back to its ground state at the same wavelength. A major problem with LIF is separating the fluorescence signal

from the intense laser radiation scattered by the gaseous components in air via Rayleigh scattering and by any aerosols present by Mie scattering (Heard, 2006a). The walls of the LIF instrument used can also add to the scattering of light. To avoid this, off-resonance fluorescence can be used meaning that the OH is excited at a different wavelength to that which it fluoresces at, i.e. not 308 nm. Any scattering of light can be reduced by exciting at 282 nm in the $A^2\Sigma^+ (v' = 1) \leftarrow X^2\Pi_i (v'' = 0)$ band and then collecting fluorescence from the $A^2\Sigma^+ (v' = 0) \rightarrow X^2\Pi_i (v'' = 0)$ transition (Heard, 2006a), shown in Figure 2.8.

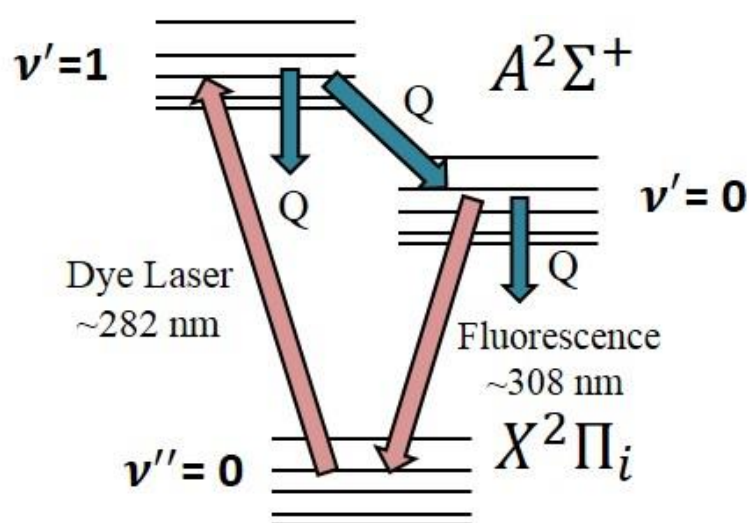


Figure 2.8. Off-resonance fluorescence detection of OH radicals. Q represents quenching. Figure adapted from Heard, 2006a.

At 760 Torr, this transition has a low quantum yield for fluorescence of excited OH. Both on and off resonance fluorescence techniques are therefore conducted in low pressure detection cells to extend the fluorescence lifetime. In addition, excitation at 282 nm using low rep rate (10 - 20 Hz), high pulse energy lasers leads to an interference caused by the photolysis of ambient O_3 to produce OH in the laser beam through R 1.1 and R 1.2. This is the major pathway for OH generation in the atmosphere, however, O_3 has a much higher absorption cross-section at 282 nm than at >290 nm and a laser has a much higher photon flux in comparison to actinic flux meaning that the OH generated from laser photolysis of O_3 is much higher at 282 nm than the ambient OH signal (Heard, 2006a).

Due to this O_3 interference, tropospheric LIF instruments tend to use on-resonance fluorescence to excite the OH at 308 nm and then measure the fluorescence at the same wavelength. The use of high rep rate (3- 5 kHz) low pulse energy lasers and low

pressures (to rapidly move sampled air from detection region) minimises the ozone interference. Furthermore, at 308 nm the absorption cross section of O₃ is much lower compared to at 282 nm thereby reducing O₃ interference, from laser generated OH (Heard, 2006a). In addition, the OH absorption cross-section at 308 nm is ~6 times higher than that at 282 nm, and the O₃/H₂O interference is about 30 times smaller at 308 nm compared to that at 282 nm (a combination of the lower O₃ absorption cross-section and lower O(¹D) quantum yield). For stratospheric LIF instruments however, the lower sampling pressure leads to a higher fluorescence quantum yield of OH and therefore a higher signal to noise ratio. This means that any interference of O₃ has a diminished effect (Heard, 2006a) making off-resonance more useable for stratosphere LIF measurements as compared to tropospheric measurements. Additionally, the much lower water vapour concentration in the stratosphere means that any O₃ which is photolysed by the laser to O(¹D) will not form OH.

The FAGE technique involves the on-resonance detection of the OH radical by LIF via the excitation of the $A^2\Sigma^+ (v' = 0) \leftarrow X^2\Pi_i (v'' = 0) Q_1(2)$ transition at ~308 nm. This is shown in Figure 2.9.

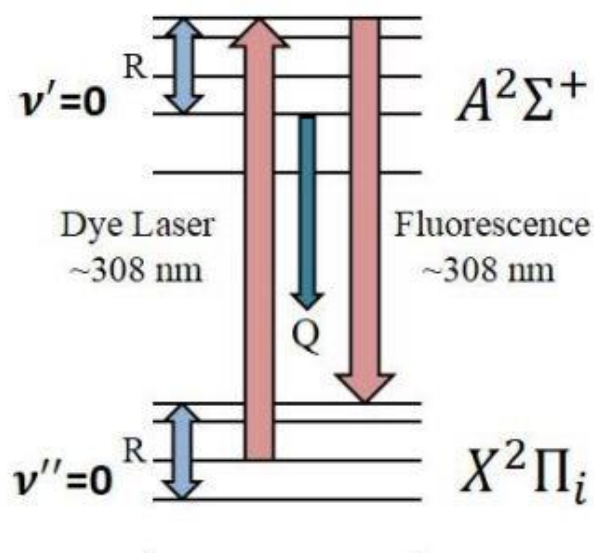


Figure 2.9. Energy level diagram showing the excitation and fluorescence of OH in the FAGE technique. R represents changes in rotational energy levels. Q represents quenching. Figure adapted from Heard, 2006a

2.5.2 FAGE Cell and the Detection of HO₂

The FAGE cell, shown in Figure 2.10, was connected to the end of the flow tube with a 0.7 mm diameter sampling pinhole in the centre axis, 4.3 cm from the end of the flow tube. The cell was kept at ~1.3 Torr by a rotary pump (Edwards E1M80) and a roots blower (Edwards, EH1200). This increased the lifetime of the OH fluorescence so as to ensure it was distinguishable from the laser scatter background using a gated multi-channel plate photomultiplier (MCP 325 Photek). The pressure of the cell was monitored using a pressure gauge (MKS Instruments 722A11TBA2PA). The air from the flow tube was sampled through the pinhole at ~ 5 lpm into the centre of the FAGE cell. The 308 nm laser was delivered to the baffled arms of the FAGE cell via an optic fibre (Oz Optics) and through the centre of the cell and then out the opposite baffled arm to hit a photodiode (New Focus 2032). A constant reading of the 308 nm laser power allowed for normalisation of the OH signal to fluctuations in laser power. The fluorescence of OH was detected perpendicular to the 308 nm laser and the main gas flow, with the MCP positioned above the centre of the FAGE cell. The fluorescence signal generated from the laser pulse then passed through a 308 nm bandpass filter (Barr Associates, 308 nm, FWHM=8 nm, ~ 50 % transmission) and focusing lenses before reaching the MCP detector to remove light of any other wavelength and to focus the light onto the photocathode within the detector. A back-reflector was installed at the base of the FAGE cell directly beneath the MCP to catch and reflect any downwards travelling fluorescence back up towards the detector, increasing the signal by ~ 40 %. A schematic of the detection cell is shown in Figure 2.10.

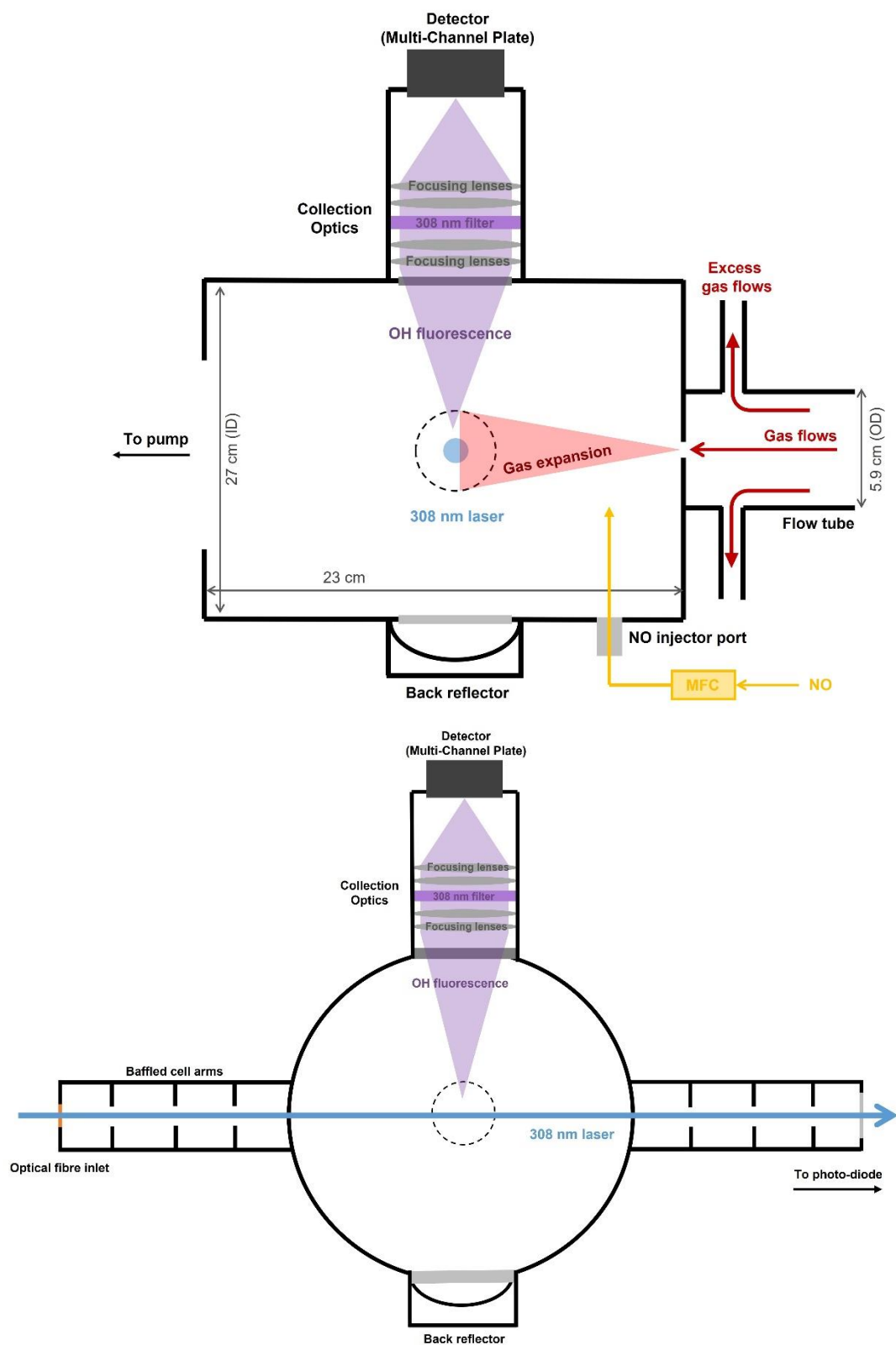


Figure 2.10. Schematic of the FAGE cell used to measure HO_2 (not to scale). Top panel shows cross-section of cell taken from the side, as if looking down the baffled arms of the cell with the laser path going through the image. Bottom panel shows a cross-section of the same cell from the front, showing the path of the laser from left to right through the arms.

NO (50 sccm, 99.5 %, BOC) was injected into the FAGE cell through a stainless-steel port in the cell, ~ 5 cm downstream of the pinhole, to convert HO₂ into OH to allow for detection.



The OH radical produced was measured using on-resonance detection by Laser Induced Fluorescence via the excitation of the $A^2\Sigma^+ (v' = 0) \leftarrow X^2\Pi_i (v'' = 0) Q_1(2)$ transition at ~308 nm (Heard, 2006a). The 308 nm radiation required was produced by a Nd:YAG pumped dye laser (JDSU Q201-HD, Q-series, Sirah Cobra Stretch) at a pulse repetition rate of 5000 Hz. The 532 nm green light produced by the Nd:YAG laser was passed through a dye cuvette containing a mixture of laser dye in ethanol/methanol to generate 616 nm red light. The red light then passed through a BBO doubling crystal to give the necessary 308 nm UV light: a process referred to as frequency doubling where 2 photons with the same frequency interact with a non-linear material and are combined to create a photon twice the frequency of the initial photons. The dye for the laser was made by dissolving 1 g of DCM ([2-[2-[4-(dimethylamino)phenyl]ethenyl]-6-methyl-4H-pyran-4-ylidene]-propanedinitrile) special into 2 L of ethanol/methanol. A schematic of the dye laser is shown in Figure 2.11.

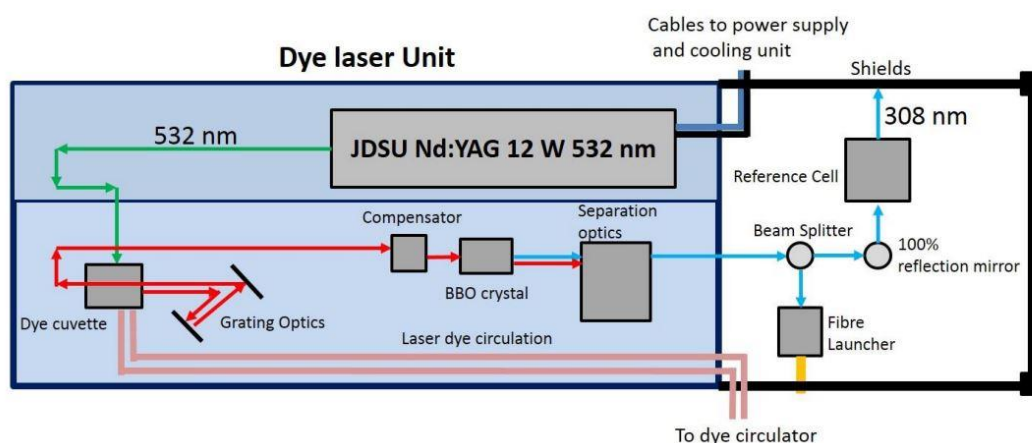


Figure 2.11. Schematic of the 308 nm pulsed dye laser and reference cell showing one beam splitter. Up to three beam splitters can be used to divide the light into up to 3 fibre launchers while still delivering 5% of laser light to the reference cell.

A maximum of 95 % of the UV light from the laser was directed to a fibre launcher (Oz Optics) and via an optical fibre cable (Oz Optics) and a fibre collimator (Oz Optics), entered the FAGE cell via a sidearm fitted with optical baffles to reduce any laser scatter. Typically, the fibre was set to deliver 2-8 mW of power though tuning the power of the green light from the YAG laser allowed finite control of the beam power entering the fibre launcher. If the power dropped below 2 mW the laser was tuned up to max UV power output. The power of the UV light entering the fibre was kept below 30 mW to avoid burning the fibre head and any long-term damage to the fibre.

2.5.3 Reference Cell

A reference cell was necessary to ensure the 308 nm laser was tuned to the peak of the OH transition; the $Q_1(2)$ rotational line of the $A^2\Sigma^+ (v' = 0) \leftarrow X^2\Pi_i (v'' = 0)$ transition. The reference cell provided a constant, high concentration of OH – generated by thermolysis of $H_2O_{(v)}$, using a hot filament made from 80:20 Ni:chrome wire attached to a power supply (~ 5.3 amps, ~ 4 V), using a beam splitter. Like the detection cell, the reference cell was held at low pressure, ~ 2 Torr. A small percentage, usually ~ 5 %, of the UV light generated by the Nd:YAG pulsed dye laser was directed into the reference cell which was used to measure the fluorescence with a Channel Photomultiplier (CPM). This allowed the laser scanning software to scan the OH transition. When the software was scanning for the transition peak, two scans had to agree to a threshold chosen by the user, usually 97 %, to ensure the maximum of the OH transition peak was found accurately. This was the “online” wavelength and was kept constant for the duration of an experiment. The online position allowed the measurement of OH fluorescence signal, laser scatter, and detector dark counts. For most FAGE cells, the detector must be switched to a low gain state, known as “gating off”, to avoid over-saturation of the detector by the laser pulse. Unlike during LIF detection in the FAGE cell, the CPM in the reference cell was left ungated. This was because the laser power at 5 % power was low enough to not lead to saturation of the detector but also because the OH concentration was high enough that it could be seen above the laser scatter without having to remove the scatter by gating, this is further explained in section 2.5.4. An example scan of the reference cell is shown in Figure 2.12.

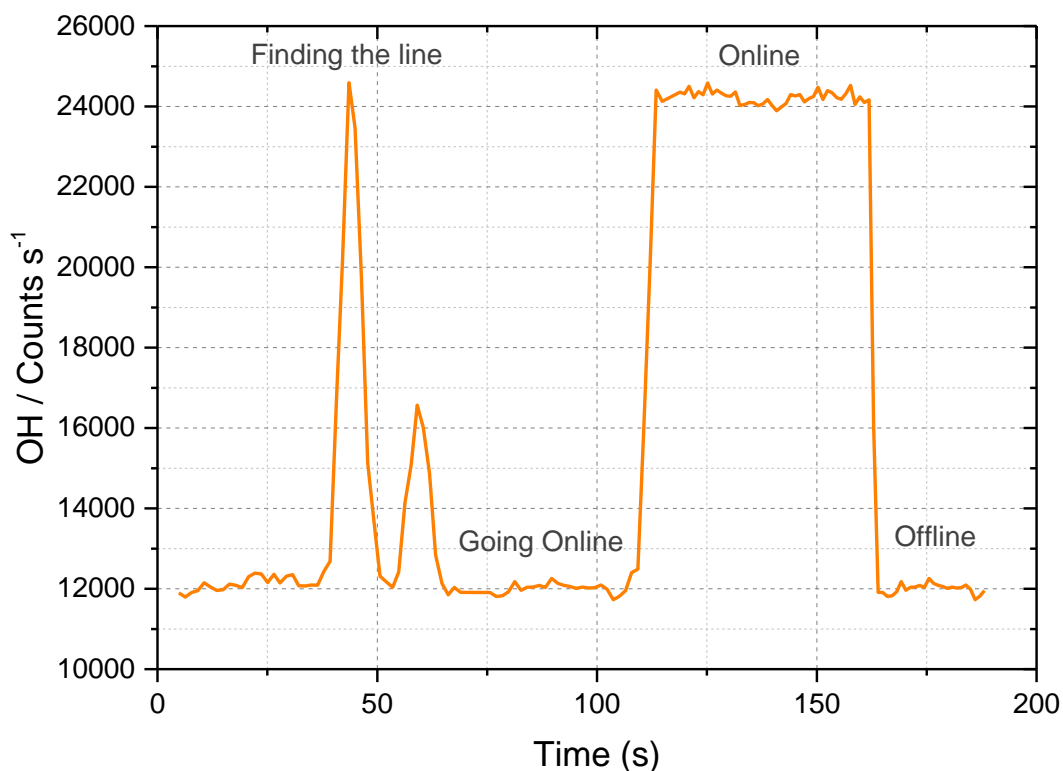


Figure 2.12. An example scan of the reference cell showing the initial scan across the peak, the online measurement and the offline measurement.

The “online” wavelength was kept constant for either a defined length of time or until the laser started to drift off the line. The laser drifting away from the OH transition peak eventually led to a drop in fluorescence signal. At this point, the laser could be moved 0.02 nm off the transition wavelength to a position where OH does not absorb UV light. This was the “offline” wavelength. Measurement of an offline position allowed the background signal generated from, scattered laser light and detector dark counts to be recorded.

2.5.4 Data Acquisition Cycle

Timing for the FAGE instrument was controlled by a delay generator (Stanford Research systems Inc. Model DG535) triggered by an internal trigger system within the laser, t_0 . t_0 was used to start the gating cycle from which the MCP and photon counting card (PCC, Becker and Hickel, PMS-400a) could be triggered. Gating of the MCP was required to reduce the measurement of the laser scatter that overlaps with the OH fluorescence. The MCP was therefore “gated off” meaning the flow of electrons to the MCP was halted (held in a low gain state) for a certain length of time

to allow the laser pulse (~ 40 ns) and ensuing scatter to drop to a level low enough to be minor compared to the OH fluorescence signal. The MCP was then gated back on to allow the measurement of the OH signal and any background signal (detector dark counts) by the PCC. The background signal alone was measured by the PCC during gate B to allow for subtraction of this from the OH signal (Eq 2.1). The gate timings are shown in Figure 2.13.

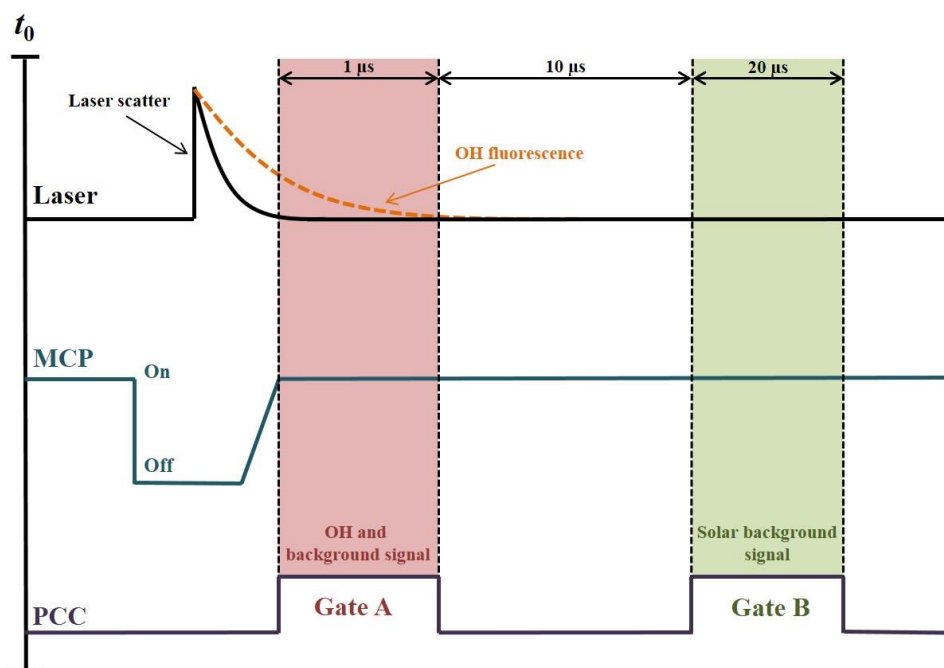


Figure 2.13. Schematic showing the data acquisition cycle for the FAGE instrument measuring HO₂ uptake. MCP: multi-channel plate. PCC: photon counting card. Image is not to scale. Gate A is 1 μs in length and measures the OH present and any background signal while Gate B is 20 μs in length and measures the solar background signal (which is not relevant for these experiments).

A full gating cycle lasted 200 μs and is started with the Nd:YAG pumped dye laser sending a t_0 trigger to both the Q-Switch within the laser to fire a pulse of light and to the delay generator to switch on the MCP and the PCC. The MCP was “on” for the entire cycle with the exception of the gated region whereas the PCC was off for the entire cycle with the exception of the two gates, Gate A, directly after the return of the MCP to the on/high gain state, and Gate B, where it was triggered on. Once the MCP was on, the OH fluorescence signal was collected within a 1 μs bin (Gate A, A_{sig}). The signal in Gate B was then subtracted, though this signal was negligible for this experiment due to lack of solar background.

$$OH\ signal = A_{sig} - \frac{B_{sig}}{20} \quad \text{Eq 2.1}$$

2.6 FAGE Calibration

FAGE is not an absolute technique meaning that to determine the absolute concentration of OH or HO₂, a calibration is required. Calibrating yields a calibration constant, C_{HO_2} , which can then be used to convert the FAGE signal into an absolute HO₂ concentration via the following relationship:

$$S_{HO_2} = C_{HO_2}[HO_2] \quad \text{Eq 2.2}$$

where S_{HO_2} is the FAGE signal produced in counts $\text{mW}^{-1} \text{s}^{-1}$, C_{HO_2} is the calibration factor in counts $\text{mW}^{-1} \text{s}^{-1} \text{molecule}^{-1} \text{cm}^3$ and $[HO_2]$ is the concentration of HO₂ in molecule cm^{-3} .

C_{HO_2} also provides information about the instrument sensitivity with high values of C_{HO_2} indicating a high degree of sensitivity to changes in HO₂ concentration and therefore a lower limit of detection.

C_{HO_2} was calculated by recording the HO₂ signal at different known concentrations of HO₂, by the photolysis of water vapour in the presence of oxygen using the mercury lamp to produce OH and HO₂ in a 1:1 ratio as shown in R 2.1 and R 2.2. The rate of production of OH and HO₂ can then be given by:

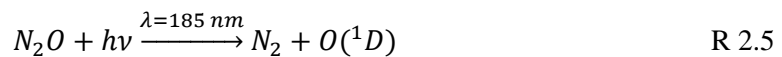
$$\frac{d[HO_2]}{dt} = \frac{d[OH]}{dt} = [H_2O] \cdot \sigma_{H_2O} \cdot \varphi_{OH} \cdot F \quad \text{Eq 2.3}$$

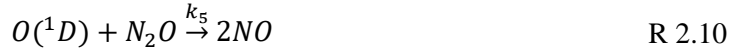
where σ_{H_2O} is the absorption cross-section of water at 185 nm ($\sigma_{H_2O,185 \text{ nm}} = 7.14 \times 10^{-20} \text{ cm}^2 \text{ molecule}^{-1}$ (Cantrell et al., 1997)), φ_{OH} is the quantum yield of OH radicals produced by photolysis of water (1) and F is the photon flux of the mercury lamp ($\text{photons cm}^{-2} \text{s}^{-1}$).

Integrating Eq 2.3 with respect to the irradiation time, t , gives an expression from which an absolute concentration of HO₂ was calculated:

$$[HO_2]_t = [H_2O] \cdot \sigma_{H_2O} \cdot \varphi_{OH} \cdot F \cdot t \quad \text{Eq 2.4}$$

σ_{H_2O} and φ_{OH} are both well defined but $F \cdot t$ had to be determined using chemical actinometry which involved passing N₂O in air through the calibration system. The following reactions then occurred:





For a residence time in front of the calibration wand lamp (0.074 s at 40 lpm flow), less than a ppb of O₃ is produced from the trace amounts of O₂ in cylinder nitrogen. This coupled with the slow rate coefficient of O₃ + NO, i.e. $k_{O_3+NO}=1.8 \times 10^{-14} \text{ cm}^3 \text{ molecules}^{-1} \text{ s}^{-1}$ (Atkinson et al., 2004), means that the [NO] is not significantly reduced by any O₃ produced. As such the reaction of NO and O₃ is not considered in Eq 2.6. Actinometry experiments have been done previously in both air and N₂ and the same flux, within error, was calculated once quenching of O¹D was considered showing NO+O₃ does not have a significant effect on the [NO].

The NO produced was measured using an NO_x analyser and the $F \cdot t$ at different lamp currents was determined using Eq 2.6 determined after applying the steady state approximation for O¹D), shown in Eq 2.5.

$$\frac{d[O(^1D)]}{dt} = [N_2O] \cdot \sigma_{N_2O} \cdot \varphi_{O(^1D)} \cdot F \quad \text{Eq 2.5}$$

$$F_{185}t = \frac{[NO](k_1[O_2] + k_2[N_2] + (k_3 + k_4)[N_2O])}{2k_5\sigma_{N_2O}\varphi_{O(^1D)}[N_2O]^2} \quad \text{Eq 2.6}$$

The FAGE calibration setup consisted of a narrow aluminium flow tube, known henceforth as the “calibration wand”, containing a mercury penray lamp through which a flow of humidified air was passed. The air was humidified using a bubbler and the concentration of water within the flow was measured using a dew-point hygrometer (CR4, Buck Research Instruments). The mercury lamp was located at the end of the wand closest to the FAGE inlet so as to reduce OH wall losses and losses to impurities in the gas flow. The outlet of the wand was placed at 45° to FAGE inlet so as to not directly push the flow into the pinhole, thereby minimising radical losses to the pinhole surface. The lamp outputted 184.5 nm radiation which photolysed water vapour to give OH and HO₂ radicals, as shown in R 2.1. A schematic of the calibration set up is shown in Figure 2.14.

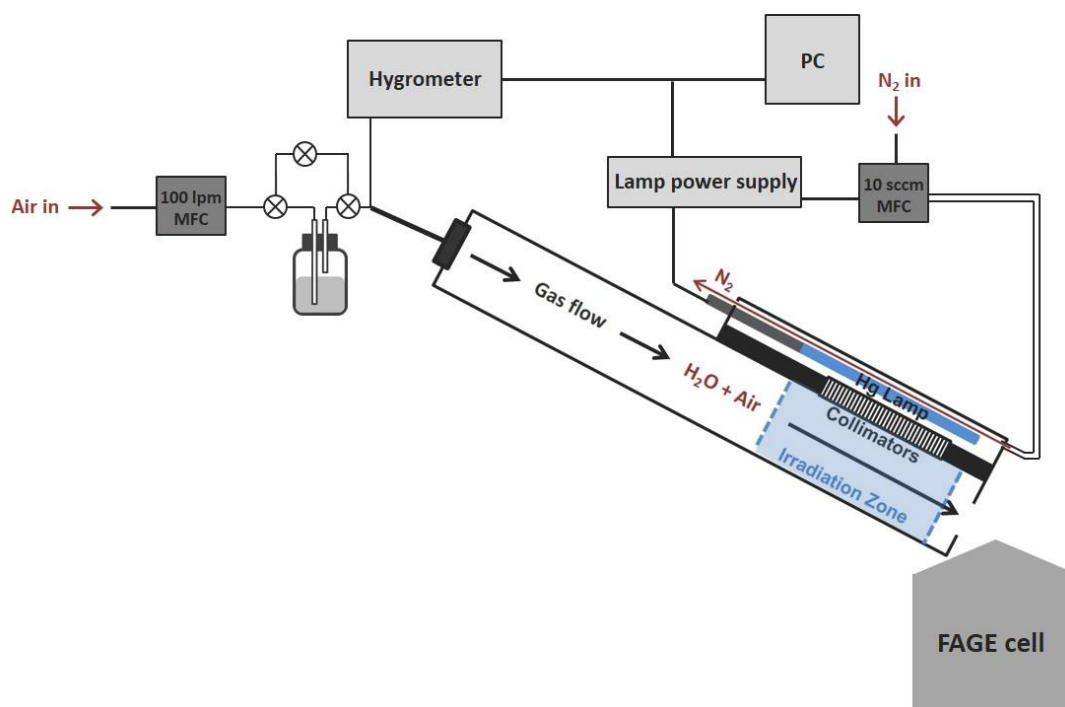


Figure 2.14. Schematic of FAGE calibration set up. MFC: Mass Flow Controller. FAGE: Fluorescence Assay by Gas Expansion.

The HO_2 signal was measured over a range of known HO_2 concentrations. The FAGE signal was normalised to laser power and plotted against the concentration of HO_x entering the FAGE cell. From Eq 2.2 the gradient of the plot was equal to C_{HO_2} . An example calibration plot is shown in Figure 2.15.

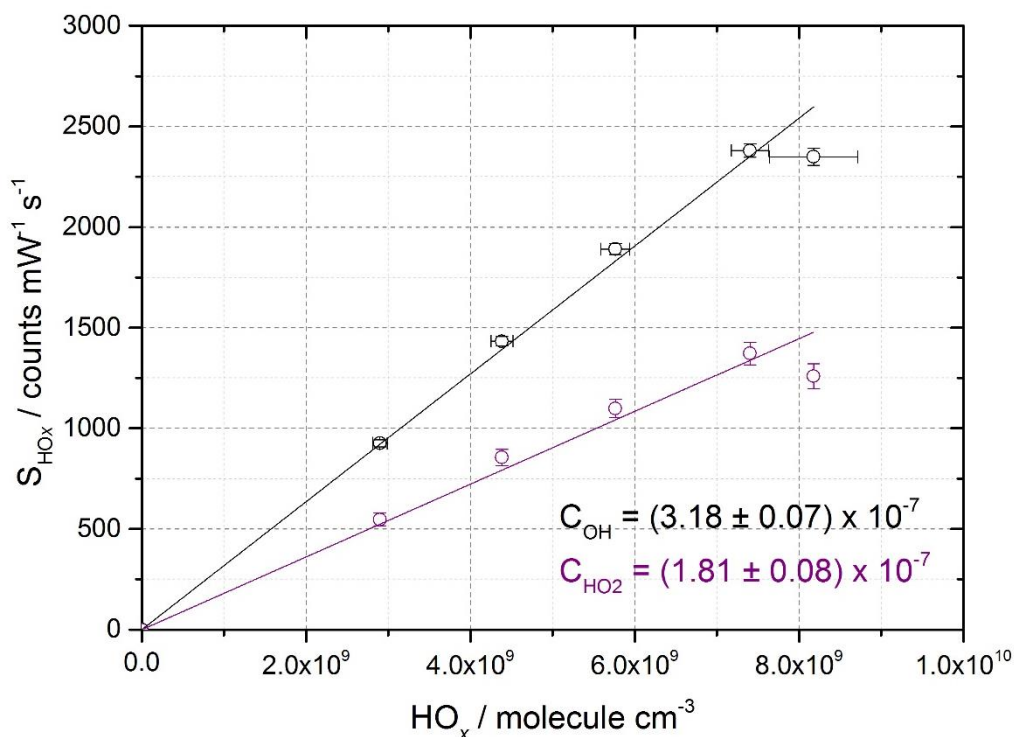


Figure 2.15. HO₂ (purple) and OH (black) calibration curves. Error bars represent $\pm 1\sigma$ with the linear least squares fit shown in black (OH) and purple (HO₂). The gradient (i.e. the calibration factor) is in units of $\text{counts s}^{-1} \text{mW}^{-1} \text{molecule}^{-1} \text{cm}^3$ and the intercept is in units of $\text{counts s}^{-1} \text{mW}^{-1}$.

2.7 Experimental Procedure and Data Analysis

The procedures for measuring the heterogeneous uptake of HO₂ onto aerosols described in the next section are based off several studies (George et al., 2013;Lakey et al., 2015;Lakey et al., 2016a;Lakey et al., 2016b;Moon et al., 2018).

2.7.1 Background Signal measurement

A background signal measurement was always done at the start of the experiment to determine the zero of the FAGE instrument. The injector was placed 30 cm from the pinhole of the FAGE cell and the following background conditions were recorded:

Condition	Mercury lamp	NO flow to FAGE cell	Background Measurement
1	Off	Off	Measured dark counts and laser scatter
2	On	Off	Measured OH produced from photolysis of water in the production of HO ₂ from injector lamp, darks counts and laser scatter. Usually very similar to condition 1 as OH was rapidly lost to the walls of the injector between the lamp and the injector tip.
3	Off	On	Contaminants from the NO gas cylinder.

Table 2.1. Description of background measurements for FAGE instrument measuring HO₂ uptake from aerosol surfaces.

2.7.2 Moving Injector Experiment

The moving injector experimental procedure was used for water soluble aerosols that could be generated by the atomiser, i.e. inorganic salt aerosols and TiO₂, and for experiments using SOA generated in the PAM chamber, fully described in Section 2.4. This procedure measured the HO₂ signal from the injector, i.e. HO₂ source, at different positions along the flow tube, typically ranging from 30 cm to 70 cm from the FAGE inlet, generally in 5 or 10 cm intervals. A computer controlled linear stepper drive (Parker L50i) was used to control the position of the injector from the inlet. Taking measurements without the presence of aerosols allowed the measurement of a wall loss rate of HO₂ (k_{wall}). Wall loss decays were taken periodically throughout the course of an experiment. The HO₂ signal was averaged over 30-60 s (an average of 30-60 points at 1 s increments) at each injector position with a slight delay at each position to allow the flow tube to flush through. This ensured that the FAGE signal seen was from the HO₂ produced at the injector's current position rather than its previous position and allowed for any mechanical movement effects to diminish. Having completed the full run of injector positions with aerosols present the entire procedure was repeated at different aerosol concentrations.

From first order principles the loss of HO₂ due to uptake is:

$$\frac{d[HO_2]}{dt} = -kt \quad \text{Eq 2.7}$$

The HO₂ concentration as a function of t can therefore be expressed as:

$$\ln \frac{[HO_2]_t}{[HO_2]_0} = -kt \quad \text{Eq 2.8}$$

Where $[HO_2]_t$ is the concentration of HO₂ at time t and $[HO_2]_0$ is the concentration of HO₂ at time = 0 (generally defined as when the injector is in its initial position), k is the sum of k_{obs} and the k_{wall} values for the injector position. k_{obs} is the observed pseudo-first-order rate coefficient for the uptake of HO₂. k_{obs} and k_{wall} were obtained from the gradient of a plot of $\ln(\text{HO}_2 \text{ signal})$ against residence time, t , with and without aerosols present respectively: an example of which is shown in Figure 2.16.

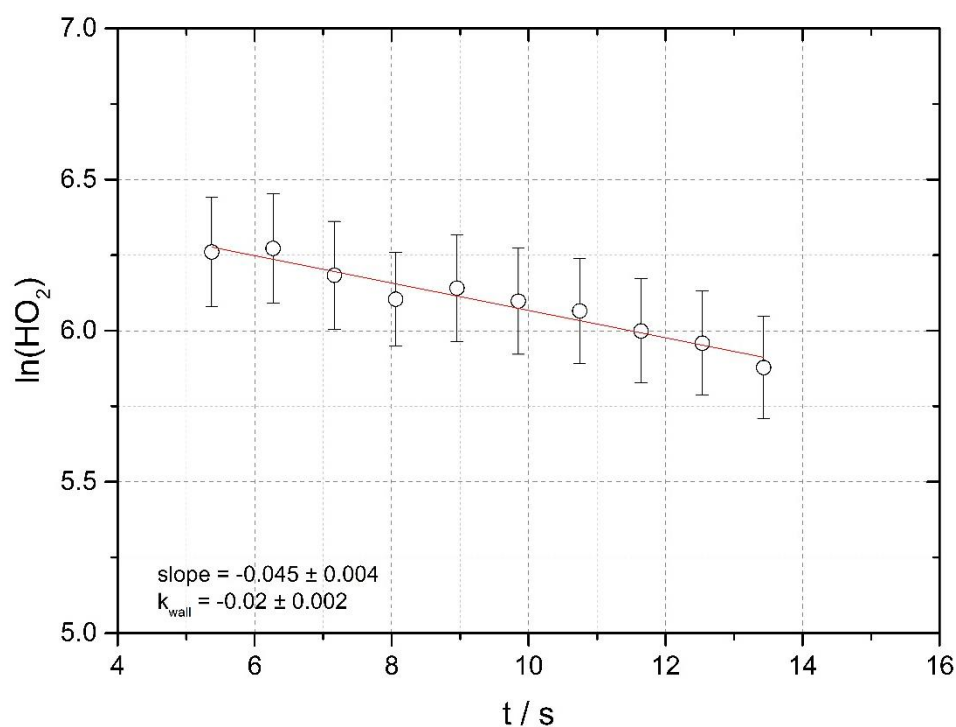


Figure 2.16. Example of $\ln(\text{HO}_2)$ vs t / s for a wall loss experiment i.e. without the presence of aerosols for a relative humidity of 65 %. The error bars represent 1σ . The gradient of the wall loss (k_{wall}) was -0.02 ± 0.001 .

k_{obs} could then be corrected for wall losses by subtracting k_{wall} . This however does not account for non-plug flow conditions (where the flow at the centre of the flow tube is faster than that at the walls due to friction and there is therefore a HO₂ gradient moving from the walls). Using a methodology described in Brown et al., (1978), k_{obs} was corrected for wall loss and diffusion under non-plug flow conditions which gave k' , the pseudo-first-order uptake of HO₂ onto aerosols (Brown, 1978). The corrected

k' values were ~10-40% higher than the $k_{obs}-k_{wall}$ values. An example of the difference in corrections is shown in Figure 2.17.

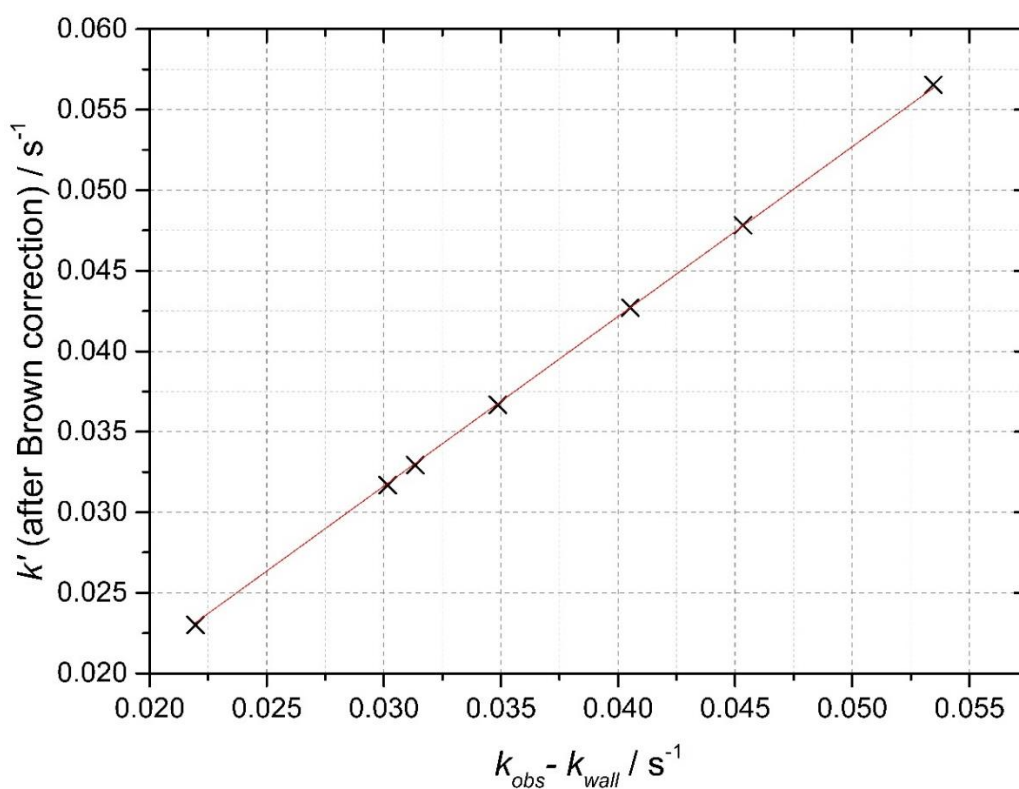


Figure 2.17. An example showing difference between Brown corrected k' values and $k_{obs}-k_{wall}$ values for an experiment with limonene-derived SOA aerosols. The gradient is 1.054, giving an increase of 5.4 % in k' compared to $k_{obs}-k_{wall}$.

The Brown corrected rate coefficient, k' is then related to γ_{obs} by the following equation:

$$k' = \frac{\gamma_{obs}\omega_{HO_2}S}{4} \quad \text{Eq 2.9}$$

Where ω_{HO_2} is the molecular thermal speed of HO_2 (m s^{-1}), and γ_{obs} is the observed uptake of HO_2 obtained from a plot of k' vs S_a , an example of which is shown in Figure 2.18.

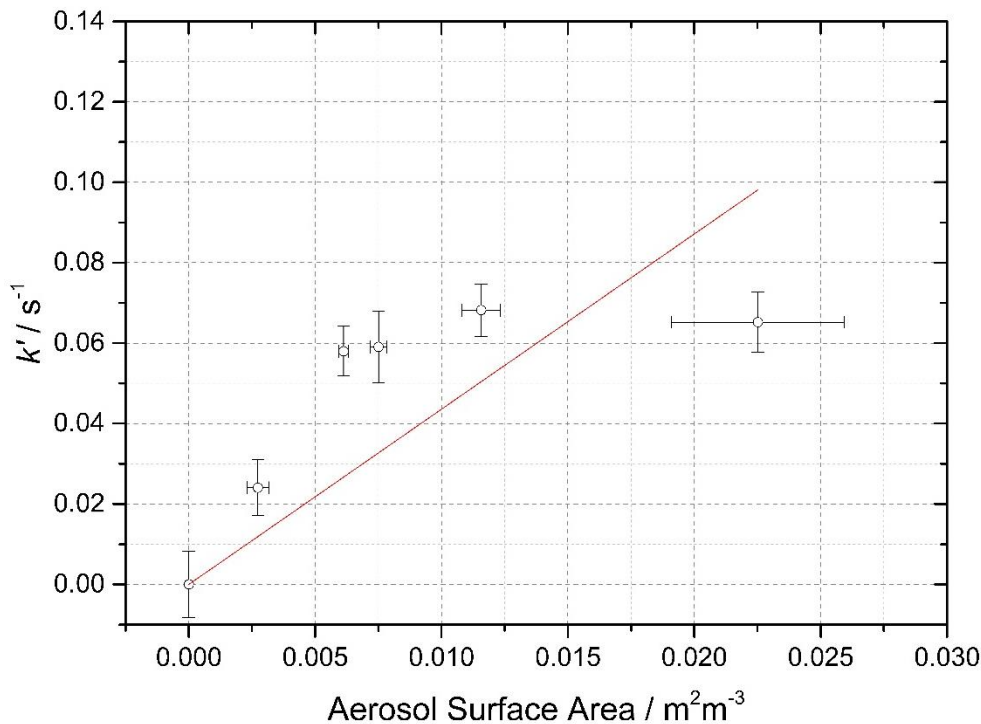


Figure 2.18. First order rate coefficient, k' (s^{-1}), after brown correction, plotted against aerosol surface area ($m^2 m^{-3}$) for ammonium sulphate aerosols. $RH = 65 \pm 2\%$. Uptake coefficient of HO_2 of 0.04 ± 0.01 calculated from the gradient. Error bars represent 1σ .

The uptake coefficients calculated should be corrected for gas phase diffusion. If there is a large uptake of HO_2 or the aerosol radius is large, the concentration of HO_2 could be depleted by the surface leading to an under-prediction of the uptake coefficient. To correct for diffusion limitation the following formulas can be used:

$$\gamma = \frac{\gamma_{obs}}{(1 - \gamma_{obs}\lambda(r))} \quad \text{Eq 2.10}$$

Where $\lambda(r)$ is a function of the Knudson number:

$$\lambda(r) = \frac{0.75 + 0.283K_n}{K_n(1 + K_n)} \quad \text{Eq 2.11}$$

And the Knudson number is defined as:

$$K_n = \frac{3D_g}{\omega_{HO_2}r_s} \quad \text{Eq 2.12}$$

Where r_s is the geometric mean of the radius of the aerosols and D_g is the gas phase diffusion coefficient.

However, diffusion limitations are not significant for the size of the aerosols used in these experiments. For copper-doped aerosol uptake, γ_{obs} would likely be large enough for diffusion limitations to have an effect, as seen in George et al., 2013.

A lower limit estimate (limit of detection) was calculated from Eq 2.9 with a fixed surface area/volume of the flow tube as $0.17 \text{ m}^2 \text{ m}^{-3}$ and k_{wall} . For an average k_{wall} of 0.035 s^{-1} the lower limit uptake coefficient was 0.002.

2.7.3 Error Analysis

The FAGE software recorded a signal every second. For sliding injector experiments, at each injector position the signal was averaged over the measurement period (30-60 secs) and so error in this signal (σ_{signal}) was therefore the standard deviation of these averaged points. Similarly, error in the OH background ($\sigma_{background}$) was be calculated from the standard deviation in the background measurements. After subtracting the background from the signal the error can be found using the following equation propagated using sum in quadrature:

$$\sigma_{signal-background} = \sqrt{\sigma_{signal}^2 + \sigma_{background}^2} \quad \text{Eq 2.13}$$

To calculate the error in k_{obs} the error in the natural log of the background subtracted signal was first calculated:

$$\sigma_{\ln(signal-background)} = \frac{\sigma_{signal-background}}{signal - background} \quad \text{Eq 2.14}$$

The graph of the natural log of the HO₂ signal vs the residence time, t , then yielded a gradient of k_{obs} . The error in the gradient of this graph was taken as $\sigma_{k_{obs}}$. The Brown correction was then applied to both k_{obs} and k_{wall} which were then subtracted from each other to account for wall loss, giving k' and its error. The Brown correction is complex as is done using a python program, written from the original FORTRAN code entitled ROOT. To propagate the error through the correction, a correction factor (A) was calculated by plotting k' vs $k_{obs} - k_{wall}$ and taking the gradient. This gradient was then multiplied by $\sigma_{k_{obs}-k_{av.wall}}$ to give $\sigma_{k'}$ as shown in the following equation:

$$\sigma_{k'} = A. \sigma_{k_{obs}-k_{av.wall}} \quad \text{Eq 2.15}$$

The error in the gradient of the plot of k' versus S_a was taken as the error in $\frac{\gamma_{obs} \cdot \omega_{HO_2}}{4}$. The error in the gradient was therefore multiplied by 4 and divided by ω_{HO_2} to obtain

the error in γ_{obs} . Lastly the error was corrected for gas diffusion limitations by multiplying $\sigma_{\gamma_{obs}}$ by $\frac{\gamma_{corr}}{\gamma_{obs}}$.

2.8 Summary

This chapter summarises the FAGE technique and the apparatus used to measure HO₂ uptake on aerosol surfaces. In order to measure the uptake of HO₂, thereby allowing an uptake coefficient to be calculated, HO₂ was generated and injected into an aerosol flow tube. The injector position was varied to alter the HO₂ exposure time thereby allowing a decay of HO₂ onto aerosol surfaces as well as wall loss decay to be measured using a FAGE cell. Inside the FAGE cell HO₂ was converted into OH using NO to allow sensitive detection by on-resonance fluorescence detection. Changes in aerosol size were measured using a Scanning Mobility Particle Sizer (SMPS). This chapter details the experimental procedure as well as the data analysis and error analysis procedures for the sliding injector experiment. The FAGE detector was calibrated for both OH and HO₂ with sensitivity factors of $(3.2 \pm 0.1) \times 10^{-7}$ counts s⁻¹ mW⁻¹ molecule⁻¹ cm³ being measured for OH and $(1.8 \pm 0.1) \times 10^{-7}$ counts s⁻¹ mW⁻¹ molecule⁻¹ cm³ being measured for HO₂. The detection limits of 6.7×10^5 molecule cm⁻³ and 1.2×10^6 molecule cm⁻³ were calculated for OH and HO₂ were calculated respectively for a 30 s averaging period.

3 Photo-Fragmentation Laser Induced Fluorescence Technique for Measuring HONO Production from Aerosols

This chapter describes the photo-fragmentation laser induced fluorescence (PF-LIF) instrumentation used for the measurement of HONO production from aerosol surfaces.

3.1 Previous Instrumentation for the measurement of HONO

This section provides a short summary of different well-established instrumentation used to measure HONO. HONO instruments developed for field measurements can be separated into three categories: wet chemical methods, mass spectrometry and optical spectroscopy. The most common methods of HONO measurement, besides laser induced fluorescence are Differential Optical Absorption Spectroscopy or using a Long Path Absorption Photometer (detailed description given in Table 3.1).

3.1.1 DOAS

Differential Optical Absorption Spectroscopy measures trace gas concentrations by recording their differential absorption of UV-Vis light over a long path length of a few kilometres. A long path length is necessary to allow gases with very low tropospheric concentrations to be measured (Plane and Nien, 1992).

For Long Path DOAS (LP-DOAS) a laser light source is sent into a multiple reflection cell containing collimator mirrors to focus the light towards the detector. Using a multiple reflection cell allows long path absorption measurements to be taken within a small air volume. Using a long path however causes the beam of light to wander and broaden. The beam is passed through the cell twice by a rotating triple prism forcing the exiting light to travel back through the cell in the exact but opposite direction to its first passage. The exit spot is then much larger than the entrance spot allowing the separation of the beams using a mirror with a small aperture in the centre. The exit beam is then reflected towards the detector. An absorption plot can then be generated by the spectrometer and by comparing with the known output of the lamp it is possible to determine the concentrations of a range of atmospheric species (Hausmann et al., 1997).

DOAS has several advantages. Firstly, the instrument has a wider scan range from 300-700 nm meaning there is potential for real time measurements of many

atmospheric species with one instrument simultaneously. Secondly, DOAS does not suffer from uncertainties brought about by experimental conditions such as wall losses or chemical changes linked to relative humidity. The uncertainties in the concentration of a species come from the accuracy of the cross section of that species, the quality of the absorption spectrum and the errors associated with the spectral deconvolution procedure. In addition, unlike with LIF, DOAS is an absolute method meaning that no calibration is required. Lastly, as atmospheric species are measured over a long path length, localised sources of emissions are averaged out producing a more representative image of tropospheric chemistry in the area (Plane and Nien, 1992): cavity DOAS methods covered in Table 3.1.

3.1.2 LOPAP

A Long Path Absorption Photometer (LOPAP) is an *in-situ* instrument used to measure gaseous HONO using wet chemical sampling and photometric detection. LOPAP was designed to be a cheap, small and sensitive method of continuously monitoring HONO in ambient conditions. LOPAP works by collecting HONO from a sample flow in a liquid phase using a glass stripping coil. The stripping solution used contains sulphanilamide in HCl which forms a diazonium salt with HONO. The air is then separated from the liquid using a debubbler before the solution is pumped into an azo dye unit where it meets the *n*-(1-naphthyl)ethylenediamine-dihydrochloride solution which forms the final azo dye. This final solution is then pumped into a detection unit consisting of a long Teflon tube acting as an adsorption cell. Visible light is then focussed via fibre optics into the tubing. Due to the refractive index of the Teflon being less than that of the liquid solution, the light undergoes multiple reflections on the inner walls of the Teflon tubing, remaining inside the liquid for absorption. The light is then collected by a glass fibre and detected with a mini-spectrometer. A multi-channel LOPAP system is used to remove as much interference as possible. The first stripping coil, or channel 1, removes almost all the HONO from the gas with only a small amount of any interfering species while the second coil, channel 2, removes the same amount of interfering species with little HONO. By subtracting channel 2 from channel 1 it is possible to more accurately measure the true HONO concentration. These channels must be calibrated using a liquid nitrate standard (Heland et al., 2001).

An inter-comparison between LOPAP and DOAS was done in 2001. DOAS is an established technique with low cross interference from other atmospheric species and has been used for an inter-comparison with LOPAP in Heland et al., 2001. Excellent agreement was shown between DOAS and LOPAP for smog chamber experiments. LOPAP however, did measure systematically higher than DOAS though still within error of each other (Heland et al., 2001). During a later campaign using the EUPHORE smog chamber weighted regression analysis of LOPAP against DOAS data gave an agreement of 0.9987 (Kleffmann et al., 2006). A detailed table of the different instrumentation for measuring HONO is shown in Table 3.1.

Technique	Short description	Advantages	Disadvantages	Detection limit	References
DOAS <i>Differential optical absorption spectroscopy</i>	Records differential absorption of UV light over a path length of several kilometres	Well established technique, no calibration required, simultaneously measures multiple species	Poor spatial resolution, poor performance when visibility is low, detection limits are too high for certain species such as NO ₂ to be measured in clean air environments	~ 10 ppt per 3 min (Pinto et al., 2014)	Plane and Nien, 1992,
LOPAP <i>Long path absorption spectroscopy</i>	HONO sampled from gas flow using a stripping coil to then be mixed to form an azo dye. HONO is then detected using an long path adsorption spectrometer	Easy calibration method, simple and easy to use, good agreement with DOAS	Calibration required, overestimation of HONO, interferences present need to be corrected for using 2 channel set up	1 ppt per 5 min	Heland et al., 2001
LIF <i>Laser induced fluorescence</i>	HONO is fragmented into OH and NO. The OH fragment is then excited, and the resulting fluorescence is detected.	Highly sensitive, high time resolution (real time measurement), low background signal	Calibration required, interference from laser generated OH	15 ppt per min	Liao et al., 2007, Bottorff et al., 2021
BBCEAS <i>Broadband cavity enhanced absorption spectroscopy</i>	Measures adsorption along an optical cavity using an UV LED light source	Highly sensitive and interference free. Maintains a high level of spatial resolution. Low power consumption and compact design	Mirror reflectivity requires calibration. May be perturbed by changes in environmental or experimental conditions i.e. vibrations or variations in pressure	90 ppt per 30 secs	Duan et al., 2018
CIMS <i>Chemical ionisation mass spectrometry</i>	Ion flow tube coupled to a quadrupole mass spectrometer. Ion reacts with sample gas to produce anions which are mass filtered and detected. Veres et al., 2015 used iodine (I) as reagent ions.	High sensitivity and time resolution	High background counts from impurities in flow	30 ppt (Veres et al., 2015), 10-20 ppt per 1 s (Pinto et al., 2014)	Veres et al., 2015
Ion chromatography	HONO is collected then converted to form in which it can be detected by ion chromatography. E.g. in SC (stripping coil) IC a coil is used to convert HONO to NO ₂ , whereas in MC (mist chamber) IC a mist of ultra-pure water scavenges soluble gases from the air.	High sensitivity	Long integration time and sample interferences (pernitric acid identified as an interferent)	8 ppt per 15 min (Cheng et al., 2013), < 5 ppt per 5 min (MC-IC, Pinto et al., 2014)	Dibb et al., 2004; Cheng et al., 2013; Pinto et al., 2014

Table 3.1. Summary of different HONO measurement instrumentation.

3.2 Overview of Experimental Set-up

The production of HONO from aerosol surfaces was studied using an aerosol flow tube system, coupled to a PF-LIF cell which allowed the highly sensitive detection of the OH radical formed through photo-fragmentation of HONO into OH and NO followed by Laser-Induced Fluorescence (LIF) detection. A schematic of the experimental set up is shown in Figure 3.1.

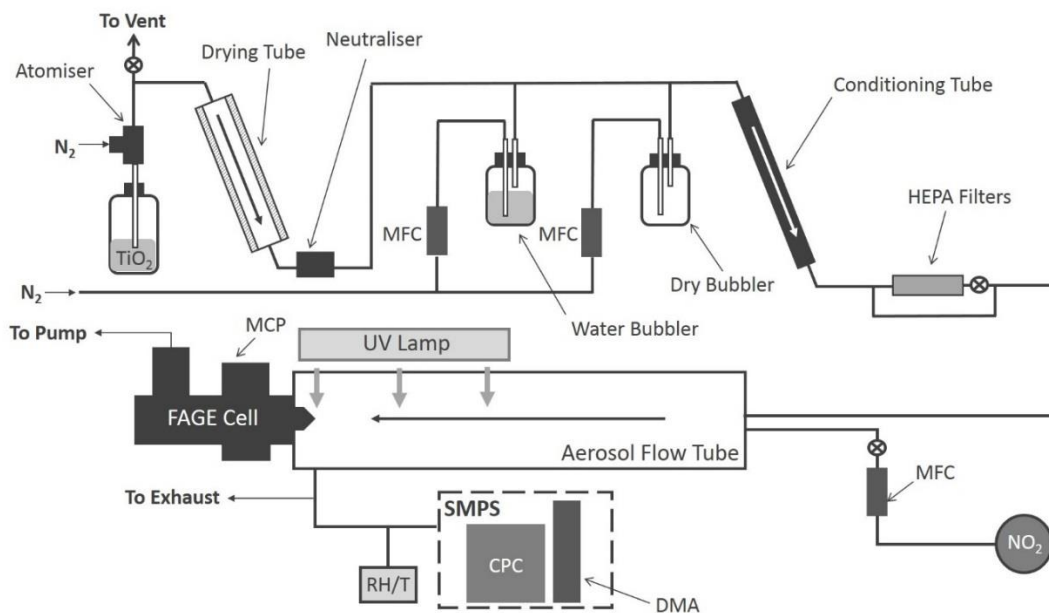


Figure 3.1. Schematic of the Leeds aerosol flow tube system coupled to a photo-fragmentation laser-induced fluorescence detector for HONO. CPC: condensation particle counter; DMA: differential mobility analyser; HEPA: high efficiency particle air filter; FAGE: fluorescence assay by gas expansion; MCP: microchannel plate photomultiplier; MFC: mass flow controller; RH/T: relative humidity/ temperature probe; SMPS: scanning mobility particle sizer.

Almost all aerosol experiments were conducted at room temperature (295 ± 3 K) using nitrogen as a carrier gas. Several experiments were done in air to test the effect of oxygen on the production of HONO. The results for air were well within the error limits of those done in nitrogen (less than 7 %). Aerosols were generated from an aerosol solution using an atomiser. Whenever departmental nitrogen was used as the carrier gas for the experiment, the flow was passed through a gas purification system (TSI 3074 B), described fully in Section 2.1.

A humidified flow of aerosols in nitrogen ~ 6 lpm (leading to a total residence time of ~ 103 s), was introduced through an inlet at the start of the aerosol flow tube (Quartz,

1000 mm in length, 57.5 mm ID). The flow tube was covered by a black box to filter out background room light. A 15 W UV lamp (XX-15LW Bench Lamp, $\lambda_{\text{peak}}=365$ nm, 50 mm length) was placed on the outside of the flow tube to promote the photo-production of HONO from aerosol surfaces (illumination period was half that of the residence time). The PF-LIF cell sampled from the end of the flow tube via a protruding turret containing an offset pinhole (1 mm in diameter), further details in Section 3.4.3, at a rate of 5 lpm. Exhaust ports were fitted at the end of the flow tube to remove excess flow not drawn in by the PF-LIF cell. The detection cell was kept at low pressure, ~ 1.5 Torr, in order to elongate the OH fluorescence lifetime; this was achieved using a rotary pump (Edwards, E1M80) and a roots blower (Edwards, EH1200) in combination. The aerosols leaving the flow-tube via the exhaust ports were characterised using a Scanning Mobility Particle Sizer (SMPS). As with the FAGE detection cell described in Section 2.5.2, all gas flows were controlled using mass flow controllers (MKS and Brooks). The relative humidity (RH) and temperature of the gas flow leaving the flow tube was measured using a RH/T probe (Rotronics HC2-S, accuracy ± 1 % RH) calibrated using a chilled mirror hygrometer (General Eastern Optica).

3.3 Aerosol Generation and Characterisation

3.3.1 Generating Aerosols and Neutralising Charge

Polydisperse aerosols were generated from an aerosol solution using an atomiser (TSI model 3076). A high velocity jet was created by pushing nitrogen or air at high pressure (~ 2 -3 atm) through a small pinhole, 0.034 cm in diameter. This jet was then passed over the aqueous aerosol solution which was drawn up from a feed bottle below the atomiser. Titanium dioxide solutions were made by dissolving 5 g of the titanium dioxide (Aldrich Chemistry 718467, 99.5% Degussa, 80 % anatase:20 % rutile) into 500 ml of milli-Q water. Smaller aerosols were picked up by the gas flow and travelled up to the top of the atomiser while larger aerosols condensed and fell back into the feed bottle. The resulting aerosol flow was passed through a silica drying tube to remove any excess moisture that had potentially accumulated inside the atomiser, forming a dry aerosol flow meaning the relative humidity can be more easily controlled later in the system (Matthews, 2014). A cross section of the mounted atomiser system is shown in Figure 3.2.

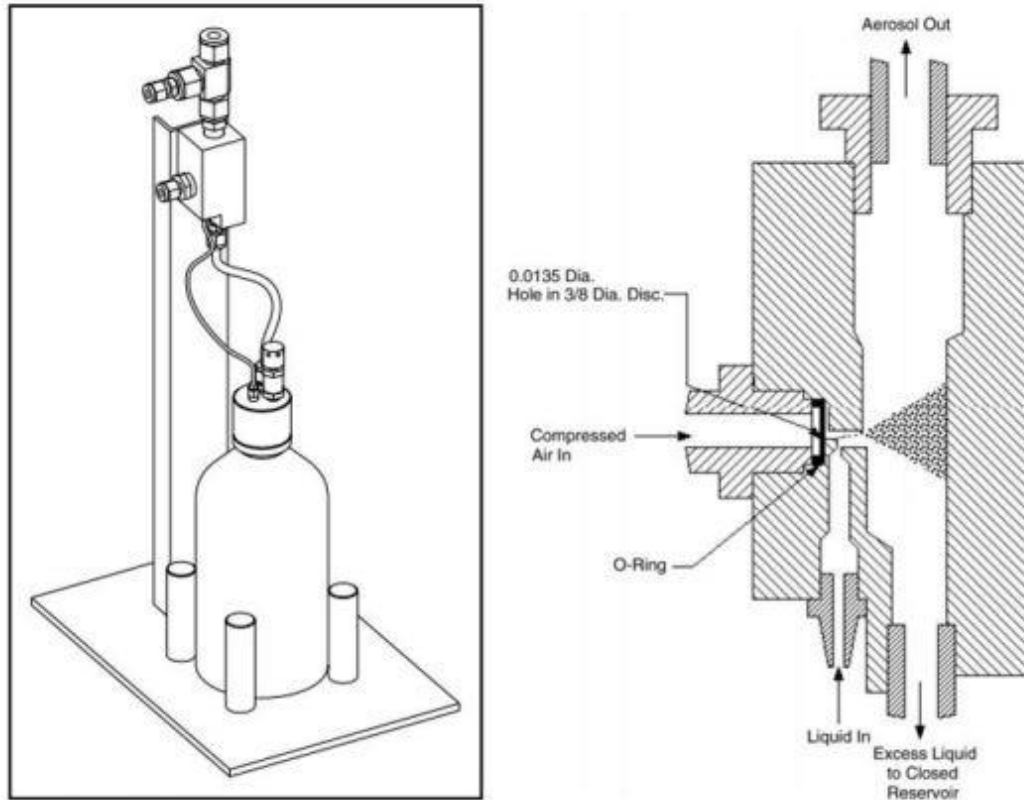


Figure 3.2 Cross section of the mounted TSI 3076 atomiser. Image taken from TSI, 2005.

The aerosols leaving the atomiser were highly charged leading to an increased wall loss as the experiment progresses. The Differential Mobility Analyser (TSI 3080, further described in Section 3.3.4) included within the aerosol measurement system also found it difficult to characterise highly charged aerosols. This is because differential mobility analysis relies on knowledge of the probability distribution of charge states as a function of the particle size. The particle charge state was not known at this point however, so a neutraliser was used to apply a known charge distribution by exposing the aerosol flow to an electrically neutral ion cloud. Within a neutraliser the ion cloud is produced through exposure of the gas to ionizing radiation from a radioactive source. Over a long enough exposure time a steady state charge distribution will be asymptotically approached (Flagan, 2008).

3.3.2 Controlling Relative Humidity (RH)

After the neutraliser, the aerosol flow was then mixed with a humidified gas flow to control the relative humidity (RH) of the system. The RH of the humidified flow was altered by changing the ratio of the dry nitrogen flow and the nitrogen flow passed through a water bubbler using 2 mass flow controllers (MKS 1179). A conditioning tube was then used to allow water adsorption or desorption onto aerosols to equilibrate for the preferred RH. For this aerosol flow tube system, a range of ~10-70% RH can be reliably generated depending on the aerosol composition (however, it was found that the TiO₂ aerosols coagulated and blocked the lines above 35 % RH for example making this the maximum RH for TiO₂ aerosols with the current setup). The RH for the system was then measured using the RH/T probe in the exhaust of the aerosol flow tube.

3.3.3 Controlling Aerosol Concentration

Controlling the percentage of the aerosol flow which passes through a High Efficiency Particulate Air (HEPA) filter allowed for better control of the aerosol concentration. A HEPA filter is composed of a mat of fibre-glass fibres arranged in random orientation which filter out the aerosol through impaction, interception or diffusion of the aerosols onto the fibres. This is depicted in Figure 3.3.

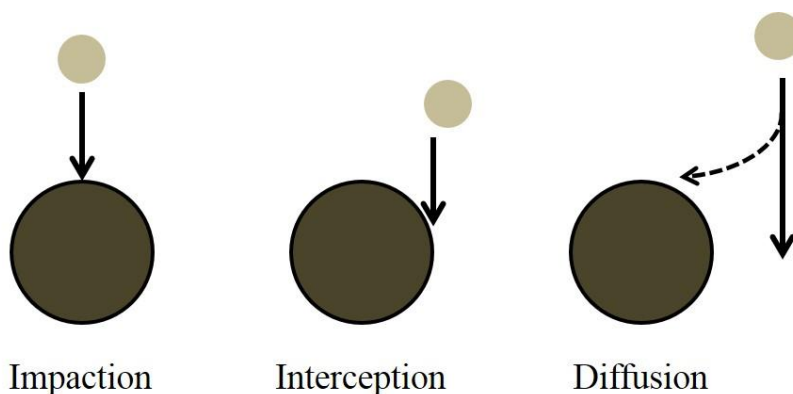


Figure 3.3. Schematic of aerosol removal processes present within a HEPA filter. Black circles represent glass fibres and the beige circles represent aerosol particles.

A portion of the aerosol flow was passed through the HEPA filter fitted with a bypass loop and a bellows valve allowing control of the aerosol number concentration and ensuring the flow rate could be kept constant overall.

3.3.4 Characterisation of Aerosols Using a Scanning Mobility Particle Sizer (SMPS)

A Scanning Mobility Particle Sizer (SMPS) was used to measure the size distribution of the aerosols either before entering, or after leaving the aerosol flow tube (no difference in size distribution was seen between these two setups). The aerosols generated by the atomiser were poly-disperse, empirically observed as a lognormal distribution of aerosol sizes. A vertical cross-section of the SMPS instrument used is shown in Figure 3.4.

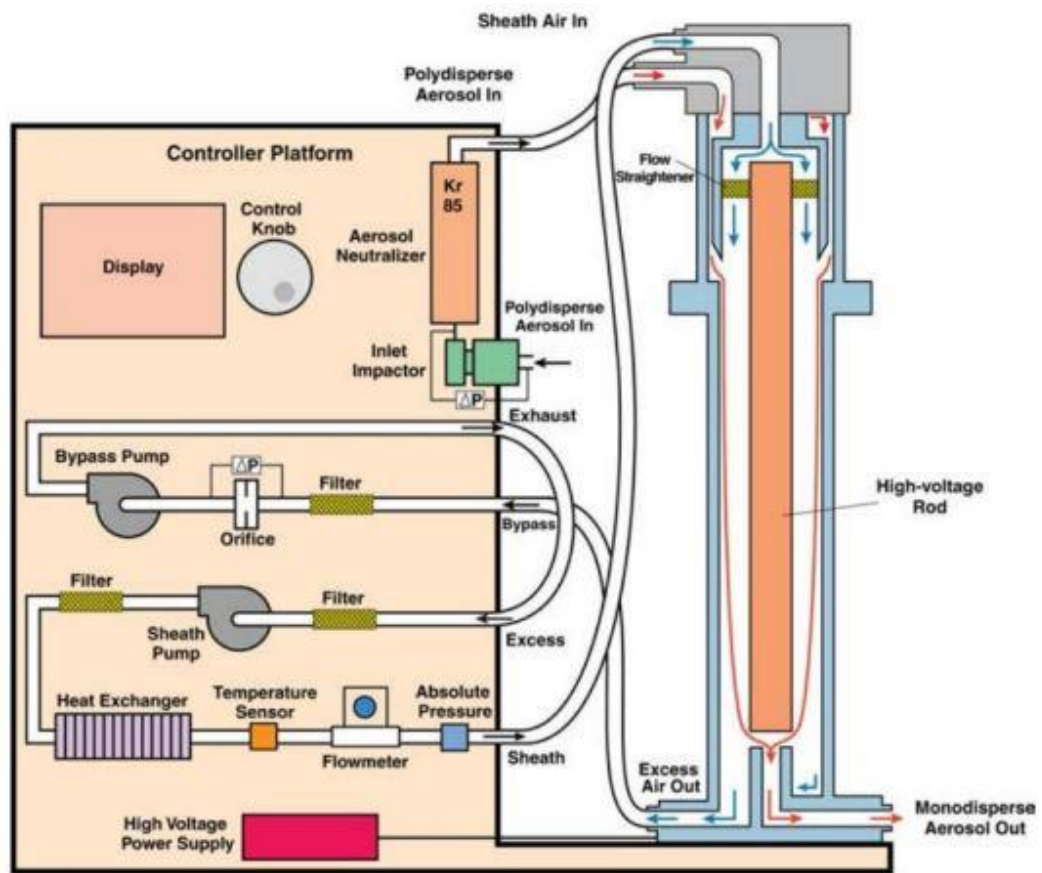


Figure 3.4. Vertical cross-section of SMPS instrument. Image taken from TSI, 2008a

The SMPS instrument contains a neutraliser, in addition to the one described earlier in section 3.3.1, a DMA (TSI 3081) and a Condensation Particle Counter (CPC, TSI 3775). The DMA is made of two metal cylinders; the inner of which has a negative charge and the outer of which is grounded. There is also a central rod meaning that a voltage difference can be applied between the inner cylinder and the central electrode. A DMA classifies particles according to their electrical mobility. The aerosol flow entered at the top of the DMA, as did a sheath flow which was usually set to a tenth

of the aerosol flow rate. The particles then move down the DMA and are drawn towards the central rod at a velocity related to their electrical mobility. The small flow which exits at the base of the DMA contains the particles that have electrical mobility's within a small chosen range. The electrical mobility of the particles is effected by the electrical field, the size and shape of the DMA and the sheath flow rate. The size range of the DMA is determined by the voltage range that can be applied (Flagan, 2008).

Aerosols leaving the DMA and entering the CPC are mono-disperse. Within the CPC, the aerosols were grown using a vapour, typically n-butanol, under conditions which produced supersaturation of the vapour. Standard optical particle counters are not able to measure particles much smaller than 50 nm by light scattering (Kulkarni et al., 2011). To count smaller particles it is necessary to grow the aerosols to a size at which they can be counted optically by the CPC (Flagan, 2008). After growth a CPC can conventionally detect particles down to ~ 1 nm (Kulkarni et al., 2011).

The SMPS used in the aerosol flow tube setup described in this work, could measure aerosols with diameters between 14.6-661.2 nm (for a sheath flow ~3 lpm, 10-20 % error depending on particle counting method) with a full scan taking 2 minutes and 15 seconds. To vary the aerosol sizes measured the sheath flow and the voltage of the SMPS could be changed to vary the electrical field in the DMA thereby varying the mobilities of the particles. Any surface area not measured due to the diameter upper limit was corrected for during analysis by assuming a log normal distribution, which was verified using an aerosol particle counter with a higher diameter range (Matthews et al., 2014b). However above 90 % of the aerosol surface area used in these experiments however were within the diameter range. Aerosols bigger than ~662 nm were removed by an impactor placed inline before the DMA. An impactor removes particles above a certain size by inertial impaction where upon the aerosol flow is accelerated through a nozzle and directed onto a flat plate which will deflect the flow by 90 °. Larger aerosol particles have a greater inertial impact onto the plate whereas the smaller particles will be able to make the sharp turn to avoid collision with the impactor plate. This successfully removes larger particles from the aerosol flow (Matthews, 2014). This is illustrated in Figure 3.5.

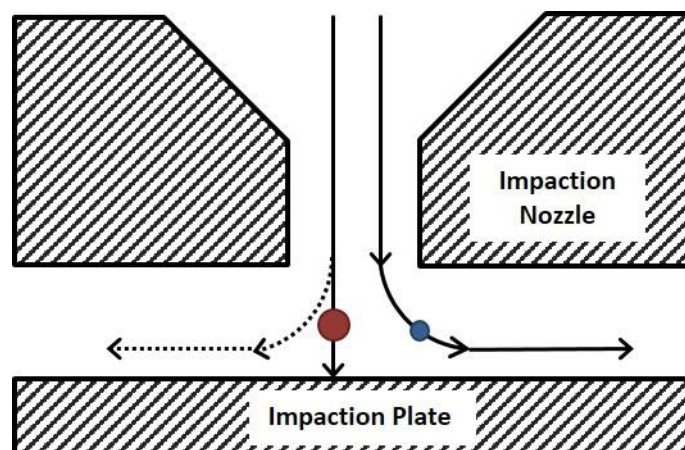


Figure 3.5. Cross-sectional schematic of an inertial impactor. Image recreated from reference TSI, 2008a.

The detection limit of the CPC is 1×10^7 #/cm³ (number of particles per cubic centimetre). However, for particle numbers bigger than 5×10^4 #/cm³ extended single particle counting smoothly transitions into photometric mode counting to allow the CPC to have a higher detection limit. At lower concentrations, the optical detector counts the individual pulses created as each butanol grown particle passes over the detector. At higher concentrations, particles are counted based on total light scattering. This method is less accurate however with single particle counting being accurate to 10% and photometric mode being accurate to 20%. The SMPS can be calibrated using latex beads of known sizes, as discussed below (TSI, 2007).

3.3.5 SMPS Calibration

To check the accuracy of the SMPS, more specifically the DMA, solutions of carboxylate polystyrene latex beads of known diameters (100, 300, 400 and 500 nm) were made up into a solution and atomised allowing the SMPS to measure the size distribution of the beads. The mode diameters given in the size distribution from the SMPS can then be compared to the accurate sizes given by the manufacturer. This allowed a judgement to be made on the accuracy of the DMA. Unfortunately, no easy method to calibrate the particle number, i.e. the y axis, of the SMPS has been determined. An average particle number distribution determined experimentally using the Leeds SMPS showing the size distributions for the different latex bead sizes in shown in Figure 3.6.

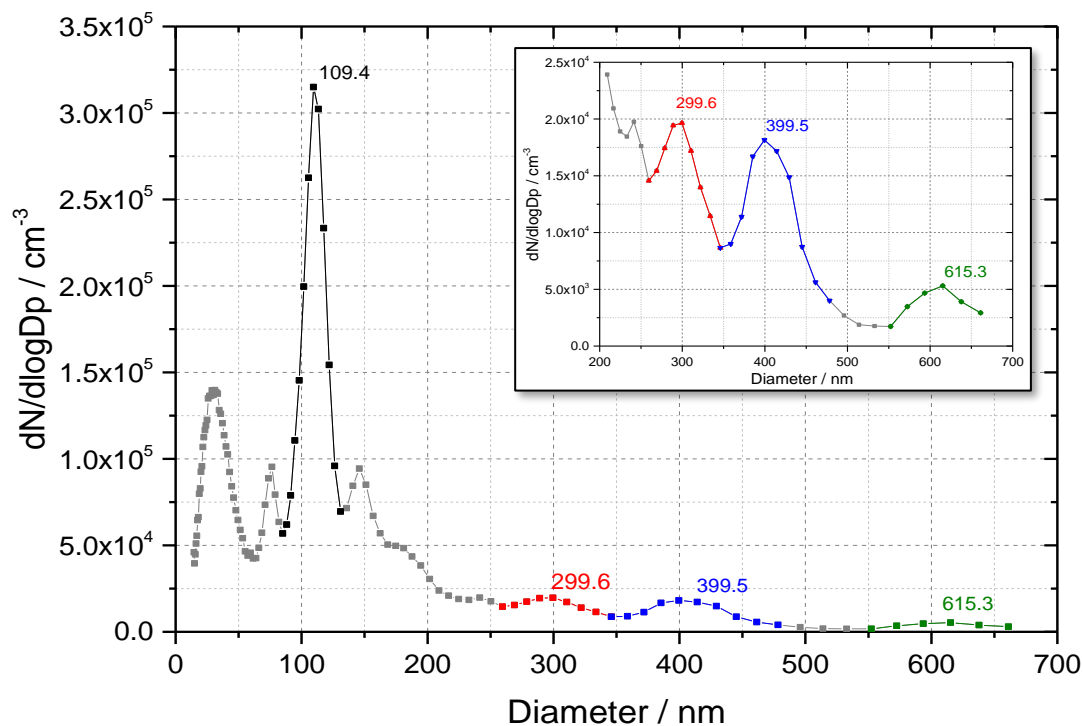


Figure 3.6. Average particle number size distributions for latex calibration beads of known diameters 100 nm (black), 300 nm (red), 400 nm (blue) and 600 nm (green).

3.4 Description of the HONO Instrument

3.4.1 Fragmentation of HONO

As HONO is not directly detectable by LIF, it is necessary to fragment the HONO molecule into OH and NO. The OH fragment can then be detected using LIF at 308 nm. A strong absorption peak is seen in the HONO absorption cross section at ~ 355 nm (Brust et al., 2000), shown in Figure 3.7. The fragmentation process occurs due to the excitation of an electron in a non-bonding orbital on the terminal oxygen to the lowest energy Π^* orbital in the N=O double bond. This electron transfer leads to excitation of the A state (first excited electronic state), lengthening the N=O bond. The vibration along this extended bond causes a recoil along the O-N bond leading to the breaking of this bond to form NO and OH in the ground electronic state (Shan et al., 1989). The different vibrational modes of HONO are detailed in Table 3.2.

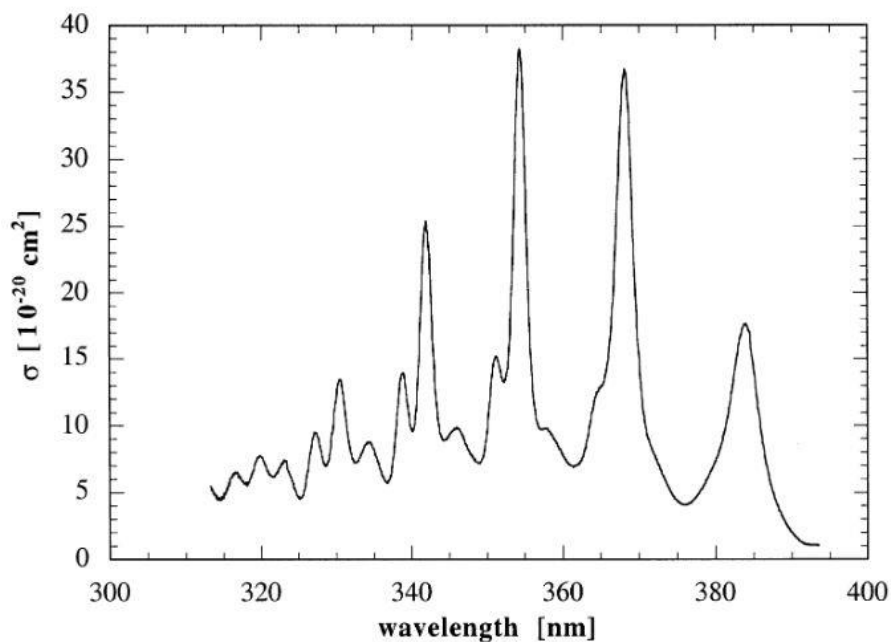


Figure 3.7. UV absorption spectrum of HONO at 0.5 nm optical resolution. Image taken Brust et al., 2000.

Vibration	Description
ν_1	O-H stretch
ν_2	N=O stretch
ν_3	HO-N bend
ν_4	O-N stretch – recoil coordinate
ν_5	O=N-O bend
ν_6	O-H torsion

Table 3.2. Vibrational modes of HONO (Shan et al., 1989).

The HONO produced, either from aerosol surfaces or as a background in the system, was photo-fragmented to produce OH and NO using a 355 nm laser due to the corresponding strong absorption peak (Figure 3.7). Owing to the addition of NO₂ as an experimental reagent, it was easier to detect the OH fragment compared to the NO fragment, the concentration of which was increased within the system by NO₂ photolysis. Cylinder NO₂ also contains trace concentrations of NO. The amount of NO₂ added during an aerosol experiment significantly exceeded (by a factor of 100 or more) the concentration of HONO produced and therefore any NO produced from the

photolysis of NO₂ or due to NO impurities would overshadow the NO fragment created from the photolysis of HONO. Due to the much lower OH interference and the large cross-section for OH at 308 nm, detection of the OH fragment by LIF was therefore much more sensitive leading to a lower detection limit. Though the NO fragment can be measured by LIF at 226 nm, this wavelength is less easy to generate. NO can also be measured using the chemi-luminescence technique through the addition of O₃ (Villena et al., 2012).

The Nd:YAG pulsed photolysis laser (Spectron Laser Systems) used to fragment HONO in the PF-LIF system is shown in Figure 3.8. The laser was operated at a 10 Hz repetition rate, generating 1064 nm light from a flash lamp pumped Nd:YAG crystal. The 1064 nm light was then frequency doubled to 532 nm before the 1064 and 532 nm light were mixed to generate 355 nm light by third-harmonic generation. Using separation optics, the 355 nm light was separated from any remaining 532 and 1064 nm light using dichroic beam splitters before being fed into the detection cell. The power of the 355 nm laser was maintained around 200 mW (energy per pulse=20 mJ).

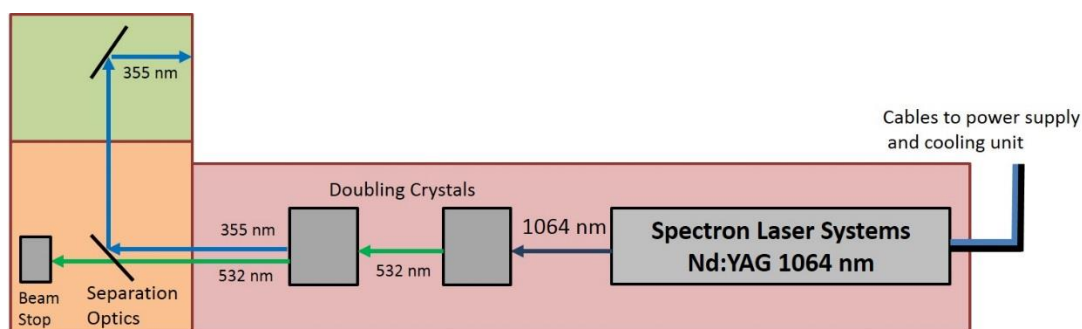


Figure 3.8. Schematic of the Spectron Laser Systems Nd:YAG 1064 nm laser and optics used for the generation and delivery of 355 nm light to the OH detection cell.

3.4.2 Detection of OH

Detection of the OH fragment involves the FAGE technique followed by LIF detection. In short, Fluorescence Assay by Gas Expansion (FAGE) involves expanding of the gas flow through a small pinhole into a detection cell where the OH radical can be measured using on-resonance detection by Laser Induced Fluorescence via the excitation of the $A^2\Sigma^+ (v' = 0) \leftarrow X^2\Pi_i (v'' = 0) Q_1(2)$ transition at ~308 nm Heard, 2006a. The FAGE technique is explained fully in Section 2.5.1.

The 308 nm radiation required was produced by a Nd:YAG pumped dye laser (JDSU Q201-HD, Q-series, Sirah Cobra Stretch) at a pulse repetition rate of 5000 Hz. A

schematic of this laser can be found in Section 2.5.2. A maximum of 95 % of the UV light was delivered by fibre launcher (Oz Optics), an optical fibre cable (Oz Optics) and a fibre collimator (Oz Optics) to the PF-LIF cell via a sidearm fitted with optical baffles to reduce any laser scatter. The fibre was typically set to deliver 2-8 mW of power to the centre of the LIF detection cell. Changing of the power of the green YAG laser allowed control of the beam power entering the fibre launcher. Any more than 30 mW of power into the fibre head would cause burning and long term damage to the fibre.

3.4.3 Detection Cell

Figure 3.9 shows a cross-sectional schematic of the PF-LIF instrument. The detection cell is made from multiple black anodised aluminium cylinders, 50 mm in internal diameter. At the front of the cell, an off-centre pinhole on a turret was used to sample air from the flow tube into the cell. Inside the turret a mirror was placed with the aim of decreasing 355 nm laser scattered light. The mirror prevents the photolysis laser from hitting the bare metal of the turret and scattering randomly. The 355 nm laser hits the mirror instead, generating plasma from which OH is generated. Any OH plasma formed was therefore directly in the path of the gas expansion through the cell and was detected by the MCP detector. To reduce this interference, the pinhole was manufactured off centre to keep the OH plasma formed away from the gas expansion through the cell. The distance between the pinhole and the central axis of the cell, directly below the detector, was as small as possible to reduce wall loss of HONO and OH. The pressure of the cell was kept low, ~ 1.5 Torr using a rotary pump (Edwards, E1M80) and a roots blower (Edwards, EH1200) in combination due to the rotary pump alone only dropping the pressure to ~ 9 Torr. A pressure gauge (Tylan General, CDC 11) was mounted after the detector was used to monitor the pressure of the cell.

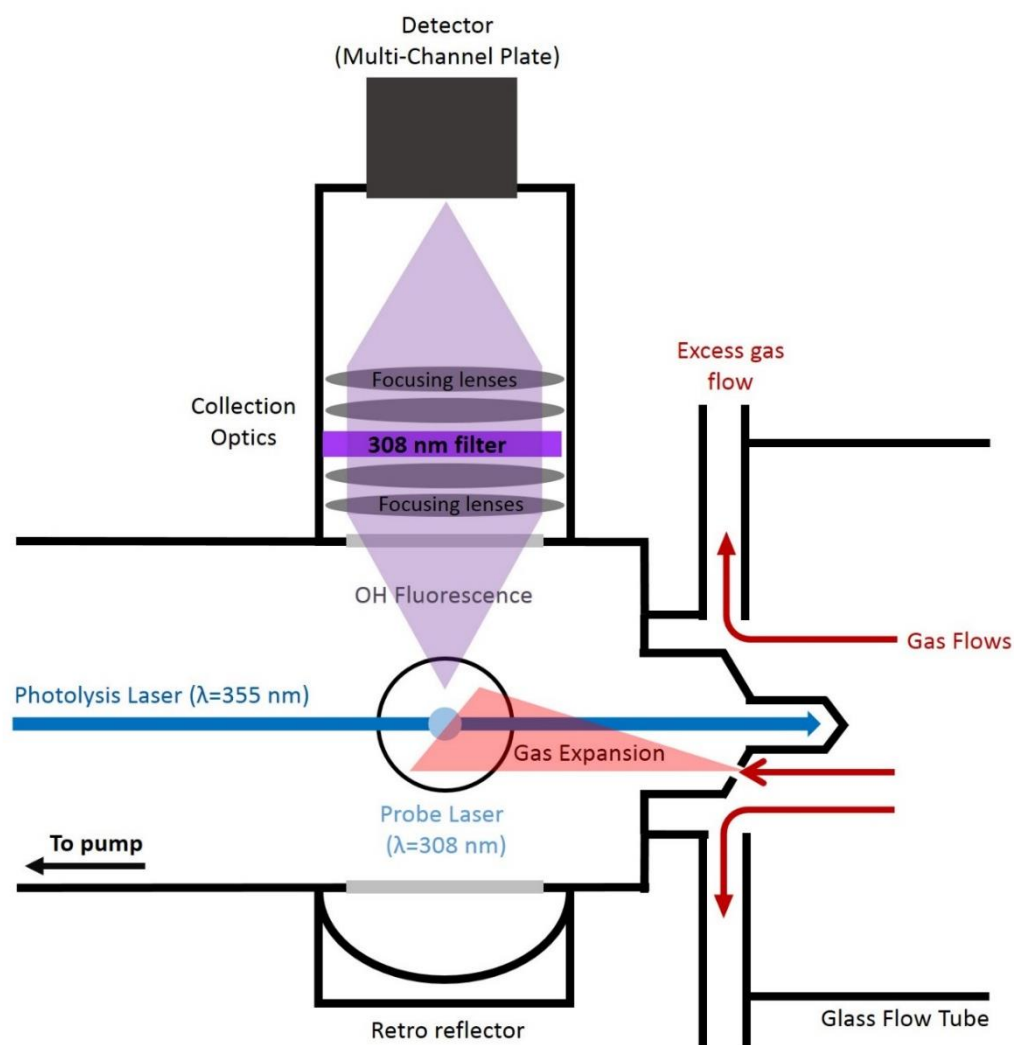


Figure 3.9. Schematic of the detection cell and the aerosol flow tube. The gas expansion through the pinhole into the central axis of the cell is shown. The photolysis laser (blue) and the probe laser (light blue) are fired perpendicular to each other but also perpendicular to the collection optics and detector. Image adapted from Boustead, 2019.

The 308 nm light from the Nd:YAG pulsed dye laser was delivered through a fibre (Oz Optics) connected to the arm of the cell via a collimating unit. The 308 nm light then travelled through the baffled arm into the central axis of the cell and out via the opposite arm and through an anti-reflective 308 nm coated window before being measured by a photodiode (New Focus 2032) at the exit of the arm. The photodiode measured the relative laser power to allow for normalisation of any signal to fluctuations in laser power. Both arms of the cell were baffled to reduce scattered light by blocking any diffuse light that was not travelling directly down the central axis of the arms. Perpendicular to the path of the 308 nm laser through the cell, the 355 nm

photolysis laser beam entered the detection cell through a quartz window at the end of the cell opposite the turret. The light then travelled down the cell in the opposite direction to the gas flow, before striking the 355 nm coated mirror in the turret. This mirror then directed the 355 beam back down the cell, increasing the percentage of HONO photolysed within the cell as well as reducing the laser scatter from reflection off the metal turret, as mentioned above.

A Multi-Channel Plate detector (Photek, MCP 325) was placed on top of the cell to measure the fluorescence perpendicular to the path of both lasers. The top of the cell was separated from the collection optics by a window coated to aid the transmission of 308 nm light. The fluorescence which passed through this window was then focused through optics and passed through a 308 nm interference filter (Barr Associates, 308 nm, FWHM=8 nm, ~ 50 % transmission) to remove light at any other wavelength. This also served to remove any background room light or scatter from the 355 nm laser from entering the detector. A back reflector mirror was installed beneath the cell to catch and reflect any downwards moving fluorescence back up towards the collection optics and the detector, thereby increasing sensitivity by ~40 %. The MCP detector was gated (Photek gating box, GM10-50BL) to avoid it “seeing” the laser pulse and oversaturating, as well as to minimise the collection of laser scatter, shown in detail in Figure 3.10 and explained fully in the next section. As with the HO₂ uptake FAGE instrument, a reference cell is necessary to ensure the 308 nm laser is tuned to the peak of the OH transition: this is described fully in Section 2.5.3.

3.4.4 Data Acquisition

Timing for the HONO instrument was controlled by a delay generator (BNC 555) which acted as the master clock for the entire system. This generator was run with an internal trigger at 5000 Hz. This was used to trigger the 308 nm laser and the gating for the detectors and the photo-counting card. However, the 355 nm laser, both the trigger and the Q-switch, and the initiation of the photon counting card were triggered off a 10 Hz signal so the trigger from the master clock was pulse divided by 500. Using one master clock ensured that timing for both lasers remain consistent with respect to each other and that the trigger of each laser was identical for every run.

Due to the PF-LIF technique for detection of OH being an “on-resonance” technique, meaning that both excitation and detection of OH occur at 308 nm, gating was required

to stop the detector measuring a signal from the laser pulse: photons from the laser pulse are scattered by the walls of the chamber or via Rayleigh scattering and will be collected by the fluorescence collection optics and directed through the 308 nm filter onto the MCP. The number of photons from this scattering process directly after the laser pulse gives a much higher signal than the OH fluorescence signal. For the large gain necessary to see individual photons, a large signal from laser scattered light may cause over saturation of the MCP. The gating unit was therefore used to separate the laser pulse from the fluorescence signal. The MCP was gated off, into a low gain state, during the 308 nm laser pulse to avoid oversaturation and on during the fluorescence decay signal. The width of the low gain state was varied to remove the maximum residual laser scatter before the gating returns to the high gain state and MCP began detecting signal once more. The optimum width can be determined by finding the ratio of lowest scatter to highest fluorescence detected. When the MCP in high gain state detected a photon it generated an electronic pulse which was then passed through a pre-amplifier (Photek, PA200-10P) which provided a factor of 10 amplification to the signal voltage height before the signal reached the photon counting card allowing the signal to be easily distinguished above the background noise.

The data collection for the HONO instrument was complex due to the data acquisition cycle including two lasers running at different pulse repetition rates, one at 5000 Hz and one at 10 Hz, shown fully in Figure 3.10. To begin the cycle, a pulse generator (Quantum composers, 9520 series) sent out a t_0 trigger which started the delay for the 308 nm laser trigger, i.e. switched on the flash lamp and started the q-switch delay, and sent a signal to a delay generator (Berkley Nucleonics Corporation, model 555) which controlled both the triggers for the gating on the 5000 Hz system and the 355 nm laser on the 10 Hz system. The delay generator then triggered the photon counting card (Becker and Hickl, PMS-400a) and the MCP. An initial OH signal was then measured for ~0.01 seconds. This provided a background measurement of the OH present in the system before HONO was photo fragmented. Unlike the data collection for an OH instrument, which used two distinct bins after the probe laser pulse (gates A and B, fully described in Section 2.5.4), the HONO instrument software collected a continuous sequence of 2 μ s wide bins which reduced the interference from any background noise had on the overall signal. The photon counting card was on and counting for the entire cycle with the exception of a short period just before the MCP

was gated off to avoid the counting of a large electrical ringing noise caused by the MCP quickly switching from a high to low gain state. Immediately after the MCP fell to the low gain state the photo counting card then switched on and continued counting for the rest of the cycle. At $t_0 + 0.01$ s the delay generator triggered the lamp and the q-switch for the 355 nm laser. The position of this laser pulse was set so that it fired 800 ns before the 308 nm probe pulse. The MCP gate then triggered off the 5000 Hz system and switched to a low gain state just before the 308 nm laser fired to avoid oversaturation of the detector. It was advantageous to measure the fluorescence signal from OH generated from HONO photolysis as immediately after the 355 nm pulse as possible to ensure the OH signal measured was what was generated close to the probe region and has not been spatially diluted. OH signal was then measured to the end of the cycle. A schematic of the data acquisition cycle is shown in Figure 3.10.

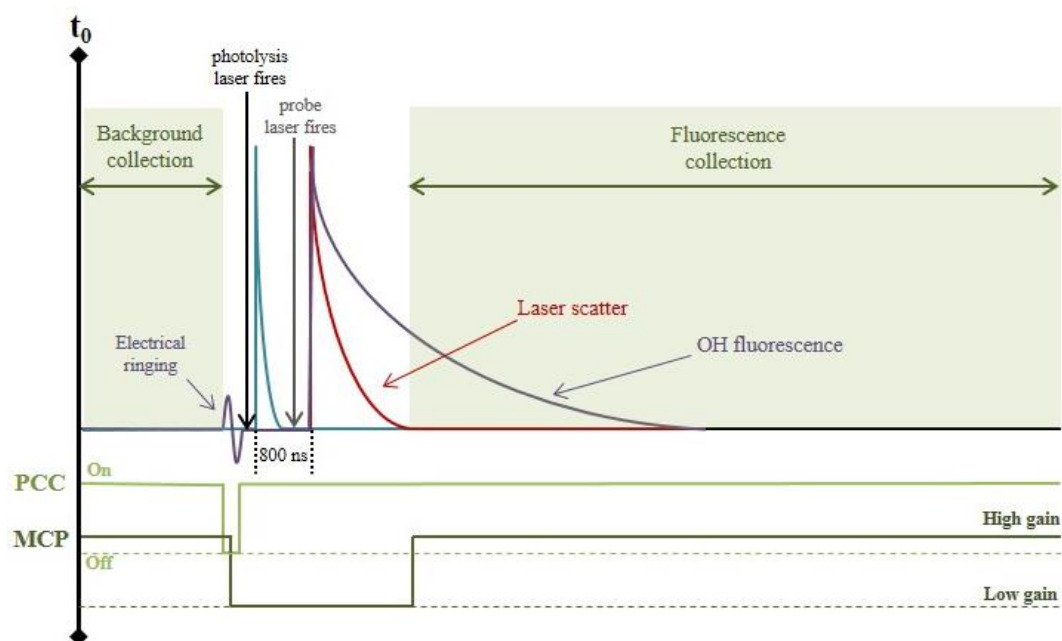


Figure 3.10. Schematic showing the data acquisition cycle for the PF-LIF instrument measuring HONO after fragmentation to OH. PCC: photon counting card, MCP: multi-channel plate. Shaded regions show when MCP and PCC are both on and data is being collected. The photolysis laser pulse is shown in blue and OH signal following the probe laser firing is shown in purple (OH fluorescence signal) and red (laser scatter signal).

The time period between the initial t_0 trigger of the photon counting card and the end of the OH measurement time was known as a sweep. Multiple sweeps were collected per run, often 500, with the signal in each bin being added to the corresponding bin in the previous sweep leading to an increase in the observed signal meaning the measured

OH signal could be distinguished above the background noise. This also increased the measurement time for each run and therefore reduced the time resolution.

3.4.5 Measuring a Background Signal

Online and offline measurements were taken throughout the experiment. Offline measurements allowed the background signal generated from noise, scattered laser light and detector dark counts to be recorded. There were two main types of background measurement it was possible to take with this set-up. An OH background can be seen shaded in orange in Figure 3.11, taken before the photolysis laser triggers at $\sim 160 \mu\text{s}$. The low background signal hereafter referred to as the OH background, was generated from laser scatter from the 308 nm laser and from any OH present in the cell, either from the laser 355 nm laser pulse (i.e. plasma remaining from previous laser fire) or from HONO impurities in the cylinders or in the lines.

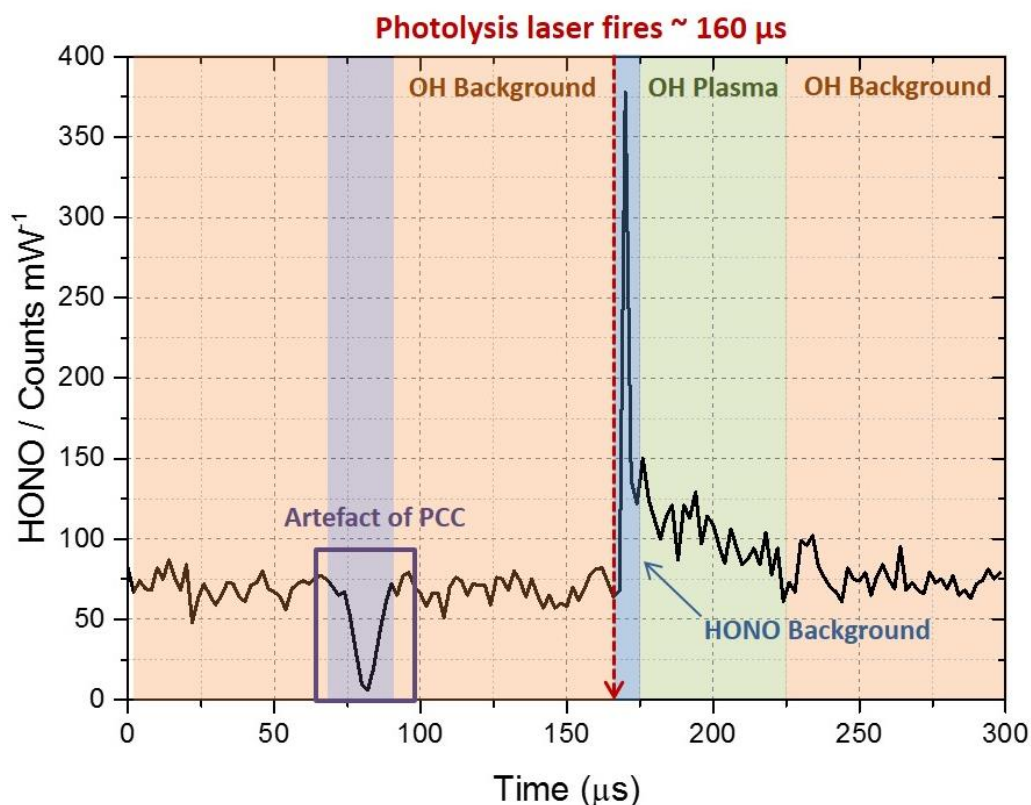


Figure 3.11. Example data acquisition cycle with OH background not subtracted. All counts before photolysis laser trigger (shaded orange) at $\sim 160 \mu\text{s}$ can be treated as a background signal in the cell from either laser scatter from the 308 nm probe laser, residual OH plasma from the previous 355 nm laser fire in the previous run or any HONO impurities present in the cell. The dip in the OH background at $\sim 80 \mu\text{s}$ (shaded purple) is an artefact of the photon counting card (PCC) which was always present and was ignored during analysis. The peak after the photolysis laser fire (shaded blue) was due to OH formed from fragmentation of HONO, either from production on aerosols, impurities in the nitrogen or NO_2 cylinders or from formation on the walls of the cell or in the Teflon tubing. This signal then dropped off rapidly. Immediately following the peak at $\sim 160 \mu\text{s}$ a broad peak due to OH plasma formed in the cell can be seen (shaded green). This peak changed as a function of RH. The signal then returned to the OH background level (shaded orange).

After the photolysis laser fires at $160 \mu\text{s}$, followed 800 ns later by the probe laser firing, a peak can be seen corresponding to the OH formed from the fragmentation of HONO in the cell. This peak will, ideally, be larger with aerosols present in the cell if HONO is being formed on aerosol surfaces. A HONO background was observed before aerosols were added to the aerosol flow-tube. Any background HONO was produced from heterogeneous conversion on the walls of the cell or flow tube or was from impurities in the nitrogen and NO_2 flows. Measurements were also taken without NO_2 present to ascertain the contribution of impurities in the NO_2 cylinder to the overall

HONO production seen. This background HONO concentration depended on the experimental conditions and on how recently the flow tube and PF-LIF cell had been cleaned to remove any build-up of TiO₂ deposits. However, the build-up of TiO₂ on the flow tube walls was relatively slow and back-to-back measurements were made in the presence and absence of aerosols to obtain an accurate background which was then subtracted from the signal. Additional experiments showed no significant production of HONO on TiO₂ aerosol surfaces without the presence of NO₂. A small broad peak was visible after the main HONO peak at ~ 160 μs. This was due to plasma formed on the mirror in the turret which then generates OH. Increasing the relative humidity of the system increased the plasma peak. This was because OH forms easier from plasma with higher concentrations of H₂O vapour present.

The total concentration of HONO measured, once the offline and OH background measurements have been subtracted, by the PF-LIF detector is given by:

$$[\text{HONO}] = [\text{HONO}]_{\text{illuminated aerosols}} + [\text{HONO}]_{\text{illuminated walls}} + [\text{HONO}]_{\text{dark aerosols}} + [\text{HONO}]_{\text{dark walls}} + [\text{HONO}]_{\text{impurities}} \quad \text{Eq 3.1}$$

Taking background measurements allowed us to ascertain the HONO produced from illuminated aerosol surfaces, $[\text{HONO}]_{\text{illuminated aerosols}}$.

3.5 Calibration

3.5.1 OH Calibration

The FAGE technique does not provide an absolute measurement and therefore FAGE instruments must be calibrated in order to directly relate the signal counts to a radical concentration. The FAGE calibration technique is described fully in Section 2.6. Though the HONO instrument was used to measure HONO, it was important to first do an OH calibration to judge the sensitivity of the instrument to OH allowing us to compare to previous OH calibrations. As the HONO produced during experiments was fragmented to produce OH using the 355 nm laser, it was important to know the sensitivity of the instrument to detecting OH.

The OH calibration was performed using a metal calibration wand which generated OH and HO₂ (for calibration done in air) in equal concentrations from the photolysis of H₂O vapour by a 185 nm collimated mercury penray lamp. The mercury lamp was located at the end of the wand opposite to the gas inlet. The UV light generated was

collimated to allow a constant irradiation zone to be calculated. The OH calibration setup, including a cross-sectional schematic of the wand is shown in Figure 3.12.

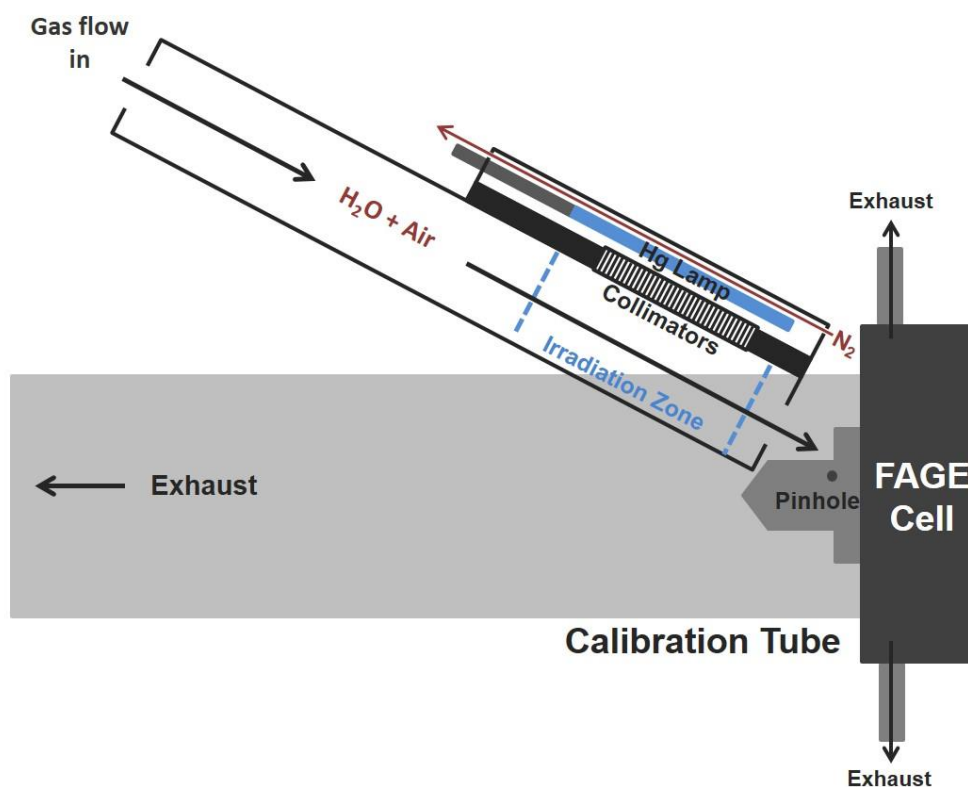


Figure 3.12. Schematic of the OH calibration set-up using the OH calibration wand. Humidified air at 40 lpm is flown down the calibration wand past a collimated light source towards the pinhole of the FAGE cell. Exhaust tube is used to take excess flow to a fumehood.

The flow rate of the gas through the wand was kept high, 40 lpm, so the flow down the tube was turbulent (Reynolds number > 2300). This ensured a constant radial profile down the wand. A laminar flow would result in a parabolic flow leading to the centre of the flow being faster than the outer edges of the flow due to friction by the flow tube walls. A turbulent flow therefore stops a concentration gradient of OH forming and reduces the loss of radicals to the walls.

In order to calculate the absolute concentration of OH radicals produced in the calibration the following equation was used:

$$[OH] = [H_2O]\sigma_{H_2O}\phi_{OH}F.t \quad \text{Eq 3.2}$$

where σ_{H_2O} is the absorption cross section of H₂O at 185 nm ($\sigma_{H_2O,185\text{ nm}} = 7.14 \times 10^{-20} \text{ cm}^2 \text{ molecule}^{-1}$ (Cantrell et al., 1997; Creasey et al., 1997)), ϕ_{OH} is the quantum yield for photodissociation of H₂O which is 1, F is the lamp flux and t is the irradiation time. $F.t$ was determined using chemical actinometry of N₂O which relies on the photolysis of N₂O to produce NO which can then be measured, described fully in Section 2.6. O₃ actinometry can also be used similarly.

The calibration was performed using 40 L min⁻¹ of nitrogen, humidified by diverting the flow through a water bubbler before entering the calibration wand. A smaller flow of 1 L min⁻¹ was diverted to the hygrometer to measure the water content. The tip of the wand containing the lamp was positioned 45° to the centre of the pinhole to the FAGE cell so the nitrogen flow leaving the calibration wand was directed towards the pinhole. To ensure the sampled flow was from the wand and not the gas within the calibration tube surrounding the pinhole, a large excess was flown down the wand compared to the sampling rate of the pinhole. This meant, however, that a large exhaust was necessary to remove the ~ 38 lpm excess flow. This was especially important when performing HONO calibrations as NO was added to the flow to generate HONO from OH. NO is toxic and must be removed by the exhaust into a ventilated fume-hood. For OH calibrations using the PF-LIF set-up however, NO is not injected and therefore any HO₂ formed from H atoms is not measured. Previous work has shown, however, that HO₂:OH formed is 1:1.

The gradient of the plot of observed OH signal (counts s⁻¹ mW⁻¹) versus calculated OH concentration (molecule cm⁻³) gives the sensitivity of the instrument, an example plot shown in Figure 3.13. The sensitivity achieved using an MCP detector was $6.36 \times 10^{-8} \text{ counts s}^{-1} \text{ mW}^{-1} \text{ molecule}^{-1} \text{ cm}^3$.

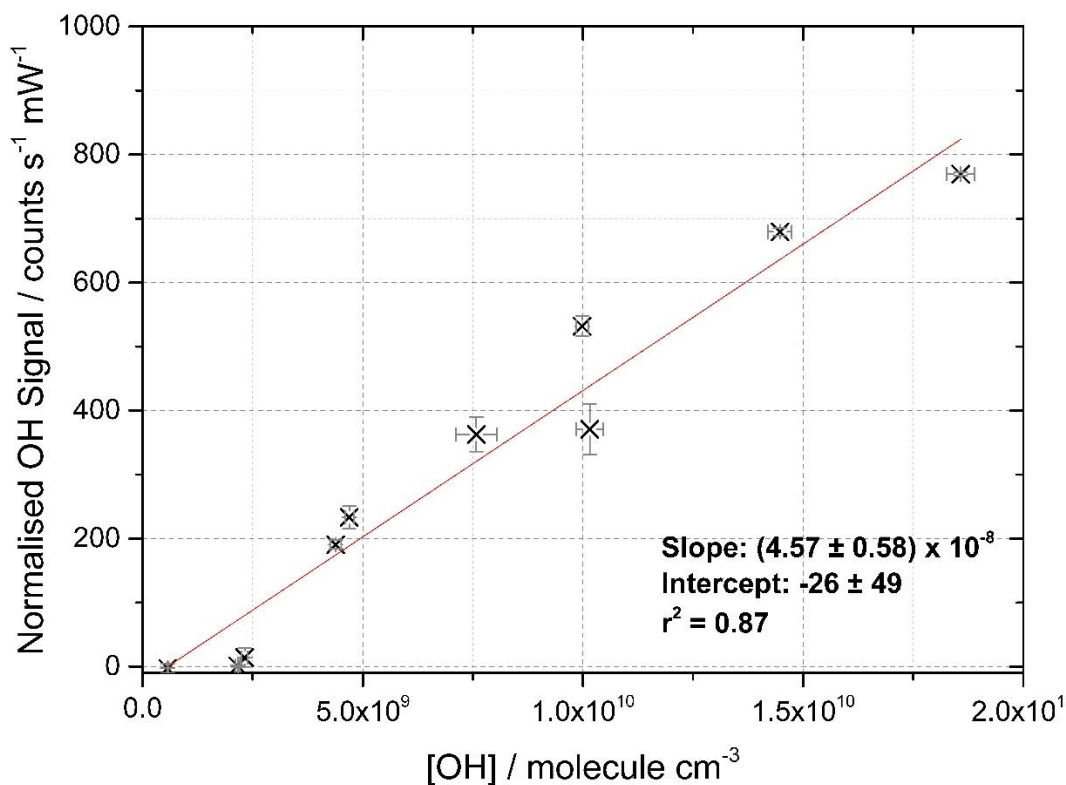


Figure 3.13. Dependence of OH signal (counts s⁻¹ mW⁻¹) normalised to laser power on [OH] (molecule cm⁻³). Error bars represent $\pm 1\sigma$ with the linear least squares fit shown in red. The gradient (i.e. the calibration factor) is in units of counts s⁻¹ mW⁻¹ molecule⁻¹ cm³ and the intercept is in units of counts s⁻¹ mW⁻¹.

3.5.2 HONO Calibration

As the LIF instrument was used to detect OH from HONO, a HONO calibration was also necessary. The setup for the HONO calibration followed the same principle as the OH calibration however a different calibration wand was used. This was due to the need to use a non-collimated mercury lamp to generate more OH. The collimated lamp in the previous metal wand did not produce enough OH to react quickly with NO and produce large concentrations of HONO. A non-collimated light source produces UV light in all directions meaning that considerably more OH can be formed from the photolysis of water vapour than with a collimated light. A sodium hydroxide filter (Ascarite) was placed after the NO cylinder to reduce any background HONO signal from the NO cylinder by removing any acidic gases from the flow. Dilutions of NO were made up to introduce 1 – 5 ppm NO to the main gas flow through the wand to the detection cell.

The calibration wand used for HONO calibrations was made of glass and comprised of an inlet pipe for humidified N₂ and NO, an outlet pipe for these gases plus HONO and OH produced and a mercury penray lamp placed adjacent to the outlet. The wand outlet was connected via a short piece of steel tubing to the pinhole, as shown in Figure 3.14.

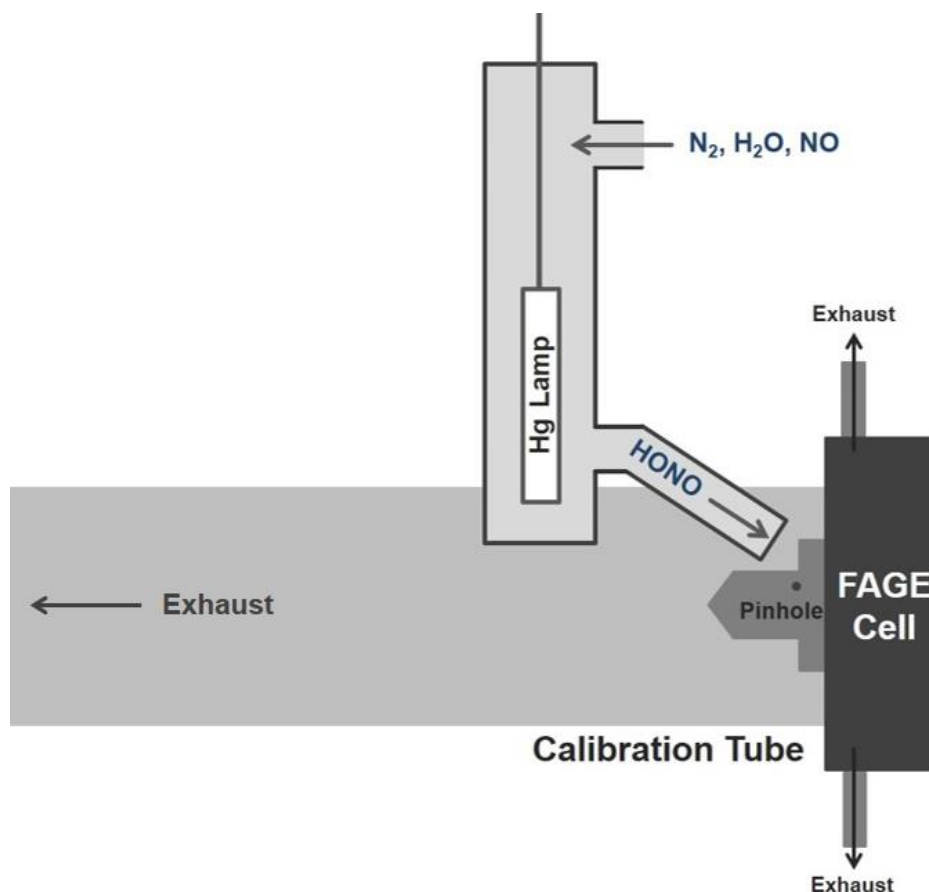


Figure 3.14. HONO calibration set up using a non-collimated light source. Humidified nitrogen flow containing NO, 20 lpm, was flown into a glass wand and past non-collimated mercury lamp to generate HONO in large concentrations which flows over the pinhole. Exhaust tube used to remove toxic NO excess flow.

As with the OH calibration described in Section 3.5.1, the HONO calibrations were performed using a humidified flow of nitrogen. This flow entered the glass wand with a smaller flow of 1 Lmin⁻¹ diverted to the hygrometer. A slower flow of 20 Lmin⁻¹ was chosen so as not to shatter the glass wand due to pressure build up. The Reynolds number was calculated to be laminar at 1460, however, with the multiple flow restrictions from the lamp being in the direct path of the flow and the bends in the wand the flow was forced around it was considered unlikely the flow remained laminar. From the HONO calibration, the concentration of H₂O vapour and the HONO

counts produced for given lamp currents could be recorded and compared to those produced by actinometry. Comparison with actinometry values allows the removal of the $F \cdot t$ variables from the Eq 3.4 making calculating the calibration factor easier.

3.5.3 O₃ actinometry

Either O₃ actinometry, or N₂O actinometry (explained in Section 3.6), can be used to calculate the lamp flux, F , in the calibration wands. O₃ actinometry was performed using the same set up as the HONO calibration to measure the photolysis loss of O₂ to O₃, (Eq. 3.3 and Eq. 3.4), thereby calculating the product of the flux of the calibration lamp, F , and the illumination time, t . This actinometry method has been used by several FAGE groups previously (Hofzumahaus et al., 1996; Creasey et al., 1997). Humidified air was flowed past the mercury lamp where upon equal amounts of OH and HO₂ were produced following the photolysis of water vapour. At the same time ozone was formed by photolysis of O₂, (Eq 3.3). The lamp current was varied to produce different concentrations of O₃, the results of which is shown in Figure 3.15.

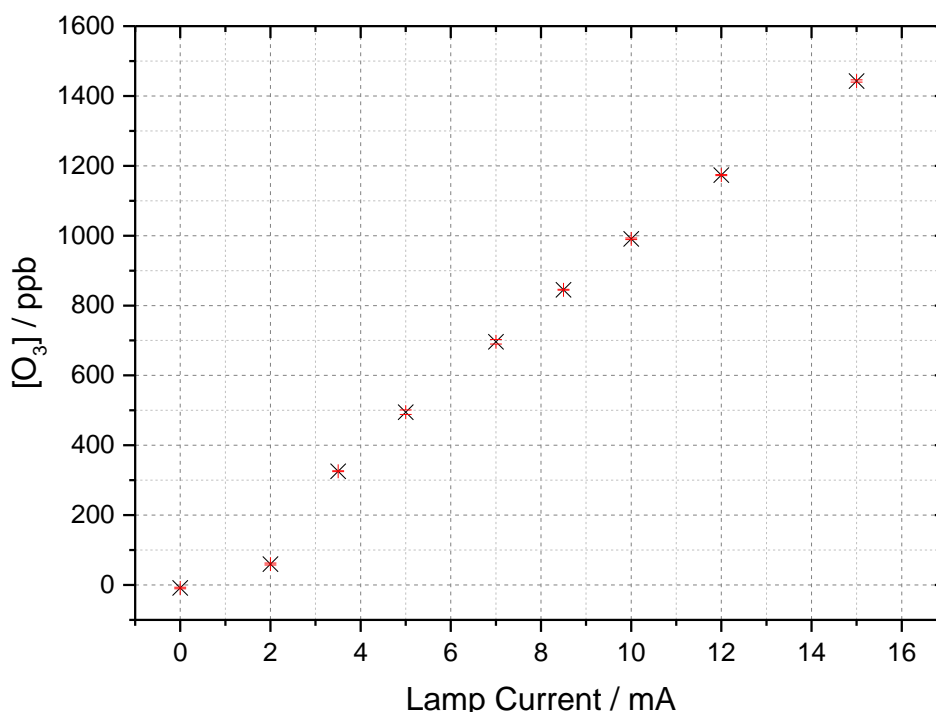


Figure 3.15. Example of O₃ actinometry showing the linear relationship between [O₃] / ppb and lamp current / mA. Error bars show 1 σ . Value at 2 mA is a slight outlier due to flickering of the lamp at low current.

The concentration of O₃ produced was given by:

$$[O_3] = [O_2] \sigma_{O_2(184.9 \text{ nm})} \phi_{O_3(184.9 \text{ nm})} F t \quad \text{Eq 3.3}$$

where $\sigma_{O_2(184.9 \text{ nm})}$ is the O₂ absorption cross section at 184.9 nm and $\phi_{O_3(184.9 \text{ nm})}$ is the yield of O(³P) and hence O₃ from the photo-dissociation of O₂. (i.e. 2, (Sander et al., 2011))

O₃ actinometry was chosen in tandem with the HONO calibration due to the convenience of not needing to know the $F_{185 \text{ nm}} t$ value, as these terms can be very difficult to determine.

$$[OH] = [HO_2] = \frac{[O_3][H_2O]\sigma_{H_2O(184.9 \text{ nm})}\phi_{OH}}{[O_2]\sigma_{O_2(184.9 \text{ nm})}\phi_{O_3(184.9 \text{ nm})}} = \frac{[O_3][H_2O]\sigma_{H_2O(184.9 \text{ nm})}}{2[O_2]\sigma_{O_2(184.9 \text{ nm})}} \quad \text{Eq 3.4}$$

OH and HO₂ have been shown in previous work to form in equal 1:1 ratio from the H₂O of water in the presence of O₂. Using the Kintecus kinetic model and IUPAC rate coefficients, it was shown that with NO in excess in the HONO calibration system all HO₂ will convert to OH and to HONO within the residence time of the calibration wand. All HONO formed can then be photolyzed to give OH which is detected. A factor of 2 is included in Eq 3.4 to take account of half the OH detected being from HO₂.

All the terms in Eq 3.4 can be either calculated or measured if they are not known values. In this way, OH concentration can be calculated and the calibration factors can be determined. A calibration plot showing the relationship between HONO counts and [HO_x] / molecules cm⁻³ is shown in Figure 3.16.

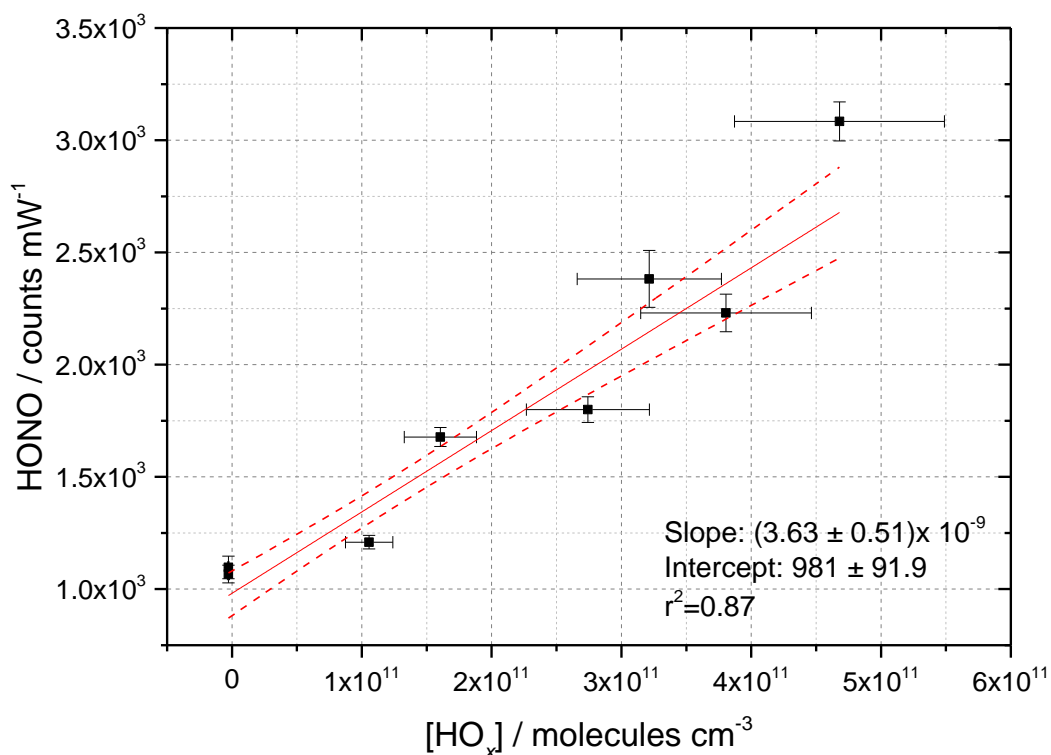


Figure 3.16. Example of HONO calibration using O₃ actinometry showing the relationship between the HONO counts and the [HO_x] / molecules cm⁻³. C_{HONO} for this calibration was $(3.63 \pm 0.51) \times 10^{-9}$ counts mW⁻¹ molecule⁻¹ cm³. Linear least squares fit shown in red with the dashed lines showing the 68 % confidence limits. The intercept is in units of counts mW⁻¹ and the gradient of the slopes are in counts mW⁻¹ molecule⁻¹ cm³. The errors are 1 σ .

During the calibration an assumption was made that [OH]=[HONO]. This was because the reaction of OH with NO is much faster at high concentrations of NO than other loss reactions of OH, verified using a Kintecus model and IUPAC rate coefficients which showed OH had completely reacted to HONO within 2 μ s (Boustead, 2019).

3.5.3.1 Calibration Uncertainty

The total uncertainty in the calibration factor, C_{HONO} , was calculated as a sum in quadrature of the uncertainties connected to each term in Eq 3.4. A summary of these uncertainties is shown in Table 3.3.

Parameter	Typical Value	Uncertainty
[O ₃]	1 × 10 ¹³ molecule cm ⁻³	~ 1% (<i>sd. of values</i>)
[H ₂ O]	1.2 × 10 ¹⁷ molecule cm ⁻³	~ 1-10% (<i>sd. of values</i>)
[O ₂]	1.5 × 10 ¹⁹ molecule cm ⁻³	~ 2% (accuracy of quoted [O ₂] content of BOC air cylinders)
$\sigma_{H_2O(184.9\text{ nm})}$	7.14 × 10 ⁻²⁰ cm ² molecule ⁻¹ (Cantrell et al., 1997)	2.8% (Cantrell et al., 1997)
$\sigma_{O_2(184.9\text{ nm})}$	8.8 × 10 ⁻²¹ cm ² molecule ⁻¹ (Washida et al., 1971)	~ 16% (Smith, 2007)
Final Uncertainty		~ 20 %

Table 3.3. Uncertainty in calibration parameters.

The uncertainties in the [O₃] and [H₂O] were taken as the standard deviation of the measured values, usually ~ 1%. The [O₂] error was reliant mostly on the accuracy with which the oxygen content of air cylinders was quoted and so was taken as ~ 2%. The value for $\sigma_{H_2O(184.9\text{ nm})}$ was taken from Cantrell et al., 1997 which quoted the error as 2.8%. The value of $\sigma_{O_2(184.9\text{ nm})}$ taken from Washida et al., 1971 had no associated error in this study. A large uncertainty with this came from the flow rates controlled by MFCs. In the thesis of S. C. Shona, a fractional uncertainty of ~ 16% was given for the adsorption cross section of oxygen (Smith, 2007) due to this being dependent on experimental conditions such as lamp temperature and lamp supply current.

The uncertainties in each term are propagated to give an error in the OH concentration obtained through calibration with O₃ actinometry, as shown in Eq 3.5:

$$\sigma_{OH} = [OH] \sqrt{\left(\frac{\sigma_{[O_3]}}{[O_3]}\right)^2 + \left(\frac{\sigma_{[H_2O]}}{[H_2O]}\right)^2 + \left(\frac{\sigma_{\sigma_{H_2O}}}{\sigma_{H_2O}}\right)^2 + \left(\frac{\sigma_{[O_2]}}{[O_2]}\right)^2 + \left(\frac{\sigma_{\sigma_{O_2}}}{\sigma_{O_2}}\right)^2} \quad \text{Eq 3.5}$$

3.6 Using NO₂ Actinometry to Measure the Photolysis Rate of NO₂

The photolysis rate of NO₂, j_{NO_2} , was measured by actinometry of NO₂ for the aerosol flow tube setup with one, two and four lamps outside the flow tube turned on. The flow conditions were kept the same as during an aerosol experiment, i.e.

approximately 6 lpm of N₂ at approximately 15 % RH. The concentration of NO₂ in the mixture of NO₂ in N₂ administered to the flow tube was increased slowly throughout the actinometry and the loss to NO was measured under illumination. NO₂ actinometry is based on the following reaction occurring under illumination:



Using basic first order kinetics, it can be said that the loss of NO₂ within the illuminated region is given by:

$$-\frac{d[NO_2]}{dt} = j_{NO_2}[NO_2] \quad Eq\ 3.6$$

where $j(NO_2)$ is the photolysis frequency of NO₂ for the lamp used in these experiments. From the measured loss of NO₂ in the illuminated region, and with knowledge of the residence time, t , the photolysis frequency, $j(NO_2)$ could be determined. Integrating Eq 3.6 gives a value for jNO_2 based on the concentration of NO₂ and NO and the residence time in the flow tube:

$$\frac{d[NO_2]}{[NO_2]} = -j_{NO_2} dt \quad Eq\ 3.7$$

$$\frac{1}{[NO_2]} d[NO_2] = -j_{NO_2} dt \quad Eq\ 3.8$$

$$\int_0^t \frac{1}{[NO_2]} d[NO_2] = -j_{NO_2} \int dt \quad Eq\ 3.9$$

$$\left(\int_a^b \frac{1}{x} = \ln x_b - \ln x_a = \ln \frac{x_b}{x_a} \right) \quad Eq\ 3.10$$

$$\ln[NO_2]_t - \ln[NO_2]_0 = -j_{NO_2} \times t \quad Eq\ 3.11$$

$$j_{NO_2} = -\frac{\ln\left(\frac{[NO_2]_t}{[NO_2]_0}\right)}{t} \quad Eq\ 3.12$$

where $[NO_2]_t$ is the mixing ratio in ppb with the lamp on, i.e. including NO₂ photolysis, and $[NO_2]_0$ is the mixing ratio in ppb with the lamp off, t is the residence time within the flow reactor.

A small correction was made for any NO₂ coming off the walls of the flow tube and therefore artificially increasing the NO₂ value under illumination. The profiles of NO and NO₂ throughout the actinometry are shown in Figure 3.17.

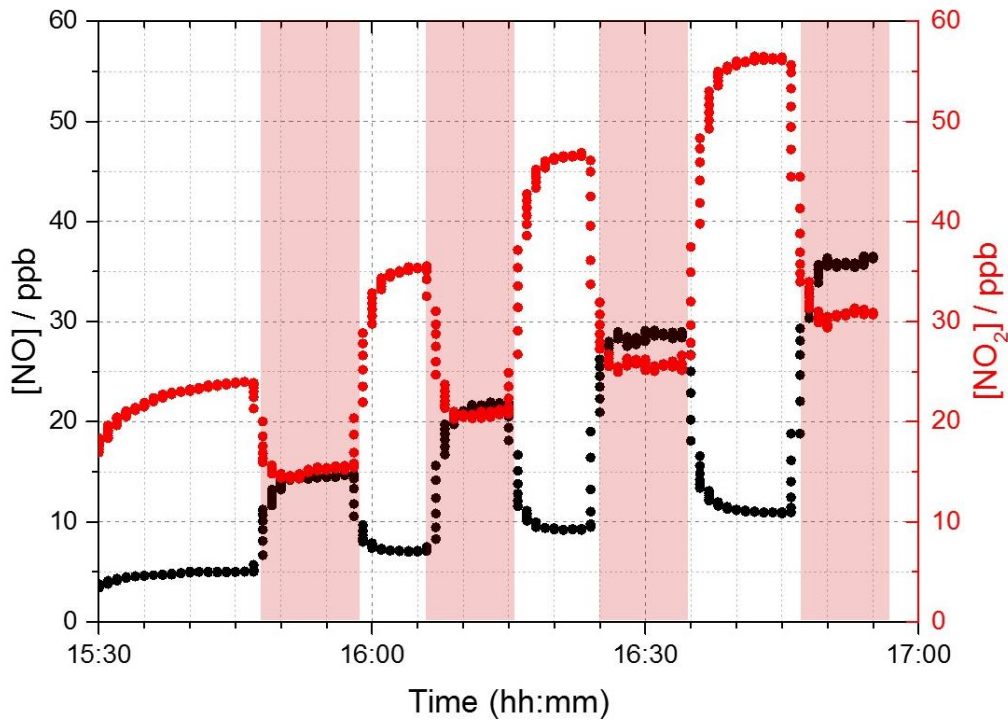


Figure 3.17. NO_x profile with time during NO_2 actinometry. The illuminated periods are shaded in pink, with NO_2 (red) decreasing during these periods due to photolysis and NO (black) increasing. As the experiment progressed increasing known concentrations of NO_2 were added in a stepwise manner.

An increase in the number of UV lamps (Analytica Jena XX-151W Bench Lamps, $\lambda = 300\text{--}400\text{ nm}$) led to an increase in $j\text{NO}_2$. The increase in $j\text{NO}_2$ was slightly higher than directly proportional due to the mirror coating on the inside of the lamp casings reflecting light back into the flow tube slightly increasing the effective light intensity. For one lamp, the photolysis frequency, $j\text{NO}_2$, was determined to be $(6.43 \pm 0.30) \times 10^{-3}\text{ s}^{-1}$. $j\text{NO}_2$ is given by:

$$j(\text{NO}_2) = \int_{\lambda_1}^{\lambda_2} \sigma_{\lambda} \phi_{\lambda} F_{\lambda} \quad \text{Eq 3.13}$$

where λ_1 and λ_2 represent the range of wavelengths over which the lamp emits, and σ_{λ} is the wavelength-dependent absorption-cross section, ϕ_{λ} is the photo-dissociation quantum yield of NO_2 and F_{λ} is the flux of the lamp at a given wavelength.

From the measured $j\text{NO}_2$, and with knowledge of σ_{λ} for NO_2 , the flux of the lamps could be determined; for one lamp the flux was determined to be $(1.65 \pm 0.02) \times 10^{16}\text{ photons cm}^{-2}\text{ s}^{-1}$ integrated over the 290 – 400 nm wavelength

range of the lamp. Using the flux calculated and the known σ_λ and ϕ_λ for HONO over the same wavelength range, $j(\text{HONO})$ was determined to be $(1.66 \pm 0.04) \times 10^{-3} \text{ s}^{-1}$ for one lamp. The measured $j(\text{NO}_2)$ and the calculated flux and $j(\text{HONO})$ values for the different number of lamps is shown in Table 3.4.

Number of Lamps	$j(\text{NO}_2)$ value / s^{-1}	$j(\text{HONO})$ / s^{-1}	Flux / photons $\text{cm}^{-2} \text{ s}^{-1}$
1	$(6.43 \pm 0.30) \times 10^{-3}$	$(1.66 \pm 0.10) \times 10^{-3}$	$(1.63 \pm 0.09) \times 10^{16}$
2	$(1.41 \pm 0.21) \times 10^{-2}$	$(3.65 \pm 0.59) \times 10^{-3}$	$(3.58 \pm 0.56) \times 10^{16}$
4	$(3.23 \pm 0.92) \times 10^{-2}$	$(8.35 \pm 2.49) \times 10^{-3}$	$(8.29 \pm 2.39) \times 10^{16}$

Table 3.4. $j(\text{NO}_2)$, $j(\text{HONO})$ and flux values calculated through NO_2 actinometry with 1, 2 and 4 bench lamps used.

The lamp flux increased as a function of lamps increasing to $(8.29 \pm 2.39) \times 10^{16} \text{ photons cm}^{-2} \text{ s}^{-1}$ for 4 lamps. The flux of the lamp, the spectral intensity of which was measured using a Spectral Radiometer (Ocean Optics QE65000) as a function of wavelength is shown in Figure 3.18.

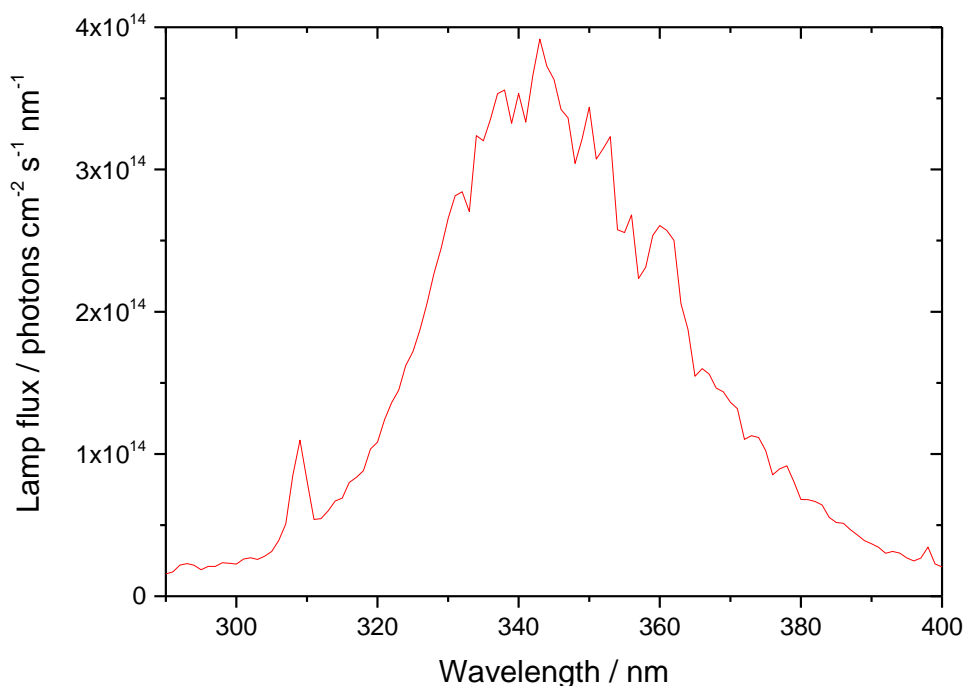


Figure 3.18 UVA emission spectrum for the 15 W bench lamp used in these experiments between 290-400 nm. The integrated photon flux over this wavelength range is $(1.65 \pm 0.02) \times 10^{16} \text{ photons cm}^{-2} \text{ s}^{-1}$ determined from the measured $j(\text{NO}_2)$ of $(6.43 \pm 0.30) \times 10^{-3} \text{ s}^{-1}$.

3.7 Calculating a Limit of Detection

The limit of detection is defined as the lowest concentration that can be reliably distinguished above the background noise for a given averaging period. For a 50 second averaging period and a SNR of 1, the limit of detection was calculated to be 9 ppt.

$$[HONO]_{min} = \left(\frac{SNR}{C_{HONO} \times LP} \right) \times \left(\sqrt{\frac{S_{OH, Background}}{t} \left(\frac{1}{m} + \frac{1}{n} \right)} \right) \quad \text{Eq 3.14}$$

where C_{HONO} is the calibration factor (3.63×10^{-9} counts mW^{-1} molecule $^{-1}$ cm^3), SNR is the signal to noise ratio, $S_{OH, Background}$ is the OH background signal (60 counts), t is the averaging time for each data point (0.1 s), LP is the laser power (2 mW), m is the number of offline points (500) and n is the number of online points (500).

3.8 Summary

In this chapter, the experimental setup for the PF-LIF aerosol flow tube system was described. This setup was used for measuring the production of HONO from illuminated aerosol surfaces. An atomiser was used to aerosolise solutions containing photo-reactive compounds or inorganic salts, the RH of which was controlled using a humidified gas flow. The flow tube was illuminated using up to 4, 15 W UV bench lamps half the length of the flow tube with a typical illumination time of 52 seconds for a residence time of 103 seconds. The aerosols were characterised using an SMPS. The HONO formed during the experiments was detected by laser induced fluorescence at 308 nm following fragmentation of HONO to produce OH at 355 nm.

The photolysis rate of NO_2 was determined using NO_2 chemical actinometry to obtain $j(\text{NO}_2)$ and calculating the photon flux from this using our knowledge of the relationship between $j(\text{NO}_2)$, σ_λ for NO_2 and the spectral intensity of the lamp over the wavelength range of 290 -400 nm. $j(\text{HONO})$ was then calculated using the flux and the known σ_λ for HONO in the same wavelength range. $j(\text{NO}_2)$, $j(\text{HONO})$ and lamp flux were determined for 1 – 4 UV lamps ranging from $(6.43 \pm 0.30) \times 10^{-3}$ to $(3.23 \pm 0.92) \times 10^{-2} \text{ s}^{-1}$ for $j(\text{NO}_2)$, $(1.66 \pm 0.04) \times 10^{-3}$ to $(8.35 \pm 0.18) \times 10^{-3} \text{ s}^{-1}$ for $j(\text{HONO})$ and $(1.65 \pm 0.02) \times 10^{16}$ to $(8.29 \pm 0.09) \times 10^{16}$ photons $\text{cm}^{-2} \text{ s}^{-1}$ for lamp flux.

The HONO instrument has been successfully calibrated for both OH and HONO with calibration factors, C_{OH} and C_{HONO} determined in N_2 to be $(6.34 \pm 0.96) \times 10^8$ counts cm^{-3} molecule $^{-1}$ s $^{-1}$ mW $^{-1}$ and $(3.63 \pm 0.51) \times 10^{-9}$ counts mW $^{-1}$ respectively, leading to a calculated limit of detection of 9 ppt for a 50 s averaging period and a signal-to-noise (SNR) of 1. The HONO instrument was used to study the production of HONO from TiO_2 and ammonium nitrate aerosols as a function of RH and NO_2 concentration. Further details of this are contained in subsequent chapters.

4 HONO Production from Illuminated TiO₂ and mixed TiO₂/Ammonium Nitrate Aerosol Surfaces

4.1 Results of TiO₂ Aerosol experiments

4.1.1 Production of HONO from TiO₂ Aerosol Surfaces

The production of HONO on TiO₂ aerosol surfaces was measured as a function of initial NO₂ concentration. It was shown that for all initial NO₂ concentrations, HONO production increased as a function of aerosol surface area. An example experiment, at 200 ppb NO₂, is shown in Figure 4.1.

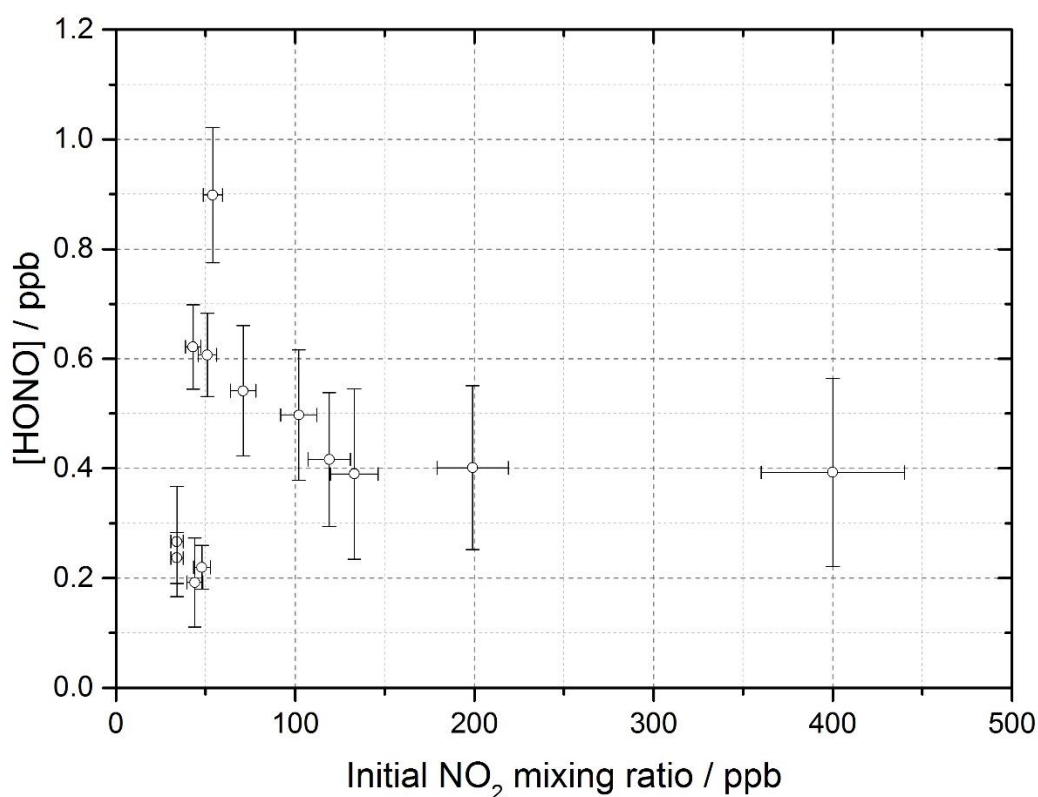


Figure 4.1. Dependence of HONO production on TiO₂ aerosol surface area. [NO₂] = 200 ppb, RH = 15 ± 1 %, illumination time = 52 s, photon flux = $(1.63 \pm 0.09) \times 10^{16}$ photons cm⁻² s⁻¹, in N₂ at 295 ± 3 K. Errors ± 1σ showing variation in HONO signal. The non-zero intercept was due to HONO produced from the walls of the system without the presence of an aerosol surface

In order to investigate the trend in HONO production with increasing initial NO₂ concentration, a fixed aerosol concentration of 0.016 ± 0.0008 m²m⁻³ was chosen and all HONO produced at this aerosol surface for each NO₂ concentration was averaged; the results of which are shown in Figure 4.2. A rapid increase in HONO production was seen at low NO₂ concentration followed by a slower decrease after a peak at

~ 54 ppb NO₂. No plateau in HONO production was seen as a function of NO₂ concentration (Stemmler et al., 2007; Dupart et al., 2014). The highest concentration of HONO measured during all experiments was 4×10^{10} molecules cm⁻³ (~1.6 ppb) seen at 54 ppb NO₂ for an aerosol surface of ~ 0.022 m²m⁻³.

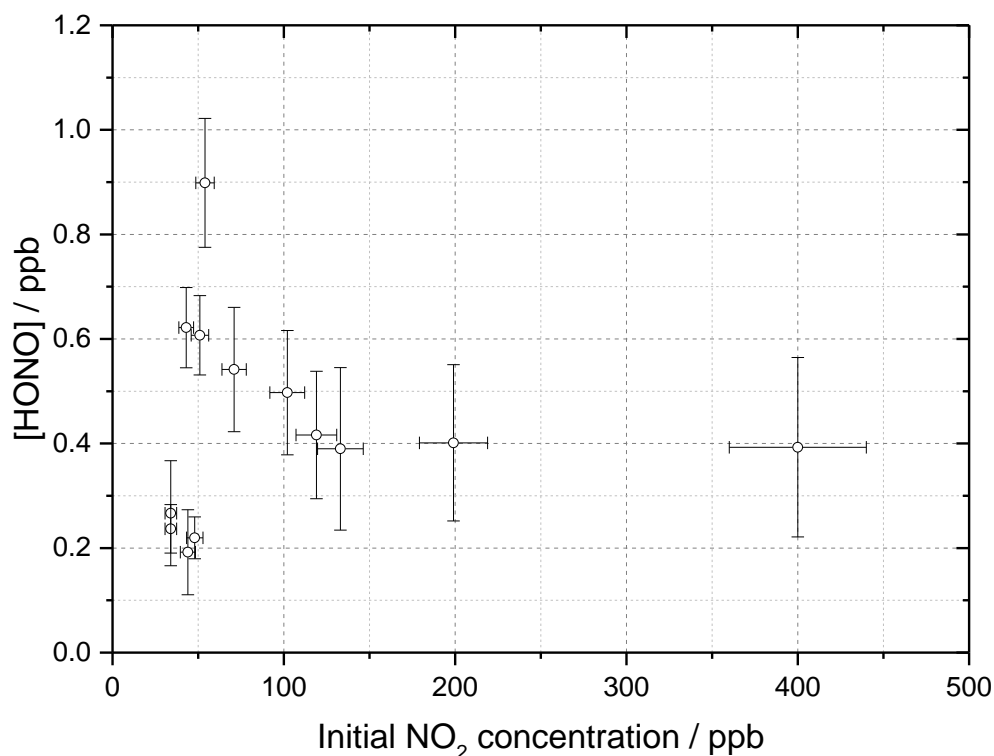


Figure 4.2. HONO concentration measured at the end of the flow tube as a function of the initial NO₂ concentration, for the aerosol surface area density of $(1.6 \pm 0.8) \times 10^{-2}$ m²m⁻³, relative humidity 15 ± 1 %, photon flux $(1.63 \pm 0.09) \times 10^{16}$ photons cm⁻² s⁻¹ (290-400 nm wavelength range), reaction time of 52 seconds and N₂ carrier gas. Each point is an average of up to 20 measurements at the same aerosol surface area and NO₂ concentration. The highest average concentration of HONO measured for the aerosol surface area density in this plot was 0.90 ± 0.12 ppb at [NO₂] = 54 ± 5 ppb. The x error bars represent the sum in quadrature of the errors in the N₂ and NO₂ gas flows and the NO₂ dilution. The y error bars represent 1σ. The SA varied over the experiments at different NO₂ concentrations leading to a larger error in the quoted SA.

4.1.2 Relative Humidity Dependence of HONO Production from TiO₂ Aerosol Surfaces

The production of HONO was measured over a range of humidity's for a fixed aerosol surface area concentration for multiple NO₂ concentrations. The results show a peak at between 25 – 30 % RH. Figure 4.3 shows the HONO concentration measured at a

range of RH values for a fixed aerosol surface area density of $(1.59 \pm 0.16 \times 10^{-2} \text{ m}^2 \text{ m}^{-3})$ and at two NO_2 mixing ratios.

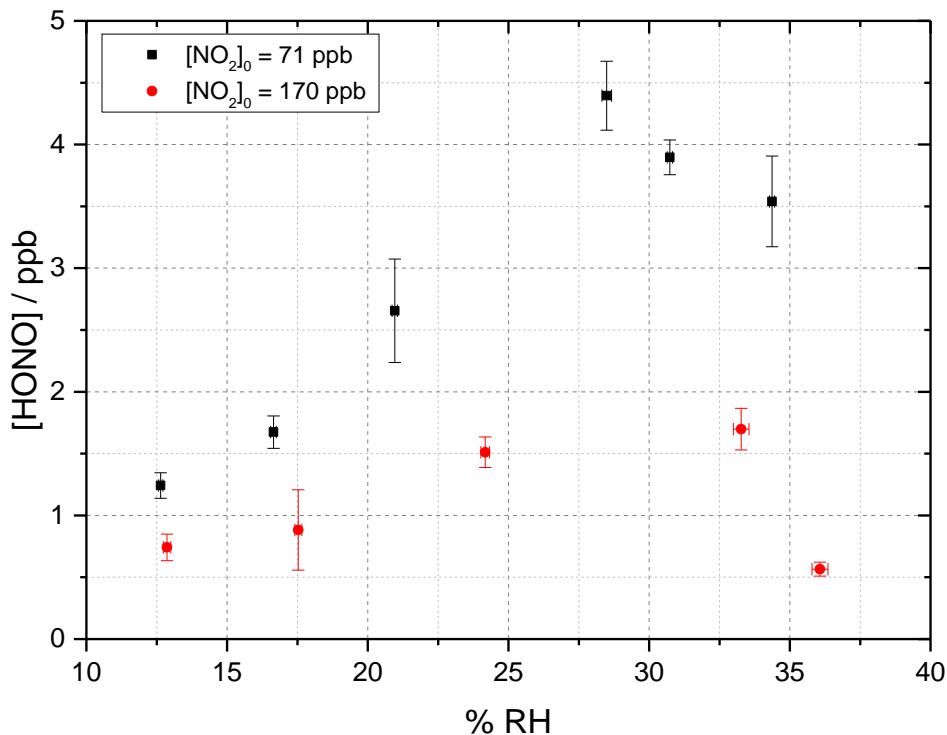


Figure 4.3. RH dependence of HONO production from illuminated TiO_2 aerosol surfaces at 298 K in N_2 at 71 (black) and 170 (red) ppb initial NO_2 concentration. Aerosol surface area density was kept constant at $(1.59 \pm 0.16) \times 10^{-2} \text{ m}^2 \text{ m}^{-3}$. Photon flux = $(1.63 \pm 0.09) \times 10^{16} \text{ photons cm}^{-2} \text{ s}^{-1}$, illumination time = 52 ± 2 secs. The error bars represent 1σ .

The fractional surface coverage of water on the TiO_2 aerosol core, V/V_m , was calculated using the parameterisation below, determined using transmission IR spectroscopy (Goodman et al., 2001).

$$\frac{V}{V_m} = \left[\frac{c \left(\frac{P}{P_0}\right)}{1 - \left(\frac{P}{P_0}\right)} \right] \left[\frac{1 - (n+1) \left(\frac{P}{P_0}\right)^n + n \left(\frac{P}{P_0}\right)^{n+1}}{1 + (c-1) \left(\frac{P}{P_0}\right) - c \left(\frac{P}{P_0}\right)^{n+1}} \right] \quad \text{Eq 4.1}$$

where V is the volume of gas, i.e. water vapour in this case, in monolayers of coverage adsorbed at equilibrium pressure, V_m is the volume of gas necessary to cover the surface of TiO_2 particles with a complete monolayer, P is the equilibrium pressure, P_0 is the saturation vapour pressure, c is the temperature dependant constant related to the enthalpies of adsorption of the first and higher layers (taken as 78.4 kJ mol^{-1} for TiO_2 (Goodman et al., 2001)) and n is the asymptotic limit of monolayers (8 for TiO_2

(Goodman et al., 2001)) at large values of P/P_0 . The fractional coverage of water as a function of RH (%) is shown in Figure 4.4.

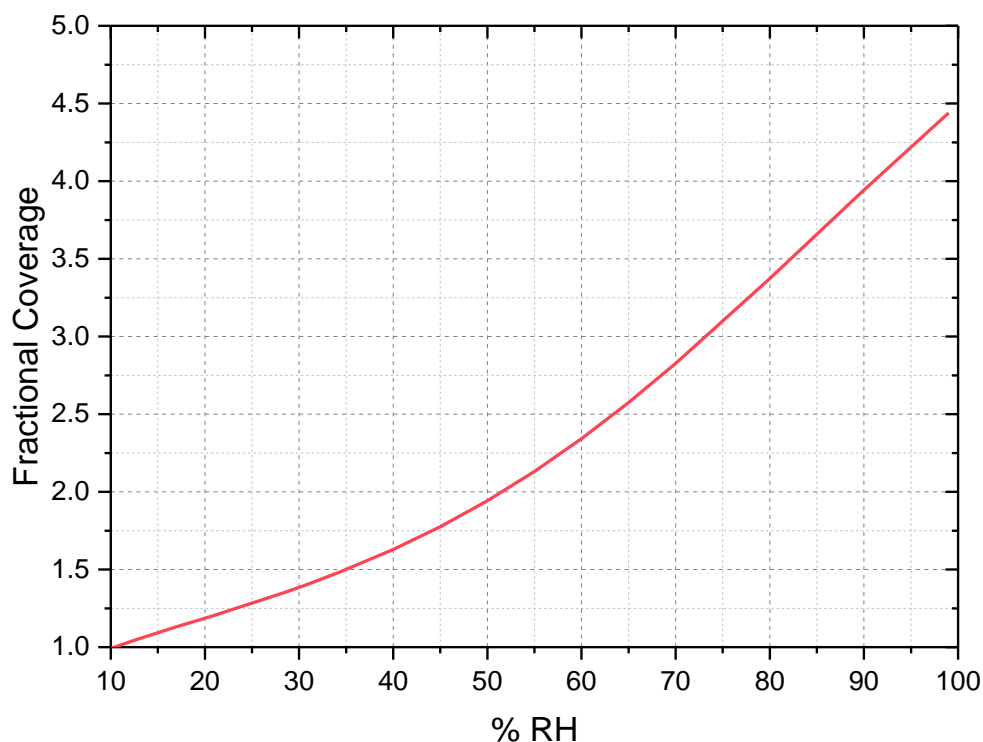


Figure 4.4. Monolayers of water on the surface of TiO_2 at 298 K as a function of % RH calculated using parameterisation by Goodman et al., 2001.

Monolayer coverage was achieved for the relative humidity (~ 15 % RH) used during TiO_2 experiments. Increasing the humidity to 35 % RH, after which the RH dependence in Figure 4.3 has turned over, lead to an increase from 1 to 1.5 monolayers. In Syomin and Finlayson-Pitts, 2003, it was shown that HONO can be displaced by water from a surface due to the preferential adsorption of water, leading to an increase in HONO measured in the gas phase with RH. Therefore, the increase in [HONO] with RH to ~ 30 % could be due to both the increase in available water leading to more HONO formation and an increase in the displacement of HONO from the aerosol surface due to water being preferentially adsorbed. The decrease in production at ~ 30 % would therefore be due to an increase in water absorption inhibiting NO_2 absorption and/or electron/hole transfer processes at the TiO_2 /gas interface (Gustafsson et al., 2006). This could also be exacerbated by the super-hydrophilic properties of TiO_2 surfaces under UV radiation meaning that water monolayers are formed quickly on the surface of TiO_2 due to light-induced surface tension changes (Takeuchi et al., 2005; Gustafsson et al., 2006). At the higher concentration of NO_2 ,

less HONO was produced at all RHs. This was expected given the decrease in HONO produced with increasing NO_2 concentration seen experimentally (Figure 4.2).

Gustafsson et al., 2006 also reported a strong dependence of the uptake coefficient of $\text{NO}_2 \rightarrow \text{HONO}$ on RH, with a peak at $\sim 15\%$ RH, decreasing at larger RH. A similar trend for the uptake coefficient of NO_2 onto Arizona Test Dust (ATD) aerosol surfaces (0.3% TiO_2) was observed in a later study by Dupart et al., 2014, with a peak in γ_{NO_2} at $\sim 25\%$ RH. This slightly higher trend inversion seen by Dupart et al., 2014 was ascribed to the lower concentration of TiO_2 present in ATD aerosols as compared to pure TiO_2 aerosols used in this work and by Gustafsson et al., 2006 as well as due to differences in particle size distribution. Gustafsson et al., 2006 reported a larger, bimodal aerosol size distribution with mode diameters at ~ 80 and ~ 350 nm for pure TiO_2 aerosols in comparison to the smaller, unimodal aerosol size distribution for ATD aerosols, with a lower mode diameter at ~ 110 nm reported by Dupart et al., 2014. This is similar to the unimodal aerosol size distribution for pure TiO_2 seen in this work, an example size distribution is shown in Figure 4.5, with a mode diameter at ~ 180 nm, though the size distribution is wider than that observed by Dupart et al., 2014. Similar to Dupart et al., 2014 we also observe a higher trend inversion of $[\text{HONO}]$ vs RH at between 25-30 % RH.

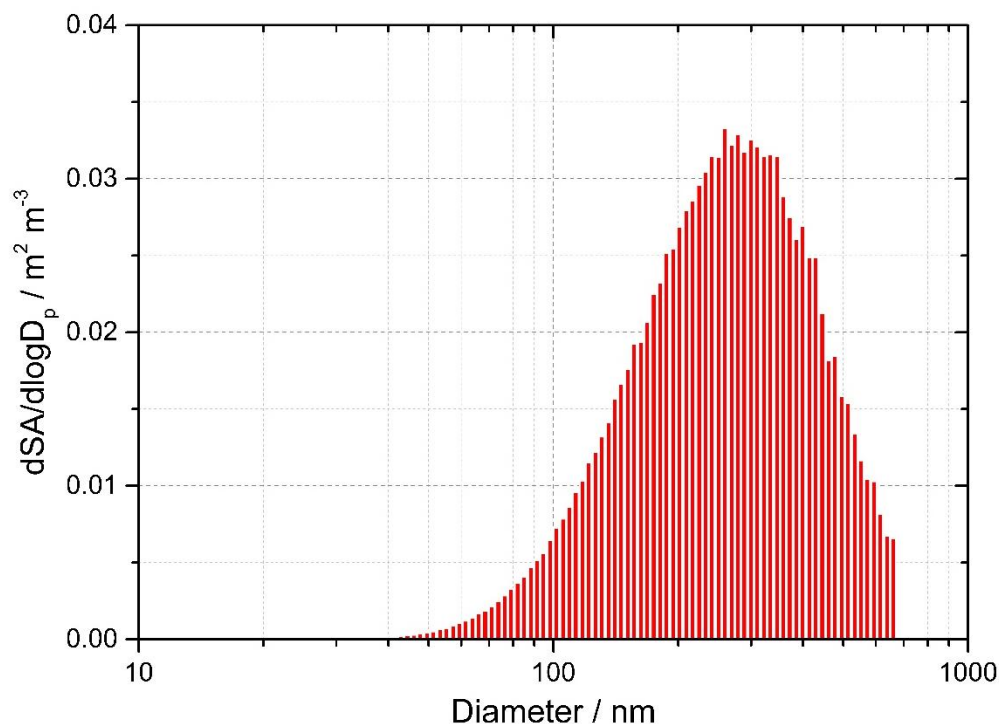


Figure 4.5. Typical aerosol surface area distribution for single component TiO₂ aerosols (RH = 15 ± 1 %) measured after the flow tube. Total surface area is 0.018 m² m⁻³.

4.1.3 NO₂ Uptake Coefficient Calculations

The reactive uptake coefficient, $\gamma_{NO_2 \rightarrow HONO}$ for NO₂ → HONO on TiO₂ aerosol particle surfaces was determined experimentally for 18 initial NO₂ mixing ratios. The uptake coefficient, $\gamma_{NO_2 \rightarrow HONO}$ was defined as reactive NO₂ loss per collisions with the TiO₂ aerosol surface that resulted in the production of HONO and was calculated using the expression:

$$\gamma_{NO_2 \rightarrow HONO} = \frac{4 \times k}{v \times SA} \quad \text{Eq 4.2}$$

where v is the mean thermal velocity of NO₂ (m s⁻¹), given by $v = \sqrt{(8RT/(\pi M))}$ with R , T and M as the gas constant, the absolute temperature and the molar mass of NO₂, respectively, SA is the aerosol surface area (m²m⁻²) and k is the first order rate coefficient (s⁻¹) for the reaction of NO₂ → HONO.

To determine the uptake coefficient, the pseudo-first order rate coefficient, k , for the transformation of NO₂ to HONO on TiO₂ aerosol surfaces was first calculated. It was assumed that the yield of HONO was 100 % and all other loss processes of NO₂ are ignored.

In the presence of illuminated aerosols, the rate of removal of NO₂ at the aerosol surface to generate HONO is given by:

$$-\frac{d[NO_2]}{dt} = k[NO_2] \quad \text{Eq 4.3}$$

Integration of Eq 4.3 gives:

$$k = -\frac{\ln\left(\frac{[NO_2]_0 - [HONO]_t}{[NO_2]_0}\right)}{t} \quad \text{Eq 4.4}$$

Where k is the pseudo-first order rate coefficient for the loss of NO₂ at the aerosol surface leading to the formation of HONO, $[NO_2]_0 - [HONO]_t$ is the concentration of NO₂ at time t assuming that each NO₂ is converted to a HONO molecule once taken up onto the surface, $[NO_2]_0$ is the initial concentration of NO₂, and t is the illumination period.

Therefore with knowledge of the initial NO₂ mixing ratio, the HONO concentration measured and the illumination t , k can be determined from Eq 4.4). Rearrangement of Eq 4.2 gives the uptake coefficient as a gradient of the plot of k (s⁻¹) vs SA (m²m⁻³) for each TiO₂ experiment at differing NO₂ mixing ratios:

$$\frac{k}{SA} (\text{gradient of } k \text{ vs } SA \text{ plot}) = \frac{\gamma_{NO_2 \rightarrow HONO} \times v}{4} \quad \text{Eq 4.5}$$

Figure 4.6 shows the variation of k , determined using Eq 4.4 with $t = 52$ s (illumination time in the flow tube), as a function of aerosol surface area density, SA, for $[NO_2]_0 = 200$ ppb, from which the gradient using Eq 4.5) yields $\gamma_{NO_2 \rightarrow HONO} = (2.17 \pm 0.09) \times 10^{-5}$.

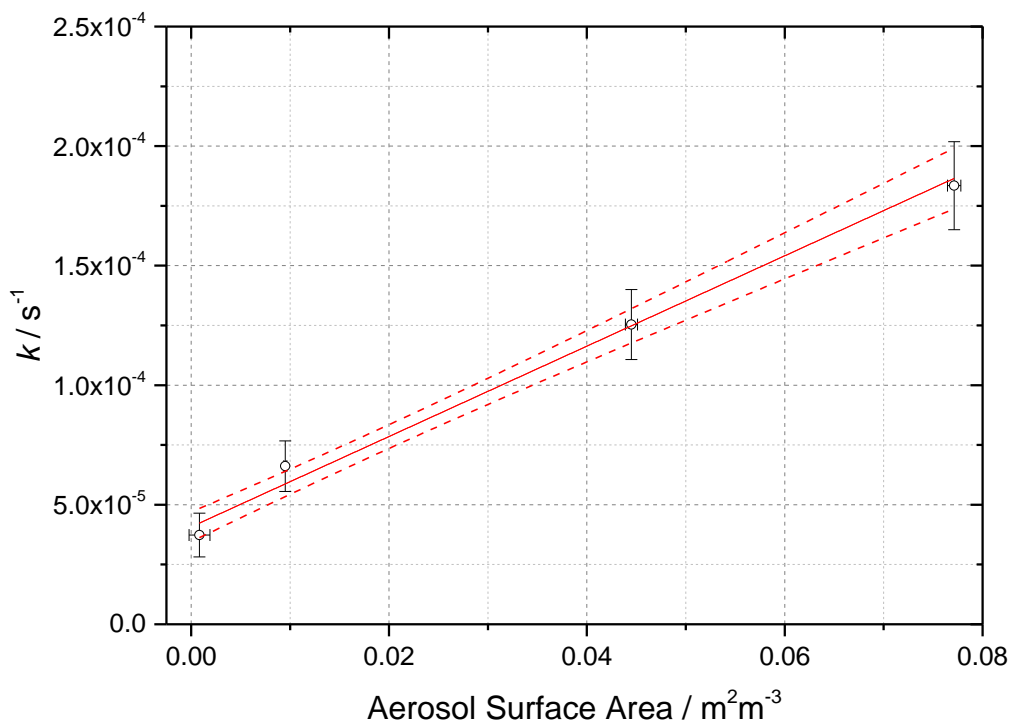


Figure 4.6. Pseudo-first-order rate coefficient for HONO production, k (open circles) as a function of aerosol surface area for $[\text{NO}_2]=200$ ppb and $\text{RH}=15 \pm 1 \%$, $T = 293 \pm 3$ K and a photolysis time of 52 ± 2 seconds. The red line is a linear-least squared fit including 1σ confidence bands (dashed lines) weighted to both x and y errors (1σ), the gradient of which yields $\gamma_{\text{NO}_2 \rightarrow \text{HONO}} = (2.17 \pm 0.09) \times 10^{-5}$, with the uncertainty representing (1σ). The total photon flux of the lamp = $(1.63 \pm 0.09) \times 10^{16}$ photons $\text{cm}^{-2} \text{s}^{-1}$.

The reactive coefficient, $\gamma_{\text{NO}_2 \rightarrow \text{HONO}}$, onto TiO_2 aerosol surfaces as a function of initial NO_2 mixing, from 34 to 400 ppb of NO_2 , is shown in Figure 4.7.

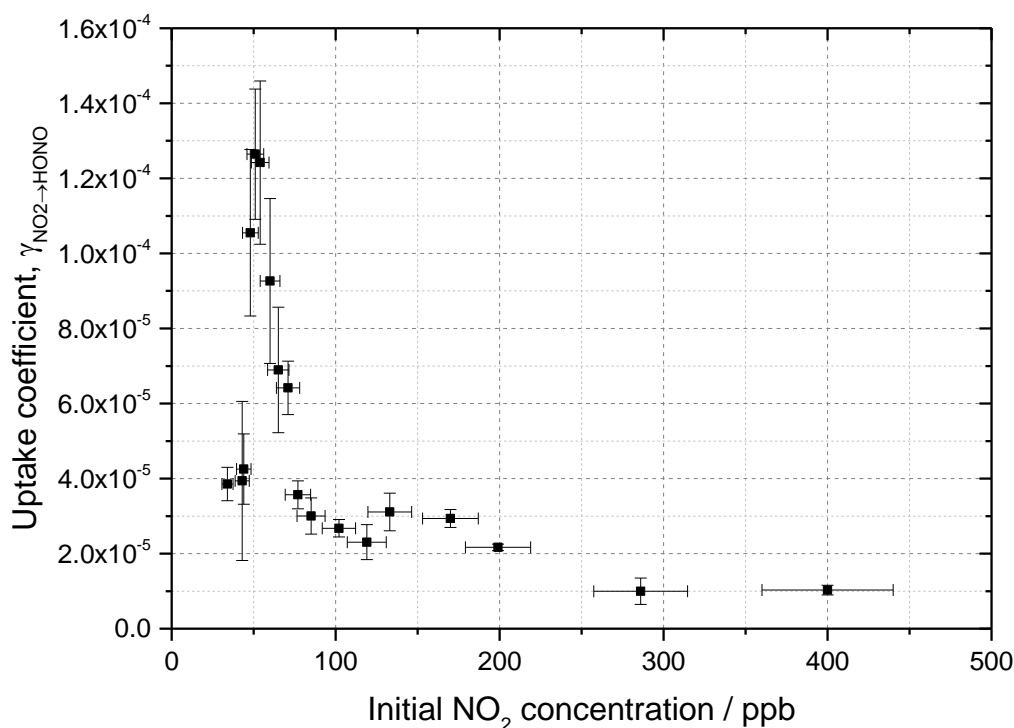


Figure 4.7. Experimental results for the reactive uptake coefficient of NO_2 to form HONO on TiO_2 aerosol surfaces, $\gamma_{\text{NO}_2 \rightarrow \text{HONO}}$, as a function of initial NO_2 concentration. All experiments conducted in N_2 at $15 \pm 1\%$ RH and 295 K. Photon flux = $(1.63 \pm 0.09) \times 10^{16}$ photons $\text{cm}^{-2} \text{s}^{-1}$, illumination time = 52 ± 2 seconds. The uptake coefficient was determined from the gradient of the pseudo-first order rate coefficient, k , versus aerosol surface area density varied from 0- $\sim 0.04 \text{ m}^2 \text{ m}^{-3}$, using equation Eq 4.5.

The increase in $\gamma_{\text{HONO} \rightarrow \text{NO}_2}$ as a function of NO_2 mixing ratio at low (< 51 ppb) NO_2 has not been seen in previous studies of light-driven HONO production from the surfaces of TiO_2 containing aerosols (Gustafsson et al., 2006; Ndour et al., 2008; Dupart et al., 2014) or from other aerosol surfaces (Bröske et al., 2003; Stemmler et al., 2007). It is, however, worth noting that several of these studies reported the uptake of NO_2 onto the surface, γ_{NO_2} , and not specifically the uptake of NO_2 to form HONO, $\gamma_{\text{HONO} \rightarrow \text{NO}_2}$, though in all studies HONO was indirectly measured (Gustafsson et al., 2006; Ndour et al., 2008; Dupart et al., 2014). For pure TiO_2 aerosol surfaces, Gustafsson et al., 2006 reported a reactive uptake coefficient, γ_{NO_2} of 9.6×10^{-4} at 15 % RH and 100 ppbv NO_2 . Though at a similar RH this is ~ 36 times higher than the reactive uptake coefficient observed in this work for the same NO_2 mixing ratio ($\gamma_{\text{HONO} \rightarrow \text{NO}_2} = (2.68 \pm 0.23) \times 10^{-5}$). Gustafsson et al., 2006 reported a HONO yield from NO_2 uptake of 0.75. Taking this into account, an estimated

$\gamma_{NO_2 \rightarrow HONO} = 7.2 \times 10^{-4}$ was determined, ~ 27 times higher than the value determined in this work: this was mostly attributed to the lower experimental lamp flux in our work, calculated to be ~ 19 less at a wavelength maximum of 365 nm due to the use of only one 15W UV lamp (consisting of two bulbs) in comparison to the four 18W UV lamps used by Gustafsson et al., 2006. The uptake coefficients calculated from our experiments showed a rapid increase at low NO₂ to a peak at ~ 51 ppb before a rapid decrease with further increase in NO₂. A kinetic box model was used to investigate the origins of this increase at lower NO₂ with the aim of providing a possible mechanistic interpretation for this experimental result, described fully in Section 4.2.1.

4.1.3.1 Surface Area Corrections

Any aerosol surface area not counted by the SMPS, an example of which is shown in Figure 4.5, due to the upper limit diameter range of the combined SMPS/ CPC instrument (14.6-661.2 nm range, sheath flow = 3 lpm, instrumental particle counting error ~10-20% dependant on counting method) was corrected for during analysis by assuming a lognormal distribution Matthews et al., 2014a and correcting for the percentage of surface area not accounted for by SMPS. An average underestimation in total surface area of 11.2 ± 3.15 % was then applied to all data.

4.1.3.2 NO₂ and HONO Photolysis Corrections

An initial NO₂ concentration was calculated from the ratio of NO₂ flow to N₂ carrier gas flow multiplied by the dilution of the NO₂ cylinder (NO₂ diluted in N₂).

$$[NO_2]_{init}(ppb) = \frac{NO_2 \text{ flow (sccm)}}{\text{Total flow of } N_2 \text{ and } NO_2 \text{ (sccm)}} \times \text{dilution factor}(ppb) \quad \text{Eq 4.6}$$

Through NO₂ actinometry the percentage of initial NO₂ added that was photolysed to give NO by the lamps was determined giving the effective NO₂ concentration within the system. The following table shows the average percentage conversion of NO₂ to NO with one, two and four lamps illuminating the flowtube. From this a correction can then be applied to give the effective NO₂ concentration experienced by the system. Alternatively initial NO₂ concentration can be quoted with consideration given to the photolysis of NO₂. All uptake coefficient and HONO concentration data was quoted as a function of initial NO₂ concentration to make the results more comparable with

previous work (Gustafsson et al., 2006;Stemmler et al., 2007;Ndour et al., 2008;Dupart et al., 2014).

Number of Lamps	Percentage of NO ₂ converted to NO (± one standard deviation)
1	48.7 ± 1.6
2	76.6 ± 5.2
4	96.7 ± 3.8

Table 4.1 Percentage of NO₂ converted through photolysis of UV lamps to NO

Using a UV-Vis absorption instrument the dilution of the NO₂ cylinder used in the experiments was checked. Any degradation of the NO₂ mixing ratio in the cylinder was then modified to give corrected NO₂ initial mixing ratios.

From $j(\text{NO}_2)$, $j(\text{HONO})$ was calculated as detailed in Section 3.6. From the ratio of $j(\text{HONO})$ to $j(\text{NO}_2)$ a scale factor was decided. The HONO photolysis correction was calculated from the sum of the scale factor and percentage of NO₂ photolysed by 1 lamp at $j(\text{NO}_2)$ of $(6.43 \pm 0.30) \times 10^{-3} \text{ s}^{-1}$.

$$SF = \frac{j(\text{HONO})}{j(\text{NO}_2)} \quad \text{Eq 4.7}$$

For a $j(\text{NO}_2)$ of $(6.43 \pm 0.30) \times 10^{-3} \text{ s}^{-1}$ and a $j(\text{HONO})$ of $(1.66 \pm 0.10) \times 10^{-3} \text{ s}^{-1}$, a scale factor (SF) of 0.26 was calculated, i.e. the rate of gas phase photolytic removal of HONO is 26 % that of NO₂.

$$\text{HONO photolysis correction} = \text{photolytic loss of NO}_2(\%) \times SF \quad \text{Eq 4.8}$$

For 1 lamp, for which the percentage conversion of NO₂ to NO due to photolysis was $48.7 \pm 1.6 \%$, the HONO photolysis correction was estimated as 12.56 % (a scale factor correction of 1.126)

4.1.3.3 Error Propagation for the Uptake Coefficient of NO₂ onto TiO₂ Aerosol Surfaces

The uncertainty in k , and therefore the uncertainty in γ_{NO_2} , was controlled mainly by the uncertainty in the HONO concentration, the initial NO₂ mixing ratio (~10%) and the photolysis time (~3 %). Keeping the surface area constant leads to ~4 % variation in HONO counts so an error of ~4-10% was taken for $\sigma_{\text{HONO counts}}$. The σ_{SA} was

estimated to be 15 % due to the accuracy of the SMPS being between 10 and 20 % depending on the method of particle counting. Below $5 \times 10^4 \text{ cm}^{-3}$ the CPC counts particles by extended single particle counting which has an associated error of 10 %. Above this however the CPC smoothly transitions into photometric mode counting to allow the detection limit to increase to 10^7 cm^{-3} . This mode however has a higher associated error of 20 % as particles are counted based on total light scattering rather than the optical detector counting individual pulses generated by each butanol grown particle. The errors in the MFCs are given as 1 % by Brooks and MKS.

Before plotting a graph of k vs SA to obtain the uptake coefficient a correction was made for the trend in the lamp off measurements throughout the day as any increase or decrease in the lamp off background measurement could lead to an artificially inflated/deflated trend in k and therefore the uptake coefficient with increasing aerosol surface area. To compensate for this the gradient of the graph of $[HONO]$ vs t throughout the day for the lamp off measurements was subtracted from the illuminated measurements. The error in the illuminated HONO counts, following removal of variation in lamp off measurements, was then calculated using Eq 4.9.

$$\sigma_{illuminated\ HONO\ counts} = \sqrt{\sigma_{dark\ HONO\ correction}^2 + \sigma_{HONO\ counts}^2} \quad \text{Eq 4.9}$$

The trend in lamp off throughout the day for an experiment with 200 ppb NO_2 is shown in Figure 4.8. Changes in lamp off background throughout the day was thought to be due to any HONO left from previous experiments coming off the walls.

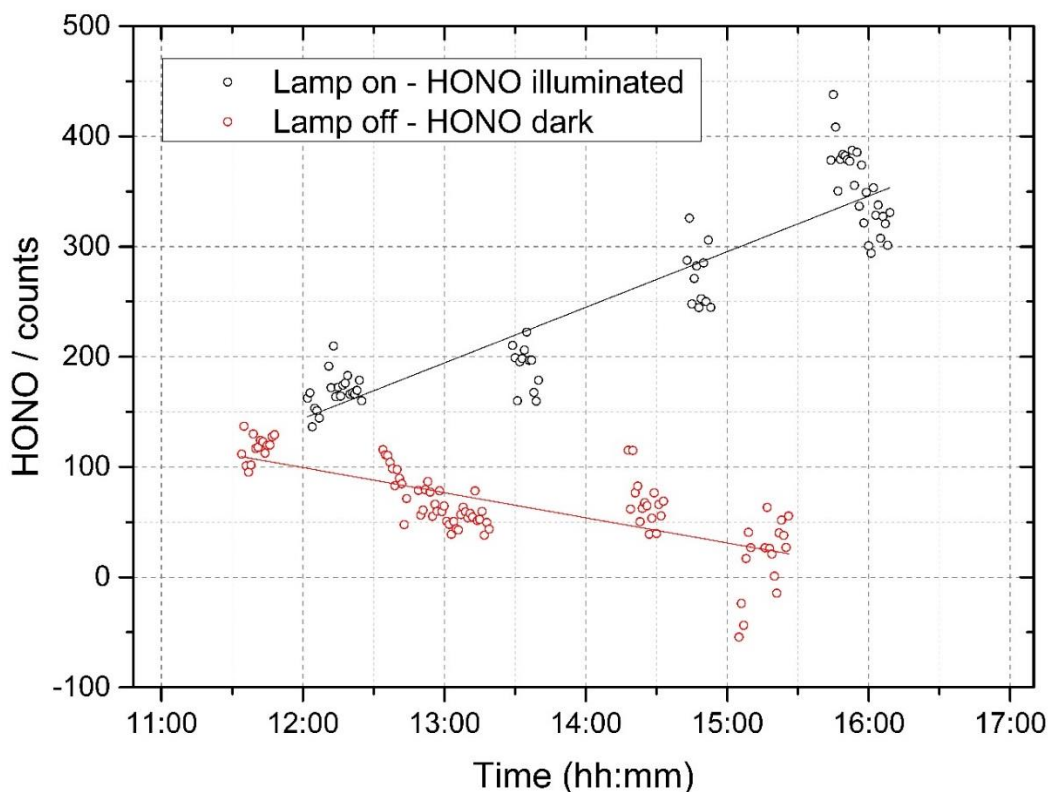


Figure 4.8. Time series of HONO / counts throughout an experimental day with HONO produced with UV lamps on (black circles) i.e. production from illuminated TiO₂ surfaces, and with UV lamps off (red circles) i.e. HONO background in the lines/reacting off the walls of either the cell or the flow-tube. The gradient and intercept of the lamp off HONO dark trend was removed from the illuminated HONO data values to offset any varying background.

To convert the HONO counts into concentration, the counts were multiplied by a calibration factor, C_{HONO} , fully described in Section 3.5.2. The $\sigma_{C_{HONO}}$ was taken from the calibration curve and was typically less than 20 %. The error in the HONO concentration was therefore calculated using Eq 4.10:

$$\sigma_{[HONO]} = [HONO] \times \left(\sqrt{\left(\frac{\sigma_{corrected\ HONO\ counts}}{corrected\ HONO\ counts} \right)^2 + \left(\frac{\sigma_{C_{HONO}}}{C_{HONO}} \right)^2} \right) \quad \text{Eq 4.10}$$

To calculate the uptake coefficient, the pseudo-first order rate coefficient, k , (s⁻¹) was first calculated for the reaction of NO₂ → HONO, Eq 4.11. The error in k was calculated from the sum in quadrature of the errors associated with [NO₂], [HONO] and t :

$$\ln \left(\frac{[NO_2]_0 - [HONO]}{[NO_2]_0} \right) = -kt \quad \text{Eq 4.11}$$

$$\sigma_{[NO_2]_0-[HONO]} = \sqrt{(\sigma_{[HONO]})^2 + (\sigma_{[NO_2]})^2} \quad \text{Eq 4.12}$$

$$\sigma_{\left(\frac{[NO_2]_0-[HONO]}{[NO_2]_0}\right)} = \left(\frac{[NO_2]_0-[HONO]}{[NO_2]_0}\right) \times \left(\sqrt{\left(\frac{\sigma_{[NO_2]_0-[HONO]}}{[NO_2]_0-[HONO]}\right)^2 + \left(\frac{\sigma_{[NO_2]}}{[NO_2]}\right)^2}\right) \quad \text{Eq 4.13}$$

$$\sigma_{\ln\left(\frac{[NO_2]_0-[HONO]}{[NO_2]_0}\right)} = \frac{\sigma_{\left(\frac{[NO_2]_0-[HONO]}{[NO_2]_0}\right)}}{\left(\frac{[NO_2]_0-[HONO]}{[NO_2]_0}\right)} \quad \text{Eq 4.14}$$

As the illumination time was calculated from the flow rate and the calculated flow tube volume, σ_t was propagated using the error in the flows of NO₂ and N₂ and the error in the calculated volume.

$$\sigma_t = t \times \sqrt{\left(\frac{\sigma_{flow}}{total\ flow}\right)^2 + \left(\frac{\sigma_{volume}}{volume}\right)^2} \quad \text{Eq 4.15}$$

$$\sigma_{\frac{1}{t}} = \frac{1}{t} \times \frac{\sigma_t}{t} \quad \text{Eq 4.16}$$

The error in k can therefore be propagated from $\sigma_{\ln\left(\frac{[NO_2]_0-[HONO]}{[NO_2]_0}\right)}$ and $\sigma_{\frac{1}{t}}$.

$$\sigma_k = k \times \sqrt{\left(\frac{\sigma_{\ln\left(\frac{[NO_2]_0-[HONO]}{[NO_2]_0}\right)}}{\ln\left(\frac{[NO_2]_0-[HONO]}{[NO_2]_0}\right)}\right)^2 + \left(\frac{\sigma_{\frac{1}{t}}}{\frac{1}{t}}\right)^2} \quad \text{Eq 4.17}$$

$\sigma_{\gamma_{NO_2}}$ was then be calculated from the plot of k vs SA by multiplying $\sigma_{gradient\ of\ k\ vs\ SA}$ by 4 and dividing by ω . It is worth noting that the value for γ_{NO_2} (with typically ~ 20 % error) was for experiments done in nitrogen was well within the error range as the equivalent NO₂ experiment done in air (usually within 7 %).

4.1.4 Effect of Light Intensity on the Production of HONO from TiO₂ Aerosol Surfaces

The effect of increasing light intensity on the production of HONO from TiO₂ aerosols was studied for 2 different j_{NO_2} values. The NO₂ mixing ratio was kept the same for the two experiments as was the aerosol concentration. The increase in light intensity however lead to an increase in NO₂ photolysis and therefore a decrease in NO₂ concentration. Ideally this should have been taken into account so that the NO₂

experienced by the aerosols after photolysis was the same and therefore the only difference between the experiments would have been the lamp intensity. As such, the decrease in HONO produced with an increase in lamps illuminating the system was most likely due to the decrease in effective NO_2 as a result of increasing NO_2 photolysis. The $j\text{NO}_2$ value increases from $(6.43 \pm 0.30) \times 10^{-3} \text{ s}^{-1}$ for 1 lamp to $(1.41 \pm 0.21) \times 10^{-2} \text{ s}^{-1}$ for 2 lamps. The percentage conversion of NO_2 to NO via photolysis however also increased from 48.7 ± 1.6 to 76.6 ± 5.2 . Future work should take into account the increase in NO_2 photolysis and therefore would add a higher initial NO_2 concentration.

4.2 Modelling HONO Production from NO_2 Adsorption on Illuminated TiO_2 Aerosol Surfaces

4.2.1 Box Model Description and Results

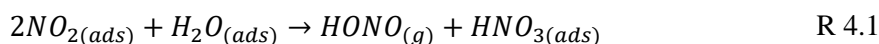
As stated in section 4.1.3, an increase in $\gamma_{\text{HONO} \rightarrow \text{NO}_2}$ as a function of NO_2 mixing ratio at low NO_2 has not been seen in previous studies of light-driven HONO production from the surfaces of TiO_2 containing aerosols (Gustafsson et al., 2006; Ndour et al., 2008; Dupart et al., 2014) or from other aerosol surfaces (Bröske et al., 2003; Stemmler et al., 2007). In order to investigate the production mechanism of HONO on illuminated TiO_2 aerosol surfaces, a kinetic scheme within a box model was created and used together with the differential equation solver Facsimile 4.5.53 (MCPA software Ltd., 2020). The models produced were semi-explicit, focusing instead on the stoichiometric amount of NO_2 needed in order to produce a single HONO molecule rather than trying to produce the absolute concentrations observed experimentally. These models were then compared to the experimental dependence of $[\text{HONO}]$ on NO_2 mixing ratios and the reactive uptake coefficient, $\gamma_{\text{NO}_2 \rightarrow \text{HONO}}$, with the hope that this would then provide a predictive framework for the parameterisation of HONO production rate as a function of NO_2 in the atmosphere.

4.2.1.1 Model 1

The first model, hereafter referred to as Model 1, was designed to consider the adsorption of a single molecule of NO_2 , as previous literature would suggest, for the uptake of NO_2 to give HONO on aerosol surfaces. Light-driven heterogeneous conversion to HONO on the surface followed by desorption of HONO was also

included with the desorption process assumed to occur rapidly. Previous literature (Stemmler et al., 2007;Ndour et al., 2008) has reported a decrease in NO₂ uptake coefficient as a function of NO₂ mixing ratio, eventually levelling off at high NO₂ mixing ratios caused by maximum surface coverage being reached. A decrease in the uptake coefficient of NO₂, γ_{NO_2} , onto dust aerosol surfaces has also been seen in studies where the formation of HONO from NO₂ uptake was not directly studied (Ndour et al., 2008;Dupart et al., 2014).

The mechanism in Model 1, outlined fully in Table 4.3, described the adsorption of one NO₂ molecule to a surface site which could then undergo reaction to form HONO followed by desorption of HONO to the gas phase. As a starting point, rate coefficients were estimated an order of magnitude faster than HONO loss rates to chamber surfaces reported by Finlayson-Pitts et al., 2003, with desorption taken as rapid so as to not be the rate limiting step. The primary focus of this model was to produce the relationship between $\gamma_{NO_2 \rightarrow HONO}$ and the NO₂ mixing ratio, rather than discern a specific chemical mechanism for the conversion of NO₂ to HONO on the aerosol surface. It was thought that the light-driven production of HONO from NO₂ could occur via the photo-enhancement of R 4.1:



Gustafsson et al., 2006 reported a yield of 75 % of HONO from NO₂, however, the dark disproportionation reaction (R 4.1) would predict a 50% yield of HONO. Therefore, the HONO observed in their work was not simply a product of the photo-enhancement of the NO₂ hydrolysis reaction to produce HONO and HNO₃ in equal parts. Gustafsson et al., 2006 suggested that an oxidant on the surface was produced following the creation of the electron-hole pair giving H₂O₂ as a probable product, which is consistent with the observation of HO_x radicals produced from the surface of illuminated TiO₂ aerosols (Moon et al., 2019). Future work would be to measure the pH of the aerosols produced to ascertain if H₂O₂ is a by-product. The reactions included in Model 1 are outlined in Table 4.2.

Reactions		Rate coefficient
Model 1		
R4.2	$NO_{2(g)} + surface \rightarrow NO_{2(ads)}$	1×10^{-3}
R4.3	$NO_{2(ads)} \rightarrow HONO_{(ads)}$	1×10^{-3}
R4.4	$HONO_{(ads)} \rightarrow HONO_{(g)}$	1×10^{-2}

Table 4.2. Full reaction mechanism included in Model 1 used to model the uptake of NO_2 to form HONO on TiO_2 aerosol surfaces. All rate coefficients are estimated, as described below,

The modelled concentration of HONO and the reactive uptake coefficient, $\gamma_{NO_2 \rightarrow HONO}$, as a function of initial NO_2 mixing ratio for Model 1 are shown in Figure 4.9.

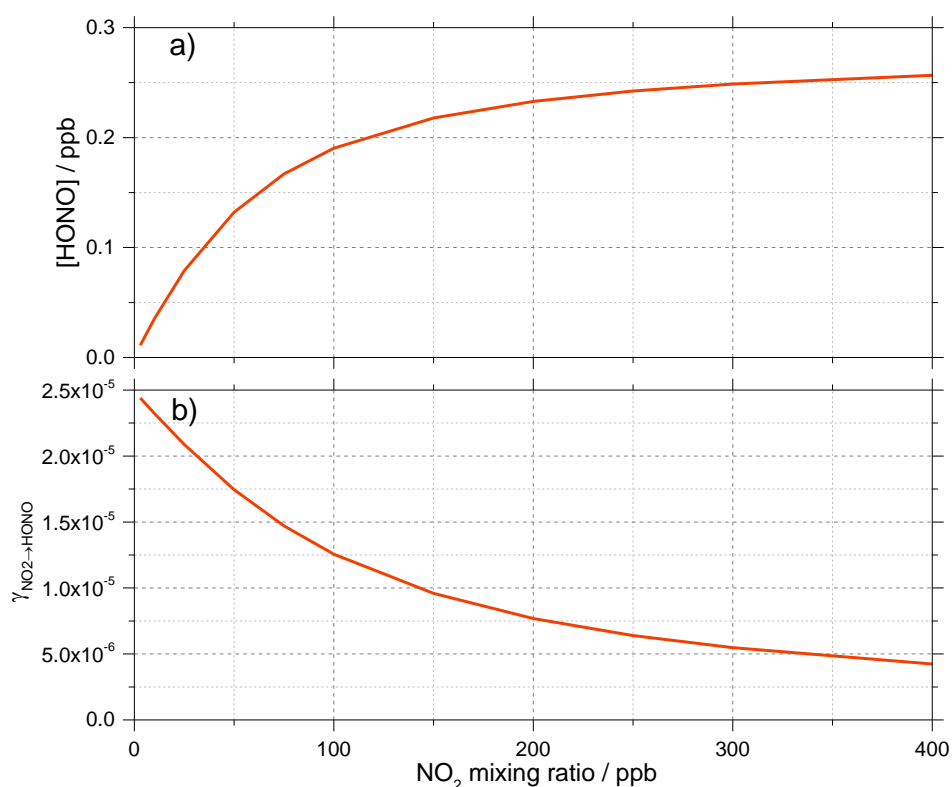


Figure 4.9. Model 1 calculations for (a) the concentration of HONO and (b) the reactive uptake coefficient to form HONO, $\gamma_{NO_2 \rightarrow HONO}$, as a function of NO_2 mixing ratio for a model run time of 52 s. The estimated rate coefficients used in this model are shown in Table 4.3.

Model 1 predicted an increase in $[HONO]$ as a function of NO_2 mixing ratio until the $[HONO]$ started to level off, reaching ~ 0.25 ppb at $[NO_2] = 400$ ppb, owing, most likely, to saturation of the active surface sites by NO_2 . The reactive uptake coefficient was calculated from the modelled $[HONO]$ and showed a monotonic decrease with

increasing NO₂ mixing ratio; a variation in uptake coefficient similar to that seen in previous light-driven NO₂ aerosol uptake studies (Bröske et al., 2003; Stemmler et al., 2007; Ndour et al., 2008; Dupart et al., 2014). Model 1 did not predict the experimental variations in [HONO] or uptake coefficient shown in Figure 4.2 and Figure 4.7, in which there is a rise and then fall in both [HONO] and $\gamma_{NO_2 \rightarrow HONO}$ with increasing NO₂ mixing ratio suggesting a different stoichiometric relationship between NO₂ adsorbed and HONO formed. Further models were designed to introduce additional processes to postulate on this behaviour.

4.2.1.2 Models 2 and 3: The role of NO₂ dimerization

To investigate the effect of a 2:1 stoichiometric relationship between the amount of NO₂ adsorbed to the surface sites of TiO₂ and the HONO desorbing from the surface, two further models were designed: the first describing an Eley-Rideal type mechanism characterised by the adsorption of a single NO₂ molecule to the surface of TiO₂ following the adsorption of a second molecule of NO₂ to the first molecule, leading to the creation of the NO₂ dimer species hereafter referred to as Model 2; and the other describing a Langmuir-Hinshelwood type mechanism of NO₂ adsorption in which both NO₂ molecules adsorb to the surface before diffusing to one another and colliding on the surface to form the NO₂ dimer, most likely the more stable *cis*-ONO-NO₂ conformer (Finlayson-Pitts et al., 2003; de Jesus Madeiros and Pimentel, 2011; Liu and Goddard, 2012; Varner et al., 2014), hereafter referred to as Model 3.

Both models assume the formation of the stable *cis*-ONO-NO₂ conformer, following NO₂ adsorption, via a van der Waals complex followed by isomerisation to form *trans*-ONO-NO₂: a pathway which has been suggested to have a much lower enthalpic barrier; $\sim 170 \text{ kJ mol}^{-1}$ than direct isomerisation from the symmetric N₂O₄ dimer (Liu and Goddard, 2012). NO₂ dimerization and the ensuing isomerisation to form *trans*-ONO-NO₂ has been proposed under dark conditions to lead to the production of HONO and HNO₃ in the presence of water (Finlayson-Pitts et al., 2003; de Jesus Madeiros and Pimentel, 2011; Liu and Goddard, 2012; Varner et al., 2014). However, to our knowledge, this pathway has not been experimentally observed under illuminated conditions. The *trans*-ONO-NO₂ dimer has also been suggested to be more reactive with water than the symmetric N₂O₄ dimer (Finlayson-Pitts et al., 2003; Ramazan et al., 2004b; Ramazan et al., 2006; Liu and Goddard, 2012; Dyson et al., 2021) and has been experimentally observed in several studies (Fateley et al.,

1959;Givan and Loewenschuss, 1989a, b, 1991;Pinnick et al., 1992;Forney et al., 1993;Wang and Koel, 1998, 1999;Beckers et al., 2010). This proposed increased reactivity of the *trans*-ONO-NO₂ dimer with water is due to the auto-ionisation to form (NO⁺)(NO₃⁻) which we propose to be light-driven in some way. The (NO⁺)(NO₃⁻) ion pair is then proposed to react with water on the surface which can then lead to the formation of HONO and HNO₃, the feasibility of which is supported by molecular dynamics simulation studies (Varner et al., 2014). More recently, an *ab initio* study by Murdachaew et al., 2013 into NO₂ adsorption at the air-water interface suggested an orientational preference of NO₂ on the surface, with both oxygen atoms facing away from the interface implying that the asymmetric dimer, ONO-NO₂ could form directly on the surface, without N₂O₄ dimer being formed first. This removes the issue of the high energy barrier between the symmetric and asymmetric forms needing to be surmounted to lead to HONO production (Murdachaew et al., 2013). It is also possible that the energy barrier to isomerisation of N₂O₄ to ONO-NO₂ may be reduced by the interaction with surface adsorbed water. We therefore make the assumption that the dimer formation is occurring on the water saturated surface preferentially and rule out the possibility of the dimer in the gas phase adsorbing onto the surface first then reacting to form HONO (Varner et al., 2014).

Within Models 2 and 3 we do not specify the exact mechanism by which the electron-hole pairs in TiO₂ interact with any surface bound species in the formation of HONO but instead propose that the interaction of light increases the rate of auto-ionisation of *trans*-ONO-NO₂ to (NO⁺)(NO₃⁻), included in $k_{R4.6}$ and $k_{R4.8}$ in Models 2 and 3 (Table 4.3 below), which can then go on to react rapidly with water adsorbed to the surface and lead to HONO production (Varner et al., 2014;Dyson et al., 2021).

Figure 4.10 shows a schematic diagram of the proposed mechanism within Models 2 and 3, and consists of (i) the adsorption of NO₂ onto a surface site, (ii) the conversion of NO₂ to form HONO via the formation of an NO₂ dimer intermediate on the surface via either a Eley-Rideal or Langmuir Hinshelwood- type mechanism, (iii) subsequent desorption of HONO from the surface, and finally (iv) competitive removal processes for HONO both on the surface and in the gas phase that are either dependent or independent on the NO₂ mixing ratio. Gas phase photolysis of NO₂ and HONO and the gas phase reactions of both HONO and NO₂ with OH and O(³P) atoms were also included (Dyson et al., 2021).

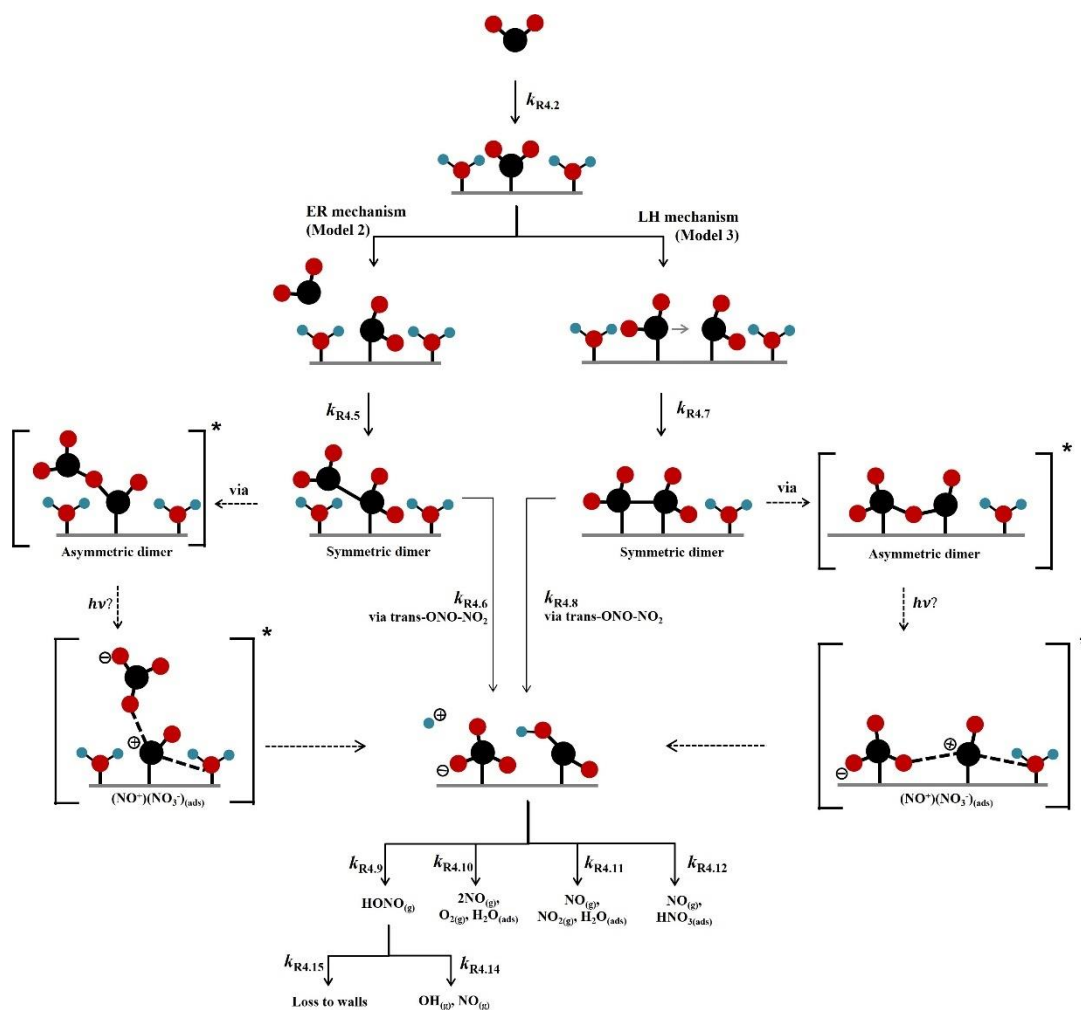


Figure 4.10. Schematic diagram of proposed light-driven mechanism of HONO formation via the adsorption of NO_2 and subsequent dimerization on an aerosol surface in the presence of water. Loss reactions of HONO dependent and independent of NO_2 are also shown. Both Eley Rideal, Model 2, and Langmuir Hinshelwood, Model 3, mechanisms are shown with relevant estimated and calculated rate coefficients used also shown, detailed fully below. Nitrogen shown in black, oxygen shown in red and hydrogen shown in blue. * denotes intermediate steps of the isomerisation of symmetric N_2O_4 to *trans-ONO-NO*₂ which is then predicted to form HONO. Image taken from Dyson et al., 2021.

To our knowledge the enthalpy of adsorption of NO_2 onto TiO_2 surfaces (aerosol or coated) has not been determined, nor the rate coefficients for the surface reactions shown in Figure 4.10. Because of this, for each step in the model, a rate coefficient (s^{-1} or $\text{cm}^3 \text{ molecule}^{-1} \text{ s}^{-1}$) was assigned, detailed in Table 4.3, with the aim of reproducing the experimentally determined NO_2 dependence of HONO production and uptake coefficient. Some rate coefficients were chosen based off modelling studies in the literature, while others were varied to fit the shape of the trend in experimental variation of $[\text{HONO}]$ and $\gamma_{\text{NO}_2 \rightarrow \text{HONO}}$ versus $[\text{NO}_2]$. The exceptions to this were the experimentally determined $j(\text{NO}_2)$ and the calculated $j(\text{HONO})$. Justification for the chosen values of rate coefficients is given below:

Reactions	Rate coefficient
Model 2 and 3	
<i>Model 2 only – Eley-Rideal mechanism</i>	
R4.5	$NO_{2(g)} + NO_{2(ads)} \rightarrow NO_2 - NO_{2(ads)}$ 1×10^{-2}
R4.6	$NO_2 - NO_{2(ads)} \xrightarrow{\text{via trans-ONO-NO}_2} HONO_{(ads)} + HNO_{3(ads)}$ 5×10^{-3}
<i>Model 3 only – Langmuir-Hinshelwood mechanism</i>	
R4.7	$NO_{2(ads)} + NO_{2(ads)} \rightarrow NO_{2(ads)} - NO_{2(ads)}$ 1×10^{-3}
R4.8	$NO_{2(ads)} - NO_{2(ads)} \xrightarrow{\text{via trans-ONO-NO}_2} HONO_{(ads)} + HNO_{3(ads)}$ 5×10^{-3}
<i>Common to both Models 2 and 3</i>	
R4.2	$NO_{2(g)} + \text{surface} \rightarrow NO_{2(ads)}$ 1×10^{-1}
R4.9	$HONO_{(ads)} \rightarrow HONO_{(g)}$ 5×10^{-2}
R4.10	$HNO_{3(ads)} + HONO_{(ads)} \rightarrow 2NO_{(g)} + O_{2(g)} + H_2O_{(ads)}$ 1×10^{-3}
R4.11	$HONO_{(ads)} + HONO_{(ads)} \rightarrow NO_{(g)} + NO_{2(g)} + H_2O_{(ads)}$ 1×10^{-3}
R4.12	$NO_{2(g)}(\text{or species such as } NO_2^+) + HONO_{(ads)} \rightarrow NO_{(g)} + HNO_{3(ads)}$ 5×10^{-3}
R4.13	$NO_{2(g)} + h\nu \rightarrow NO_{(g)} + O(^3P)_{(g)}$ 6×10^{-3a}
R4.14	$HONO_{(g)} + h\nu \rightarrow OH_{(g)} + NO_{(g)}$ 2×10^{-3b}
R4.15	$HONO_{(g)} \rightarrow \text{wall loss}$ 1×10^{-4}
R4.16	$HONO_{(g)} + OH_{(g)} \rightarrow NO_{2(g)} + H_2O_{(g)}$ 4.5×10^{-12c}
R4.17	$NO_{2(g)} + OH_{(g)} \xrightarrow{M} HNO_{3(g)}$ 1×10^{-11c}
R4.18	$O(^3P)_{(g)} + NO_{2(g)} \rightarrow O_{2(g)} + NO_{(g)}$ 1×10^{-11c}
R4.19	$O(^3P)_{(g)} + O_{2(g)} \xrightarrow{M} O_3$ 1.5×10^{-14c}
R4.20	$O(^3P)_{(g)} + NO_{(g)} \xrightarrow{M} NO_{2(g)}$ 1.7×10^{-12c}

Table 4.3. Full reaction mechanism included in models 1-3 used to model the uptake of NO₂ to form HONO on TiO₂ aerosol surfaces. All rate coefficients are estimated with the exception of the NO₂ and HONO photolysis rate coefficient.^aMeasured using chemical actinometry with the knowledge of the experimentally determined spectral output of the lamp and the cross-sections and quantum yields of NO₂ and HONO, see Section 3.6 for more detail. ^bCalculated using a photon flux of $(1.63 \pm 0.09) \times 10^{16}$ photons cm⁻² s⁻¹.^cSander et al., 2003. Rate coefficients are in the units of s⁻¹ or cm³ molecule⁻¹ s⁻¹.

Pimental et al., 2007 estimated the modelled Gibbs free energy barrier for the isomerisation of N_2O_4 to form the asymmetric ONO-NO_2 isomer to be 87 kJ mol^{-1} in the aqueous phase at 298 K, lower than in the gas phase, with a maximum rate coefficient of $2 \times 10^{-3} \text{ s}^{-1}$ at room temp, increasing to $1.2 \times 10^{-2} \text{ s}^{-1}$ at 373 K, confirming the Finlayson-Pitts model for the hydrolysis of NO_2 on surfaces via *trans*- ONO-NO_2 (Finlayson-Pitts et al., 2003). From this the modelled rate coefficients for the isomerisation, auto-ionisation and desorption of HONO for Models 2 and 3, $k_{\text{R4.6}}$ and $k_{\text{R4.8}}$, were estimated as $5 \times 10^{-3} \text{ s}^{-1}$, increased slightly compared to those estimated by Pimental et al., 2007 due to the presence of light in this study. For $k_{\text{R4.5}}-k_{\text{R4.8}}$, initial values were implemented and were then adjusted to fit the shape of the trend in experimental variation of $[\text{HONO}]$ and $\gamma_{\text{NO}_2 \rightarrow \text{HONO}}$ versus $[\text{NO}_2]$, shown in Figure 4.2 and Figure 4.7. Syomin and Finlayson-Pitts (2003) proposed a rate coefficient for the decomposition of HONO on borosilicate glass chamber walls to be $(1.0 \pm 0.2) \times 10^{-4} \text{ s}^{-1}$ increasing to $(3.9 \pm 1.1) \times 10^{-4} \text{ s}^{-1}$ with a pre-conditioned chamber coating of HNO_3 on the walls. From this, the light-driven loss rate of $\text{HONO}_{(\text{ads})}$ via reaction with $\text{HNO}_{3(\text{ads})}$ and self-reaction, respectively $k_{\text{R4.10}}$ and $k_{\text{R4.11}}$, was estimated as $1 \times 10^{-3} \text{ s}^{-1}$. An assumption was made that the loss of HONO to the walls of the flow tube during this experiment was less than that of the loss reactions occurring at the TiO_2 aerosol surface leading to a $k_{\text{R4.15}}$ of $1 \times 10^{-4} \text{ s}^{-1}$ as seen by Syomin and Finlayson-Pitts, 2003. Gas phase loss reactions of HONO and NO_2 with OH (R4.16-R4.17) and the reactions of $\text{O}(^3\text{P})$ with NO, NO_2 and O_2 (R4.18-R4.20) were also included in the model, of which experimentally determined values were used (Sander et al., 2003). However, their inclusion had little effect on the HONO concentration, as the rates of R4.16-R4.20 were much slower than HONO loss reactions on the surface (R4.10-R4.12) and the photolysis reactions (R4.14) within the model. The adsorption of an NO_2 molecule to the surface, $k_{\text{R4.2}}$, was assumed to be rapid and not the rate determining step in Models 2 and 3. The desorption of HONO was also assumed to be rapid, faster than the rate of loss of adsorbed HONO but slower than the adsorption of NO_2 ; these assumptions were necessary for the model to reproduce the trend in the experimental results of $[\text{HONO}]$ versus $[\text{NO}_2]$, discussed fully in Sections 4.1.1 and 4.1.3.

An interesting question posed by this modelling is whether the first NO_2 molecule adsorbed to the surface dimerises via the addition of another gaseous NO_2 molecule

via an Eley-Rideal (ER) type process, or whether a Langmuir-Hinshelwood (LH) type mechanism is occurring in which both NO_2 molecules are first adsorbed to the surface before diffusing together to form N_2O_4 . It is worth noting that while Langmuir-Hinshelwood mechanisms are widely assumed to be the mechanism for heterogeneous catalysis, Emeline et al., 2005 cast doubt on the use and validity of this assumption, concluding that the Langmuir-Hinshelwood mechanism can account for experimental observations for some heterogeneous catalysis reactions but not for heterogeneous *photo*-catalysis reactions. The outputs for Models 2 and 3 (see Table 4.3 for full details of the reactions included) for the HONO concentration and $\gamma_{\text{NO}_2 \rightarrow \text{HONO}}$ as a function of NO_2 are shown in Figure 4.11; the experimental data is also shown. In order to reproduce the experimental trend of first an increase and then a decrease of both the HONO concentration and the reactive uptake coefficient with increasing initial NO_2 mixing ratio the stoichiometric relationship of 2 NO_2 molecules adsorbed to the surface and used to form one HONO was necessary (Dyson et al., 2021).

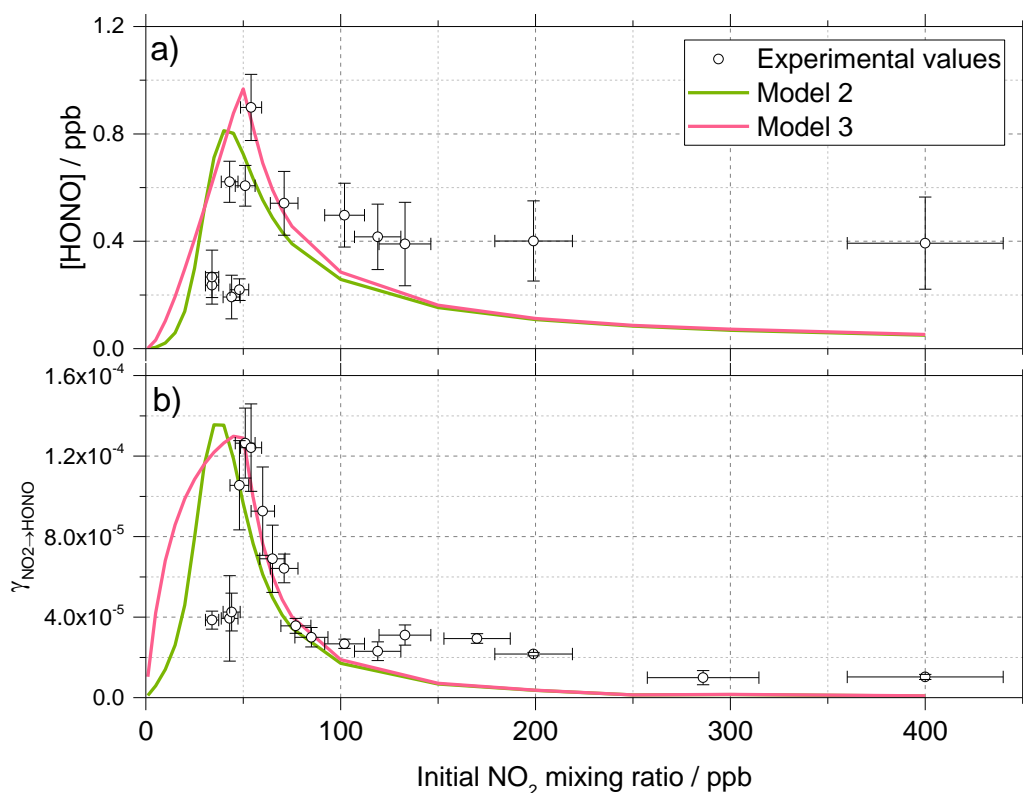
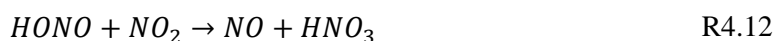
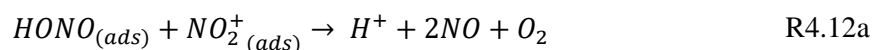


Figure 4.11. Experimental values (open circles with 1σ error bars), Model 2 (green line) and Model 3 (pink line) calculations for (a) HONO concentration after 52 s illumination and (b) NO_2 reactive uptake coefficient, $\gamma_{\text{NO}_2 \rightarrow \text{HONO}}$, as a function of the initial NO_2 mixing ratio. The mechanisms used for these model runs included a 2:1 stoichiometric relationship between the NO_2 adsorbed on the TiO_2 aerosol surface and the HONO produced, as well as additional HONO loss reactions which are dependent on NO_2 , see Table 1 for details. Models 2 and use an Eley-Rideal and Langmuir-Hinshelwood mechanisms, respectively, for the formation of the NO_2 dimer on the aerosol surface.

Previous work by Stemmler et al., 2007 into the production of HONO from humic acid aerosols showed $[\text{HONO}]$ plateauing off with increasing NO_2 mixing ratio, with the decreasing uptake coefficient, $\gamma_{\text{NO}_2 \rightarrow \text{HONO}}$, with increasing NO_2 being attributed to NO_2 fully saturating available surface sites. However, the observed decrease of $[\text{HONO}]$ at the high NO_2 mixing ratios shown in this work (Figure 4.2 and Figure 4.7) suggests that additional surface loss processes of HONO may be present. Due to the observed $[\text{HONO}]$ decreasing as a function NO_2 mixing ratio after ~ 54 ppb, the removal process most likely involves NO_2 directly:



or potentially a species made rapidly from NO₂ on the surface, such as NO₂⁺:

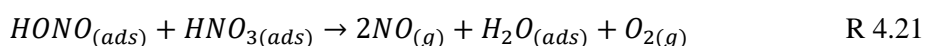


which may be present if high enough concentrations of HNO₃ are present on the surface (Syomin and Finlayson-Pitts, 2003) or following reaction with h^+_{VB} , or a product of the reaction of O_2^- (or e^-_{CB}) with NO₂ (R4.12) i.e. NO₂⁻ (Dyson et al., 2021). A study by Bedjanian and El Zein, 2012 observed the formation of NO₂ (from the oxidation of HONO) and NO (from the reduction of HONO) from the reaction of adsorbed HONO on TiO₂ surfaces in both dark and illuminated conditions proposed to be via the reaction of gas-phase and adsorbed HONO to generate NO⁺ and NO₂⁻. A later paper from the same group, assumed the presence of additional HONO surface loss pathways occurring under illumination due to the presence of e^- and h^+ (El Zein et al., 2013).

The reaction of HONO with NO₂ in the gas phase is too slow to be important for this system: Transition state theory (TST) studies of the reaction of HONO with NO₂ in the gas phase to form HNO₃ calculated a large activation energy which varied dependant on the abstraction channel: via O abstraction by HONO (159 kJ mol⁻¹) or via OH abstraction via NO₂ (~133-246 kJ mol⁻¹) (Lu et al., 2000). However, these reactions could be enhanced on the surface, especially in the presence of light. The NO₂ dependant loss reaction, $k_{R4.12}$ in Table 3, was necessary in the model to reproduce the rapid decrease in trend in [HONO] versus NO₂ seen experimentally after ~54 ppb NO₂. Without $k_{R4.12}$ the modelled [HONO] continued to increase to a plateau, as seen in Model 1 (see Figure 4.9) where no NO₂ dependant loss reactions were considered. In order to see the model results as shown in Figure 4.11 for model 2 and 3, $k_{R4.12}$ also had to be slower than the desorption of HONO from the surface, $k_{R4.9}$. Another key condition was that $k_{R4.9}$, the rate of desorption of HONO, had to be larger than $k_{R4.10}$ and $k_{R4.11}$, the adsorbed HONO loss rates, but slower than the initial adsorption rate of NO₂, $k_{R4.2}$.

Of all the loss reactions of HONO included in Models 2 and 3, the NO₂ dependent loss reaction, R4.12, had the most significant effect on the variation in modelled [HONO]. It is also possible that a secondary product, i.e. HNO₃, could remain adsorbed and therefore block active sites on the TiO₂ surface, effectively poisoning the photocatalyst and slowing the adsorption of NO₂ and formation of HONO. However,

addition of the NO₂ independent loss reactions in the model, $k_{R4.10}$ and $k_{R4.11}$ had little effect on the variation in [HONO] with increasing NO₂ mixing ratio, only having an effect on the overall [HONO], suggesting NO₂ is involved in the loss of HONO. It is likely that this effect is more than just TiO₂ surface poisoning given the short time period of the model. HNO₃, for example, has been shown to remain adsorbed to surfaces once formed (Sakamaki et al., 1983;Pitts et al., 1984;Finlayson-Pitts et al., 2003;Ramazan et al., 2004a) and may also react with adsorbed HONO, further reducing the product yield of gaseous HONO (Finlayson-Pitts et al., 2003): these NO₂ independent loss reactions may therefore become more important at higher NO₂ concentrations when surface concentrations of HONO and HNO₃ will be higher:



Particulate nitrate photolysis was not considered in Models 2 or 3, due to the lack of particulate nitrate as either an input parameter or intermediate within the models. The gas-to-particle conversion of any HNO₃ formed was not considered to be important as it was assumed that any HNO₃ formed would remain adsorbed to the aerosol surface (Sakamaki et al., 1983;Pitts et al., 1984;Finlayson-Pitts et al., 2003;Ramazan et al., 2004a).

Several conditions were required for each model to reproduce the trend in observed HONO and $\gamma_{NO_2 \rightarrow HONO}$ as a function of NO₂ mixing ratio. For Model 2 (Eley-Rideal type mechanism), in order to reproduce the experimentally observed rapid increase followed by a rapid decrease in both [HONO] and $\gamma_{NO_2 \rightarrow HONO}$ as a function of increasing NO₂ mixing ratio (Figure 4.2 and Figure 4.7), the modelled rate coefficient for the adsorption of a gas-phase NO₂ molecule to another the surface adsorbed NO₂ leading to the initial formation of the symmetric N₂O₄ dimer, $k_{R4.5}$, had to be greater than $k_{R4.6}$, the isomerisation step via *trans*-ONO-NO₂ to form HONO and HNO₃ (Dyson et al., 2021). In comparison, for Model 3 (Langmuir-Hinshelwood type mechanism), the modelled rate coefficient for the diffusion of one NO₂ molecule onto and across the surface leading to the formation of the dimer with another NO₂ molecule, $k_{R4.7}$, had to be smaller than the isomerisation step, $k_{R4.8}$, to more closely represent the experimental results for the uptake coefficient (Dyson et al., 2021). Furthermore, in order to reproduce the experimental increase in HONO formation at >54 ppb NO₂, the rate coefficient for the NO₂ dependent loss reaction, $k_{R4.12}$, had to

be larger than those for the NO₂ independent reactions, $k_{R4.10}$ and $k_{R4.11}$, leading to $k_{R4.12} = 5 \times 10^{-3} \text{ s}^{-1}$, a factor of 5 larger (justification for $k_{R4.10}$ and $k_{R4.11}$ values given in Section 4.2.1). In addition to the NO₂ independent loss reactions, the modelled [HONO] was also sensitive to the active site surface concentration. This is due to the difference in active site occupation in the two models: Model 3 required an active site surface concentration 2.5 times that of Model 2 to reproduce the peak in [HONO] at ~ 54 ppbv NO₂ observed in the experimental results owing to one active site being occupied by two NO₂ molecules as opposed to Model 3 where two active sites are occupied per HONO formed (Dyson et al., 2021). Both models reproduce the general shape of [HONO] and $\gamma_{NO_2 \rightarrow HONO}$ with increasing NO₂ mixing ratio, providing evidence that two NO₂ molecules are required to form HONO regardless of whether the mechanism is considered Langmuir Hinshelwood or Eley Rideal.

It is worth noting that the $\gamma_{NO_2 \rightarrow HONO}$ values calculated from observed HONO production on TiO₂ aerosol surfaces in this work, as detailed in Section 4.1.3, assumes a 1:1 stoichiometric relationship between NO₂ adsorbed to the aerosol surface and HONO formed. If, as proposed by the modelling studies in Section 4.2.1, the stoichiometric relationship is 2:1, the calculation of k , the pseudo-first order rate coefficient for the loss of NO₂ to produce HONO on aerosol surface, shown in Eq. 4.4 should be corrected to take this into account meaning that $\gamma_{NO_2 \rightarrow HONO}$ will be a factor of 2 smaller than the values quoted in this thesis chapter for all NO₂ concentrations. It was decided that this correction, would not be implemented in this work, in order to make the $\gamma_{NO_2 \rightarrow HONO}$ values more comparable with those measured in previous literature (Gustafsson et al., 2006; Ndour et al., 2008 Dupart et al., 2014)

4.3 HONO Production from TiO₂ and Ammonium Nitrate Aerosol Mixture

Particulate nitrate photolysis has been suggested as a light-driven source of HONO under ambient conditions during several field campaigns, with both aircraft and ground based instruments (Reed et al., 2017; Ye et al., 2017a; Ye et al., 2017b). In this work, experiments were carried out to investigate if TiO₂ could make the nitrate in ammonium nitrate chemically available for reduction to HONO. This is thought to be relevant in marine environments where the photolysis of particulate nitrate has been observed to produce HONO (Reed et al., 2017; Ye et al., 2017a; Ye et al., 2017b). Areas

such as off the coast of Asia are of particular interest for this process due to the availability of TiO₂ dust within the dust plumes which blow off the Gobi desert and the high concentrations of NO₂ from the Beijing area (Saliba et al., 2014).

Using the aerosol flow tube setup, described fully in Section 3.2, an aqueous solution of ammonium nitrate (5 g NH₄NO₃ in 500 ml milli-Q water) was used to generate nitrate aerosols using an atomiser. The relative humidity used for the pure nitrate aerosol experiments was higher than that used in the TiO₂ experiments as, unlike TiO₂ where the photocatalytic activity is negatively affected by RH above ~15 %, ammonium nitrate aerosols have a higher efflorescence point of between ~13.7-23.9 % RH, as determined by a recent Raman micro spectroscopy study (Wu et al., 2019). As such the aerosols were kept above 30 % to ensure their state was deliquesced. The residence time within the flow tube was 30 seconds (flow rate ~ 6 lpm) with the aerosols being under illumination for the entire residence time. The number of lamps used was increased from 1, used in the TiO₂/NO₂ experiments described in Section 4.1.3, to 4, thereby increasing the photon flux from $(1.63 \pm 0.09) \times 10^{16}$ to $(8.21 \pm 2.39) \times 10^{16}$ photons cm⁻² s⁻¹ and $j(\text{NO}_2)$ from $(6.43 \pm 0.30) \times 10^{-3}$ to $(3.23 \pm 0.92) \times 10^{-2}$ s⁻¹. The $j(\text{NO}_2)$, $j(\text{HONO})$ and photon flux values increased slightly more than directly proportionally between 1 and 4 lamps due to the mirrored interior of the lamp casings leading to an increase in the effective light intensity felt by the aerosols within the flow tube. The production of HONO was then measured as a function of aerosol surface area density with no gas-phase NO₂ added. Figure 4.12 shows the HONO concentration as a function of aerosol surface area density for pure ammonium nitrate aerosols compared to a 50:50 mix of nitrate/TiO₂. Although a small amount of HONO was observed at the higher aerosol loadings, no statistically significant production of HONO was seen.

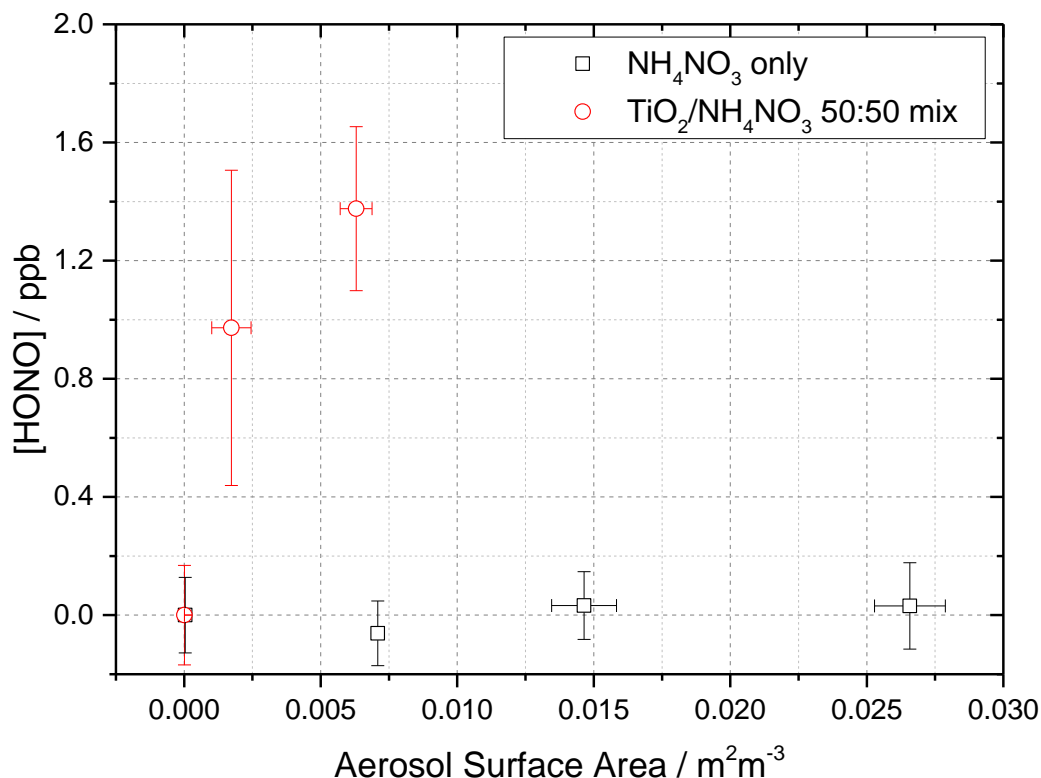


Figure 4.12. Dependence of the HONO concentration generated as a function of aerosol surface area density for pure NH_4NO_3 aerosol (black open squares, error bars represent 1σ) and 1:1 $\text{TiO}_2/\text{NH}_4\text{NO}_3$ mixed aerosol (red open circles, error bars represent 1σ). Both experiments were performed in N_2 at 295 K, an illuminated residence time of 30 s, and a lamp photon flux of $(8.29 \pm 2.39) \times 10^{16}$ photons $\text{cm}^{-2} \text{s}^{-1}$. The NH_4NO_3 only experiment was performed at $\sim 50 \pm 5$ % RH while the $\text{TiO}_2/\text{NH}_4\text{NO}_3$ mix experiment was performed at 20 ± 2 % RH. For all points, the background HONO seen observed without illumination has been subtracted. At zero aerosol surface area density there is no HONO generated from the walls of the flow tube. The variation in HONO produced for the mixed nitrate dust aerosol was thought to be due to the difficulties that arose from TiO_2 and ammonium nitrate not being completely miscible with TiO_2 tending to precipitate out of solution.

As shown in Figure 4.12, a second set of experiments was conducted with an aqueous aerosol solution of TiO_2 and ammonium nitrate in a 1:1 mass ratio (5 g NH_4NO_3 and 5 g TiO_2 in 500 ml milli-Q water) to investigate the effect of the TiO_2 , as a photo-catalyst, on the production of HONO from ammonium nitrate without the addition of gas-phase NO_2 . For this set of experiments, the RH was decreased back to ~ 20 % RH to aid the photo-catalytic activity of TiO_2 . However, it is possible the aerosols were still wet at this low RH (Wu et al., 2019). The presence of TiO_2 in the aerosol mixture lead to a significant production of HONO without the addition of NO_2 , a potentially significant result for the production of HONO in low NO_x , high dust environments

such as the oceanic regions off the coast of West Africa, e.g. Cape Verde or intercontinental regions impacted by the air masses from the Gobi desert.

4.3.1.1 Calculation of the Particulate Nitrate Photolysis Rate with and without the Presence of a Photo-catalyst

The particulate nitrate photolysis rate, $j(\text{pNO}_3)$, was calculated from the experiments with mixed nitrate/TiO₂ aerosols. An upper limit estimate (due to high scatter in data) for the experiment with single component ammonium nitrate aerosols was also made.

Using the Aerosol Inorganic Model (AIM) Clegg et al., 1998; Wexler and Clegg, 2002, the nitrate content of an aerosols at both 20 % and 50 % RH was calculated to match the experimental conditions of TiO₂/NH₄NO₃ and NH₄NO₃ respectively. The TiO₂ content was assumed to not have an effect on this amount of nitrate within the aerosol phase. From this, and the aerosol volume distribution measured by the SMPS during the experiments, the [NO₃⁻] within the aerosol phase was calculated. The production of HONO by the photolysis of particulate nitrate is given by:

$$\frac{d[\text{HONO}]}{dt} = j(\text{pNO}_3)[\text{NO}_3^-] \quad \text{Eq 4.18}$$

And hence:

$$[\text{HONO}] = j(\text{pNO}_3)[\text{NO}_3^-]t \quad \text{Eq 4.19}$$

where $j(\text{pNO}_3)$ is the photolysis rate of particulate nitrate (s⁻¹) for the lamps used in these experiments and t is the illumination time (s).

With knowledge of [HONO], [NO₃⁻] and an illumination time of 30 s, $j(\text{pNO}_3)$ was calculated from the gradient of the plot of [HONO] as a function of [NO₃⁻]. Figure 4.13 shows the dependence of [HONO] on [NO₃⁻] for mixed nitrate/TiO₂ aerosol experiment.

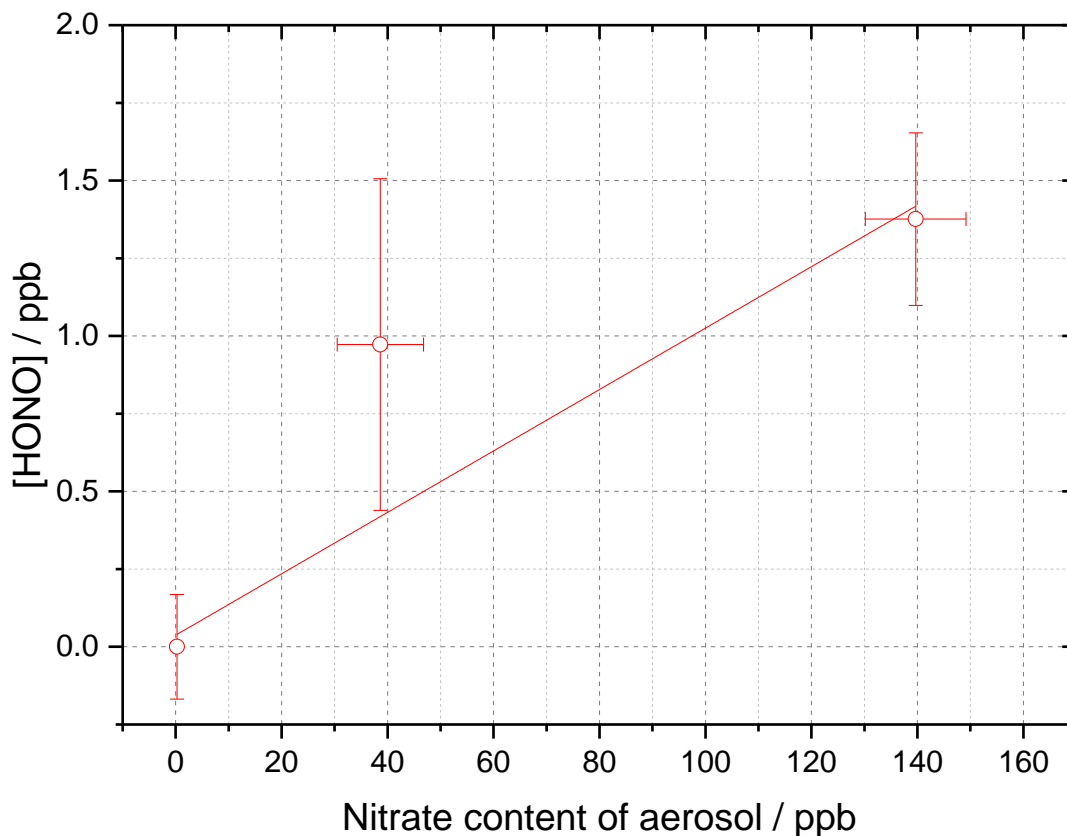


Figure 4.13. Dependence of [HONO] on the nitrate content within the aerosol phase, calculated using the AIM model for the mixed nitrate/TiO₂ experiment. From the gradient of this plot, $j(\text{pNO}_3)$ was calculated to be $(3.29 \pm 0.89) \times 10^{-4} \text{ s}^{-1}$. Experiment performed at $15 \pm 1 \%$ RH, in N₂ at 295 K with a lamp photon flux of $(8.29 \pm 2.39) \times 10^{16} \text{ photons cm}^{-2} \text{ s}^{-1}$. For all points, the background HONO seen observed without illumination has been subtracted.

For the mixed nitrate/TiO₂ experiment, the experimental particulate nitrate photolysis rate, $j(\text{pNO}_3)$, was determined to be $(3.29 \pm 0.89) \times 10^{-4} \text{ s}^{-1}$ for a photon flux of $(8.29 \pm 2.39) \times 10^{16} \text{ photons cm}^{-2} \text{ s}^{-1}$. From this experimental value, it was possible to estimate an ambient $j(\text{pNO}_3)$ typical of the tropical marine boundary layer. The ratio of the experimental $j(\text{HONO})$ for 4 lamps ($(8.35 \pm 0.18) \times 10^{-3} \text{ s}^{-1}$) and the measured $j(\text{HONO})$ from the RHaMBLe campaign ($1.2 \times 10^{-3} \text{ s}^{-1}$) held at the Cape Verde Atmospheric Observatory [May-June,2007] (Carpenter et al., 2010;Whalley et al., 2010;Reed et al., 2017) was used to normalise $j(\text{pNO}_3)$ to ambient conditions by assuming that $j(\text{pNO}_3)$ and $j(\text{HONO})$ scale in the same way. As such ambient $j(\text{pNO}_3)$ was determined from:

$$j(\text{pNO}_3)_N = j(\text{pNO}_3) \times \frac{1.2 \times 10^{-3}}{j(\text{HONO})} \quad \text{Eq 4.20}$$

where $j(\text{pNO}_3)_N$ is the photolysis rate of particulate nitrate at Cape Verde, $j(\text{pNO}_3)$ is the experimentally determined photolysis rate of particulate nitrate \rightarrow HONO and $j(\text{HONO})$ is the HONO photolysis rate coefficient calculated from the experimentally determined $j(\text{NO}_2)$ (Dyson et al., 2021), fully described in Section 3.6.

Using Eq 4.20 and $j(\text{pNO}_3) = (3.29 \pm 0.89) \times 10^{-4} \text{ s}^{-1}$, calculated from the mixed nitrate/TiO₂ experiment, the rate of HONO production from ambient particulate nitrate photolysis at Cape Verde was calculated to be $j(\text{pNO}_3)_N = (4.73 \pm 1.01) \times 10^{-5} \text{ s}^{-1}$ (Dyson et al., 2021). In comparison, for pure nitrate aerosols in the absence of TiO₂ (Figure 4.13) the data was scattered and the HONO production was small even at the highest aerosol surface area. As such, an upper limit estimate of $j(\text{pNO}_3)_N = (1.06 \pm 1.15) \times 10^{-6} \text{ s}^{-1}$ under ambient conditions at Cape Verde was made using Eq 4.20, as done for the rate of HONO production from mixed nitrate/TiO₂ aerosols. The atmospheric implications of this are discussed below.

4.3.2 Atmospheric Implications of HONO production Experiments

4.3.2.1 Production of HONO from Illuminated TiO₂-containing Aerosols in the Presence of NO₂

A maximum reactive uptake coefficient for the conversion of NO₂ to HONO on the surface of illuminated TiO₂ aerosol particles was experimentally determined to be $\gamma_{\text{NO}_2 \rightarrow \text{HONO}} = (1.26 \pm 0.17) \times 10^{-4}$ at 51 ± 5 ppb NO₂ for a photon flux from the lamp of $(1.63 \pm 0.09) \times 10^{16} \text{ photons cm}^{-2} \text{ s}^{-1}$. For the experiments with TiO₂ in the presence of NO₂, single component TiO₂ particles were used, and so for dust aerosols which comprise of 0.1-10 % TiO₂, a value of $\gamma_{\text{NO}_2 \rightarrow \text{HONO}} = (1.26 \pm 0.17) \times 10^{-5}$ is appropriate assuming a maximum of 10 % of TiO₂ and/or other photoactive materials in mineral dust (Hanisch and Crowley, 2003). This uptake coefficient value could be important for areas such as urban China: dust aerosols are transported from the Gobi desert to areas of high NO₂ and nitrate aerosols concentrations, such as Beijing where HONO production catalysed by photoactive materials in dust could be important (Saliba et al., 2014; Dyson et al., 2021). Under haze weather conditions, i.e. when $\text{PM}_{2.5} > 75 \mu\text{g m}^{-3}$, when O₃ was low and NO₂ was high, He et al., 2014 reported a full aerosol chemical composition from 5 haze episodes in the Beijing-Tianjin-Hebei regions of China in January 2013, showing that mineral dust can reach up to 10 % of

total aerosol composition. For the same campaign in Beijing it was reported that on average 12 ± 1 % of aerosol was particulate nitrate (He et al., 2014).

A production rate of HONO from the experimental results in this work was estimated for a non-haze period in summer in Beijing (AIRPRO campaign in central Beijing in May-June 2017) to investigate the effect on HONO budget that NO₂ uptake could have in urban China. The average daytime maximum values for [NO₂], $j(\text{NO}_2)$ and aerosol surface area for a non-haze (PM_{2.5} < 75 µg m⁻³) period in May-June 2018 in Beijing was 50 ppb, 1×10^{-2} s⁻¹ and 2.5×10^{-3} m² m⁻³ (a maximum of 0.3 % was assumed to be TiO₂, though this could be higher for dust impacted events (Schleicher et al., 2010) respectively. Using these values for [NO₂], $j(\text{NO}_2)$ and aerosol surface area, a production rate of HONO of 1.70×10^5 molecules cm⁻³ s⁻¹ (~24.8 ppt h⁻¹) has been estimated using $\gamma_{\text{NO}_2 \rightarrow \text{HONO}} = (1.26 \pm 0.17) \times 10^{-4}$ which was then scaled by a factor of 1.55 to account for the small difference in experimental and ambient photon flux for Beijing (Dyson et al., 2021). The scaling was necessary as the lamp used to illuminate the surface of the TiO₂ aerosols in these experiments gave rise to a $j(\text{NO}_2) = (6.43 \pm 0.3) \times 10^{-3}$ s⁻¹, a factor of 1.55 less than noontime $j(\text{NO}_2)$ measured in Beijing during AIRPRO campaign. This value is similar to the maximum production of HONO from urban humic acid aerosols in Europe reported to be 17 ppt hr⁻¹ at 20 ppb NO₂ by Stemmler et al., 2007. For comparison, the net gas phase production rate of HONO, P_{HONO} , under the same conditions, midday in Beijing summer 2018, was determined from the measured gas phase production and losses:

$$P_{\text{HONO}} = k_{\text{OH}+\text{NO}}[\text{OH}][\text{NO}] - (j(\text{HONO}) \times [\text{HONO}] + k_{\text{OH}+\text{HONO}}[\text{OH}][\text{HONO}]) \quad \text{Eq 4.21}$$

where $k_{\text{OH}+\text{NO}} = 3.3 \times 10^{-11}$ cm³ molecule⁻¹ s⁻¹ (Atkinson et al., 2004), $k_{\text{OH}+\text{HONO}} = 6 \times 10^{-12}$ cm³ molecule⁻¹ s⁻¹ (Atkinson et al., 2004) and $j(\text{HONO}) = 1 \times 10^{-2}$ s⁻¹ for an average maximum noontime OH concentration of 8×10^6 molecules cm⁻³ (Whalley et al., 2021), NO concentration of 1.45 ppb (Whalley et al., 2021) and HONO concentration of 0.8 ppb (Whalley et al., 2021).

P_{HONO} was calculated to be -3.8 ppt hr⁻¹. This net loss suggested the production of HONO from TiO₂ aerosol surfaces in the presence of NO₂ would have little effect on the overall HONO budget for summertime in Beijing due to HONO destruction being dominated by loss via photolysis at solar noon (Dyson et al., 2021).

4.3.2.2 Production of HONO from Pure Nitrate and Mixed Dust/Nitrate Aerosols without NO₂

Marine environments, for example off the coast of West Africa which is impacted by both dust aerosols from the Sahara and mixed nitrate aerosols from sea spray, could be important for particulate nitrate photolysis as a source of HONO despite the low NO₂ concentrations present (Hanisch and Crowley, 2003; Ye et al., 2017b). As described in section 4.3.1.1, from laboratory experiments into HONO production without the addition of NO₂ on mixed ammonium nitrate/TiO₂ aerosols, a particulate nitrate photolysis rate of a $j(\text{pNO}_3) = (3.29 \pm 0.89) \times 10^{-4} \text{ s}^{-1}$ was estimated. $j(\text{pNO}_3)$ was then scaled to typical ambient light levels for Cape Verde (location chosen as an example marine boundary layer environment with high concentrations of mineral dust aerosols). Using $j(\text{pNO}_3)_N$ and an average midday concentration of nitrate aerosols of 400 ppt measured at Cape Verde (Reed et al., 2017), a rate of HONO production from particulate nitrate, $P_{\text{pNO}_3 \rightarrow \text{HONO}}$, was calculated as $4.65 \times 10^5 \text{ molecule cm}^{-3} \text{ s}^{-1}$ (68 ppt hr⁻¹). This calculated $P_{\text{pNO}_3 \rightarrow \text{HONO}}$ was estimated to be ~50 times larger than with pure nitrate aerosols alone. For comparison, the missing HONO production from the RHaMBLe campaign in Cape Verde was calculated from the measured [HONO] and the known gas phase production and loss routes of HONO:

$$P_{\text{other}} = [\text{HONO}](j(\text{HONO}) + k_{\text{OH}+\text{HONO}}[\text{OH}]) - k_{\text{OH}+\text{NO}}[\text{OH}][\text{NO}] \quad \text{Eq 4.22}$$

where $k_{\text{OH}+\text{NO}} = 3.3 \times 10^{-11} \text{ cm}^3 \text{ molecule}^{-1} \text{ s}^{-1}$ (Atkinson et al., 2004), $k_{\text{OH}+\text{HONO}} = 6 \times 10^{-12} \text{ cm}^3 \text{ molecule}^{-1} \text{ s}^{-1}$ (Atkinson et al., 2004) and $j(\text{HONO}) = 2 \times 10^{-3} \text{ s}^{-1}$ for an average maximum concentrations of $1 \times 10^7 \text{ molecules cm}^{-3}$ for OH (Whalley et al., 2010), $5.41 \times 10^7 \text{ molecule cm}^{-3}$ for NO (Whalley et al., 2010) and $1.23 \times 10^8 \text{ molecule cm}^{-3}$ for HONO (Whalley et al., 2010).

The missing HONO production rate, P_{other} , for Cape Verde was calculated to be 34.6 ppt hr⁻¹ suggesting a particulate nitrate photolysis rate of 68 ppt hr⁻¹ could be significant in closing the HONO budget for this environment (Whalley et al., 2010; Reed et al., 2017; Ye et al., 2017a; Dyson et al., 2021).

4.3.3 Experimental Summary: HONO Production from Aerosol Surfaces

The production of HONO from illuminated TiO₂ aerosol surfaces in the presence of NO₂ was investigated. The reactive uptake coefficients of NO₂→HONO onto the illuminated TiO₂ aerosol surfaces were determined for NO₂ mixing ratios from 34 to 400 ppb, with a maximum $\gamma_{NO_2 \rightarrow HONO}$ value of $(1.26 \pm 0.17) \times 10^{-4}$ for single-component TiO₂ aerosols observed at 51 ppb NO₂ and for a lamp flux of $(1.63 \pm 0.02) \times 10^{16}$ photons cm⁻² s⁻¹ (integrated between 290 and 400 nm). The measured uptake coefficients varied with increasing NO₂ mixing ratio showing an increase, peaking at 51 ppb \pm 5 ppb NO₂, then subsequent decrease as a function of NO₂ mixing ratio: a dependence on NO₂ not supported by reaction of NO₂ with H₂O to give HONO and HNO₃, seen previously as a dark reaction (Syomin and Finlayson-Pitts, 2003). Kinetic box modelling studies supported a mechanism involving two NO₂ molecules per HONO molecule generated, suggesting the formation of an NO₂ dimer intermediate, the exact mechanism of which is unclear. Using previous studies we propose the process occurs via the isomerisation of the symmetric N₂O₄ dimer to give *trans*-ONO-NO₂, either via *cis*-ONO-NO₂ or directly, suggested to be more reactive with water than the symmetric dimer (Finlayson-Pitts et al., 2003; Ramazan et al., 2004b; Ramazan et al., 2006; de Jesus Madeiros and Pimentel, 2011; Liu and Goddard, 2012; Murdachaew et al., 2013; Varner et al., 2014). Using the experimentally determined uptake coefficient for HONO production from NO₂ uptake, $\gamma_{NO_2 \rightarrow HONO}$, the rate of HONO production from illuminated aerosols in Beijing in Summer 2017 for typical NO₂ mixing ratios, light levels and aerosol surface areas was found to be similar to that estimated previously for HONO production on urban humic acid aerosols in Europe, 24.8 ppt hr⁻¹ and 17ppt hr⁻¹ respectively (Stemmler et al., 2007; Dyson et al., 2021).

The relative humidity dependence of HONO production on TiO₂ surfaces with NO₂ mixing ratio was also investigated showing a peak in HONO production at approximately ~30 %. At much higher NO₂ concentrations the peak is shifted slightly to a lower RH and shows more production of HONO at all RHs. This could be due the active sites on the surface filling faster with increasing RH due to the higher number of NO₂ already adsorbed to the surface. It is also possible the higher concentration of NO₂ on the surface leads to more UV light being absorbed by the NO₂ thereby reducing effective light intensity available for the photolytic reactions that form

HONO on the surface of the aerosols. The increase in HONO production with RH can be attributed to a higher concentration of water on the surface increasing the availability for the NO₂ hydrolysis reaction until ~ 30% RH whereupon the production is observed to decrease due most likely to increased water surface concentration inhibiting the NO₂ adsorption process.

In the absence of NO₂, the production of HONO from nitrate aerosols was also investigated to determine if nitrate aerosols alone were a significant source of HONO from particulate nitrate photolysis or whether TiO₂, when added, could make the nitrate in ammonium nitrate available for HONO formation. With addition of TiO₂, significant production of HONO was seen with increasing aerosol surface area. Using experimental results, a rate of HONO production from nitrate photolysis, in the presence of TiO₂, was calculated for ambient conditions in marine environments, scaled to the ambient conditions encountered at Cape Verde Atmospheric Observatory, to be 68 ppt hr⁻¹ for the $j(\text{pNO}_3)_N$ calculated from the mixed nitrate/TiO₂ experiments. This is similar in magnitude to the missing HONO production rate calculated previously for the RHaMBLe campaign suggesting for low NO_x, high dust environments particulate nitrate photolysis could be important for the HONO budget (Ye et al., 2016a; Ye et al., 2016b; Ye et al., 2017a; Ye et al., 2017b).

In comparison, production of HONO from pure, deliquesced ammonium nitrate aerosols alone, without the addition of NO₂ or photocatalytic TiO₂, however could not be definitively confirmed for the range of conditions studied here. Future work would involve studying production of HONO from pure nitrate aerosols over a wider range of conditions with the addition of other chemical species which could promote HONO production, such as seed aerosols or halogen species typically found in marine environments.

5 Characterisation of Secondary Organic Aerosol Formation using a Potential Aerosol Mass Chamber

5.1 The Importance of SOAs

Secondary organic aerosols (SOAs) are generated from low-volatility products formed via the oxidation of volatile organic compounds (VOCs), typically monoterpenes and aromatic compounds. Once formed these low volatility products can either nucleate or partition onto existing aerosol particles. SOAs account for a large fraction of the organic matter in the troposphere with up to 90 % of the organic particulate matter in urban areas being from SOAs (Kanakidou et al., 2005; Lakey et al., 2016a). This means that they can have a significant negative effect on human health leading to respiratory and cardiovascular diseases.

There are several factors which can determine the formation of SOAs from VOC oxidation. The VOC precursor must be abundant in the atmosphere and must be reactive and therefore oxidises rapidly in order for the products to accumulate and eventually reach high concentrations in the atmosphere. And lastly, the volatility of the products must be low enough for them to either condense onto nearby particles or to homogeneously nucleate once gas phase saturation level has been reached (Donahue et al., 2011; Matthews, 2014).

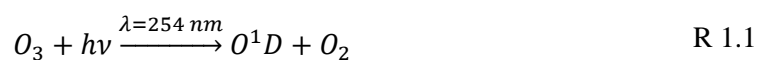
As mentioned in Section 1.1 aerosols, including SOAs, play a part in the scattering and absorption of light in the atmosphere meaning that SOAs have an important role in the global radiative balance, with atmospheric aerosols being the most uncertain aspect of climate radiative forcing (Myhre et al., 2013). Understanding the sources, atmospheric processes and chemical properties will therefore allow the impacts of SOAs on human health and climate to be more accurately predicted (Kang et al., 2007).

A large fraction of non-methane hydrocarbons are terpenes. Terpenes, such as α -pinene or limonene, are emitted from the biosphere with an estimated global emission rate of 10^{14} g yr⁻¹, ~35 % of which is α -pinene (Zhang and Zhang, 2005). As such, terpenes were chosen for study in this work due to their prevalence in the atmosphere and their ability to form high concentrations of aerosol particles via ozonolysis. The

reaction of limonene and O₃ is relatively slow, with a reaction rate of $2.13 \times 10^{-16} \text{ cm}^3 \text{ molecule}^{-1} \text{ s}^{-1}$ at 298 K, making this reaction ideal for the study of new particle formation in reaction chambers (Khamaganov and Hites, 2001b).

5.2 An Introduction to PAM Chambers as a Type of Oxidation Flow Reactor

Oxidation Flow Reactors (OFRs) are a type of environmental chamber which are used to generate higher-than-ambient oxidant concentrations typically using OH or O₃ as the oxidants formed via photolysis of H₂O, O₃ and O₂ (Peng et al., 2019; Peng and Jimenez, 2020). In recent years, the use of OFRs for the study of VOC oxidation and SOA formation has grown. A Potential Aerosol Mass (PAM) chamber is an OFR used to study the maximum aerosol mass that can be generated from oxidation of precursor VOCs allowing the investigation of SOA processes in a controlled environment. Both the precursor and the oxidant, most commonly OH or O₃ in much higher concentrations than those found atmospherically, are added into the reactor and allowed to react to produce low volatility products which partition into the aerosol phase (Kang et al., 2007). These aerosols can then be characterised using a Mass Spectrometer or a Scanning Mobility Particle Sizer (SMPS). Oxidation flow reactors, of which a PAM chamber is an example, use light at either 254 nm (“OFR254”) or both 185 and 254 nm (“OFR185”). OFR254 requires the addition of O₃, externally produced to the PAM chamber, due to the lamps inside the chamber being encased in quartz tubes, meaning only 254 nm photons are available. The O₃ introduced into the chamber can then be photolysed at 254 nm to give OH (Peng and Jimenez, 2020).



In OFR185 system, Teflon tubes encase the lamps inside the chamber so both 184 and 254 nm photons are available meaning that OH is formed through the H₂O vapour photolysis (some OH is lost to the walls if the 185 nm is external to the PAM chamber however OH will still be present in the chamber) and O₃ is formed through O₂ photolysis (Peng et al., 2015):





Laboratory studies using oxidation flow reactors, such as PAM chambers, are essential in providing information on the chemical and physical properties of SOA, as well as allowing SOA yields from different biogenic and anthropogenic VOCs to be studied. From such studies it has been shown that SOA yield depends on the VOC:NO_x ratio (Ng et al., 2007;Loza et al., 2014), the volatility and concentration of the VOC precursor (Presto and Donahue, 2006), exposure time ([OH]*t*) of the oxidant (Lambe et al., 2012;Lambe et al., 2015) and the presence of seed particles which can be used to promote condensation of volatile species into the aerosol phase (Lambe et al., 2015). Larger batch-style environmental chambers have long residence times of several hours and lower oxidant concentrations (i.e. 10⁶-10⁷ molecule cm⁻³ OH) and are designed to specifically simulate the timescale of SOA formation in the atmosphere (Lambe et al., 2015). The concept of a PAM chamber was first introduced by Kang et al.,2007 as a method of simulating atmospheric photo-oxidation at much faster time scales of a few minutes, with OH concentrations up to ~ 10⁹ molecule cm⁻³ (Kang et al., 2007;Lambe et al., 2015). This study also reported negligible wall loss effects, a big advantage over traditional environmental chambers (Kang et al., 2007).

A recent study (Kang et al., 2018) into photochemical ageing using a PAM chamber showed through High Resolution Time of Flight Aerosol Mass Spectrometry (HR-ToF-AMS) that the H:C and O:C ratios within the chamber were in close agreement with those generated ambiently despite the much higher oxidant levels, estimated to be 7 × 10¹¹ molecules cm⁻³ s, within the chamber as compared to ambient levels. This confirmed the applicability of the PAM chamber for use in field studies on the observation of aging processes of aerosols including emissions and long range transported air masses (Kang et al., 2018). In addition to laboratory studies, SOA formation has also been studied with ambient air (Ortega et al., 2016;Palm et al., 2017), as well as more recent studies on SOA production from vehicle exhaust (Pieber et al., 2018;Zhao et al., 2018).

To our knowledge the only study which investigated the uptake of HO₂ onto SOA formed from a PAM chamber was done by the Leeds group in 2016 (Lakey et al.,

2016a). In this study the first measurements for HO₂ uptake onto SOA particles were reported to be $\gamma < 0.001$ for α -pinene and $\gamma = 0.004 \pm 0.002$ for 1,3,5-trimethylbenzene (TMB). The lower uptake coefficient for α -pinene was postulated to be due to the higher viscosity of α -pinene compared to TMB and the differing water content of the aerosols, or potentially due to HO₂ + RO₂ reactions occurring within the aerosol particles (Lakey et al., 2016a). Additionally, Lakey et al., 2016 reported a FAGE interference with NO on in the cell and the mercury lamp off for TMB proposing this may be due to an RO₂ species present/formed in the aerosol flow tube.

5.3 Monoterpene Oxidation by Ozone

Secondary Organic Aerosols (SOAs) are formed through the oxidation of volatile organic compounds (VOCs). Monoterpene ozonolysis begins with the cycloaddition of ozone into the C=C double bond forming a primary ozonide. The primary ozonide formed from α -pinene, the reaction of α -pinene + O₃ being one of the main SOA forming reactions in the atmosphere (Iyer et al., 2021), decomposes into two isomeric energized Criegee intermediates (CIs). Studies suggest ~60-90 % of CI undergoes unimolecular H-shift followed by O₂ addition leading to the formation of vinyl hydroperoxides (VHP) which then release OH radicals which lead to the production of RO₂ radicals (C₁₀H₁₅O₄^{*}). C₁₀H₁₅O₄^{*} can then initiate a cascade of RO₂ autoxidation reactions and bimolecular reactions, the products of which have varied levels of functionality and volatilities and are therefore in both gas phase and particle phase. Due to the complexity of the α -pinene ozonolysis system, RO₂ autoxidation and the competing bimolecular reactions is not fully understood (Zhao et al., 2021). An example of this mechanism is given for α -pinene below:

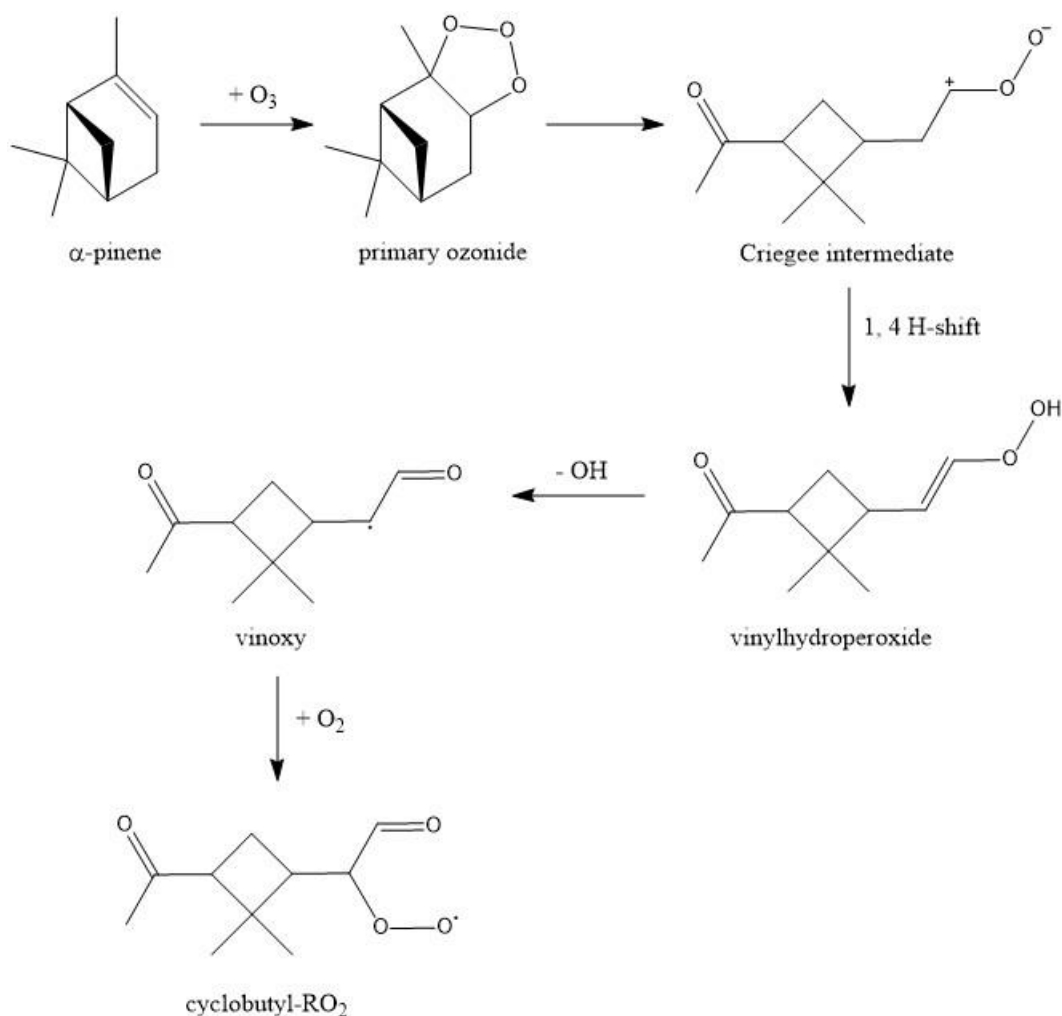


Figure 5.1. First steps in the ozonolysis of α -pinene. The addition of ozone across the double bond of α -pinene creates a primary ozonide which breaks apart to a Criegee intermediate (CI). The Criegee intermediate can then undergo a 1,4 H-shift to form a vinyl hydroperoxide (VHP). VHP can then rapidly lose an OH radical to form the vinyloxy radical (radical centre indicated by the black dot) which forms an RO_2 radical when O_2 is present. Figure reproduced from Iyer et al., 2021.

Out of the estimated mean annual biogenic VOC emissions (760 Tg yr^{-1}), $\sim 70\%$ is isoprene and $\sim 11\%$ are monoterpenes (Sindelarova et al., 2014). α -pinene, an alkene released biogenically by coniferous trees, is the most commonly studied biogenic monoterpene due to its global importance as an SOA precursor, making up $\sim 34\%$ of total monoterpene emission (Sindelarova et al., 2014; Iyer et al., 2021). While α -pinene is the most abundant monoterpene, limonene has been suggested to comprise of up to 20% of total monoterpene emissions due to its use in household cleaning products in addition to biogenic emissions (Gong et al., 2018).

α -pinene, in its liquid state, is more viscous than limonene, 1.293 mPa s and 0.923 mPa s respectively for 298.15 K (Weast and Astle, 1983;Comelli et al., 2002). Lakey et al., 2016a measured smaller uptake coefficients for HO₂ onto α -pinene derived SOA compared to TMB derived SOA due potentially to the larger viscosity of α -pinene making the diffusion of HO₂ into the bulk of the aerosol the rate limiting step. Champion et al., 2019 measured the viscosity of limonene SOA to be 3.1 mPa s at 30°C. The viscosity of α -pinene aerosols, in comparison, was estimated to be ~100 Pa s by Abramson et al., 2013. Limonene has 2 double bonds meaning two possible reaction sites with O₃ and/or OH. This and the lower viscosity suggested that limonene would more readily form SOA.

In this chapter the PAM chamber is characterised for the generation of SOA from α -pinene and limonene and the aerosol number and surface area size distributions of α -pinene and limonene-derived SOA are reported under different O₃ and VOC concentrations.

5.4 Characterising α -pinene-derived Secondary Organic Aerosols Using an SMPS

Given that α -pinene is the most common monoterpene and the uptake of HO₂ onto α -pinene has been previously studied at the Paul Scherer Institute in Switzerland by Lakey et al., 2016a, α -pinene SOA was the obvious starting point for initial characterisation of the newly built Leeds PAM chamber, system fully described in Section 2.4. The effect of changing the initial α -pinene concentration on the aerosol number and size distributions was investigated, and the particle number, surface area and volume size distributions for 4.5, 9, 22 and 44 ppm initial α -pinene concentration with 8 ppm O₃ are shown in Figure 5.2. It is worth noting that the sheath flow of the SMPS was kept at 3 lpm, a setting which allowed the DMA to measure particles of diameters between ~10 and 700 nm. As such all size distributions in this chapter will be in this range. For TSI Instruments DMA Model 3068, the maximum range of diameters that can be measured is 1-1000 nm depending on the configuration of the DMA.

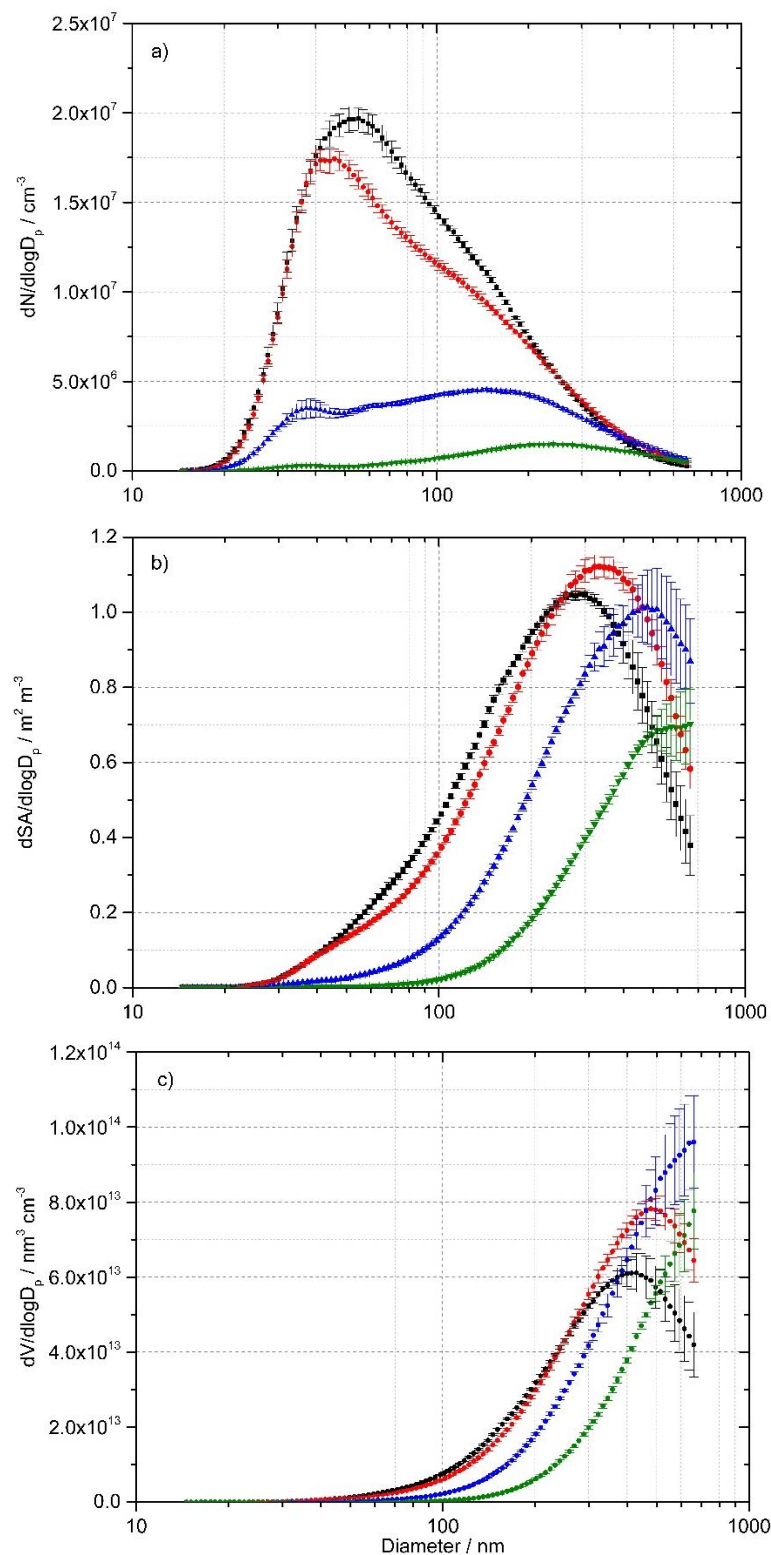


Figure 5.2. a) average particle number size distributions (cm^{-3}), b) average aerosol surface area size distributions ($\text{m}^2 \text{m}^{-3}$) and c) average volume size distribution ($\text{nm}^3 \text{cm}^{-3}$) of α -pinene-derived SOAs averaged over 5-10 runs for each initial α -pinene concentration of 4.5 ppm (green), 9 ppm (blue), 22 ppb (red) and 44 ppm (black) for an ozone concentration of 8 ppm. Experiment done in air. Temperature = 24 ± 2 °C, Pressure = 760 Torr.

As is shown in Figure 5.2, the PAM chamber was able to produce constant (i.e. little variation in particle number or aerosol surface area for a given diameter over multiple runs for the same O₃ and α -pinene concentrations) size distributions over a range of initial α -pinene concentrations. With increasing concentration of α -pinene added, from 4.5 to 44 ppm, total aerosol particle number increased from $(1.13 \pm 0.006) \times 10^6 \text{ cm}^{-3}$ to $(1.44 \pm 0.005) \times 10^7 \text{ cm}^{-3}$, while the total aerosol surface area increased from $(2.88 \pm 0.03) \times 10^{-1} \text{ m}^2 \text{ m}^{-3}$ to $(7.67 \pm 0.05) \times 10^{-1} \text{ m}^2 \text{ m}^{-3}$. With increasing oxidant concentration, SOAs generated from alkene ozonolysis are observed to become more functionalised, as evidenced by an increase in oxidation, thereby increasing in size until fragmentation supersedes and higher volatility products will fragment, evidenced by a decrease in aerosol mass, and partition out of the aerosol phase. As the α -pinene is increased in Figure 5.2 to an excess of 5.5 times the O₃ concentration, the functionalisation and growth of aerosols accordingly is less prevalent due to less effective O₃ concentration (Lambe et al., 2012; Lambe et al., 2015; Tu et al., 2016; Bianchi et al., 2019). As such the size distributions shift to smaller particles. Interestingly the bimodal shape of the particle number size distribution changed with increasing α -pinene initial concentration from the second mode being larger to the first mode being larger indicating a change in size/composition of the aerosols. Kang et al., 2007 reported an increase in SOA yield as a function of O₃ from the ozonolysis of α -pinene, with aerosol mass increasing with additional O₃ until a stable maximum value of SOA yield was reached.

The PAM chamber was able to create reproducible SOA surface area size and number distributions over different experimental days provided the conditions were the same, validating the PAM chamber for use in HO₂ uptake experiments. Figure 5.3 shows the aerosol number, surface area and volume size distributions over 2 different experimental days for the same initial α -pinene and O₃ concentration.

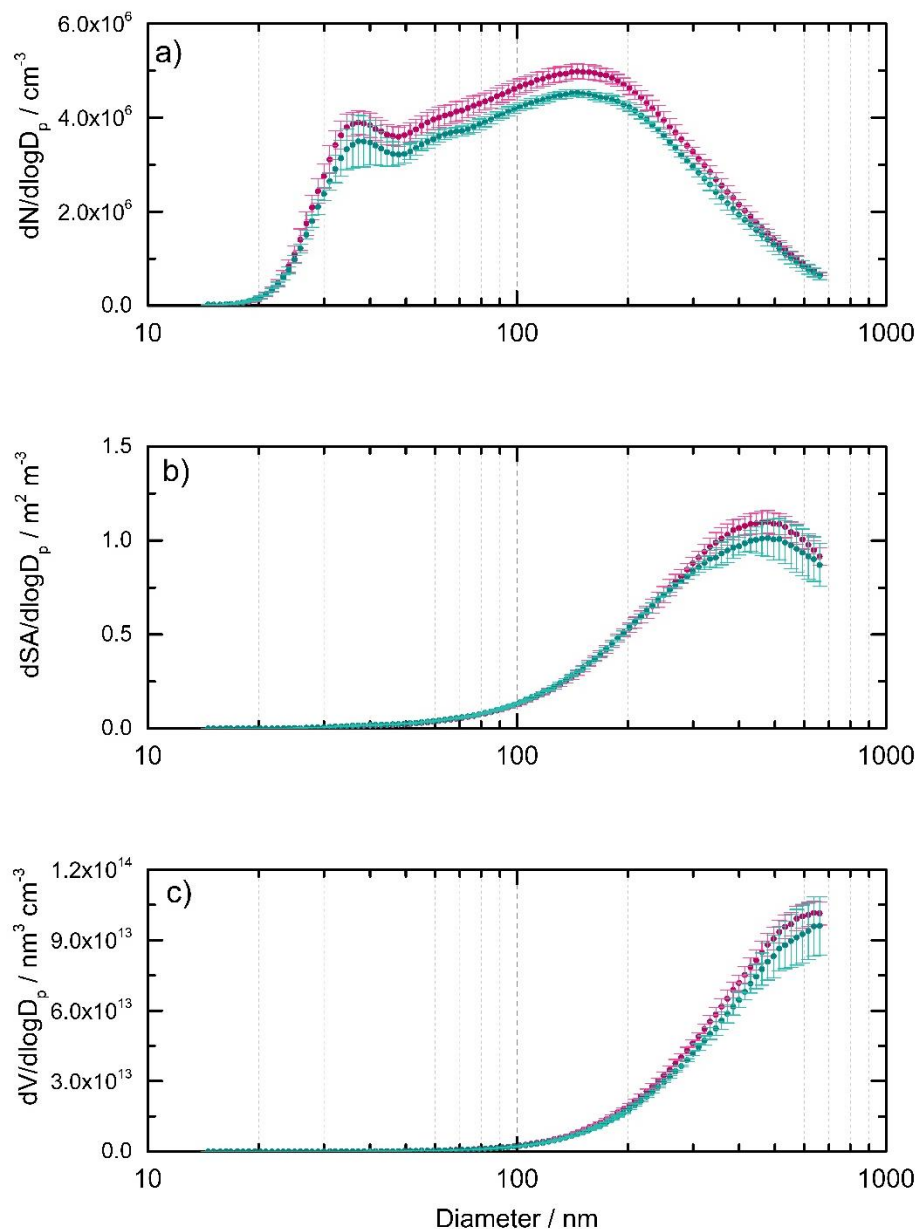


Figure 5.3. a) average particle number size distributions (cm^{-3}), b) average aerosol surface area size distributions ($\text{m}^2 \text{m}^{-3}$) and c) volume size distribution ($\text{nm}^3 \text{cm}^{-3}$) on 2 different experimental days (purple circles represent day 1 and green circles represent day 2), averaged over 5-10 runs, showing that reproducible size distributions can be generated using the PAM chamber. Initial α -pinene concentration = 9 ppm, O_3 concentration = 8 ppm. Total particle number was $(5.07 \pm 0.02) \times 10^6 \text{ cm}^{-3}$ and $(4.58 \pm 0.03) \times 10^6 \text{ cm}^{-3}$, for day 1 (pink) and day 2 (turquoise) respectively. Total aerosol surface area was $(5.94 \pm 0.04) \times 10^{-1} \text{ m}^2 \text{m}^{-3}$ and $(5.68 \pm 0.06) \times 10^{-1} \text{ m}^2 \text{m}^{-3}$, for day 1 (purple) and day 2 (green) respectively. All experimental conditions kept the same. Temperature = $24 \pm 2 \text{ }^\circ\text{C}$, Pressure = 760 Torr. Errors shown are 1σ .

5.5 Characterising Limonene-derived Secondary Organic Aerosols Using an SMPS

5.5.1 SOA Formed from the Reaction of Limonene With Ozone

As discussed in Section 5.3, due to the viscosity of α -pinene, Lakey et al., 2016 measured a low uptake coefficient of HO₂ onto α -pinene, i.e. < 0.001 . Limonene has a lower viscosity, is commonly used in household cleaning products and therefore is important to consider for indoor air quality, and has 2 double bonds making it more reactive with O₃. As such the PAM chamber was characterised for the formation of limonene-derived SOAs through both ozonolysis and OH-initiated chemistry.

5.5.1.1 Effect of Changing O₃ and Limonene Concentration on the Size Distribution of Limonene-derived SOA

Figure 5.4 shows the effect on the aerosol particle number (cm⁻³), surface area (m² m⁻³) and volume (nm³ cm⁻³) size distributions of changing the O₃ concentrations while keeping the limonene concentration constant.

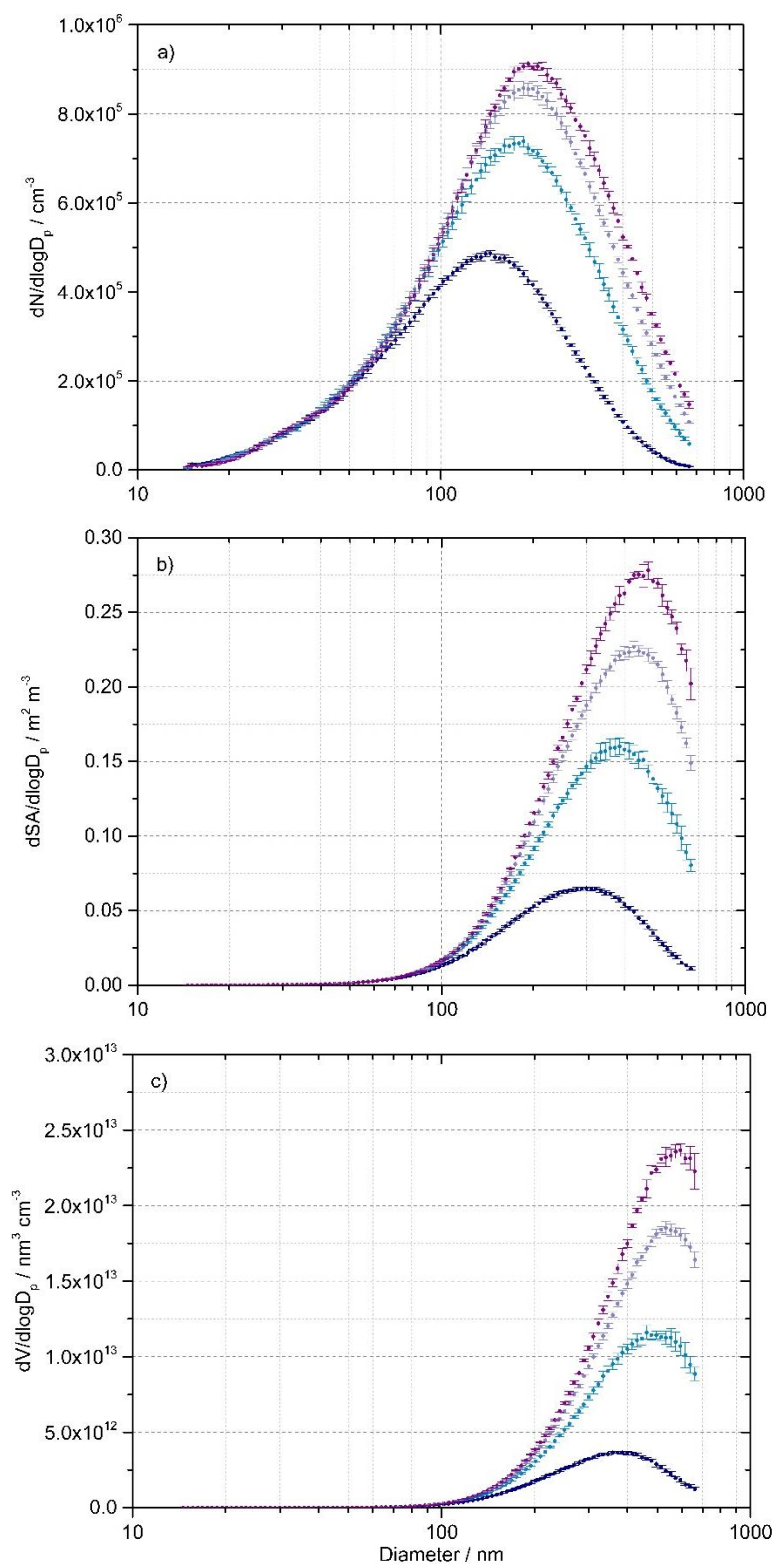


Figure 5.4. a) average particle number size distributions (cm^{-3}), b) average aerosol surface area size distributions ($\text{m}^2 \text{m}^{-3}$) and c) volume size distribution ($\text{nm}^3 \text{cm}^{-3}$) of limonene-derived SOAs, averaged over 5-10 SMPS runs, for fixed initial limonene concentrations of 1.7 ppm, ozone concentrations of 0.5 ppm (dark blue), 1.35 ppm (light blue), 2.21 ppm (light purple) and 2.85 ppm (purple). $\text{RH} = 14 \pm 4\%$, pressure = 760 Torr, temperature = $24 \pm 2^\circ\text{C}$. Errors represent 1σ .

From Figure 5.4, it can be seen that increasing the ozone concentration while keeping limonene concentration constant shifts the mode diameter of the number, surface area and volume size distributions to higher diameters. The particle number also increases for a given diameter showing more aerosols are created with an increase in ozone concentration. This is to be expected as increasing the ozone concentration from below the concentration of limonene (0.5 and 1.35 ppm), i.e. limonene was fixed at 1.7 ppm, to greater than the concentration of limonene (2.21 and 2.85 ppm) and therefore increasing the oxidation capacity of the system would result in an increased number of oxidation products in both gas and particle phases. As more O₃ was introduced to the system the size distributions shifted towards larger diameters, possibly due to coagulation (higher concentrations of aerosols leading to increased collisions of aerosols within the same volume (Ramabhadran et al., 1976)) in addition to functionalisation leading to the formation of larger more oxidised aerosols (Lambe et al., 2012; Tu et al., 2016)

As shown in Figure 5.5, varying the limonene concentration with a fixed O₃ concentration increases the number, and therefore the surface area of the SOA produced as expected, however, unlike when the O₃ concentration is increased for fixed limonene concentration, the mode diameter of the size distributions does not significantly change as seen with α -pinene. This suggests the shift in mode diameter to larger aerosols with increasing O₃ but fixed limonene is due to functionalisation as opposed to coagulation alone.

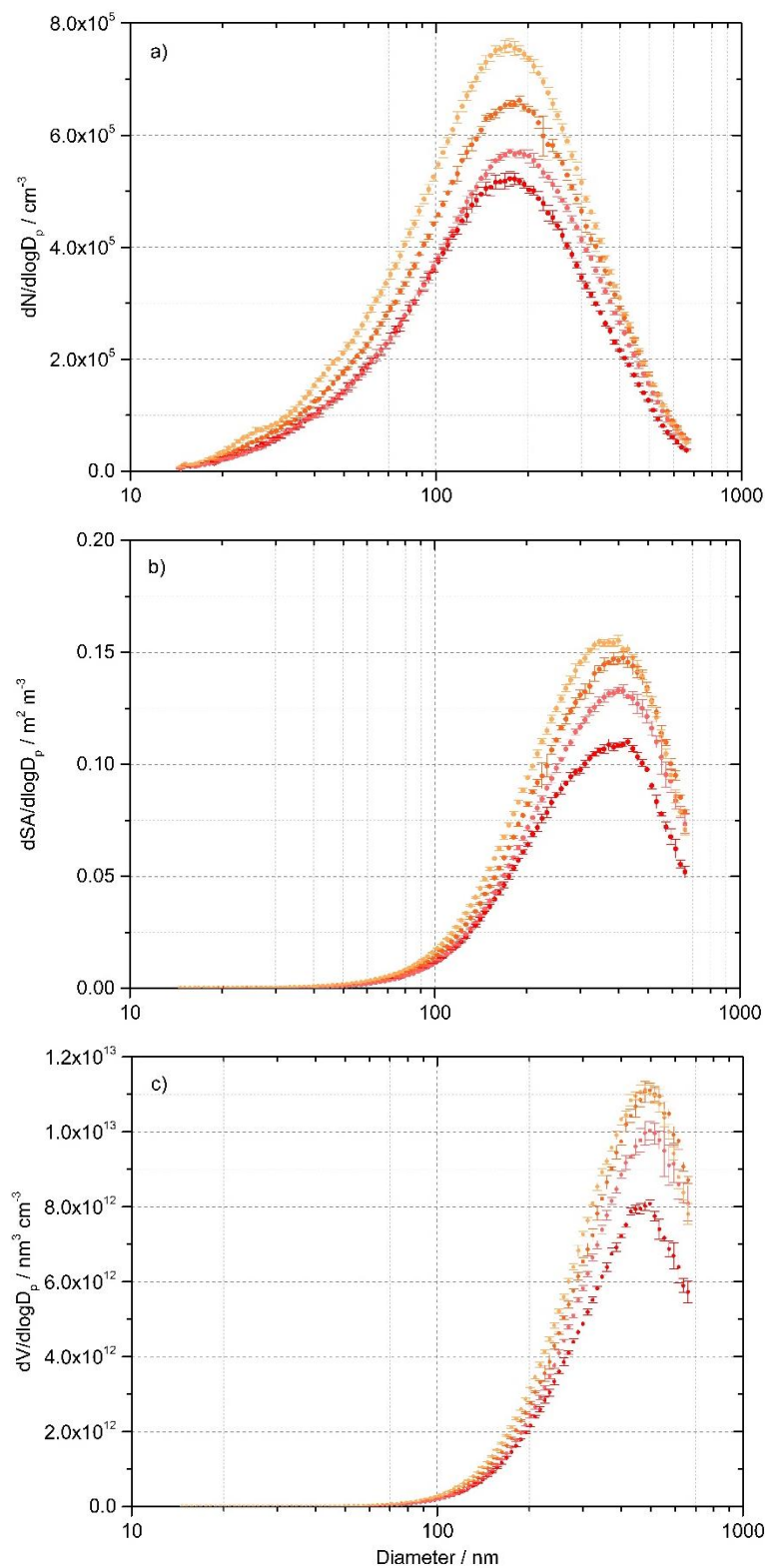


Figure 5.5. a) average particle number size distributions (cm^{-3}), b) average aerosol surface area size distributions ($\text{m}^2 \text{m}^{-3}$) and c) volume size distributions ($\text{nm}^3 \text{cm}^{-3}$) of limonene-derived SOAs, averaged over 5-10 SMPS runs, for fixed O_3 limonene concentrations of 1.35 ppm, initial limonene concentrations of 0.43 ppm (red), 0.86 ppm (pink), 1.71 ppm (orange) and 3.85 ppm (yellow). RH = 14 ± 4 % RH, pressure = 760 Torr, temperature = 24 ± 2 °C, flow rate = 4 lpm. Errors represent 1σ .

5.5.2 SOA Formed from the Reaction of Limonene and the OH radical

While O₃ is generally thought to be the most important indoor oxidant due to lack of sunlight to form OH and limonene is a common indoor pollutant due to its prevalence in household cleaning products, limonene is also biogenically emitted (Carslaw et al., 2017; Carslaw and Weschler, 2018) making limonene an important atmospheric pollutant. As such the production of SOAs via OH-initiated reactions with limonene was also investigated.

5.5.2.1 Effect of Changing OH and Limonene Concentration on the Size Distributions of Limonene-derived SOA

To generate a high concentration of OH within the PAM chamber for OH-initiated SOA formation, both 185 nm and 254 nm lamps are required. First the 185 nm lamp generates O₃ externally to the PAM chamber which is then photolysed at 254 nm to give O(¹D) atoms which subsequently react with water vapour to form OH within the PAM chamber. As such the O₃ concentration can be varied by varying the external 185 nm lamp current. However, this had no effect on the number or surface area of the aerosols produced (for 5-20 mA range) indicating the limiting condition for OH production was the 254 nm lamp intensity i.e. the SOA formation was dominated by OH initiated oxidation of limonene.

As with increasing O₃ concentration for limonene ozonolysis characterisation experiments, shown in Figure 5.4, it was expected that increasing the number of 254 nm lamps and thereby increasing the overall OH concentration, would lead to an increase in SOA production. However, due to insufficient cooling of the 254 nm lights within the chamber (described fully in Section 2.4), an increase in the number of lights coupled with an increase in time with the lights on as the experiment progressed, led to the PAM chamber increasing from room temperature, 24 °C, to 60 °C. The internal and external temperature of the PAM chamber was measured using a thermocouple (RS Pro Type K). For OH-initiated chemistry in the future, the design of the PAM chamber with regards to lamp cooling should be optimised. It is worth noting that while the O₃ concentrations within the system were measured with the O₃ box, at present the system is not set up to measure the OH concentration.

Figure 5.6 shows the effect on the particle number (cm⁻³), aerosol surface area (m² m⁻³) and volume (nm³ cm⁻³) size distributions when the number of 254 nm lamps in the chamber is increased, and therefore the OH concentration is assumed to increase,

for a fixed limonene concentration of 1.71 ppm and a fixed O₃ concentration of 1.35 ppm.

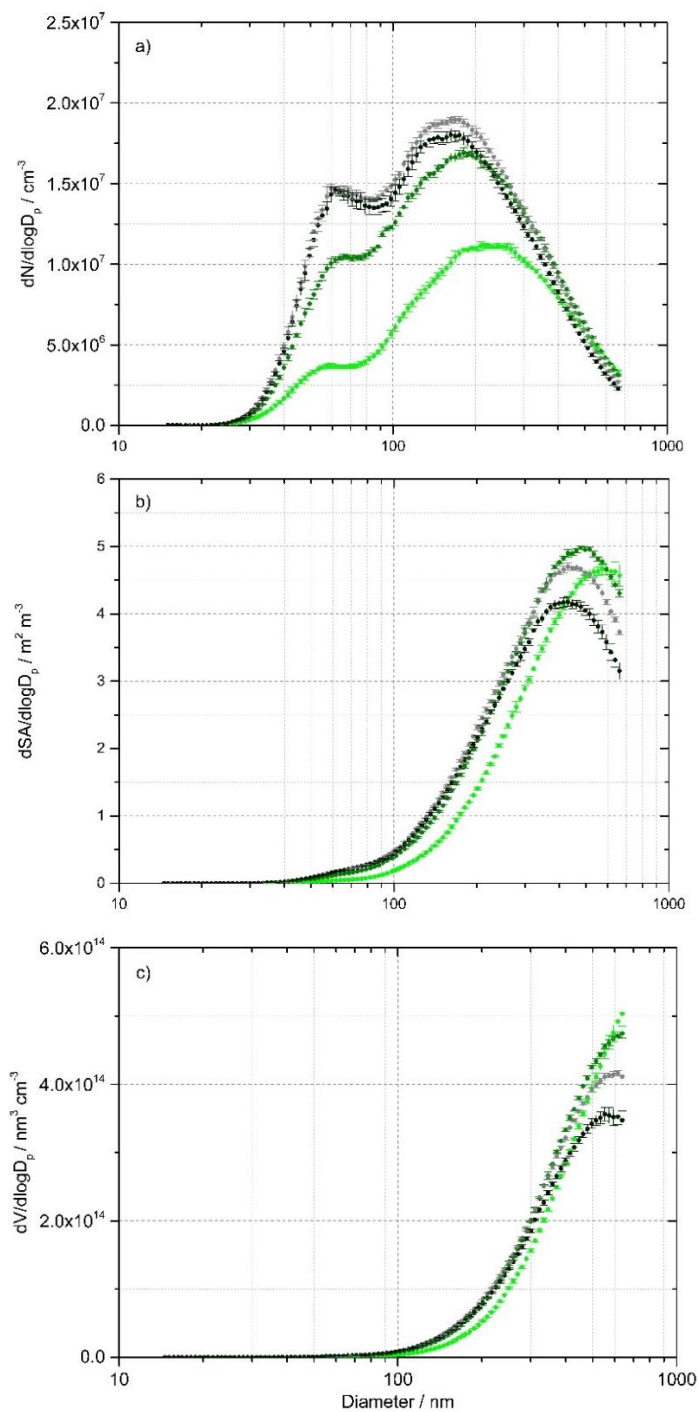


Figure 5.6. a) average particle number size distributions (cm^{-3}), b) average aerosol surface area size distributions ($\text{m}^2 \text{m}^{-3}$) and c) volume size distribution ($\text{nm}^3 \text{cm}^{-3}$) of OH-initiated limonene-derived SOAs, averaged over 5-10 SMPS runs, for fixed initial limonene concentration of 1.71 ppm, with one 254 nm lamp (light green), two lamps (dark green), three lamps (grey) and four lamps (black). O₃ concentration = 1.35 ppm, RH = 14 ± 4 %. Temperature of the chamber increased from 24 ± 2 °C to 60 ± 5 °C during the experiment. Pressure = 760 Torr, flow rate = 4 lpm. Errors represent 1σ .

In comparison to the SOA derived from limonene ozonolysis, the particle number size distribution for OH-initiated limonene derived aerosols is bimodal. This might be the result of self-nucleation of first versus second generation products of OH+limonene reaction (Yu et al., 2011). The reaction of OH and limonene occurs much faster than limonene and ozone (Khamaganov and Hites, 2001a; Braure et al., 2014) and therefore first and second generation products are produced in the gas phase. Though first generation products form much faster, second generation products are less volatile and therefore are more likely to partition into the aerosol phase via self-nucleation forming smaller nuclei (Ng et al., 2006; Yu et al., 2011). Ng et al., 2006 found that for compounds with 2 double bonds, such as limonene, second generation products contribute substantially to SOA growth. Due to the reaction of limonene and ozone being slower in comparison, the majority of SOA produced could be formed by partitioning of first generation products leading to a uni-modal size distribution.

The particle number increased by a factor of ~ 1.6 from $(0.86 \pm 0.02) \times 10^7 \text{ cm}^{-3}$ to $(1.40 \pm 0.1) \times 10^7 \text{ cm}^{-3}$ when the number of 254 nm lamps inside the PAM chamber was increased from 1 to 2 for fixed O_3 and limonene concentrations; average particle number and surface area values (for between $\sim 10 - 700 \text{ nm}$ as measured and summed by the SMPS) for 1-4 lamps are tabulated in Table 5.1. When the number of lamps was increased from 2 to 3 and then to 4, the particle number was the same within error suggesting that above 2 lamps either, the O_3 concentration was limiting and would need to be increased for further OH to be produced, or this was the effect of increasing internal PAM chamber temperature.

Number of 254 nm lamps	Average particle number / 10^7 cm^{-3}	Average aerosol surface area / $\text{m}^2 \text{ m}^{-3}$
1	(0.86 ± 0.02)	(2.04 ± 0.03)
2	(1.40 ± 0.10)	(2.51 ± 0.01)
3	(1.62 ± 0.17)	(2.52 ± 0.02)
4	(1.53 ± 0.30)	(2.29 ± 0.03)

Table 5.1. Average total particle number (cm^{-3}) and average total aerosol surface area ($\text{m}^2 \text{ m}^{-3}$) for increasing the number of 254 nm lamps inside the PAM chamber with O_3 concentration fixed at 1.35 ppm. $\text{RH} = 14 \pm 4 \%$. It is worth noting that the size distributions measured were truncated at $\sim 700 \text{ nm}$ and so these total particle number and surface areas, more importantly for surface area, are underestimated due to the maximum particle size the SMPS can measure with the current DMA.

A shift to lower mode diameter, i.e. an increase in the number of smaller aerosols, with increasing lamps can be seen in Figure 5.6, most obviously for the increase in 1 to 2 lamps, which is the opposite of what was seen by increasing the O_3 concentration in limonene ozonolysis characterisation experiments. The rate constant for the addition of OH over the double bond of limonene is faster than with O_3 and therefore initial reaction occurs more rapidly, giving more time for increased functionalisation, $k_{\text{lim}+\text{OH}} = 1.45 \times 10^{-10} \text{ cm}^3 \text{ molecules}^{-1} \text{ s}^{-1}$ (Braure et al., 2014) versus $k_{\text{lim}+\text{O}_3} = 2.12 \times 10^{-16} \text{ cm}^3 \text{ molecules}^{-1} \text{ s}^{-1}$ (Khamaganov and Hites, 2001a). Highly oxygenated molecules (HOMs) and a subset of HOMs known as Extremely Low Volatility Compounds (ELVOC) are formed from the oxidation of alkenes and are vital in new particle formation and the life cycle of SOA. HOMs can condense into the particle phase. Mutzel et al., 2015 proposed that condensed HOMs can then either remain in the condensed phase without structural change, can undergo fragmentation reactions leading to shorter chain carbonyls or they can form larger, more oxidised species. The processes could occur simultaneously meaning that HOMs could undergo further condensed phase reactions and impact the overall composition of SOA (Bianchi et al., 2019). Lambe et al., 2012 observed an increase in SOA yield followed by a decreased with increasing OH exposure, with the decrease in SOA yield correlating with an increase in oxygen content and a decrease in carbon content suggesting fragmentation as opposed to functionalisation takes place at high OH exposure. Lambe et al., 2012 reported yields in SOA as a function of O/C ratio from

the reactions of OH and alkenes showing a competition between condensation, functionalisation (i.e. oxygen addition) and fragmentation (i.e. carbon loss). At low OH exposures addition of oxygen to alkenes produces low vapour pressure, gas phase species which can easily partition to form SOA. Continued exposure to OH and therefore increased functionalisation leads to fragmentation to form more volatile species which will less readily condense into the aerosol phase (Lambe et al., 2012;Chen et al., 2013)

A shift in mode diameter of aerosol number and surface could therefore be due to increasing functionalisation of SOA leading to fragmentation processes reducing the number of larger aerosols. There could also be a heat effect due to the increase in temperature over the experiment as the lamps heated the chamber from room temperature to ~ 60 °C due to insufficient cooling. The increase in temperature will reduce the partitioning of volatile species from the gas to particle phase thereby slowing the growth of aerosols or causing the evaporation of material from larger aerosols leading to smaller aerosols (Pankow, 1987).

Unlike with limonene ozonolysis characterisation experiments (shown in Figure 5.5), when OH concentrations were fixed (two 254 nm lamps) and the limonene concentration was varied, the size distributions changed significantly. For the SOA derived from ozonolysis of limonene, an increase in limonene with fixed oxidant resulted in an increase in SOA but no change in size distribution. The particle number (cm^{-3}), aerosol surface area ($\text{m}^2 \text{m}^{-3}$) and volume ($\text{nm}^3 \text{cm}^{-3}$) size distributions when limonene concentration was varied while keeping OH concentration constant is shown in Figure 5.7.

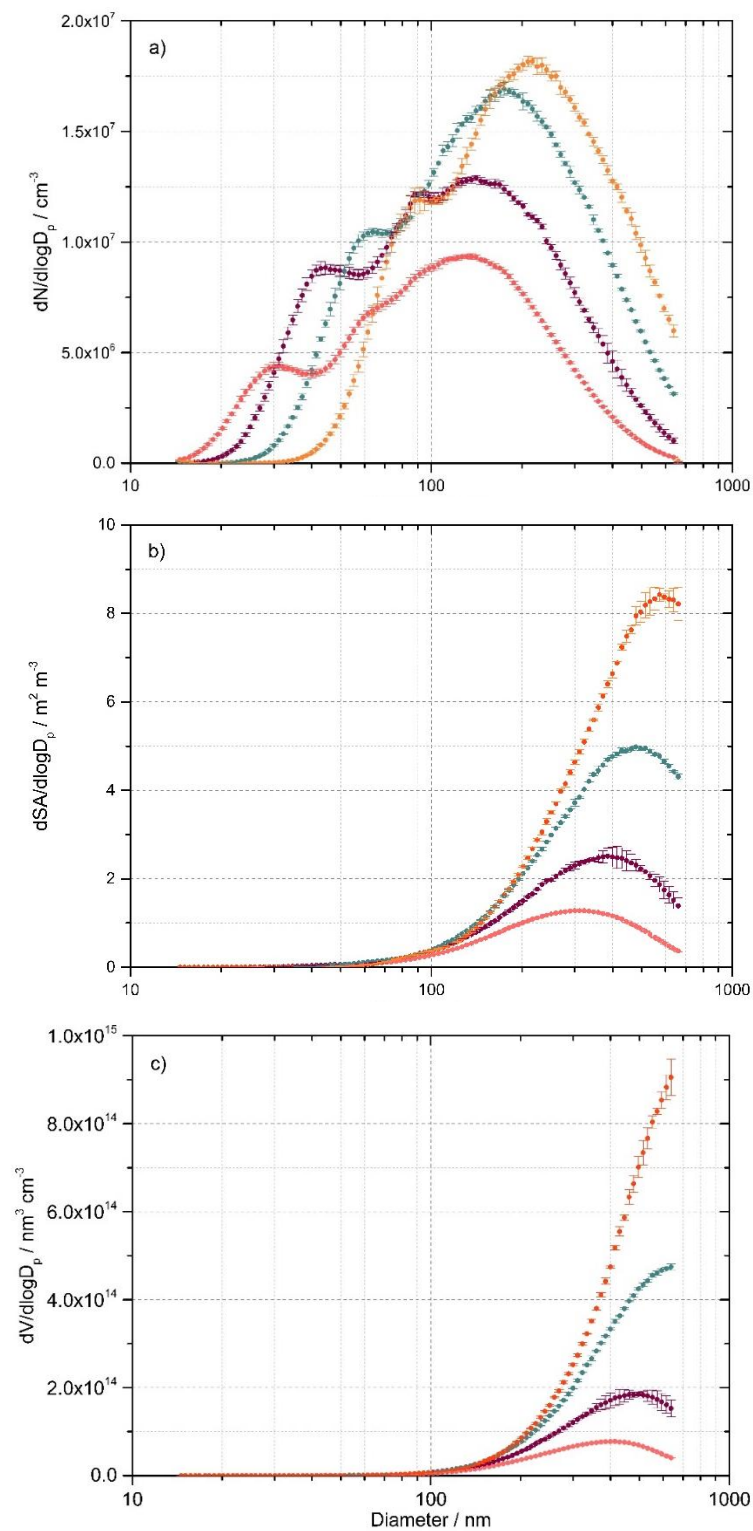


Figure 5.7. a) average particle number size distributions (cm^{-3}), b) average aerosol surface area size distributions ($\text{m}^2 \text{m}^{-3}$) and c) volume size distributions ($\text{nm}^3 \text{cm}^{-3}$) of OH-initiated limonene-derived SOAs, averaged over 5-10 SMPS runs, for two 254 nm lamps, with 0.43 ppm (pink), 0.86 ppm (purple), 1.71 ppm (blue) and 3.85 ppm (orange) initial limonene concentration. $\text{RH} = 14 \pm 4 \%$ RH. Pressure = 760 Torr, temperature of PAM chamber = $60 \pm 5 \text{ }^\circ\text{C}$, flow rate = 4 lpm. Errors represent 1σ .

Due to coalescence and aggregation, as increased concentrations of limonene were added to the chamber while keeping the oxidant the same, the number of larger aerosol particles created increased. Interestingly the particle number size distributions at 0.43 and 0.86 ppm limonene were tri-modal but for 1.71 and 3.85 ppm the size distributions become bi-modal. However, the number size distributions were bi-modal at 1.71 ppm at 1,2,3 and 4 lamps, shown in Figure 5.6 suggesting the change in modality may be due to the increase in chamber temperature throughout the day.

5.6 Summary

A potential aerosol mass chamber was built and characterised for the production of secondary organic aerosols from α -pinene and limonene by reaction with both O_3 and OH. Stable reproducible SOA aerosol surface areas were produced, validating the PAM chamber for use in HO_2 uptake experiments on SOA surfaces.

The chamber was first characterised for α -pinene derived SOAs produced by ozonolysis with stable, bi-modal number size distributions observed. Due to the viscosity of α -pinene and the difficulties in measuring uptake of HO_2 onto α -pinene surfaces encountered by Lakey et al., 2016, limonene-derived SOAs were then investigated.

A comparison of aerosol number, surface area and volume size distributions for OH-initiated and O_3 -initiated limonene-derived SOAs are shown in Figure 5.8.

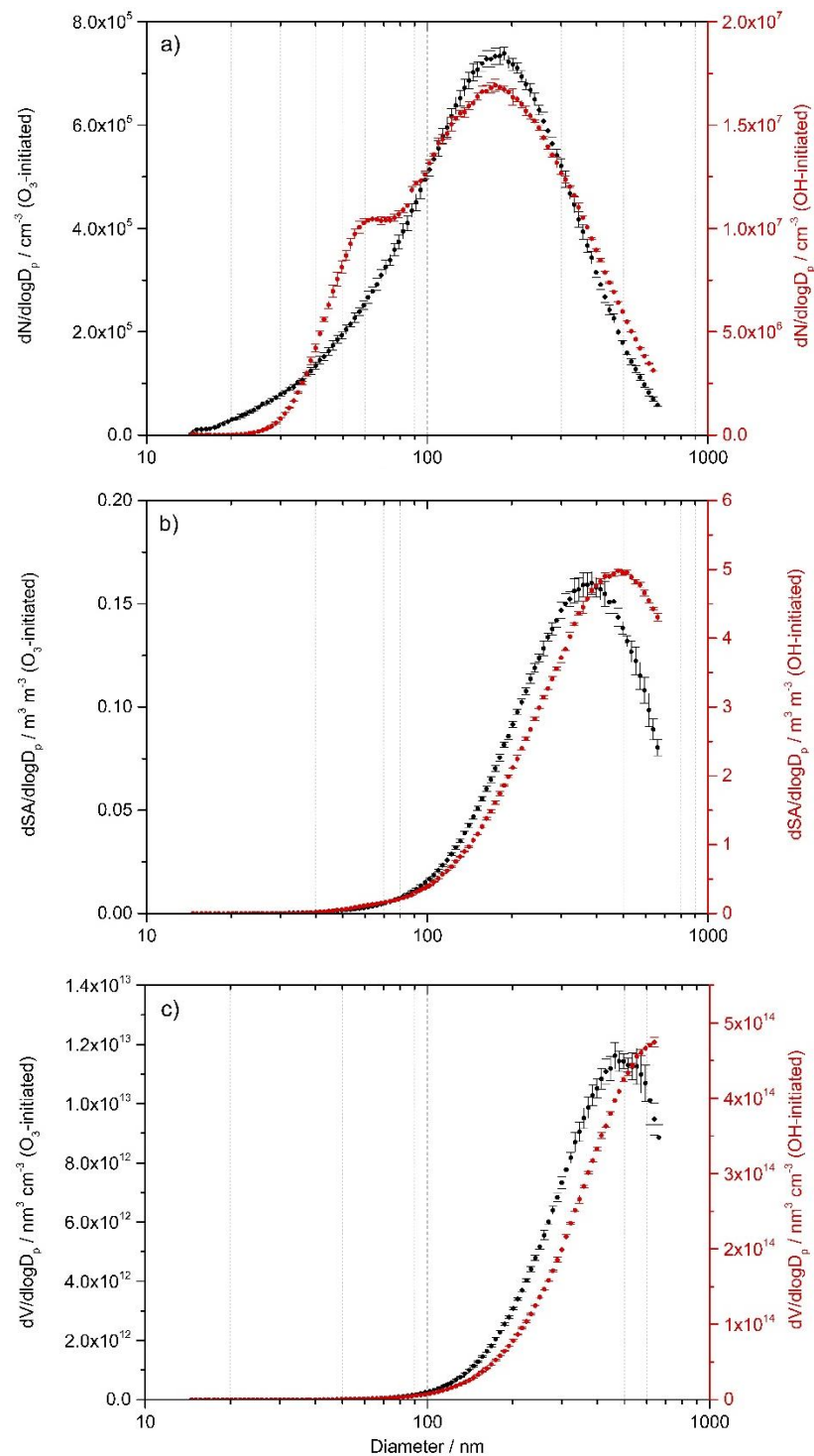


Figure 5.8. Comparison of a) particle number size distribution (cm^{-3}), b) aerosol surface area size distributions ($\text{m}^2 \text{m}^{-3}$) and c) volume size distributions ($\text{nm}^3 \text{cm}^{-3}$) for O_3 -initiated (black circles, left axis) and OH-initiated (red circles, right axis) limonene SOA formation. Limonene concentration = 1.71 ppm, O_3 concentration = 1.35 ppm. $\text{RH} = 14 \pm 4\%$. Note the right axes for particle number and surface area are 1 and 2 orders of magnitude larger than the respective left axes due to more aerosols in the case of OH initiated oxidation. Errors shown are 1σ .

SOA formed from the ozonolysis of limonene were observed to be bi-modal, with total number, surface area and volume increasing with increasing limonene added to the system. SOA formed from OH-initiated chemistry, however, was observed to be either bi- or tri- modal. For the same O₃ and limonene concentration, shown in Figure 5.8, a factor of ~29 more aerosol particles were produced with OH-initiated chemistry ($1.40 \times 10^7 \text{ cm}^{-3}$) compared to O₃-initiated chemistry ($4.87 \times 10^5 \text{ cm}^{-3}$). Due to the difficulties with keeping the PAM chamber cool when the OH-generating lamps are on, future work would involve modifying the cooling system of the lamps or mounting the lamps external to the chamber in order to stop temperature of chamber increasing throughout the day which could lead to changes in physical characteristics (i.e. number and size) of SOA generated.

6 Measurements of HO₂ Uptake Coefficient onto Secondary Organic Aerosols Generated using A Potential Aerosol Mass Chamber

HO₂ uptake coefficients were measured for the first time onto secondary organic aerosols by Lakey et al., 2016a who observed the uptake of HO₂ onto α -pinene and tri-methyl benzene derived SOAs using a PAM chamber and smog chamber in combination at the Paul Scherrer Institute in Switzerland. This chapter aims to build on these experiments by investigating the uptake of HO₂ onto limonene derived SOAs, formed by ozonolysis using a PAM chamber constructed at the University of Leeds. The uptake coefficient onto limonene derived SOA is expected to be higher compared to α -pinene derived SOA due to the lower viscosity of limonene derived SOA as well as the presence of an additional double bond in the precursor molecule (Clará et al., 2009).

6.1 Measurements of HO₂ Uptake Coefficient onto Secondary Organic Aerosols

6.1.1 Validating HO₂ Uptake Apparatus

To validate the HO₂ uptake set-up, described fully in Section 2, the uptake of HO₂ onto aqueous ammonium sulphate (AS) aerosols was measured and compared to previous measurements done by George et al., 2013. Ammonium sulphate aerosols were generated using an atomiser (set-up fully described in section 3.3.3) from a mixture of 5g (NH₄)₂SO₄ (Fisher Scientific, Analysis grade) in 500 mL milli-Q water. The HO₂ signal was observed to decrease, as expected, with increasing injector distance both with and without aerosols present. HO₂ signal decreased faster with aerosols present due to loss to walls plus loss to aerosols in the flow tube. An example HO₂ signal decay with injector distance is shown in Figure 6.1.

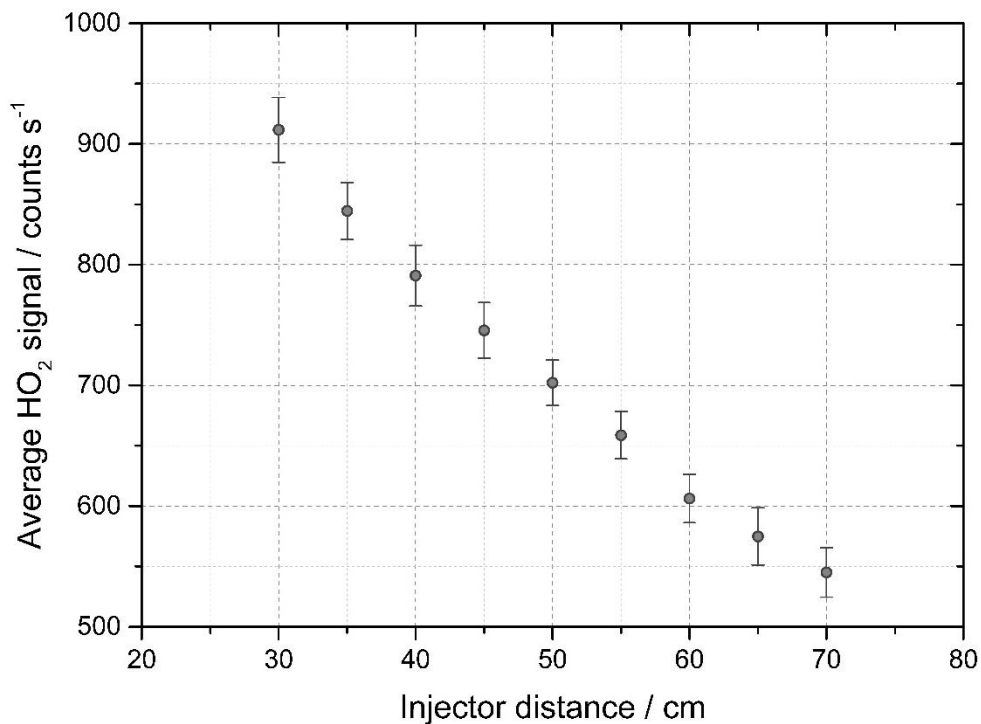


Figure 6.1. HO₂ signal decay with injector distance, k_{wall} , due to loss to the surface of (NH₄)₂SO₄ aerosols in the flow tube. Aerosol surface area = $0.006 \pm 0.0002 \text{ m}^2 \text{ m}^{-3}$. By plotting $\ln \text{HO}_2$ vs t (calculated from injector distance and flow rate), a k_{obs} value of 0.11 s^{-1} can be calculated.

Figure 6.2 shows an example of the first order rate coefficients measured as a function of aerosol surface area / $\text{m}^2 \text{ m}^{-3}$ for (NH₄)₂SO₄ at 65 and 73 % RH. The uptake coefficients of HO₂ measured for 65 and 73 % RH were 0.037 ± 0.008 and 0.010 ± 0.002 respectively, in agreement with values measured previously by George et al., 2013.

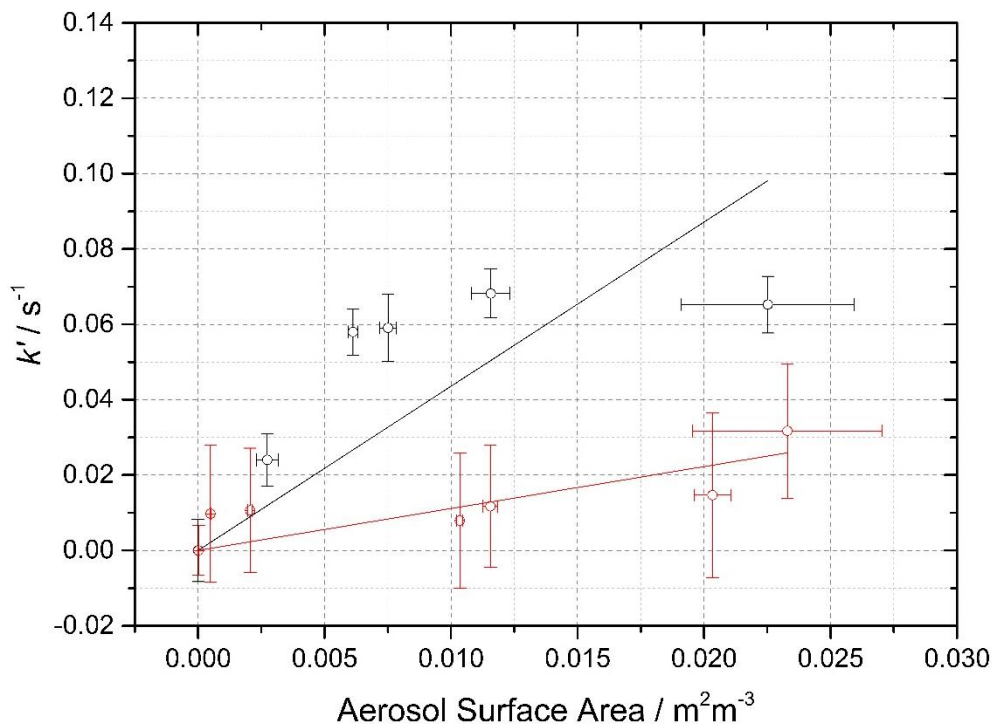


Figure 6.2. First order rate coefficient, k' (s^{-1}) following Brown correction, as a function of aerosol surface area (m^2m^{-3}) for $(NH_4)_2SO_4$ aerosols at 65 % RH (red circles) and 73 % RH (black circles). Error bars represent 1σ . Gradients give γ_{HO_2} of 0.037 ± 0.008 for 65 % RH and 0.010 ± 0.002 for 73 % RH.

Table 6.1 summarises the uptake coefficients measured for $(NH_4)_2SO_4$ previously. Taketani et al., 2008 observed higher values of γ_{HO_2} compared to both this work and George et al., 2013. This is most likely due to the higher initial concentration of HO_2 in this work compared to Taketani et al., 2008. It is also possible that transition metals could have been a contaminant during Taketani et al., 2008 experiments which would increase the γ_{HO_2} significantly. As detailed in Section 1.10.3, George et al., 2013 observed larger γ_{HO_2} at lower HO_2 concentrations on aqueous $(NH_4)_2SO_4$ aerosols. Usually it would be expected that the uptake coefficient would be higher for a higher RH (Taketani et al., 2008; George et al., 2013): this is not observed for the 65 and 73 % RH experiments in this work, due most likely to the increased HO_2 initial concentration for the 65 % RH experiment increasing the γ_{HO_2} . Some studies have shown however that an increase in water content can have a detrimental effect on uptake of HO_2 (Remorov et al., 2002).

Relative humidity / %	[HO ₂] _{initial} / molecule cm ⁻³	Uptake coefficient	Reference
20 (dry)	~10 ⁸	0.04 ± 0.02	Taketani et al., 2008
45 (dry)	~10 ⁸	0.05 ± 0.02	Taketani et al., 2008
21-54 (dry)	1 × 10 ⁹	< 0.004	George et al., 2013
45 (aqueous)	~10 ⁸	0.11 ± 0.03	Taketani et al., 2008
55 (aqueous)	~10 ⁸	0.15 ± 0.03	Taketani et al., 2008
65 (aqueous)	~10 ⁸	0.17 ± 0.04	Taketani et al., 2008
75 (aqueous)	~10 ⁸	0.19 ± 0.04	Taketani et al., 2008
42 (aqueous)	5 × 10 ¹⁰	~ 0.1	Thornton and Abbatt, 2005
55 (aqueous)	1 × 10 ⁹	0.003 ± 0.005	George et al., 2013
65-75 (aqueous)	1 × 10 ⁹	0.01 ± 0.01	George et al., 2013
65	5.6 × 10 ⁹	0.037 ± 0.008	This work
73	3.1 × 10 ⁹	0.010 ± 0.002	This work

Table 6.1. Comparison of uptake coefficients of HO₂ measured on dry and aqueous (NH₄)₂SO₄ salt aerosols at 293 ± 2 K.

6.1.2 Uptake of HO₂ onto Limonene-derived Secondary Organic Aerosols

As detailed in Section 5, the production of limonene derived secondary organic aerosols (SOA) using a PAM chamber was characterised. Importantly for this experiment, two charcoal denuders were placed in series after the PAM chamber to remove any gas phase limonene and ozone. In contrast to the ammonium salt HO₂ uptake experiment, where a clear decrease in the HO₂ signal was observed as the injector was moved away from the FAGE cell, for the experiments using SOA derived from limonene ozonolysis, the FAGE signal was observed to *increase* with increasing injector distance. This increase in FAGE signal suggests that the interaction between HO₂ and/or OH from the injector and the SOA or any gas phase species present leads to a net production of HO₂ or potentially net production of an RO₂ species that is

detectable by FAGE. Figure 6.3 shows the experimental signal of HO₂ for wall loss decay and ‘decay’ in the presence of SOA.

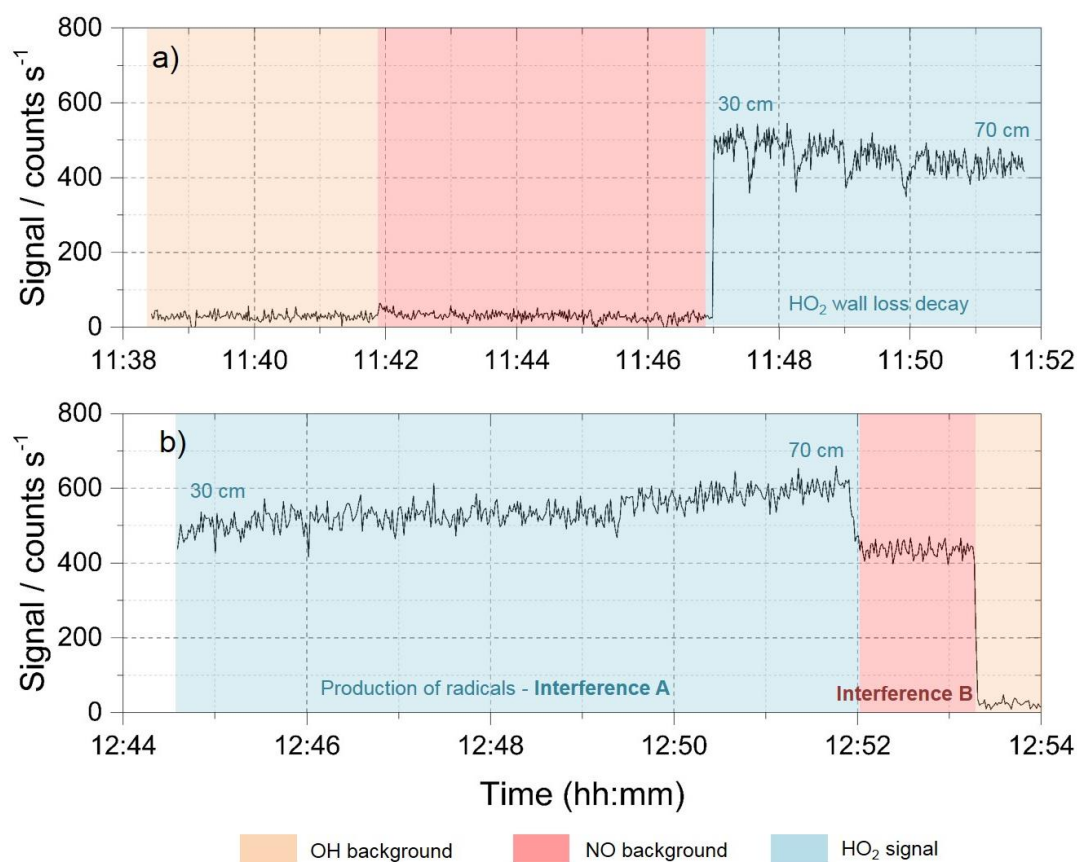


Figure 6.3. Comparison of FAGE signals with and without aerosols present. a) shows the HO₂ decay signal as injector is pulled back from 30 -70 cm due to wall loss (blue). b) shows the equivalent with the presence of limonene-derived secondary organic aerosols formed via ozonolysis. Shaded orange regions show the OH background signal when NO flow and HO₂ injector lamp is off. Any signal here is dark counts and laser scatter from 308 nm laser. Shaded red regions show the NO background when HO₂ injector lamp is off but NO flow is on at 50 sccm. This is the signal from any interfering species in the NO gas cylinder, potentially HONO. Ideally this should be as close to OH background as possible. Blue shaded region shows the laser online signal with NO flow and HO₂ generation on. The slight dips in signal when the injector is moved are assumed to be due to a small quantity of lab air (and therefore trace amounts of NO) being introduced via the injector inlet and decreasing the HO₂ concentration within the flow tube.

As seen in Figure 6.3a, in the absence of aerosols, the experiment proceeds as expected. The OH background (injector lamp on, NO flow off) is low, with little difference between the OH and NO background counts. The NO background is taken with the NO flow on at 50 sccm and the injector lamp off. Any signal during this background is due to contaminants from the NO lines or the NO cylinder. Ideally this

should be close/ the same as the OH background. On addition of HO₂ from the injector, the HO₂ signal decayed as the injector was pulled back from 30 to 70 cm and HO₂ leaving the injector tip had increased time to be lost to the walls of the flow tube (Figure 6.3a, blue shaded region). The same result was expected with SOA present, as seen with (NH₄)₂SO₄ aerosols (example in Figure 6.1), namely that k_{obs} was expected to be larger i.e. $k_{wall} < k_{aerosol}$. This was not the case however. As seen in Figure 6.3b (blue shaded region), when the injector was pulled away from the FAGE cell, and the residence time of HO₂ in the flow tube therefore increased, the signal actually increased in counts suggesting a production of HO₂ or production of RO₂ which acts as a HO₂ interference in FAGE: this signal is hereafter referred to as **interference A**.

In addition to this, when the injector lamp was turned off but with NO still flowing in the FAGE fluorescence cell, i.e. no HO₂ coming out of the injector, a signal of ~400 counts (12:50-12:53) was present, being independent of injector distance. This signal was only present when aerosols were present in the flow tube and when NO was added to the FAGE cell. When only VOC was flowed into the system, i.e. no O₃ was present in the system so reaction of limonene to produce SOA could not happen, this signal was not present. Hereafter the signal seen when HO₂ injector lamp is off but NO flow is on will be referred to as **interference B**.

6.1.2.1 Characterising the Interference Signal

The interference signals were investigated to determine the source of the interference. First it was important to check that no OH was present in the system as a bi-product of water vapour photolysis production of HO₂ in the injector. A net production of HO₂ in the flow tube would be possible if OH was leaving the injector tip, i.e. was not being lost to the walls of the injector, and therefore would have more time to react with any VOC or RO₂ eventually leading through reaction with species in the flow tube to the formation of HO₂ or an RO₂ which is detected by FAGE as the injector was pulled back from the cell. The reaction of OH and RO₂ is a relatively new field, with this loss reaction of RO₂ being especially important in remote environments when NO_x does not dominate radical loss. Assaf et al., 2016 studied the reaction between CH₃O₂ and OH using a laser photolysis cell, measuring a rate constant of $(1.60 \pm 0.4) \times 10^{-10} \text{ cm}^3 \text{ s}^{-1}$. The reaction of CH₃O₂ and OH has been shown to be fast and important in the removal of CH₃O₂ radicals in the remote boundary layer (Assaf

et al., 2017). Fittschen et al., 2019 presented experimental and modelling evidence for ROOOH as a product of the reaction of RO₂ and OH reaction.

If any OH is leaving the injector tip it will be rapidly lost either through reaction or to the walls. By moving the injector closer to the FAGE cell, any OH leaving the tip has less time to be lost and therefore can be measured. When the injector tip is too close to the FAGE inlet, signal is observed to drop due to lack of mixing time due to the injector gas flow being perpendicular to the flow tube gas flow and therefore the pinhole (Lakey et al., 2016). Figure 6.4 shows average signal / counts s⁻¹ as the injector was moved closer to the FAGE cell with no NO flowing (i.e. no HO₂ detection) and injector lamp on.

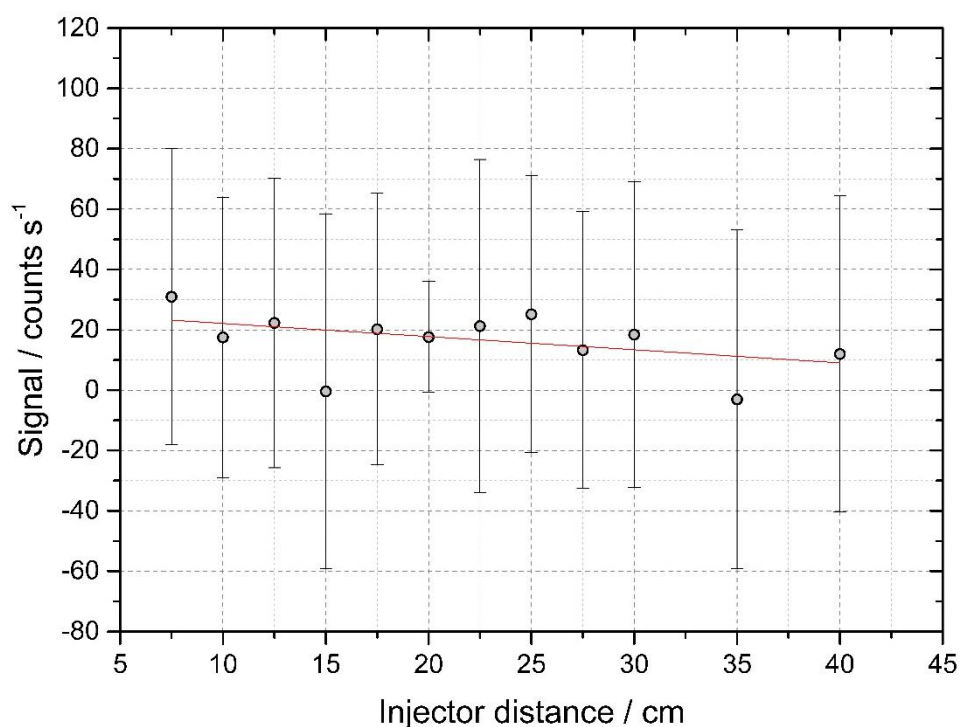


Figure 6.4. FAGE OH signal (counts s⁻¹) at different injector positions (cm). No NO was present for this experiment but the injector lamp was on and as such OH but not HO₂ was measured by the FAGE cell. Error bars represent 1 σ .

It was concluded that a small concentration of OH formed in the injector through the photolysis of water vapour was exiting the injector and therefore was present in the flow tube. This suggested the production of radicals seen when SOA or VOC were present was due to OH-initiated reactions with increased time for OH + limonene or OH + RO₂ reactions in the flow tube to give HO₂ leading to an increase in signal (interference A) as the injector was pulled back from the detection cell.

Following this, it was important to check that limonene was fully removed by the charcoal denuders placed in-line after the PAM chamber to ascertain if the production of radicals could be caused by the reaction of limonene + OH from the injector. This was achieved by removing the two charcoal denuders from the flow after the PAM chamber thereby allowing limonene to enter the flow tube: this was done without O₃ present, so there was no SOA formation. As can be seen in Figure 6.5 (condition 2), without a denuder in place and with the injector lamp on and NO added to the FAGE cell, the FAGE signal approximately doubled (to ~ 700 counts) from the equivalent HO₂ signal without VOC added to the flow (~400 counts) (condition 1). This is the production of HO₂ and RO₂ from the reaction of limonene and OH. Interference A is seen without the denuder present further suggesting the interference is due to the reaction of limonene + OH. Without the denuders in place RO₂ + OH could also be a cause of interference A. However, with the denuders in place, gas phase RO₂ would be expected to be lost to the large surface area of charcoal within the denuders. The inclusion of one denuder reduces the FAGE signal back to ~ 400 counts (condition 3), showing that limonene was mostly removed by the denuder. However, interference A is still seen when the injector is pulled back suggesting that trace amounts of limonene was still present after the denuders. Interference B however, was not present for conditions 1, 2 or 3 suggesting that limonene does not directly cause interference B. It is clear, however, that the presence of limonene when the injector lamp is on does lead to the production of radicals i.e. interference A. It is worth noting however, that this is only a hypothesis as the concentration of limonene was not measured directly.

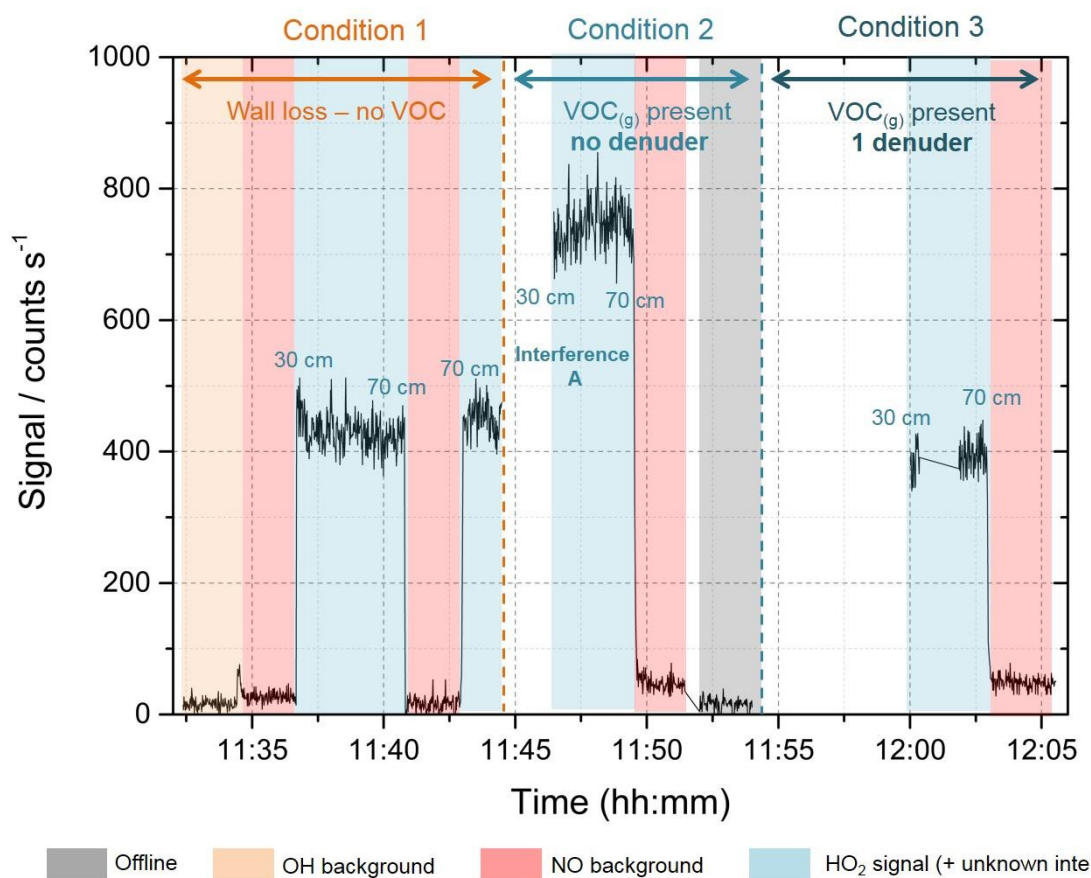


Figure 6.5. Signal time series showing the effect of adding denuder in the series to remove limonene. Condition 1: No limonene added to flow, the HO₂ signal, i.e. wall loss decay, decays from ~ 450 – 420 counts when the injector is pulled back from 30 – 70 cm. Condition 2: limonene added to the flow with no denuder in place. Signal increases to ~720 counts. Production of radicals (interference A) seen when injector pulled back from 30 – 70 cm in comparison to condition 1. Slight increase in NO background in comparison to condition 1. Condition 3: Limonene added to the flow, one charcoal denuder in place. Signal decreases back to approximately counts seen in condition 1. NO background is the same for condition 2 and 3. Shaded orange regions show OH background when NO flow and HO₂ injector lamp was off. Shaded red regions show the NO background when HO₂ injector lamp is off but NO flow is on at 50 sccm. Blue shaded region shows the online signal with NO flow and HO₂ generation on. Shaded grey region shows laser offline. No O₃ was present for this experiment.

Interference B was not seen with only limonene in the flow tube (Figure 6.5, 11:50-15:52), and was only present when SOA was present in the flow tube, though it was unclear whether the interference was caused by the SOA itself or a product of the reaction of limonene and ozone. The addition of a HEPA filter (HEPA filter described fully in Section 3.3.3) allowed any VOC or gas-phase highly oxygenated molecules formed from the reaction of limonene and ozone, and not removed by the charcoal

denuders, to be present in the flow tube in the absence of the SOA. This was done to provide clarification of the source of the interference. Figure 6.6 shows the effect on the FAGE signal (and on interference B) of removing SOA from the flow using the HEPA filter.

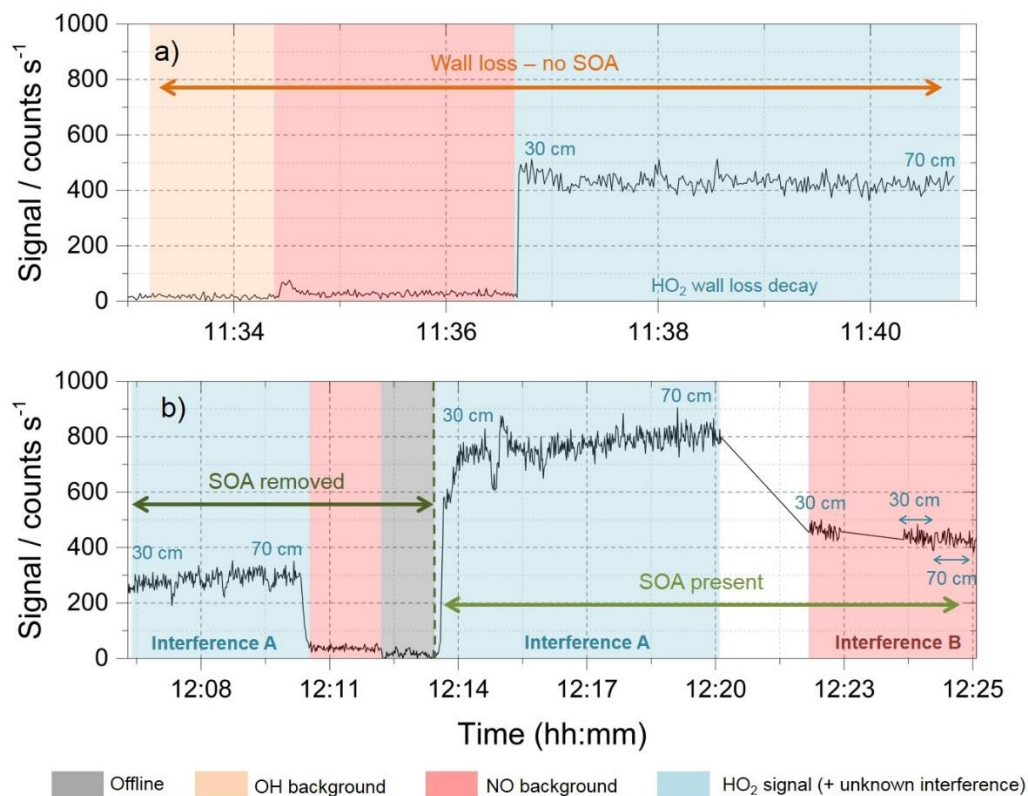
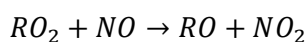


Figure 6.6. Comparison of FAGE signal without aerosols present, with SOA removed and with SOA present. a) shows the HO₂ wall loss decay signal as injector was pulled back from 30 – 70 cm. b) shows FAGE signal with SOA removed by HEPA filters vs when SOA is not removed. It is possible that denuders do not fully remove any gas phase RO₂ species or other highly oxygenated molecules and that these could be causing an interference. The shaded orange region shows OH background when NO flow and HO₂ injector lamp was off. Shaded red regions show the NO background when HO₂ injector lamp is off but NO flow is on at 50 sccm. This is the signal from any contaminants in the NO lines or cylinder. Ideally this should be as close to OH background as possible. An interference in NO background is seen however when SOAs are present. Blue shaded region shows the online signal with NO flow and HO₂ generation on. Shaded grey region shows laser offline.

As can be seen in Figure 6.6a, with no SOA present, a wall loss decay of HO₂ was present as the injector was pulled back from 30-70 cm (~11:37-11:41, blue shaded region). During a wall loss decay, no limonene or ozone (and therefore no SOA) are added to the system and therefore interference A is not seen due to limonene + OH reactions not occurring.

It is possible that the denuders do not fully remove gas-phase products, e.g. RO₂ species, of limonene ozonolysis and that these could be causing an interference. Using an ozone analyser (Thermo Fischer, model 49i), it was shown that O₃ was completely removed by the denuders (concentration of O₃ measured after the denuders did not increase above the limit of detection of the instrument when O₃ was introduced to the system), with no interference in the FAGE cell seen when only O₃ was flowed into the flow tube. Metts and Batterman, 2006 showed that VOCs like limonene can poison the activated charcoal leading to a reduction in chemisorption rates of O₃ and a reduction in the O₃ removal capacity. As such it was important to periodically replace activated charcoal in denuders to keep O₃ removal capacity at a maximum. As shown in Figure 6.6b, interference B signal is only seen when SOA are present (~400 counts in Figure 6.6b – 12:23 – 12:25, red shaded region) whereas when SOA is removed by HEPA filter the interference drops back to ~ 50 counts taken as a constant background due to contaminants in the NO lines or cylinder (12:11--12:12, red shaded region), approximately the same as seen when no aerosols are present, i.e. during the wall loss experiment as shown in Figure 6.6a. However, the production of radicals (interference A), when the injector is pulled back from 30 – 70 cm, is seen in Figure 6.6b both when SOA are removed by HEPA (~12:07-12:11, blue shaded region) and when SOA are present (~12:14-12:20, blue shaded region), as opposed to the wall-loss decay seen for the wall loss in Figure 6.6a. This suggests that whatever is causing interference B is SOA related and is different to what is causing interference A, i.e. is not directly caused by a product of the reaction of limonene + OH. If interference B was caused by OH reactions with either limonene or an RO₂ species in the flow tube, the interference signal should increase when the injector is pulled back. However, as seen in Figure 6.6b, interference B is constant with injector position suggesting it could be caused by RO₂ directly.

The dependence of interference B with the flow of NO added to the fluorescence cell was characterised to identify if these interference signals were due to HO₂ directly or the OH which is generated, via HO₂, from an RO₂ interference. RO₂ and HO₂ display different dependencies with NO concentration due to RO₂ needing to react with 2 NO molecules before OH is generated and detected by LIF (Fuchs et al., 2008; Whalley et al., 2013).



R 1.15



Thereby the signal dependence of the generated OH, if due to RO₂ interference and not direct HO₂ conversion, on NO is expected to be less steep for RO₂ than for HO₂ signal. Figure 6.7 shows the dependence of the OH signal from conversion of HO₂, when the HO₂ injector lamp and NO flow are on but without SOAs present, and also the dependence of the interference B signal upon NO flow.

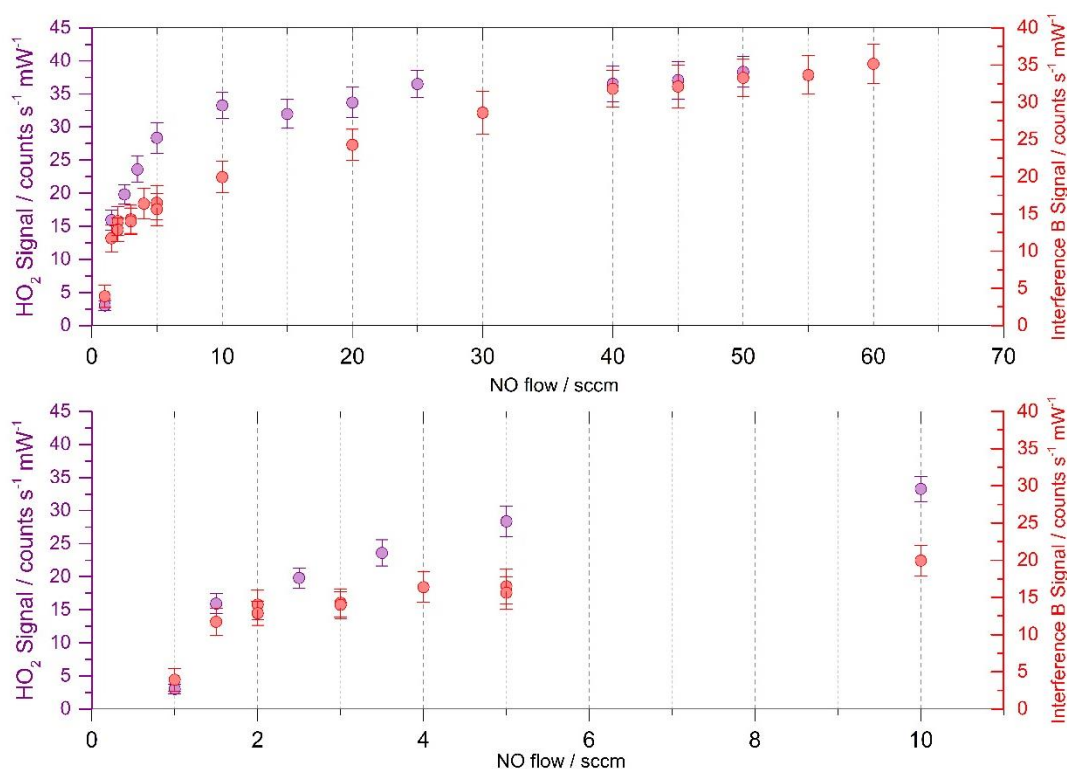


Figure 6.7. Top panel shows the NO dependence of HO₂ signal (purple circles) and interference B signal when SOAs are present (red circles) and the NO flow is on but HO₂ injector lamp is off i.e. no HO₂ generation, between 0-65 sccm. Bottom panel shows the dependence between 0-10 sccm. Typical experimental NO flow used to convert HO₂ to OH in detection cell for the uptake of HO₂ onto SOA experiments was 50 sccm, cell pressure was 1.3 Torr. Error bars represent 1σ.

As seen in Figure 6.7, the signal given by interference B when SOAs are present has a less steep dependence on NO than the HO₂ signal without SOAs, providing some evidence that the interference is due, at least in part, to RO₂ interference. Without SOA present, as seen in Figure 6.6b (12:11--12:12, red shaded region), interference B is not seen, suggesting that RO₂ interference is caused not by RO₂ in the gas phase which ought to be removed by the denuder but instead may be desorbing from SOA itself. It

is unclear if FAGE is detecting gas phase RO₂ that has desorbed off the aerosol surface or whether the SOA with RO₂ adsorbed can be detected through reaction with NO in the cell to generate gas phase OH, which is then detected.

Gong et al., 2018 quantitatively measured H₂O₂ generation from SOA produced in limonene ozonolysis, with peroxides in both the gaseous and particle phases detected (Gong et al., 2018). However, HO₂ and RO₂ radicals were not directly measured, either in the gas phase or the aerosol phase. A study by Tong et al., 2016 found that ambient and laboratory generated SOAs (α -pinene, β -pinene and limonene derived SOA formed from ozonolysis) form substantial amounts of OH radicals upon interaction with liquid water, hypothesizing that these OH radicals could then trigger autoxidation in the condensed phase.

Limonene and ozone react in the gas phase to give highly oxygenated molecules (HOMs) which are key components of SOA. Within the PAM chamber limonene will react with O₃ to give RO₂'s, HOMs and extremely low volatility compounds (ELVOC) which then partition into the aerosol phase. ELVOC are thought to aid new particle formation and consist of organic molecules with low enough volatility to condense into the particle phase. Once particles are formed, condensation of further ELVOC can grow the aerosols leading to highly oxidised aerosols including RO₂ species (Tu et al., 2016). Limonene has been experimentally shown, in comparison to isoprene, α -pinene, β -pinene and myrcene, to produce very high concentrations of ELVOC for a given concentration of reacted alkene with total molar yield of ELVOC from limonene from reaction with O₃ being 5.3 compared to 0.01, 3.4, 0.12 and 0.47 from isoprene, α -pinene, β -pinene and myrcene respectively (Jokinen et al., 2015).

In the flow tube, any gas phase RO₂ species which pass through the denuders may then react with HO₂ from the injector to form other peroxy radicals, which can then also react with HO₂. However, the lack of interference B when SOAs are removed but gas phase products of limonene and ozone reaction are present (Figure 6.6) suggests that RO₂ species responsible for interference B are chiefly coming off aerosol surfaces after the denuders as these species would usually be expected to be removed by the denuders. As the aerosols increase in size due to exposure to O₃ leading to functionalisation, fragmentation can begin to occur leading to higher volatility compounds partitioning back into the gas phase (Jokinen et al., 2015). It is therefore

possible that larger aerosols in the flow tube are fragmenting leading to interference B.

Day to day, the magnitude of the interference B varied which we postulated may be due to changing conditions of the PAM chamber over the course of several experiments – for example aged species may build up and then evaporate from the PAM chamber walls. Aged aerosols, which have been exposed to VOC and O₃ for longer, are expected to be more oxidised with a higher mass concentration (Lambe et al., 2012; Jokinen et al., 2015; Tu et al., 2016). Tu et al., 2016 reported that aged SOA samples showed new HOMs formation with higher carbon number (i.e. large aerosols) than those from fresh SOA sample.

To test the hypothesis that interference B was caused by aged aerosols, the PAM chamber was “cleaned” by turning on the four 254 nm lamps in the chamber to form OH from the O₃ generated with the mercury penray 185 nm lamp situated before the chamber. The PAM chamber was then monitored (by the SMPS) as any products were “baked off” the walls. The PAM chamber was deemed “clean” when SOA concentrations reached a negligibly low concentrations (as monitored by the SMPS). The FAGE signal with NO added and injector lamp on (interference A), and the interference B signal with SOA present was then compared to the signal before cleaning, as shown in Figure 6.8.

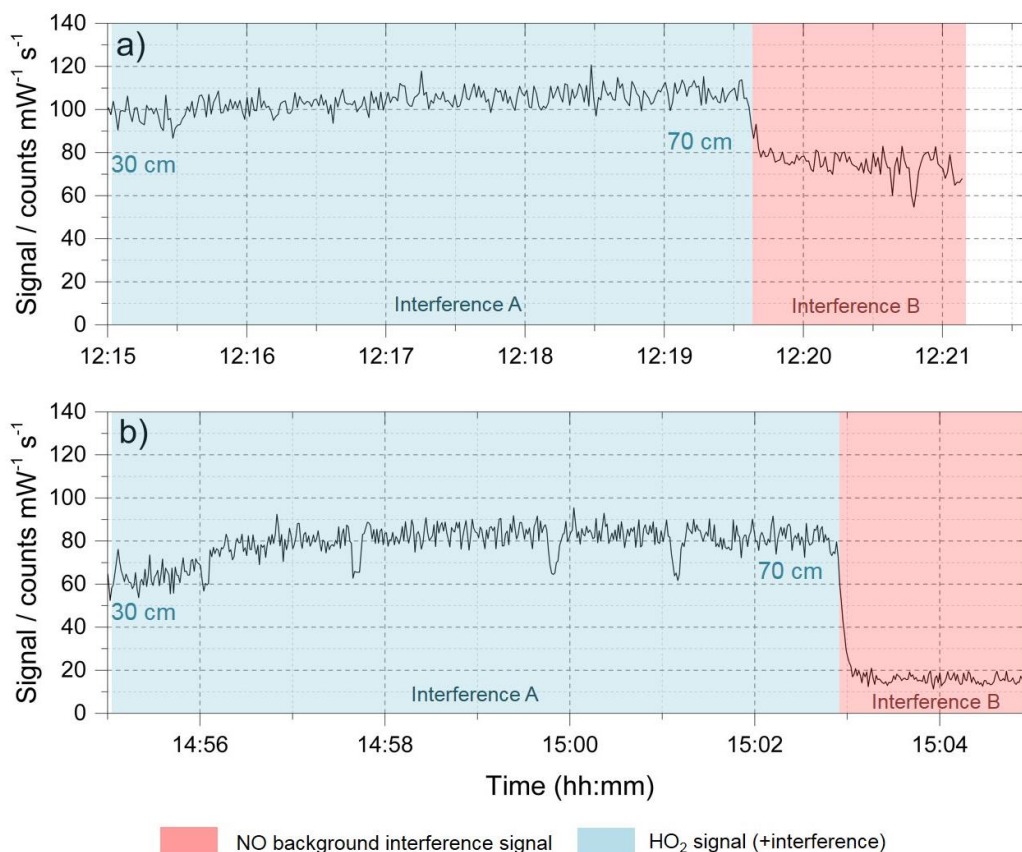


Figure 6.8. Comparison of FAGE signal a) before “cleaning” PAM chamber and b) after “cleaning” PAM chamber. Blue shaded regions show the online signal with NO flow and HO₂ generation on with injector pulled back from 30 – 70 cm. In both a) and b) a production signal is seen where a decay would be expected (interference A). Shaded red regions show the NO background when HO₂ injector lamp is off but NO flow is on at 50 sccm (interference B). This signal is should be ~5-10 counts mW⁻¹ s⁻¹ however interference B, present only when SOAs are present, is artificially increasing this background. This interference is lower in b) after the PAM chamber was cleaned. Interference A (shaded in blue) with NO and injector lamp on was also lower in counts after the PAM chamber was cleaned.

From Figure 6.8, it can be seen that reacting off (via the cleaning process) any unreacted limonene, or products adsorbed to the PAM chamber walls, by introducing oxidants but no additional limonene to the chamber, reduces interference B suggesting that the interference is caused by aged products, either from the walls of the chamber or coming off the aerosols. Throughout the day, it was observed that interference B increased with time, as shown in Figure 6.9, further reinforcing the hypothesis that aged aerosols/gas phase products are the cause of the interference.

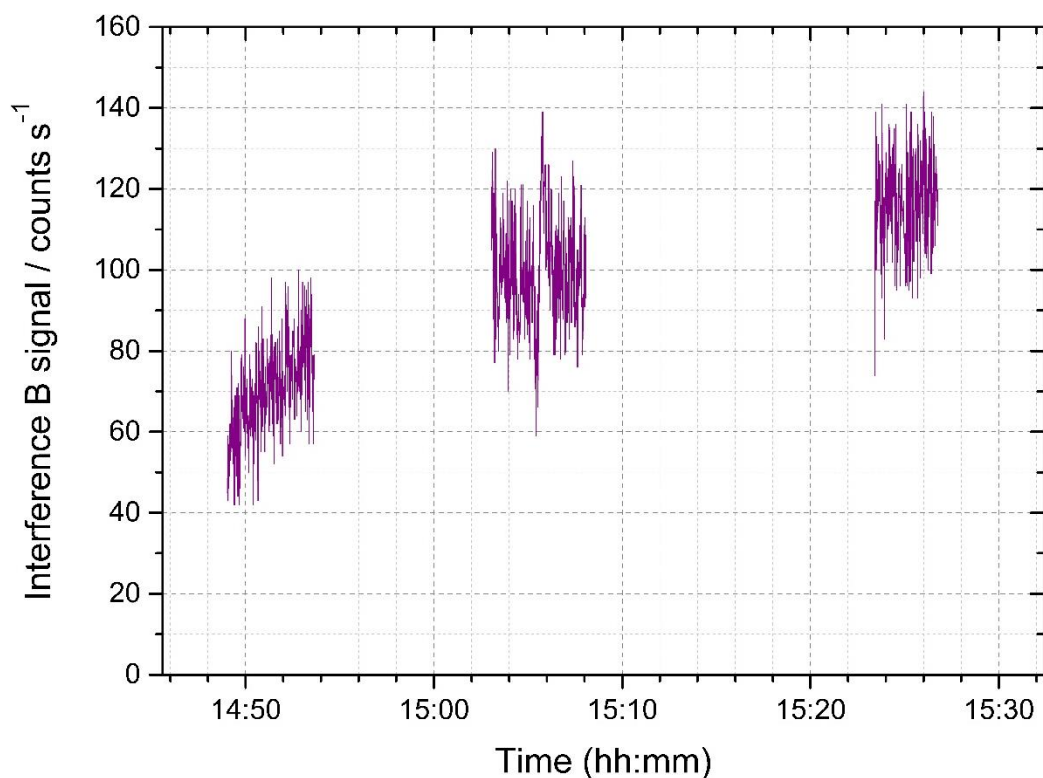


Figure 6.9. Increase in interference B signal throughout an experimental day providing strong evidence that interference is due to a build up/aging of products in the PAM chamber.

6.1.3 Using a GC Trap to Remove Interference

The addition of a packed hydrocarbon GC trap (Agilent in-line gas purifier, BHT-4, 250 psig max. pressure, 8 lpm max flow) after the first charcoal denuder decreased both interferences A and B and allowed a decay of HO₂ to be seen with SOA present when the injector was pulled back. Due to the high pressure nature of GC analysis, the trap was packed tightly which introduced a large flow restriction into the system meaning this was not an ideal long term solution to remove any interfering species due to the risk associated with a build up of pressure. If interference A and B can be removed in a similar manner to the tightly-packed GC trap, without the associated pressure risk, HO₂ uptake experiments onto SOA could be more readily performed in the future. Figure 6.10 shows example HO₂ decays for HO₂ uptake experiments with the GC trap in series showing the increase in loss of HO₂ when aerosols are present. Figure 6.11 shows the plot of first order rate coefficient, k' , after the Brown correction, versus the aerosol surface area ($\text{m}^2 \text{m}^{-3}$) for the experiment at 58 % RH. This work is preliminary and should be redone in the future to increase the quality of the data once all interferences are understood and removed/accounted for.

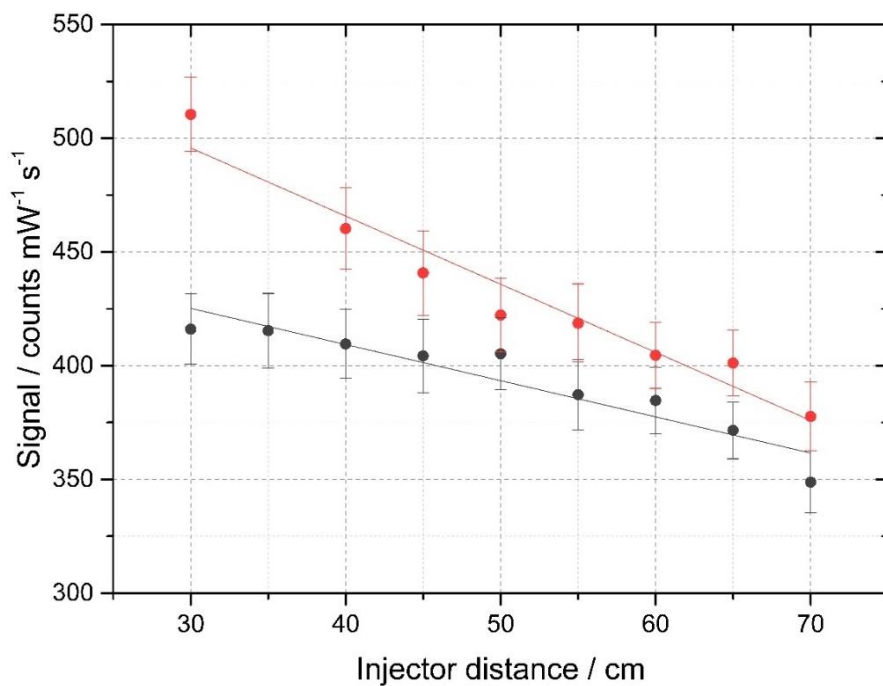


Figure 6.10. Example of HO₂ decay with injector distance for wall loss experiment (grey circles) and with the presence of limonene-derived SOAs (red circles, aerosol surface area of $2.64 \pm 0.05 \text{ m}^2 \text{ m}^{-3}$). Experiment done at $22 \pm 2 \%$ RH.

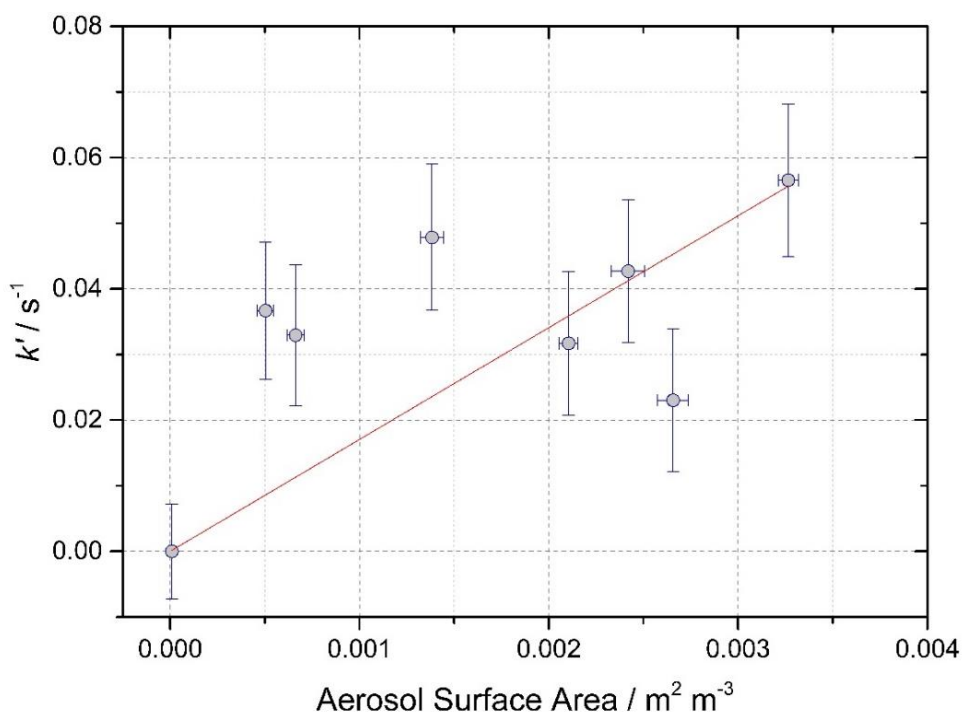


Figure 6.11. First order rate coefficient, k' (s⁻¹), after the Brown correction, plotted against aerosol surface area (m² m⁻³) for limonene-derived secondary organic aerosols formed by reaction with O₃. RH = 58%. Uptake coefficient of HO₂ of 0.15 ± 0.03 calculated from the gradient. Error bars represent 1σ .

Two experiments were done with a GC trap and one charcoal denuder in series at 22 and 58 % RH, giving uptake coefficient values of 0.10 ± 0.03 and 0.15 ± 0.03 , respectively. These uptake coefficients are higher than expected for aerosols without the presence of transition metal ions. It is therefore worth noting that even though both interference A and B were visibly reduced *significantly*, and therefore the GC trap was effective in removing any limonene or RO₂ species to a certain level, it is not possible to know for certain from these experiments if any interfering species was still present in the flow tube.

These results are preliminary. Future work will include more research into removal of hydrocarbons prior to the aerosol flow tube using denuder or other types or traps, in order to be certain that all interfering species have been removed from the flow and the decays seen are due only to loss of HO₂ to aerosol and wall surfaces and not due to any interfering species which could artificially slow a decay or even lead to a production of HO₂ with injector distance being seen. For future experiments, CO could be added to the injector flow to react away any OH to give HO₂ thereby removing the uncertain background signal associated with the formation of products from the reaction of OH with VOCs.

6.2 Summary

The HO₂ uptake system was built and validated for the measurement of uptake onto aerosols surfaces. The uptake of HO₂ onto limonene-derived SOA was measured with an interference seen (interference B), which is postulated to be due to RO₂ species coming off the SOA surface after the charcoal denuders. OH radicals were found to be exiting the injector at trace levels leading to production of radicals as the injector was pulled away from the FAGE cell through the reaction with trace levels of limonene in the system. It was observed that aged aerosols appear to increase interference B, due mostly likely to aged aerosols being larger in size and more oxidised and thereby increasing likely to fragment to give smaller oxidised molecule leading potentially to gas phase RO₂ species in the flow tube. Installing a GC hydrocarbon trap after the denuders significantly removed the interference seen and allowed a decay of HO₂ to be seen in the presence of aerosols and an uptake coefficient to be measured: $\gamma_{HO_2} = 0.10 \pm 0.03$ at 22 % RH and $\gamma_{HO_2} = 0.15 \pm 0.03$ at 58 % RH. Future work would include further studies into the source of the interference caused,

most likely indirectly, by SOA before additional experiments into the RH dependency of limonene-derived SOA can be done. It is also worth investigating whether other, less reactive, VOCs produce an interference in the system upon ozonolysis, or whether using OH or NO₃ as an oxidant to generate SOA may lead to a reduction in said interference.

7 Modelling the impact of HO₂ Uptake onto Aerosols During Summertime in Beijing with the Master Chemical Mechanism

In this chapter measurements of OH, HO₂ and RO₂ taken during the summer APHH programme in Beijing in 2017 will be compared to modelled radical concentrations with particular focus on the impact of HO₂ aerosol uptake on the modelled HO₂ radical concentration.

7.1 Introduction to the Summer AIRPRO Campaign

The Air Pollution and Human Health (APHH) in a Chinese Megacity programme was a joint venture between UK and Chinese universities and institutes funded by the Natural Environment Research Council (NERC), the Medical Research Council (MRC) and the National Natural Science Foundation of China (NSFC) which aimed to better understand the sources and health impacts of air pollutants in Beijing.

The APHH programme was split into five different projects: AIRPOLL (sources and emissions of AIR POLLutant in Beijing), AIRPRO (An integrated study of AIR pollution PROCesses in Beijing), APIC-ESTEE (Air Pollution Impacts of Cardiopulmonary disease in Beijing: an integrated study of Exposure Science, Toxicogenomics and Environmental Epidemiology), AIRLESS (effects of AIR pollution on cardiopulmonary disease in urban and peri-urban residents in Beijing) and INHANCE (Integrated assessment of the emission-health-socioeconomic nexus and air pollution mitigation solutions and interventions in Beijing), each with different aims. The University of Leeds took part in the AIRPRO (The integrated study of AIR pollution PROCesses in Beijing) project within the APHH programme.

The AIRPRO project aimed to study the chemical and physical processes governing gas and particle pollution and meteorological dynamics in the Beijing region and the links between the two. The AIRPRO project included the measurement of primary gas phase emissions, gas phase radicals and secondary products and particulate matter over two field campaigns: one in Nov-Dec of 2016 and the other from May-June of 2017. The project allowed the comparison of *in situ* chemical processing of air pollution in the winter and summer periods in Beijing. The AIRPRO project was separated into seven different sections: oxidation chemistry; nitrogen budgets; aerosol

optical and physical properties; secondary aerosols; meteorology; the link between haze, photochemistry and dynamics and modelling at multiple scales (Shi et al., 2019).

The measurements made by the Leeds group as part of the APHH programme are as follows: OH, HO₂, RO₂ (with some speciation), OH reactivity (*k*OH), HCHO and photolysis rates. The official science period for the summer campaign ran from 23/05/2017 to the 22/06/2017, with radical measurements being taken throughout this entire period. (Shi et al., 2019;Slater, 2020). Alongside the Leeds observation of OH, HO₂, RO₂, OH reactivity (*k*OH), HCHO and photolysis rates, there was a varied suite of supporting measurements operated by several universities and institutes (full details in Slater, 2020). The supporting measurements used and discussed chiefly in this chapter were provided by the Universities of York, Birmingham and Cambridge as detailed in Table 7.1.

Instrument	Species measured	University	Reference
FAGE	OH, HO ₂ , RO ₂	Leeds	Whalley et al., 2010;Slater et al., 2020;Whalley et al., 2021
OH reactivity	OH reactivity	Leeds	Stone et al., 2016;Slater et al., 2020;Whalley et al., 2021
Spectral Radiometer	Photolysis rates	Leeds	Bohn et al., 2016
Filter Radiometer	$j(O^1D)$	Leeds	Whalley et al., 2010
Teledyne CAPS	NO ₂	York	Smith et al., 2017
TEI 42c	Total NO _y	York	Smith et al., 2017
TEI 49i	O ₃	York	Smith et al., 2017
Sensor box	CO	York	Smith et al., 2017
DC-GC_FID	C ₂ -C ₇ VOCs and oVOCs	York	Hopkins et al., 2011
GCxGC-FID	C ₆ -C ₁₃ VOCs and oVOCs	York	Dunmore et al., 2015
BBCEAS	HONO	Cambridge	Le Breton et al., 2014
TEI 42i	NO	Birmingham	
LOPAP	HONO	Birmingham	Crilley et al., 2016
SMPS	Particle Size distribution	Birmingham	Shi et al., 1999
High volume sampler	PM _{2.5} filter samples, Aerosol copper	IAP	

Table 7.1. Measurements taken by different universities during the Beijing Summer AIRPRO campaign. These species are directly referred to in this chapter: full description of every instrument and measurement taken can be found in Slater, 2020. IAP: Institute of Atmospheric Physics, Beijing. ICP-MS: Inductively Coupled Plasma Mass Spectrometry. Time resolution of all instruments was averaged up to or interpolated to 15 minutes for modelling purposes with the exception of the PM_{2.5} filter samples, of which there was only 1 sample taken a day.

The average diurnals for important gas phase species and $j(\text{O}^1\text{D})$ during the Summer AIRPRO campaign are shown in Figure 7.1. The $j(\text{O}^1\text{D})$ shows a peak at solar noon peaking at $2.5 \times 10^{-5} \text{ s}^{-1}$. The diurnal variation in NO is very distinct with a peak at rush hour (~08:00) of ~8 ppbv. After the morning peak in NO, NO continued to decrease to a minimum in the afternoon of 0.3 ppbv. Low NO values observed in the afternoon were a result of very high O₃ values in the afternoon, due to the titration of NO + O₃ to give NO₂. O₃ diurnal peaked at 89 ppbv at 15:30, with a minimum of 14 ppbv observed in the morning when NO is high due to traffic. CO does not have a distinct diurnal trend with an average of ~ 460 ppbv over the day. O₃ and NO₂ diurnals show an anti-correlation with NO₂ peaking at ~32 ppbv at 06:30 when O₃ is at its lowest. As expected, HONO is high in the morning due to accumulation overnight, peaking before 07:30 at ~ 7 ppbv, after which HONO is lost to photolysis to give OH + NO. The results of modelling OH, HO₂ and RO₂ for the summer campaign period and the comparison to the measurements, with a focus on the impact of aerosol uptake, are presented in this chapter.

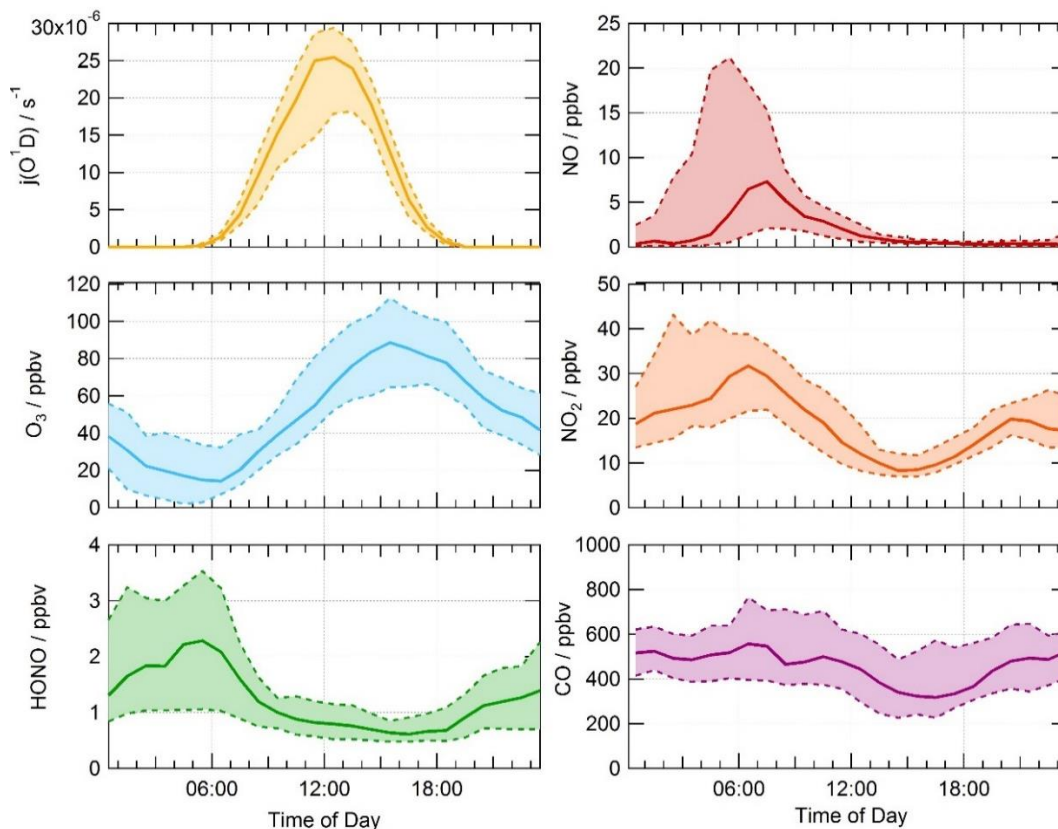


Figure 7.1. Average median diurnal profile for measurements of $j(\text{O}^1\text{D})$ (s^{-1}), O_3 (ppbv), HONO (ppbv), NO (ppbv), NO_2 (ppbv) and CO (ppbv) for the Summer AIRPRO campaign. The dashed lines represent the 25/75th percentiles. Diurnals show 60 minute averages, taken over the entire measurement period.

7.2 Model Description

In this chapter the measured radical concentrations have been compared to modelled concentrations with a focus on HO_2 concentration and the effect on radical concentrations of adding HO_2 uptake onto aerosols. The modelled predictions are given by a zero-dimensional box model which uses the Master Chemical Mechanism, MCM v.3.3.1, as described in Section 1.10.1. The model was constrained to measurements of NO, NO_2 , O_3 , CO, HCHO, HNO_3 , HONO, H_2O vapour, temperature, pressure, $j(\text{O}^1\text{D})$, $j(\text{HONO})$, $j(\text{NO}_2)$, $j(\text{ClONO}_2)$, $j(\text{HOCl})$, $j(\text{ClONO}_2)$ and specific VOC species measured using GC-FID (gas chromatography with flame ionisation) and PTR-ToF-MS (proton-transfer reaction time of flight mass spectrometry). The full list of all species constrained in the model is shown in Table 7.2 below:

Type	Species
Gas-phase inorganic species	NO, NO ₂ , O ₃ , CO, HNO ₃ , HONO, H ₂ O, SO ₂ , ClNO ₂ , HOCl
Gas-phase organic species	HCHO, PAN
VOCs	CH ₄ , C ₂ H ₆ , C ₂ H ₄ , C ₃ H ₈ , C ₃ H ₆ , isobutane, butane, C ₂ H ₂ , trans-but-2-ene, but-1-ene, Isobutene, cis-but-2-ene, 2-Methylbutane, pentane, acetone, 1,3-butadiene, trans-2-pentene, cis-2-pentene, 2-methylpentane, 3-methylpentane, hexane, isoprene, heptane, benzene, toluene, nonane, decane, undecane, dodecane, o-xylene, CH ₃ OH, CH ₃ OCH ₃ , 2-ethyltoluene, 3-ethyltoluene, 4-ethyltoluene, ethylbenzene, CH ₃ CHO, C ₂ H ₅ OH, α -pinene, limonene, isopropylbenzene, propylbenzene, m-xylene, p-xylene, 1,2,3-trimethylbenzene, 1,2,4-trimethylbenzene, 1,3,5-trimethylbenzene.
Photolysis rates	$j(O^1D)$, $j(HONO)$, $j(NO_2)$, $j(ClNO_2)$, $j(HOCl)$, $j(ClONO_2)$
Other	Mixing height, aerosol surface area

Table 7.2 Full description of measured species for Summer AIRPRO campaign, added to constrain the model

The model inputs were entered for every 15 minutes of the entire campaign, with species measured at higher time resolution averaged up to 15 minutes and those at lower time resolution interpolated to give a value every 15 minutes. Aerosol surface area was included at a time resolution of 15 minutes within the models however for γ_{HO_2} calculated with the Song parameterisation, introduced and further discussed in Section 7.3.3, aerosol copper concentration and PM_{2.5} mass concentration were given in at a time resolution of 1 day: all other measured values in the parameterisation were therefore averaged up to this resolution. This meant that γ_{HO_2} was calculated at a time resolution of 1 day also.

The different model scenarios referred to in this work are described in full below:

1. **MCM_base**: The base model run constrained to the species described in Table 7.2.
2. **MCM_αpinene**: The MCM_base model with an additional reaction converting OH into α-pinene-RO₂ at a rate equal to the product of the missing OH reactivity in the model and the OH concentration ($k_{missing}[OH]$) (Whalley et al., 2021).
3. **MCM_αpinene_SA**: This model scenario is the same as MCM_αpinene with an uptake coefficient, γ_{HO_2} , of 0.2 added for HO₂ onto aerosols, as suggested by Jacob, 2000.
4. **MCM_αpinene_gamma**: This model scenario is the same as MCM_αpinene with an uptake coefficient for HO₂ onto aerosols calculated from the new parameterisation developed by Song et al., 2020. For summer the average uptake coefficient was 0.070 ± 0.035 .

7.3 Modelling Results

7.3.1 MCM-base vs MCM_αpinene model

The MCM_base model outputs for OH, HO₂ and sum of RO₂ are shown as average diurnal profile and compared with the measured diurnal concentrations in Figure 7.2.

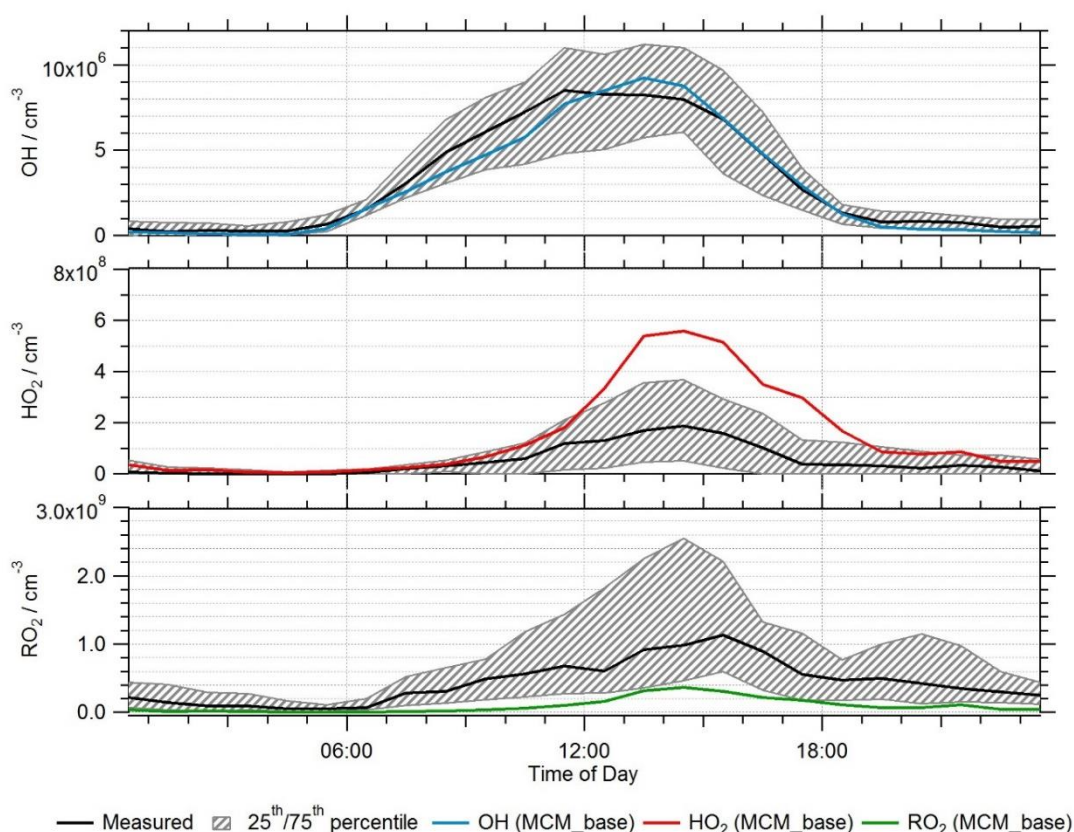


Figure 7.2. Average median diurnal for (a) measured (black) and modelled (blue) OH radical concentrations, (b) measured (black) and modelled (red) HO₂ radical concentrations, and (c) measured (black) and modelled (green) total RO₂ radical concentrations. All model outputs shown are for MCM-base runs. 25th/75th percentiles in measured concentrations shown as shaded regions. Diurnals show 60 minute averages, taken over the entire measurement period.

Figure 7.2 shows that while the model can replicate the trend in measured OH, HO₂ and RO₂ well, HO₂ is, on average, over-predicted while RO₂ is under-predicted. The model, on average, predicts daytime OH very well, with a slight under-prediction between 08:00-11:00 which coincides with higher NO emissions due to morning traffic. The night-time concentration of OH is under-predicted while the night-time concentration of HO₂ is reproduced better by the model. Day-time HO₂ is over-predicted by the base model by up to a factor of ~ 2.9 seen at the peak of the diurnal at ~14:30. In comparison, daytime RO₂ concentration is under-predicted up to a factor of 7.5 by the model with an average under-prediction of ~2.7 seen at the peak of the diel at ~14:30. This larger average under-prediction of RO₂ over the day compared to the peak of the diurnal is due to a very large under-prediction by the base model between ~6:30-10:30 when NO is at its highest (Whalley et al., 2021). Although the model is able to reproduce the measured OH concentrations reasonably well, the

inability of the model to reproduce both HO₂ and RO₂ suggests that the model is missing several key reactions. A budget analysis, in which the rates of production and destruction of radicals are compared, performed by Whalley et al., 2021 highlighted a missing OH source, resulting from the OH sinks exceeded the OH sources, which could account for some of the over-prediction in HO₂, as well as a missing RO₂ production reaction which could explain the under-prediction of RO₂ by the MCM-base model. It was also proposed that HO₂ is, in general, over-predicted due to an under-prediction in the rate of reaction of RO₂ with NO to produce a different RO₂, RO₂+NO→RO₂', which leads to termination and competes with the reaction of RO₂→RO→HO₂. This suggests that the lifetime of RO₂ is longer than considered in the model and this could explain the high measured concentrations of RO₂ in comparison to the model. This over-prediction in HO₂ could also be due to the lack of autoxidation pathways of RO₂ included within the MCM. These autoxidation pathways lead to the formation of highly oxygenated molecules (HOMs) rather than HO₂ (Whalley et al., 2021).

Due to the recycling of RO₂ to HO₂ and then to OH by NO, strong dependences of radicals on the concentration of NO have been seen for previous campaigns (Tan et al., 2018;Whalley et al., 2018;Slater et al., 2020;Whalley et al., 2021). The ratio of measured to modelled OH, HO₂ and RO₂ binned against NO mixing ratio in ppb is shown in Figure 7.3.

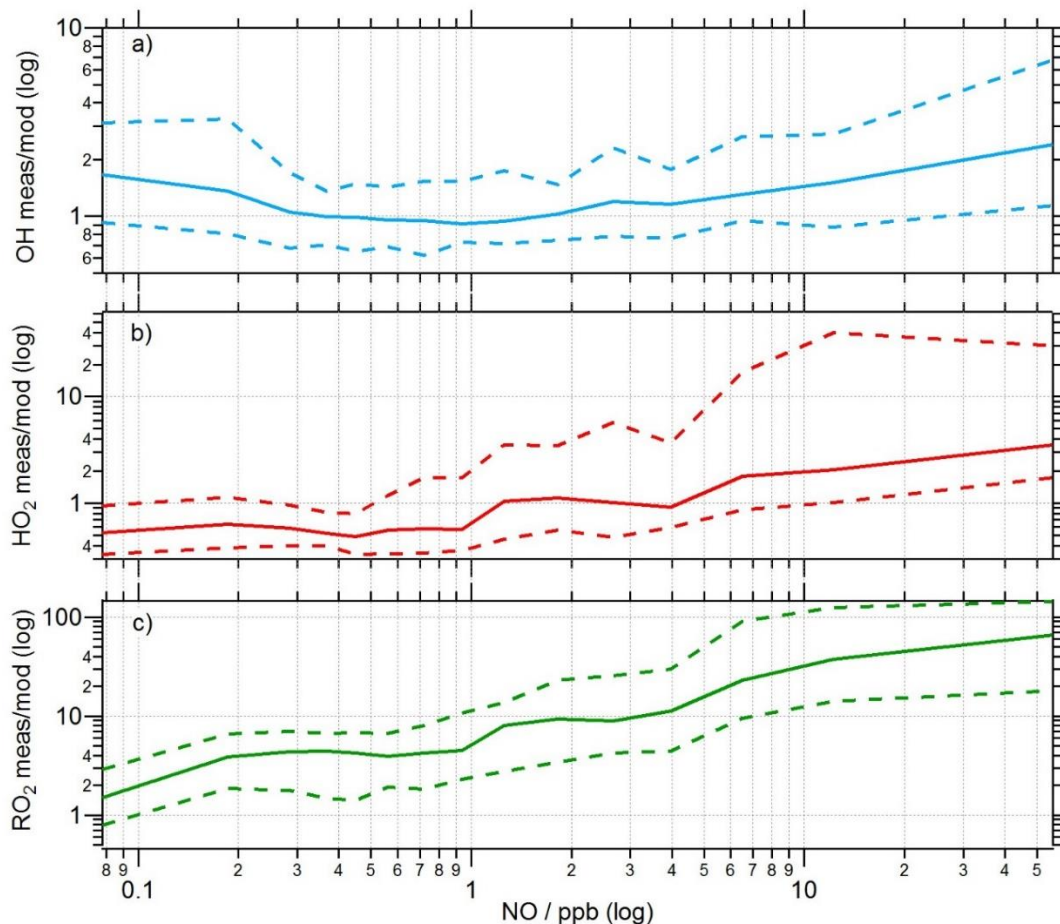


Figure 7.3. The ratio of measured/modelled for MCM_base for a) OH (blue), b) HO₂ (red) and c) RO₂ (green) binned over the range of NO concentrations for the Summer AIRPRO campaign. Solid lines show the median average radical concentrations while dashed lines show the 25th/75th percentile.

Across the range of NO concentrations observed over the summer AIRPRO campaign, the OH measured/modelled ratio is close to 1 between ~0.3-2 ppb with the model beginning to slightly under-predict OH both at <0.3 ppb and 2 ppb and above. In contrast, the model over-predicts HO₂ at the lowest NO mixing ratios, below ~1 ppb NO. Above ~ 4 ppb NO, HO₂ is under-predicted. The measured:modelled ratio for RO₂ shows a large under-prediction of RO₂ across all NO mixing ratios observed during the campaign, with the under-prediction at its largest at higher NO mixing ratios. This is likely to be what is causing the model to under-predict HO₂ at higher NO mixing ratios due to an under-estimation of the rate of propagation of RO₂ to HO₂.

For the purposes of this chapter, an additional reaction was added into the MCM_base model to account for the missing reactivity and to increase the modelled RO₂ concentration.

7.3.1.1 Addition of Missing OH Reactivity

During the Summer campaign, missing reactivity of OH reached up to 13 s⁻¹. During this period of high missing OH reactivity (15-22 June 2017), isoprene concentrations were also high (reaching up to a few ppbv Whalley et al., 2021) relative to the rest of the measurement period suggesting increased biogenic VOCs contribute more to the OH reactivity than previously taken into account (Whalley et al., 2021). In Whalley et al., 2021, to explore this, a species was added to react with OH with a rate equal to the missing reactivity to form different peroxy radical species. Adding in OH→CH₃O₂, taking methylperoxy as a proxy RO₂ product for simple RO₂ radical chemistry, led to an increase in modelled HO₂ compared to the base model due to the rapid propagation of RO₂ to HO₂. As such, RO₂ was more well represented by the model, but HO₂ was even more over-predicted and OH was under-predicted due potentially to a missing HO₂ + X reaction, with X being an species reacting like NO, but not NO, to remove HO₂ to form OH. The addition of an OH+α-pinene reaction however increased the modelled RO₂ concentration, and led to a decrease in the modelled HO₂ over-prediction. This is thought to be due to lack of understanding of the propagation of larger, complex RO₂ species to give HO₂ and the competition of this reaction with RO₂ auto-oxidation reactions leading to termination (Whalley et al., 2021). A simplified mechanism for the oxidation of VOCs, like α-pinene, to give RO₂ and RO species is shown in Figure 7.4.

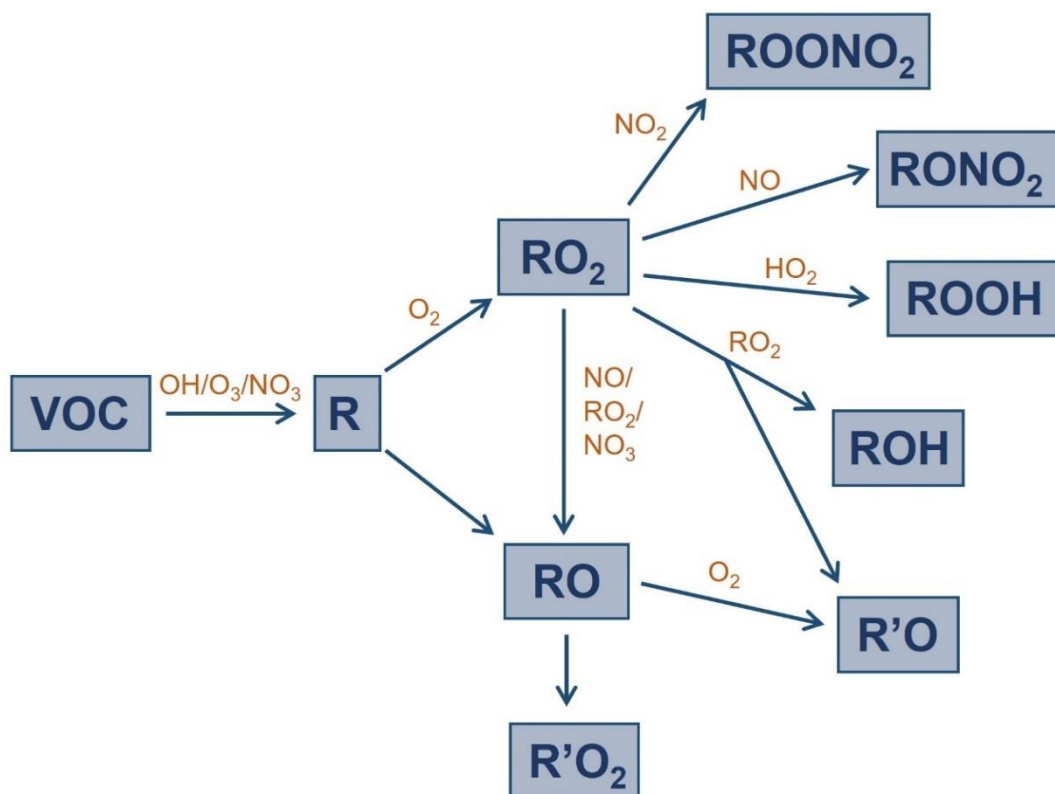


Figure 7.4. Simplified mechanism of the oxidation of VOCs. Figure reproduced from Kroll and Seinfeld, 2008.

In order to study the effect of HO_2 uptake on modelled HO_2 concentration, it was postulated that MCM_αpinene was a good starting point due to modelled HO_2 and modelled RO_2 both being more accurately represented than in MCM_base. For MCM_αpinene, an additional reaction converting OH into α-pinene- RO_2 at a rate equal to the product of the missing reactivity in the model and the OH concentration ($k_{\text{missing}}[\text{OH}]$) was included. The average diurnals for measured OH, HO_2 and RO_2 are shown in comparison to MCM_base and MCM-αpinene modelled OH, HO_2 and RO_2 concentrations in Figure 7.5.

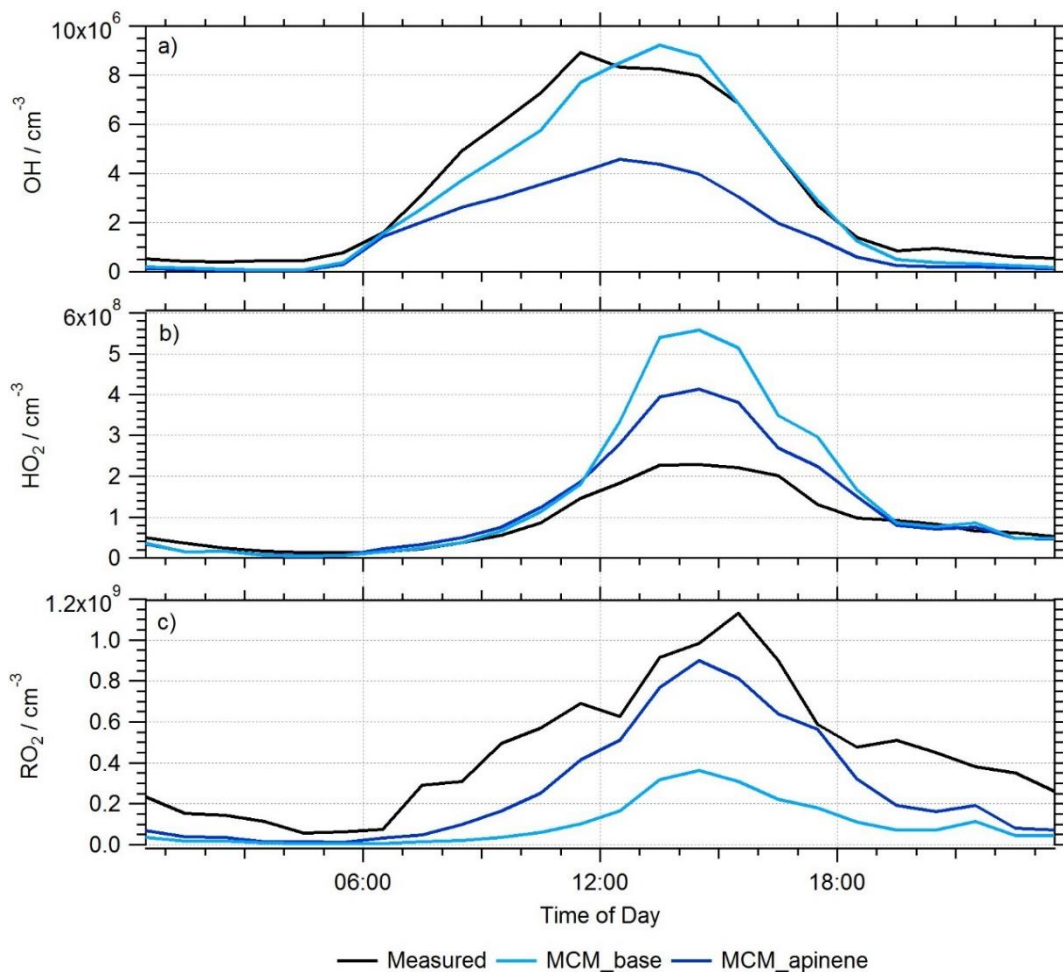


Figure 7.5. Average diurnal comparison of measured and modelled (a) OH, (b) HO₂ and (c) RO₂ values from both the MCM_base (light blue) and MCM_αpinene (dark blue) models. The diurnals show 60 minute averages, taken over the entire measurement period.

As expected, adding in the reaction of OH→α-pinene-RO₂, led to a decrease in modelled daytime OH concentration with the biggest under-prediction compared to measured OH of a factor of ~2 at between 12-14:30. Additionally, this added source of α-pinene RO₂ into the model increased the modelled RO₂ concentration, thereby decreasing the under-prediction in RO₂ to a factor of ~1.2 at the 15:00 peak, with an average under-prediction over the day (between 06:00-18:30) of ~2. The modelled HO₂ concentration decreased for the MCM-αpinene model leading to an over-prediction of the measured HO₂ concentration by a factor of ~2 at 14:30, as opposed to an over-prediction of ~2.9 for the MCM_base model at the same midday peak. This is potentially due to an increase in the rate of RO₂ + NO reactions to give a different RO₂ species, RO₂', competing with RO₂→RO→HO₂ leading to a decrease in the over-prediction of HO₂.

To compare the effect of including additional OH reactivity on OH, HO₂ and RO₂ radicals under different NO conditions, the measured to modelled ratios for MCM_base and MCM_αpinene were binned against NO as shown in Figure 7.6.

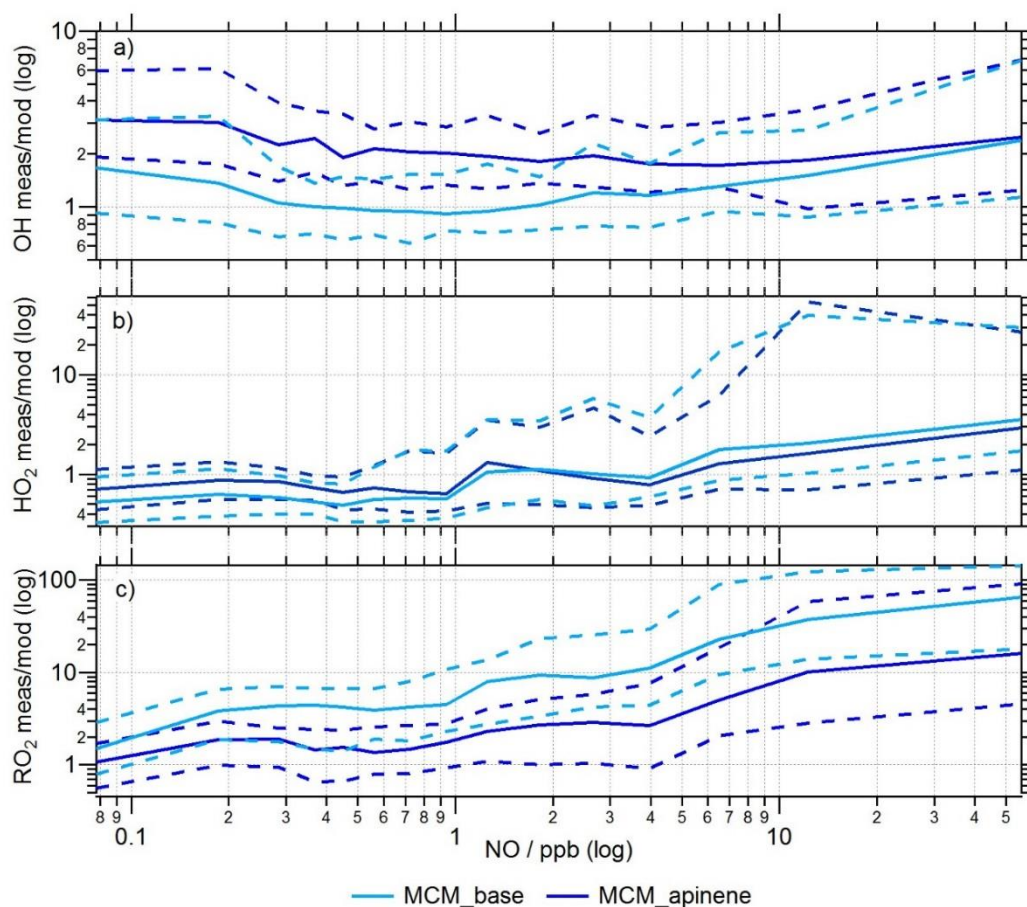


Figure 7.6. The ratio of measured/modelled a) OH, b) HO₂ and c) RO₂ for MCM-base (light blue) and MCM-αpinene (dark blue) models binned over the range of NO concentrations for the Summer AIRPRO campaign. Solid lines show the median average radical concentrations while dashed lines show the 25th/75th percentile.

Adding an additional loss of OH in MCM_αpinene led to an under-prediction of OH for all NO concentrations with respect to the MCM_base. With the addition of a reaction to form α-pinene RO₂ species, the HO₂ concentration at low NO, below ~1.5 ppb, is less over-predicted than for MCM_base due to RO₂ reacting to form other RO₂ species in addition to reacting to form HO₂. This is because α-pinene RO₂ reacting to give HO₂ is included as a 4 step process within the model to elongate the lifetime of RO₂, in-comparison to simpler RO₂ species such as CH₃O₂ which preferentially forms HO₂ from RO, so there is competition at low NO between RO₂→RO→diff RO₂ and RO₂→RO→HO₂ (Whalley et al., 2021).

Both MCM_base and MCM_αpinene over-predict HO₂ over nearly the entire range of NO values with both models beginning to under-predict HO₂ at ~1.5 ppb NO, however MCM_αpinene over-predicts HO₂ less above and ~1.5 ppb NO and over-predicts HO₂ less below ~1.5 ppb NO. Like HO₂, RO₂ was uniformly effected across the entire range of NO concentrations with the under-prediction in RO₂ decreasing significantly with the additional RO₂ source added.

7.3.2 Impact of HO₂ uptake to Aerosols

During the Summer AIRPRO campaign, particulate matter (PM) concentrations were much lower than those seen in the Winter campaign (Slater et al., 2020; Whalley et al., 2021). During the Winter AIRPRO campaign in Nov-Dec 2016, PM_{2.5} concentrations reached up to 530 μg m⁻³ (Slater et al., 2020) with multiple haze periods identified for the Winter campaign (a haze period being defined as PM_{2.5} > 75 μg m⁻³). In comparison, the majority of the Summer Beijing campaign occurred during a non-haze period, with PM_{2.5} concentrations only exceeding 75 μg m⁻³ on 6 days (28/05/2017, 31/05/2017, 05/06/2017, 07/06/2017, 17/06/2017 and 18/06/2017). Within the models, aerosol surface area was used at a time resolution of 15 minutes. PM_{2.5} mass concentration data was only available at a time resolution of one day. The average median diurnal of PM_{2.5} surface area is shown in Figure 7.7. No strong diurnal trend was seen with an average value across the campaign of $5.5 \times 10^{-6} \text{ cm}^2 \text{ cm}^{-3}$, with a maximum surface area reached during the summer campaign of $2.5 \times 10^{-5} \text{ cm}^2 \text{ cm}^{-3}$.

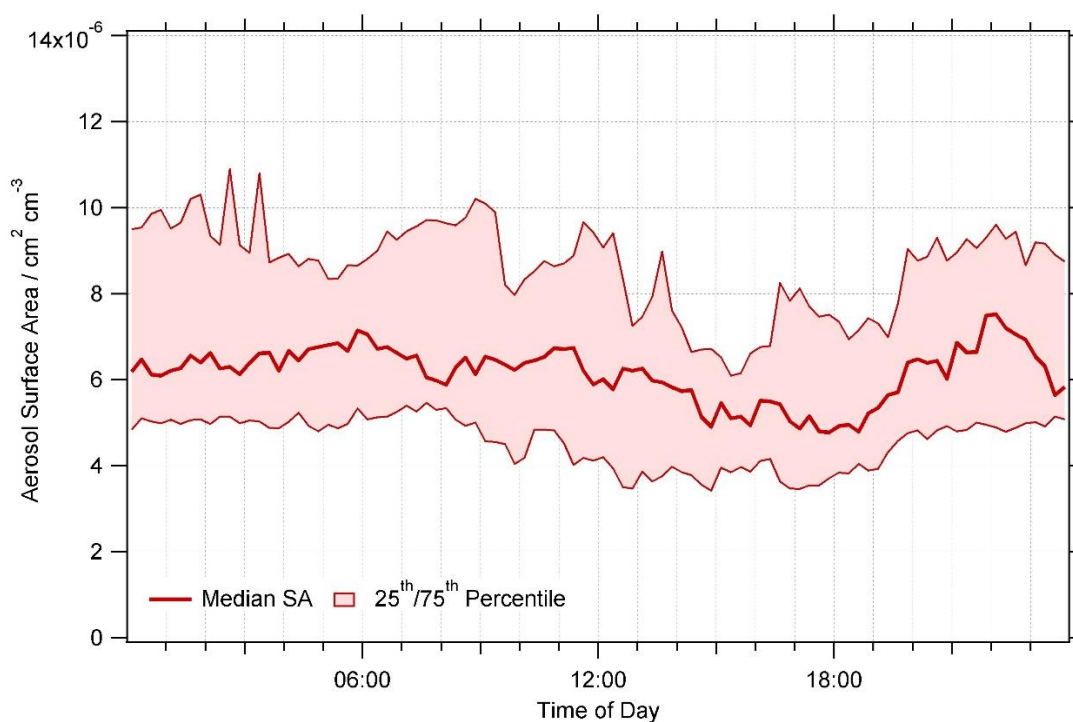


Figure 7.7. Average median diurnal of aerosol surface area ($\text{cm}^2 \text{cm}^{-3}$) for summer AIRPRO campaign. Averaged up to 15 mins.

As discussed in Section 7.3.1, the MCM_base model over-predicts HO_2 concentration by a factor of ~ 2.9 averaged over all NO_x concentrations. With the addition of an additional reaction to convert OH into α -pinene in MCM_ α pinene, the over-prediction of HO_2 was decreased to ~ 2.2 . In urban, highly polluted areas such as Chinese megacities with large aerosol surfaces areas due to high concentrations of air pollutants which are the precursors to aerosol formation, HO_2 uptake onto aerosols could potentially be an important loss of HO_2 (Mao et al., 2013). As such, the uptake coefficient of 0.2 was added into the MCM_ α pinene model, with the new model referred to as MCM_ α pinene_SA. As discussed in Section 1.10.3, an uptake coefficient of 0.2 has previously been used in many global modelling studies, as recommended by Jacob, 2000. A full explanation of the previously used uptake coefficients in modelling studies can be found in Section 1.10.3.

The comparison of modelled and measured radical concentrations for MCM_ α pinene and MCM_ α pinene_SA is shown in Figure 7.8.

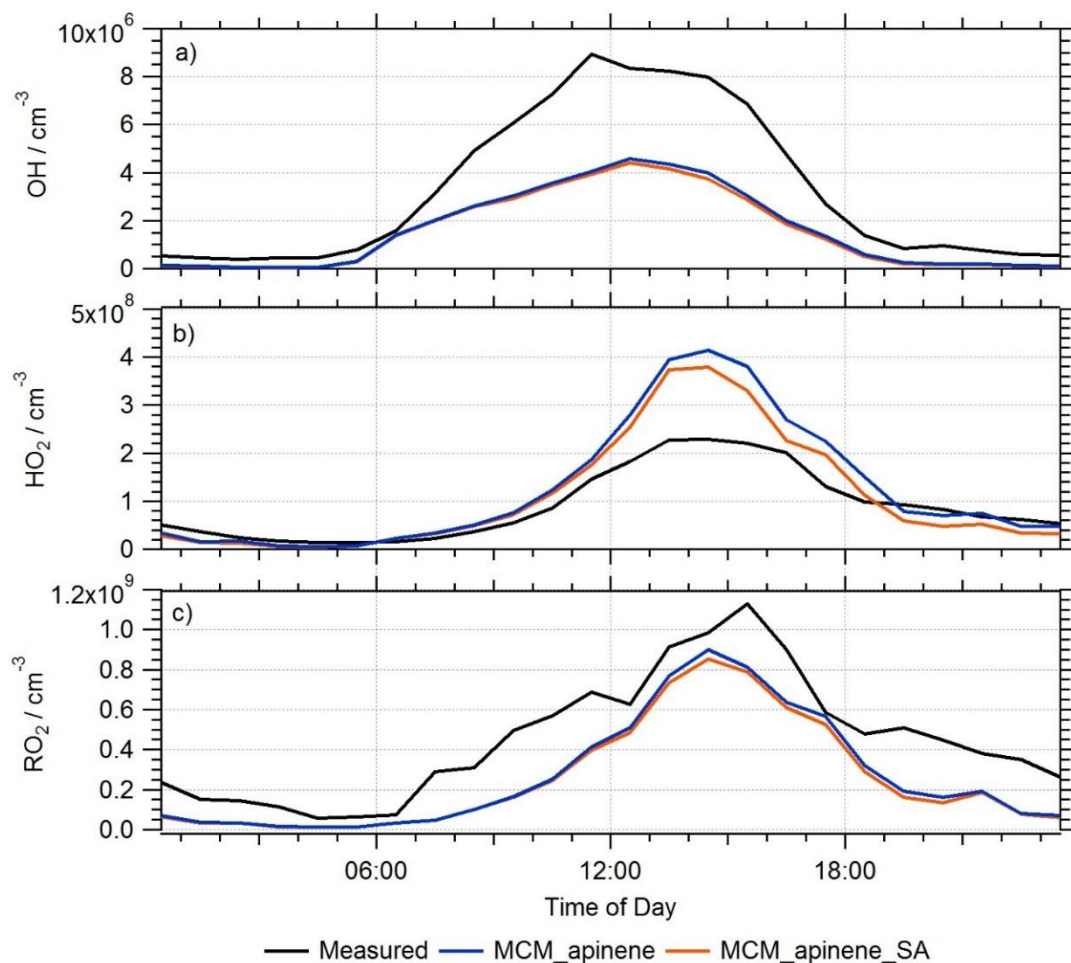


Figure 7.8. Average median diurnal comparison between measured and modelled OH, HO₂ and RO₂ values from both the MCM_apinene (blue) and MCM_apinene_SA (orange). All diurnals averaged at a time resolution of 60 minutes. 25th/75th percentile shown as dashed lines.

The median diurnal shows that, on average, the RO₂ concentration was not significantly affected by the addition of HO₂ uptake across the Summer Beijing campaign. The average median HO₂ concentration at the 14:30 peak decreases with the addition of HO₂ uptake as expected with the model overestimation of HO₂ compared to measured concentration decreasing from a factor of ~2.2 for MCM_apinene to ~2.1 for MCM_apinene_SA. The under-prediction of modelled OH concentration increased slightly from ~2 for MCM_apinene to by a factor of ~2.1 at the 12:00 peak for MCM_apinene.

To compare the effect of adding HO₂ uptake with a fixed single uptake coefficient of 0.2 into the model on OH, HO₂ and RO₂ radicals under different NO conditions the measured to modelled ratios for MCM-base and MCM-SA were binned against NO as shown in Figure 7.9.

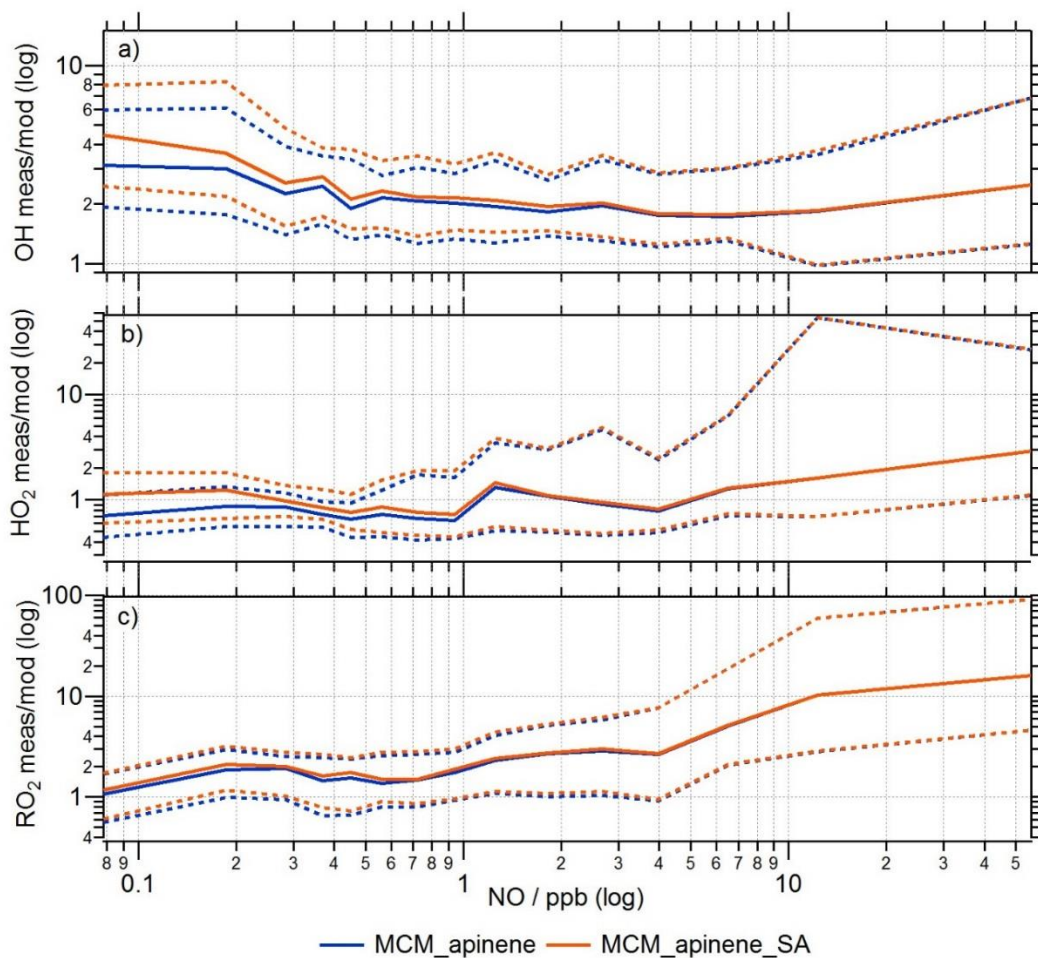


Figure 7.9. The ratio of measured/modelled a) OH, b) HO₂ and c) RO₂ for MCM_αpinene (blue) and MCM_αpinene_SA (orange) models binned over the range of NO concentrations for the Summer AIRPRO campaign. Solid lines show the median average radical concentrations while dashed lines show the 25th/75th percentile.

As shown in Figure 7.9, the addition of $\gamma_{HO_2} = 0.2$ in MCM_αpinene_SA has little effect on the concentration of OH, HO₂ and RO₂ above ~3 ppb. The biggest difference in measured/modelled for HO₂ and RO₂ can be seen below ~1 ppb NO, below ~2 ppb NO for OH. Modelled OH is under-predicted across the entire range of NO concentrations with respect to the measured OH concentrations for both MCM_αpinene and MCM_αpinene_SA with further under-prediction by MCM_αpinene_SA model below ~3 ppb NO. While MCM_αpinene over-predicts HO₂ below ~1.5 ppb NO beginning to under-predict HO₂ at above ~1.5 ppb NO, MCM_αpinene_SA under-predicts HO₂ below ~0.3 ppb NO as well as above ~1.5 ppb. At the lowest NO concentration where the lifetime of HO₂ is longer, the measured/modelled ratio for HO₂ increases from 0.71, an over-prediction of HO₂, to

1.14, a slight under-prediction of HO₂ with the addition of $\gamma_{HO_2} = 0.2$, a significant change. The modelled RO₂ concentration is not affected by the addition of an uptake coefficient of 0.2 for HO₂ above ~0.7 ppb NO. Below this, MCM_αpinene_SA underpredicts RO₂ slightly more. At the lowest NO concentration, RO₂ under-prediction increases from 1.08 for MCM_αpinene to 1.16 for MCM_αpinene_SA.

7.3.2.1 Rate of Destruction Analysis: Effect of HO₂ uptake on the HO₂ Loss Pathways within the Models Using $\gamma_{HO_2} = 0.2$.

A Rate of Destruction Analysis (RODA) is done to determine the main loss processes of a chosen radical. A RODA was done for the MCM_αpinene model with the main loss pathways of HO₂ being HO₂ + O₃, HO₂ + OH, HO₂ self-reaction, HO₂ + RO₂, net HO₂ + NO₂ (HO₂ + NO₂ ⇌ HO₂NO₂), HO₂ + NO and HO₂ uptake (for the MCM_αpinene_SA model). The dominant loss pathway of HO₂ in MCM_αpinene was HO₂ + NO (89 ± 15 %), followed by HO₂ + RO₂ (6.9 ± 11 %). The RODA of HO₂ for MCM_αpinene (no heterogeneous uptake) is shown in Figure 7.10.

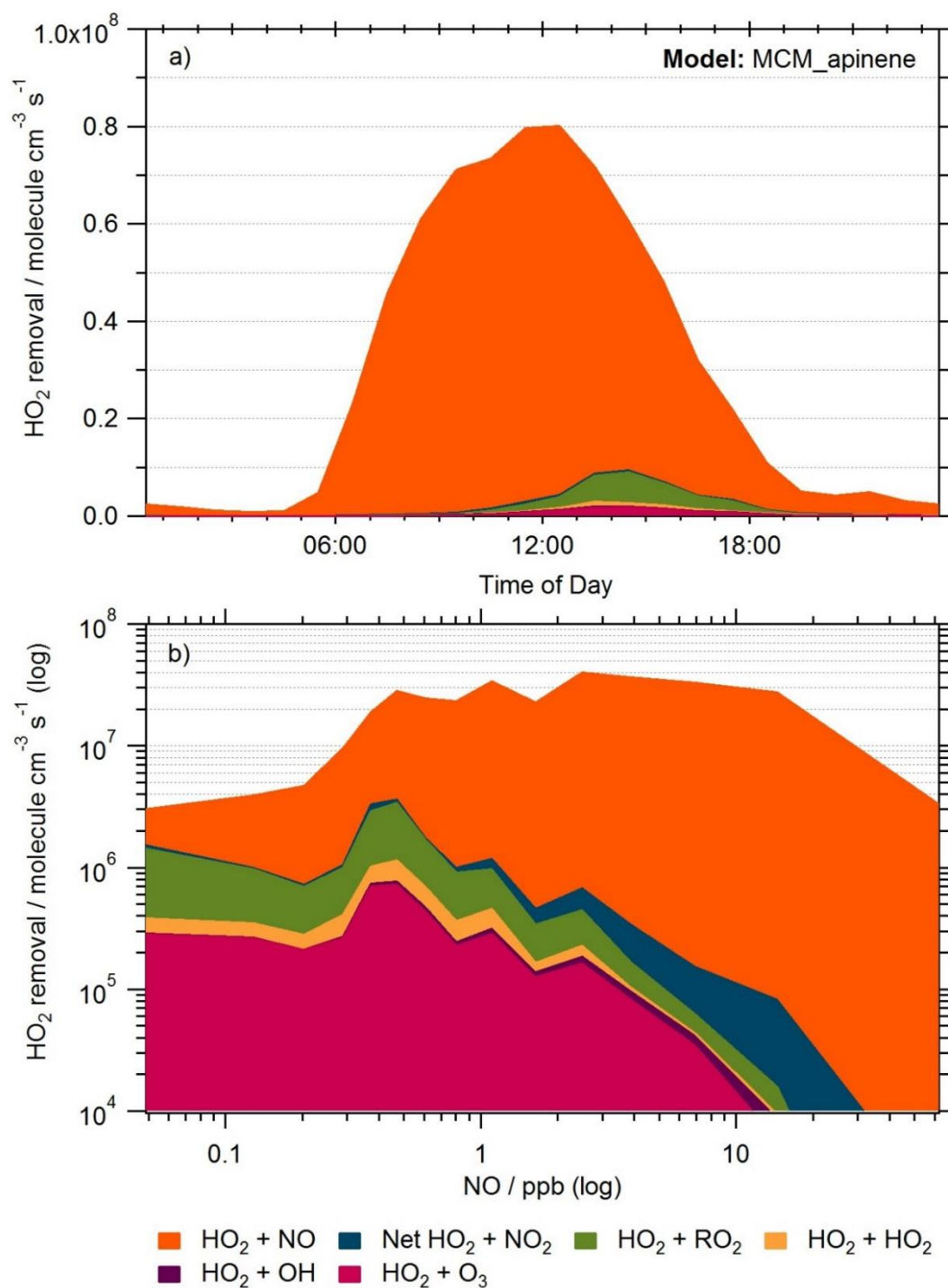


Figure 7.10. Rate of destruction analysis (RODA) showing the dominant loss pathways of HO₂ within MCM_αpinene shown as a) a diurnal variation and b) as a function of NO concentration (as a log plot) for the whole 24 hours a day.

As shown in Figure 7.10b, with decreasing NO concentration, the importance of other loss pathways, other than HO₂+NO, increases. NO concentration peaked in the morning due to rush hour traffic then decreased across the remainder of the day, as shown in Figure 7.1. At the lowest NO concentration, i.e. <0.1 ppb NO, the most

important loss pathways are $\text{HO}_2 + \text{NO}$ ($54 \pm 19 \%$), $\text{HO}_2 + \text{RO}_2$ ($31 \pm 19 \%$) and $\text{HO}_2 + \text{O}_3$ ($9.1 \pm 3.6 \%$). It is worth noting that as NO concentration decreases the fraction of HO_2 removal via $\text{HO}_2 + \text{O}_3$ reaction increases, suggesting the reaction of $\text{O}_3 + \text{HO}_2$ may be important to consider with NO_x pollution in China decreasing: this is due to the titration reaction of $\text{O}_3 + \text{NO}$, meaning that under lower NO_x conditions the O_3 levels will be higher. The loss pathways of HO_2 are compared for low NO (<0.1 ppb) and higher NO (>10 ppb) in Table 7.3.

	HO_2+O_3	HO_2+OH	HO_2+HO_2	HO_2+RO_2	Net HO_2+NO_2	HO_2+NO
Average for <0.1 ppb NO	9.1 ± 3.6	0.07 ± 0.05	2.7 ± 1.9	31 ± 19	2.6 ± 3.1	54 ± 19
Average for >10 ppb NO	$0.01 \pm$ 0.02	$0.004 \pm$ 0.007	$0.001 \pm$ 0.002	$0.009 \pm$ 0.018	0.08 ± 0.14	99 ± 0.2

Table 7.3. Average fractional contribution (%) of individual HO_2 loss pathways to total HO_2 loss in MCM_αpinene.

For the Summer Beijing Campaign, no strong correlation between $\text{PM}_{2.5}$ and NO_x was seen. This was not true for the winter Beijing AIRPRO campaign when a strong correlation between $\text{PM}_{2.5}$ and NO was seen due to the presence of haze events (Slater et al., 2020) A correlation plot between aerosol surface area ($\text{cm}^2 \text{ cm}^{-3}$) and NO_x mixing ratio is shown in Figure 7.11.

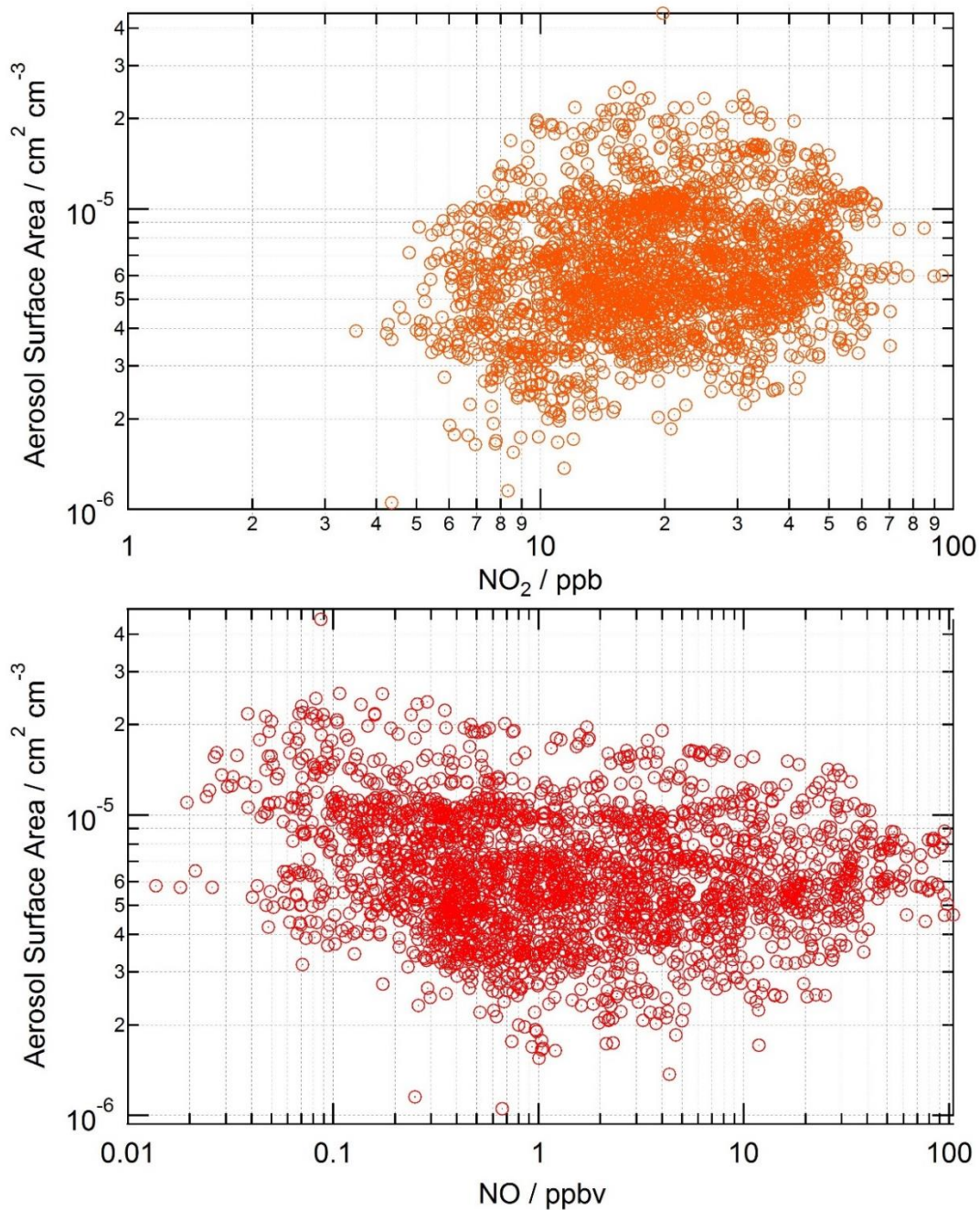


Figure 7.11. Correlation plot of aerosol surface area (cm² cm⁻³) against NO₂ (orange) and NO (red) for the Summer Beijing Campaign.

A RODA analysis was then performed with the MCM_αpinene_SA model to determine the effect adding HO₂ uptake has on the loss pathways of HO₂, shown in Figure 7.12. As with the MCM_αpinene model RODA shown in Figure 7.10, the dominant loss pathway was HO₂ + NO for all NO concentrations during the Summer AIRPRO campaign.

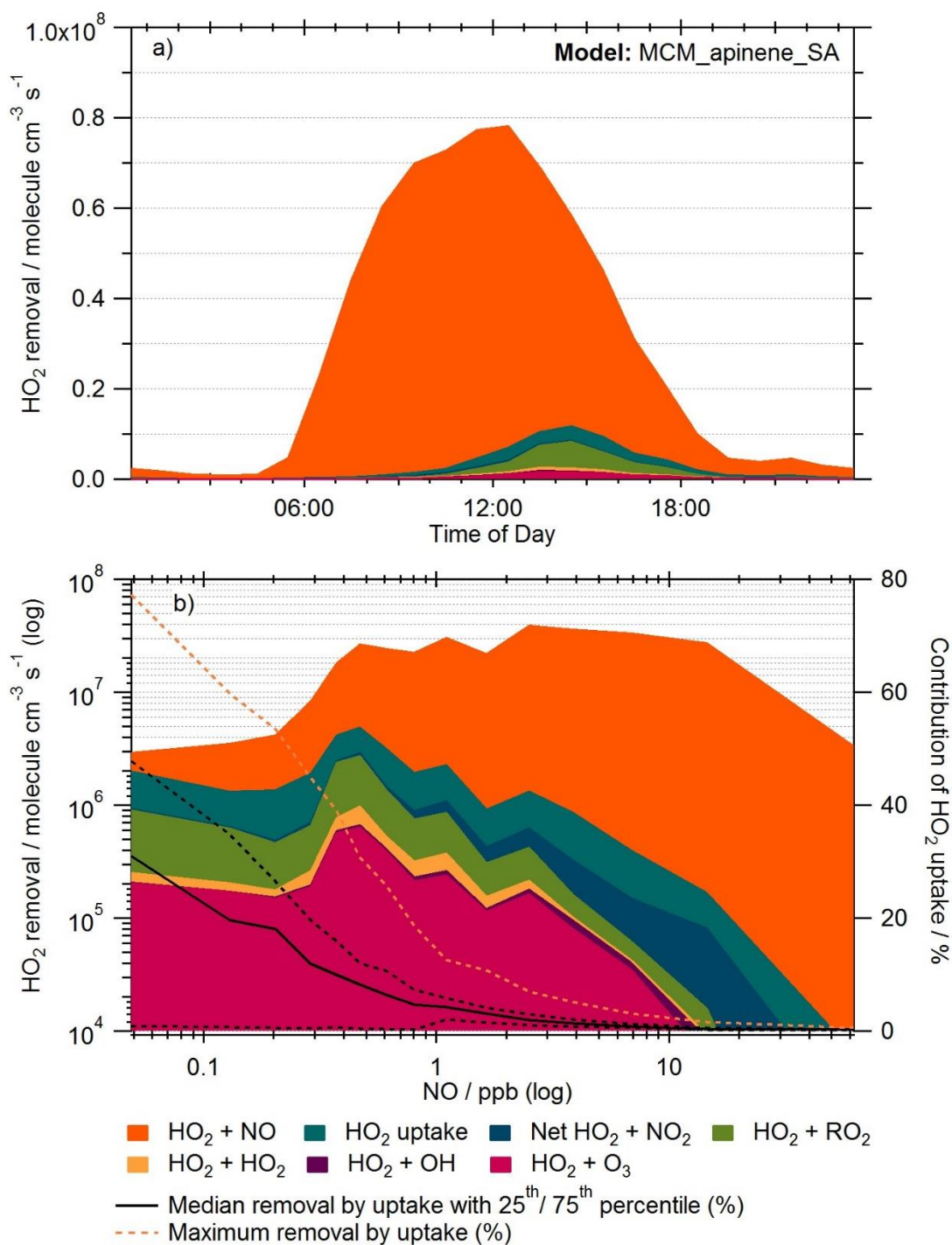


Figure 7.12. Rate of destruction analysis (RODA) showing the dominant loss pathways of HO₂ within MCM_apinene_SA shown as a) a diurnal variation and b) as a function of NO concentration (as a log plot) for the whole 24 hours a day. Median removal of HO₂ by uptake (%) as a function of NO / ppb is also shown as solid black line, with 25th/75th percentile shown as the black dashed lines. Maximum percentage removal by uptake is shown as an orange dashed line.

The contribution of HO₂ uptake to overall HO₂ removal increases with decreasing NO concentration, as do all other loss pathways with HO₂ uptake contributing 28 ± 23 %

on average below 0.1 ppb NO. The percentage contribution of the various loss pathways of HO₂ at low and high NO in the MCM_αpinene_SA are shown in Table 7.4.

	HO ₂ +O ₃	HO ₂ +OH	HO ₂ +HO ₂	HO ₂ +RO ₂	Net HO ₂ +NO ₂	HO ₂ +NO	uptake
Average for <0.1 ppb NO	6.6 ± 3.1	0.05 ± 0.05	1.4 ± 1.2	21 ± 14	1.6 ± 2.1	42 ± 23	28 ± 23
Percentage change for <0.1 ppb NO (%)^a	-27.4	-28.7	-48.2	-32.3	-38.5	-22.2	-
Average for >10 ppb NO	0.01 ± 0.02	0.004 ± 0.007	0.001 ± 0.002	0.009 ± 0.017	0.08 ± 0.14	99 ± 0.3	0.29 ± 0.24
Percentage change for <10 ppb NO (%)^a	<1	<1	<1	<1	<1	<1	-

Table 7.4. Average contribution (%) of individual HO₂ loss pathways to total HO₂ loss in MCM_αpinene_SA. ^aThe percentage change is normalised to the original MCM_αpinene model contribution for each pathway. Above 10 ppb NO, HO₂ + NO loss pathway dominates and so the addition of HO₂ uptake is not significant.

Addition of HO₂ uptake has the most effect on the relative importance of the HO₂ + HO₂ and net HO₂ + NO₂ loss pathways for low NO environment, with the percentage contribution of HO₂ + HO₂ decreasing by 48 %, and the contribution of net HO₂ + NO₂ decreasing by 38.5 %. Because both of these pathways have a much lower contribution to the total loss of HO₂, with HO₂ self-reaction only contributing 1.4 % and HO₂ + NO₂ only contributing 1.6 %, the decrease in the HO₂ + RO₂ loss reaction, by a factor of 0.68 (32 %), with the addition of HO₂ uptake is more noteworthy.

For aerosol loss using an uptake coefficient of 0.2, the average median contribution to total HO₂ loss was found to be 28 % at the lowest NO; with the maximum contribution of 78 % (on 27/05/2017 20:45). As well as in Beijing, this is also significant for high aerosol, low NO environments where other loss pathways become dominant such as off the coast of Africa. In forested areas with high SOA from biogenics emission and low NO, HO₂ uptake could also be a dominant loss pathway. To better illustrate this, the percentage contribution of HO₂ + NO, HO₂ uptake and HO₂ + RO₂ loss pathways to the overall rate of removal of HO₂ are shown as a function of NO in Figure 7.13.

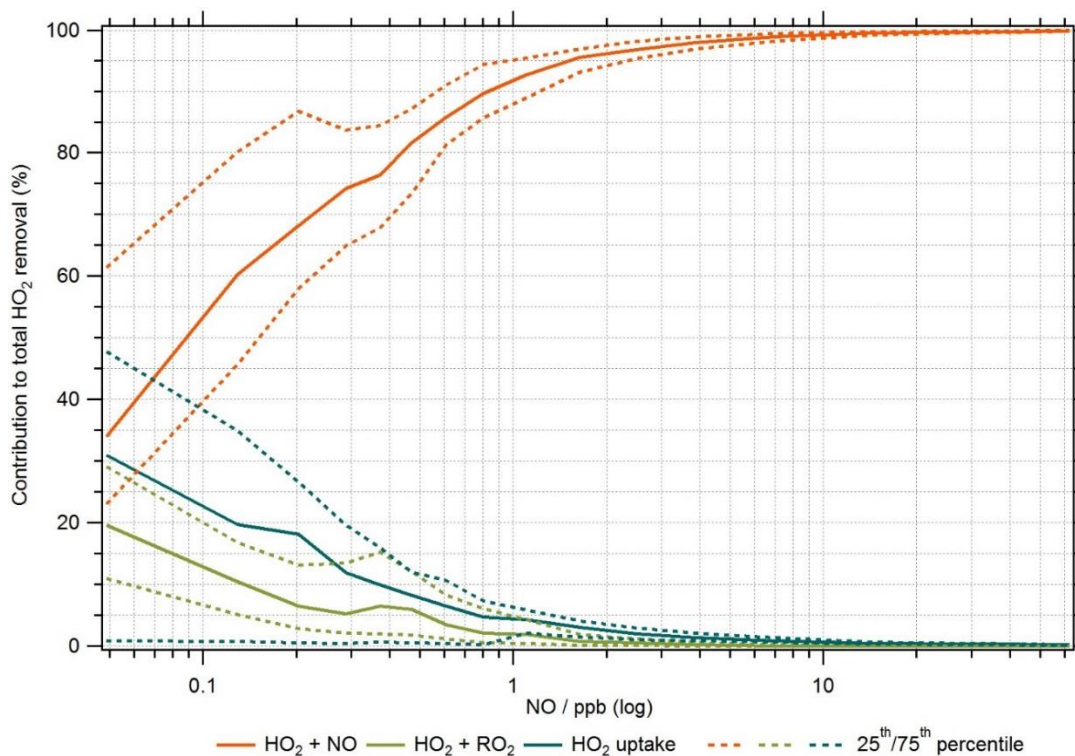


Figure 7.13. Contribution of HO₂ + NO (orange), HO₂ + RO₂ (green) and HO₂ uptake (teal) loss pathways to total HO₂ removal in the MCM_αpinene_SA model as a function of NO mixing ratio (log), calculated using rate of destruction analysis. 25th/75th percentile are shown as dashed lines.

In the last decade, in response to the poor air quality “crisis” in China, the Chinese government has implemented multiple policies with the aim to reduce emissions of pollutants (Jin et al., 2016). Following this, a number of studies have documented the decrease in NO_x and PM_{2.5} emissions. NO_x emissions over 48 Chinese cities were reported to have decreased by 21 % in the period of 2011-2015 (Liu et al., 2017) with consistent declines in NO_x reported by numerous studies (Krotkov et al., 2016; Liu et al., 2016; Miyazaki et al., 2017; van der A et al., 2017). Ma et al., 2016a reported a mean annual decrease in PM_{2.5} between 2008-2013 of 0.46 μg m⁻³ while Lin et al., 2018 reported an average decrease of 0.65 μg m⁻³ yr⁻¹ between 2006-2010 increasing to a decline of 2.33 μg m⁻³ yr⁻¹ for the period of 2011-2015. Silver et al., 2018 reported a median decrease of 3.4 μg m⁻³ yr⁻¹ across China for PM_{2.5} in the period of 2015-2017. However, with the decrease in NO_x and PM_{2.5} emissions, several studies have reported increasing ozone levels. An increase in maximum daily average 8h mean (MDA8) ozone concentrations of 1.13 ppb yr⁻¹ was reported for the period between 2003-2015 at a rural site 100 km North East of Beijing (Ma et al., 2016b). Satellite observations suggested tropospheric ozone has increased by ~7% for the period

between 2005-2010 (Verstraeten et al., 2015). For 2015-2017 a significant increase in ozone concentrations was seen with median rates of MDA8 reported to be $4.6 \mu\text{g m}^{-3} \text{ yr}^{-1}$ across China (Silver et al., 2018).

A recent study using the regional model, GEOS-Chem, suggested the increase in ozone across China between 2013-2017 could be attributed to the decrease in $\text{PM}_{2.5}$ concentration via a mechanism described below, and that changes in $\text{PM}_{2.5}$ were more important than changes in NO_x or VOC emissions in driving the increasing O_3 trends for the period studied. The decrease in $\text{PM}_{2.5}$ concentration also led to a decrease in the loss of HO_2 to aerosol uptake resulting in an increase in the concentration of HO_2 . This would then proportionally increase the rate of loss of HO_2 by reaction with NO leading to an decrease in the titration of O_3 by NO (Li et al., 2018). It is worth noting, however, that a constant uptake coefficient of 0.2 was used within the model by Li et al., 2018 with HO_2 uptake being the dominant HO_x radical loss pathway (up to $\sim 50\%$) below 2 km altitude (Li et al., 2018) when $\text{OH} + \text{NO}_2$, $\text{HO}_2 + \text{RO}_2$, $\text{HO}_2 + \text{CH}_3\text{O}_2$, $\text{HO}_2 + \text{OH}$, $\text{HO}_2 + \text{HO}_2$ and HO_2 uptake pathways were considered – this does not agree with the results of modelling studies for AIRPRO Beijing. In comparison, a more recent study using data from a 2014 field campaign in the North China Plain, reported that HO_2 aerosol uptake did not significantly impact radical chemistry with an average calculated uptake coefficient of 0.08 ± 0.13 for the conditions during the campaign (Tan et al., 2020). Box modelling studies showed that the inclusion of 0.08 as an uptake coefficient only affected the modelled HO_2 concentration by 17 % compared to the model where aerosol uptake was not included. This uptake coefficient of 0.08 is much lower than the value of 0.2 which is generally used within models, and is much more representative of experimental values, discussed fully in Section 1.10.3. To investigate the impact of HO_2 aerosol uptake on the HO_2 radical budget and therefore the hypothesis of HO_2 uptake on a trend of reducing concentration of aerosols being a cause of recent increased ozone concentration in China, an uptake coefficient for the Summer Beijing AIRPRO campaign in 2017 was calculated using a novel parameterisation.

7.3.3 Testing a Novel Parameterisation for the Influence of Aerosol Copper Concentration on HO₂ Uptake

Within modelling studies, the recommended value of 0.2 for the uptake coefficient of HO₂ onto aerosol surfaces is commonly used (Jacob, 2000). However, experimentally much lower values of the uptake coefficient have been measured with values ranging from <0.05 for dry single component salt aerosols (Taketani et al., 2008; George et al., 2013) up to 0.2 for deliquesced salt aerosols (Thornton and Abbatt, 2005; Taketani et al., 2008; George et al., 2013). Higher γ_{HO_2} have been measured for aerosols doped with copper (II) ions, with γ_{HO_2} values being in some cases significantly higher than the value of 0.2 recommended by Jacob, 2000, and approaching the mass accommodation coefficient, as discussed in Section 1.11 (Mozurkewich et al., 1987; Thornton and Abbatt, 2005; Taketani et al., 2008; George et al., 2013; Lakey et al., 2016b). Several recent studies using ambient aerosols have suggested high values for γ_{HO_2} : a study with samples taken from Mt Tai in China reported uptake coefficient values ranging from 0.13 to 0.34 (Taketani et al., 2012) while another study in Japan directly measured γ_{HO_2} values in Kyoto under ambient conditions, reporting values from 0.08 to 0.36 (Zhou et al., 2020). The Taketani et al., 2012 study measured the uptake coefficient using an offline method of collecting filter samples on location and then measuring the uptake via laser induced fluorescence in the laboratory. Zhou et al., 2020, criticised this method due to the limitation of offline methods meaning that there could be degradation of short-lived species in the aerosol during transit from the collection site to the laboratory for analysis. Another drawback for the filter collection method is that aerosols must be dissolved in a solvent to remove them from the aerosol filter and re-aerosolise for analysis: this could distort the composition of the aerosols and effect the uptake coefficient measured. In comparison, Zhou et al., 2020 measured γ_{HO_2} directly using an online method, namely via laser-flash photolysis laser induced fluorescence technique coupled with a versatile aerosol concentration enrichment system (VACES) to enrich ambient aerosols. It is not stated in this study how the VACES system effects the composition of the aerosols however, as this was not measured after the VACES, within which the RH can change drastically potentially effecting the phase and composition of the ambient aerosols. Previous studies however have shown that chemical composition of ambient PM is not affected by the VACES (Kim et al., 2001). A later study by the same group using the VACES

reported $\gamma_{HO_2} = 0.05 - 0.33$ during the 2019 Air QUALity Study (AQUAS) in Yokohama, Japan (Zhou et al., 2020). A 2014 modelling study (Xue et al., 2014) focussing on the precursors, transport and heterogeneous chemistry of ground level ozone in four major Chinese cities identified HO₂ uptake as a source of uncertainty when considering ozone production with aerosol HO₂ uptake having the largest effect in Beijing where the highest aerosol loadings were measured.

One the biggest uncertainties in determining the effect of HO₂ uptake onto aerosols in the atmosphere is the lack of understanding of the dependence of γ_{HO_2} on copper/transition metal ion concentration within the aerosol. Experimentally, the dependence of γ_{HO_2} on transition metal ion concentrations is quite well known, however the effective concentrations in ambient aerosols and the impact of aerosol liquid water concentration, [ALWC], upon γ_{HO_2} has not been incorporated into atmospheric models before. A novel parameterised equation was developed by Song et al., (2020) in the framework of the resistor model, discussed fully in Section 1.6.1, to take into account the influence of aerosol soluble copper on HO₂ uptake (Song et al., 2020). The new parameterisation for the uptake coefficient is as follows:

$$\frac{1}{\gamma_{HO_2}} = \frac{1}{\alpha_{HO_2}} + \frac{3 \times v_{HO_2}}{(4 \times 10^6) \times R_d H_{eff} RT \times \left(5.87 + 3.2 \ln \left(\frac{ALWC}{[PM] + 0.067} \right) \right) \times [PM]^{-0.2} \times [Cu^{2+}]_{eff}^{0.65}} \quad \text{Eq 7.1}$$

where γ_{HO_2} is the uptake coefficient of HO₂ onto aerosols, α_{HO_2} is the mass accommodation coefficient of HO₂, v_{HO_2} is the mean molecular speed in cm s⁻¹, R_d is the count median radius of the aerosol in cm, H_{eff} is the effective Henry's Law constant calculated from $H_{eff} = H_{HO_2} \left(1 + \frac{K_{eq}}{[H^+]} \right)$ where H_{HO_2} is the physical Henry's Law constant for HO₂ (i.e. 3900 (Thornton et al., 2008)) in M atm⁻¹, K_{eq} is the equilibrium constant for HO₂ dissociation (M), and $[H^+]$ is the hydrogen ion concentration within the aerosol calculated from the pH (M), R is the gas constant in cm³ atm K⁻¹ mol⁻¹ (i.e. 82.05), T is the temperature in K, $ALWC$ is the aerosol liquid water content in μg m⁻³ (which is related to the ambient relative humidity), $[PM]$ is the mass concentration of PM_{2.5} in μg m⁻³ and $[Cu^{2+}]_{eff}$ is the effective aerosol condensed-phase soluble copper (II) ion concentration in mol L⁻¹.

The new parameterisation can be used for typical urban environmental conditions which span aerosol mass concentrations of 10-300 μg m⁻³; aqueous copper (II)

concentrations of 10^{-5} – 1 mol L^{-1} ; and relative humidity between 40-90 %. For the Summer AIRPRO campaign data, the minimum [ALWC] the parameterisation supported was $14 \mu\text{g m}^{-3}$ so for the entire campaign, this value was used. Below this value the parameterisation returned negative values for the uptake coefficient. The average calculated [ALWC] for the campaign was $6.9 \pm 10 \mu\text{g m}^{-3}$ (variability during the campaign shown in Section 6.3.3.1).

7.3.3.1 Calculated γ_{HO_2} for Summer AIRPRO campaign

Measured values for [PM], copper (II) ion concentration, aerosol pH (used to calculate H_{eff}), and calculated values for ALWC were input into the parameterisation for the entire summer campaign. R_d was also calculated from the measured size distribution of aerosols across the entire campaign. A value of 0.5 was chosen to reflect a_{HO_2} values previously measured for copper doped inorganic salts (Thornton and Abbatt, 2005; Taketani et al., 2008; George et al., 2013). For the summer AIRPRO campaign the soluble copper ion concentration was measured by extracting copper (II) ions from filter samples and analysing using Inductively Coupled Plasma Mass Spectrometry (ICP-MS). The total copper (II) mass concentration (ng m^{-3} converted to g m^{-3}) was then divided by the aerosol volume concentration ($\text{nm}^3 \text{ cm}^{-3}$ converted to $\text{dm}^3 \text{ m}^{-3}$) and the molar mass of copper (g mol^{-1}) to give the total copper molar concentration in the aerosol, $[Cu^{2+}]_{eff}$ (mol L^{-1}), which is used in Eq 7.1. The average values used in the model are shown in Table 7.5.

Parameter	Average value across campaign
Temperature (K)	300
Relative humidity (%)	43
Aerosol pH	3
Count median radius (cm)	2.3×10^{-6}
ALWC ($\mu\text{g m}^{-3}$) ^a	14
[PM] ($\mu\text{g m}^{-3}$)	38.3
[Cu ²⁺] _{eff} (mol L ⁻¹ / ng m ⁻³)	0.0008 / 4
α_{HO_2}	0.5 (fixed)

Table 7.5. Average parameter values for the Summer AIRPRO campaign in Beijing 2017. ^aThis is the minimum required ALWC for which the parameterisation can be used. For most of the campaign the ALWC was below $14 \mu\text{g m}^{-3}$. Copper (II) ion concentration is given in both mol L⁻¹ and ng m⁻³ due to mol L⁻¹ being the unit used in the parameterisation but ng m⁻³ being a more atmospherically relevant unit.

For the average value of the parameters shown in Table 7.5, γ_{HO_2} for the Beijing Summer AIRPRO campaign 2017 was calculated to be 0.07, the uncertainty in this calculation is considered below. The calculated values of the uptake coefficient using Eq. 6.1. ranged from 0.002 to 0.15 across the campaign. The time series for the calculated uptake coefficient in addition to R_d , [PM], [ALWC] and [Cu²⁺]_{eff} is shown for the entire AIRPRO Summer campaign in Figure 7.14. Figure 7.14 shows that the parameterisation gave negative values of γ_{HO_2} some of the time when measured ALWC was used (dashed grey line, right hand axis) with the calculated uptake coefficient following the trend in ALWC closely across the campaign. When using a [ALWC] = $14 \mu\text{g m}^{-3}$, the minimum value necessary to ensure all calculated uptake values are > 0 , the calculated uptake coefficient follows [Cu²⁺]_{eff} and the inverse of [PM] more closely, as expected from Eq 7.1.

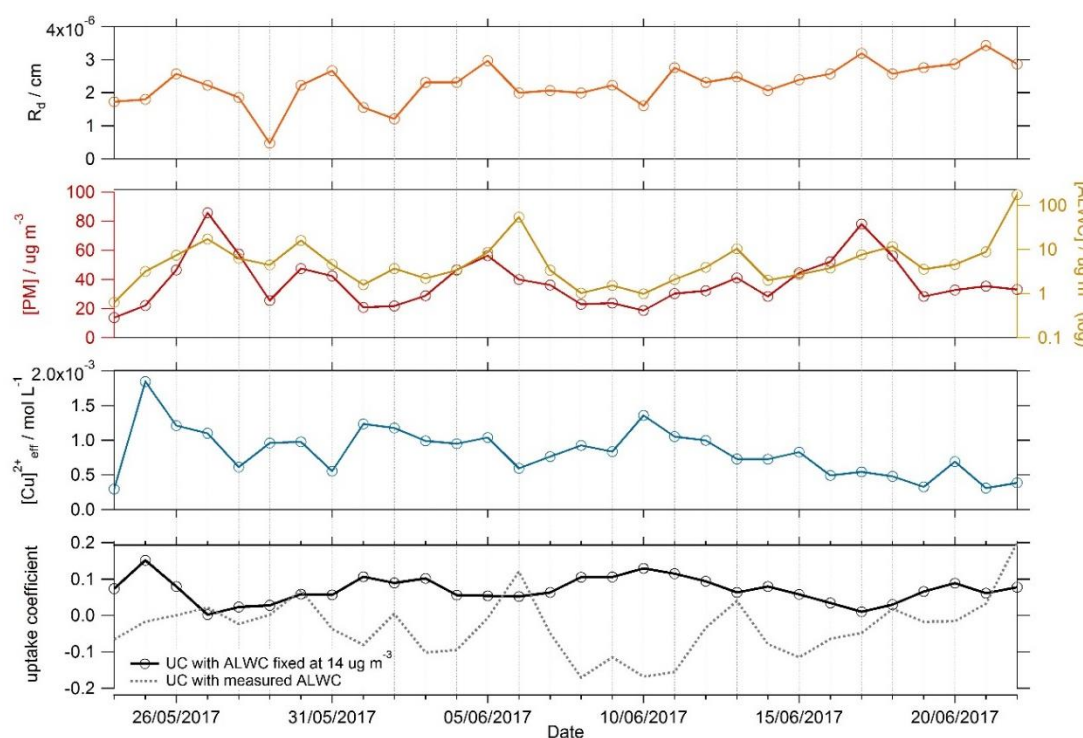


Figure 7.14. Time series of measured parameters from Beijing AIRPRO Summer campaign used to calculate HO_2 uptake coefficient using the new parameterisation (Song et al., 2020). Each parameter has been averaged up to a 1 day time resolution to calculate the uptake coefficient due to measured $[\text{Cu}^{2+}]_{\text{eff}}$ and $[\text{PM}]$ being at this resolution. The calculated γ_{HO_2} is shown in the bottom panel, for conditions where measured ALWC was used in the calculation (dashed grey line, right hand axis) in comparison to when a fixed $[\text{ALWC}] = 14 \text{ ug m}^{-3}$ was used (solid black line, left hand axis)

The uncertainty in the calculation of γ_{HO_2} using the new parameterisation comes mainly from the uncertainty in the calculated ALWC (10-20 %; calculated using ISORROPIA-II thermodynamic equilibrium model (Fountoukis and Nenes, 2007), the uncertainty in the mass accommodation coefficient, and the uncertainty of the model calculations used to formulate this new parameterisation (~ 40 %). Uncertainties in measured parameters i.e. temperature, $[\text{PM}]$, $[\text{Cu}^{2+}]$ and count median radius are due to associated instrumental error which are assumed small in comparison. Therefore, an overall error of ~60 % is assumed. It is worth noting the standard deviation of the calculated uptake coefficient across the campaign was 0.035, i.e. 49% error. As such an average value of $\gamma_{\text{HO}_2} = 0.070 \pm 0.035$ (1σ) is calculated for the Summer AIRPRO campaign using the parameterisation.

The calculation of ALWC by ISORROPIA-II model (named after the Greek for ‘equilibrium’) makes several assumptions, namely that aerosol curvature effects are not

important and that ambient water vapour pressure is not effected by aerosol water uptake. When 2 thermodynamic models, ISOPROPIA-II and SCAPE (Simulating Composition of Atmospheric Particles at Equilibrium), were compared predictions of ALWC agreed within ~13 % between the two models (Fountoukis and Nenes, 2007).

The mass accommodation coefficient of HO₂ is influenced by multiple factors such as aerosol composition, phase and temperature. As there was no measurement of the mass accommodation coefficient under the conditions for the Summer AIRPRO campaign, a sensitivity analysis was performed showing the maximum $\gamma_{HO_2} = 0.077 \pm 0.04$ (1 σ) occurred when a_{HO_2} is taken as 1 (Table 7.6). This value for γ_{HO_2} is still significantly lower than the value of 0.2 conventionally used within regional, global and box model studies.

a_{HO_2}	γ_{HO_2}
0.1	0.042 ± 0.016
0.2	0.056 ± 0.024
0.5	0.070 ± 0.035
0.8	0.075 ± 0.039
1.0	0.077 ± 0.041

Table 7.6. Sensitivity analysis showing effect of changing the mass accommodation coefficient, a_{HO_2} , on the calculated average γ_{HO_2} for the Summer AIRPRO campaign in Beijing, 2017.

7.3.3.2 Comparison to γ_{HO_2} estimated for the Wangdu Campaign

In the Song et al., 2020 study the new parameterisation was tested on data from the comprehensive 2014 field campaign at a rural site in the North China Plain (Wangdu). Beijing is located 170 km northeast of Wangdu with the closest city to Wangdu being Baoding, 35 km to the northwest. During the campaign, measurements of OH, HO₂, RO₂, OH reactivity, photolysis frequencies, O₃, NO_x, HONO, CO, CO₂, H₂O, SO₂, CH₄, HCHO and VOCs were made. Average daytime measurements for variables relevant to the novel parameterisation for the Wangdu campaign are shown in Table 7.7.

Parameters	Average Values across Wangdu campaign
Temperature (K)	300
RH (%)	61
ALWC ($\mu\text{g m}^{-3}$)	68.2
[PM] ($\mu\text{g m}^{-3}$)	67.2
[Cu] ²⁺ ($\text{mol L}^{-1}/\text{ng m}^{-3}$)	0.0005 / 35.8
Aerosol pH	3.41
Count median radius (cm)	3×10^{-6}

Table 7.7. Average measured parameters in new parameterisation for the Wangdu 2014 campaign (Song et al., 2020). Copper (II) ion concentration given in both mol L^{-1} and ng m^{-3} due to mol L^{-1} being the unit used in the parameterisation but ng m^{-3} being a more atmospherically relevant unit.

Measurements were carried out during the summer of 2014 when severe smog pollution events were noted (Tan et al., 2017). The Wangdu area is a high temperature and humidity environment with a monsoon climate and high copper concentrations. In a more recent paper, the uptake coefficient for the Wangdu campaign was calculated by comparing HO_2 field data with HO_2 modelled concentrations and estimating the HO_2 aerosol uptake coefficient required to close the radical budget for each day. The proposed γ_{HO_2} for the Wangdu campaign using this method was quoted as 0.08 ± 0.13 (Tan et al., 2020). Using the novel parameterisation, Song et al., 2020 estimated an average value of 0.116 ± 0.086 (using a mass accommodation coefficient of 0.5) for γ_{HO_2} for the conditions of the Wangdu campaign which agrees with the value calculated by Tan et al., 2020 within the uncertainty. The RH during the Wangdu campaign showed significant diurnal variation, ranging from 15 to 97% RH with an average RH value of 61 %.

In 2012, Taketani et al., 2012 measured the uptake coefficient of HO_2 on aerosol samples taken from Mt Tai and Mt Mang in North China. The measured γ_{HO_2} for Mt Tai ranged from 0.09 to 0.4 while the γ_{HO_2} for Mt. Mang samples ranged from 0.13 to 0.34. The results from these field campaigns suggest that γ_{HO_2} could be larger or smaller than the value of 0.2 commonly used in models and could vary significantly for typical conditions seen in North China.

The calculated γ_{HO_2} for Summer AIRPRO campaign of 0.07 ± 0.04 is comparable to that calculated for the Wangdu campaign by Song et al., 2020, i.e. 0.116 ± 0.086 , for the same mass accommodation coefficient of 0.5. The uptake coefficient depends on [PM], [ALWC] and $[Cu^{2+}]_{eff}$, with the strongest dependence on $[Cu^{2+}]_{eff}$. [PM] and [ALWC] were lower for Summer Beijing 2017 than for the Wangdu 2014 campaign. While total copper mass concentration in $ng\ m^{-3}$ in Beijing was lower than the Wangdu campaign, due to differences in R_d and aerosol volume, the $[Cu^{2+}]_{eff}$ for Beijing was slightly higher than the Wangdu $[Cu^{2+}]_{eff}$ concentration. The R_d value was higher for the Wangdu campaign, suggesting a higher aerosol volume which could explain the similar total copper molar aerosol concentration ($mol\ L^{-1}$) values for $[Cu^{2+}]_{eff}$ between the two campaigns despite Wangdu having a mass concentration of $35.8\ ng\ m^{-3}$ of copper compared to $4\ ng\ m^{-3}$ average in Beijing AIRPRO campaign. The similar values of $[Cu^{2+}]_{eff}$, but lower [ALWC] and [PM] explain why the estimated uptake coefficient values for Beijing are lower than that for Wangdu campaign. The [ALWC] for Wangdu campaign was much higher than for Beijing campaign, an average of $68.2\ \mu g\ m^{-3}$ compared to $6.94\ \mu g\ m^{-3}$, due to both the higher RH and the larger R_d . Table 7.8 shows a comparison of the measured parameters used within the parameterisation for the both the Wangdu and Beijing campaigns. The relationship between the calculated [ALWC] and the measured RH for Beijing Summer Campaign is shown in Figure 7.15 demonstrating that higher RH in Wangdu will be driving the increased [ALWC] for the Wangdu campaign compared to Beijing campaign.

Parameters	Average Values for Wangdu	Average Values for Beijing
ALWC ($\mu\text{g m}^{-3}$)	68.2	6.94 (fixed as 14 in parameterisation)
Relative humidity (%)	61	43
[PM] ($\mu\text{g m}^{-3}$)	67.2	38
[Cu] _{eff} ²⁺ ($\text{mol L}^{-1}/\text{ng m}^{-3}$) 3)	0.0005 / 35.8	0.0008 / 4
Count median radius, R_d (cm)	3×10^{-6}	1.5×10^{-6}

Table 7.8. Comparison of measured parameters in new parameterisation for the Summer AIRPRO Beijing 2017 Campaign and the Wangdu 2014 campaign (Wangdu campaign values from Song et al., 2020)

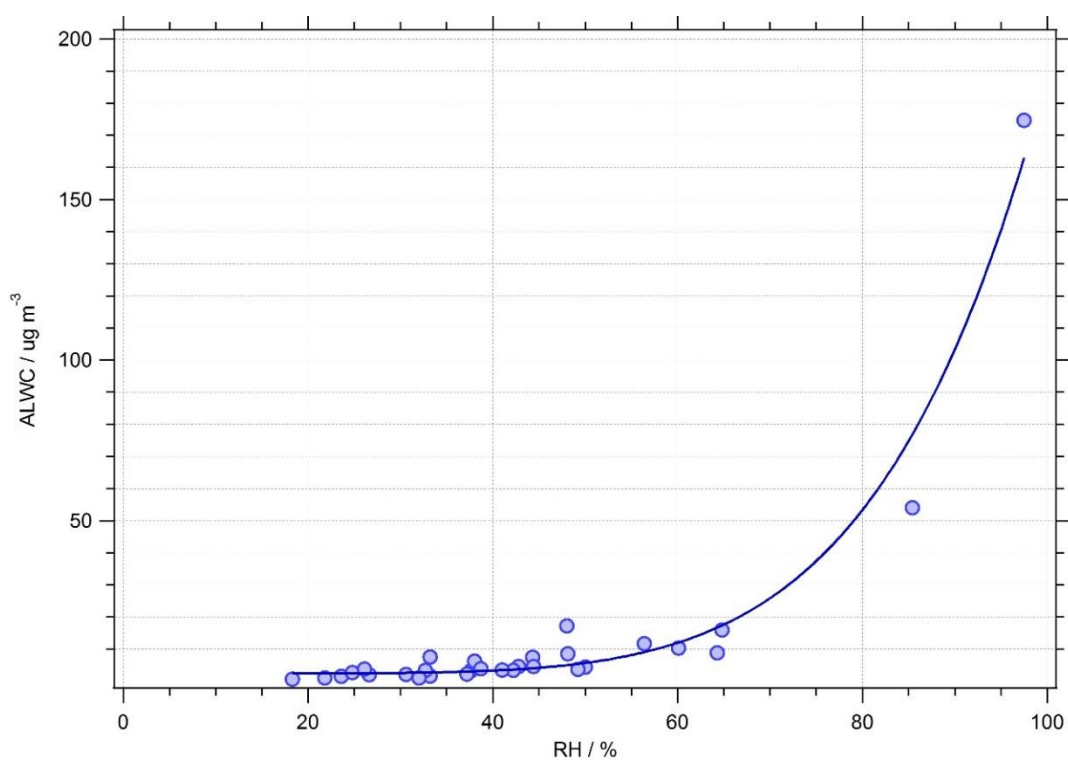


Figure 7.15. Relationship between the calculated [ALWC] / $\mu\text{g m}^{-3}$ and the measured relative humidity (RH) / % for Beijing Summer Campaign. [ALWC] calculated using ISOPROPRIA model. RH measured with a dewpoint hygrometer.

Looking at the effect of [PM] and [ALWC] on the uptake coefficient of HO₂ as a function of copper molarity for the new parameterisation (Eq 7.1) shows that for a fixed [ALWC], an increase in PM causes a decrease in the curvature of the uptake coefficient against copper (II) concentration, whereas for fixed [PM], increasing [ALWC] leads to an increase in uptake coefficient for a given copper concentration. As shown in Figure 7.16, the effect of [ALWC] and [PM] on the HO₂ uptake coefficient is the greatest between [Cu²⁺]_{eff} = 10⁻⁵ and 10⁻¹ M when the curve is at its steepest before levelling off towards the mass accommodation coefficient of 0.5. As such, if a different mass accommodation coefficient was used in the calculation, the uptake coefficient would tend towards that value instead of 0.5. For a fixed value of [ALWC] = 14 ug m⁻³ and a fixed value of [PM] = 38.3 ug m⁻³ (the average values for the Beijing AIRPRO Summer campaign), the variation of the calculated uptake coefficient as a function of [Cu²⁺]_{eff} is also shown in Figure 7.16. For these fixed [ALWC] and PM values, the curve is at its steepest between [Cu²⁺]_{eff} ~ 10⁻³ and 10⁻¹ M. The average [Cu²⁺]_{eff} for the Beijing campaign was 8 × 10⁻⁴ M, with values ranging from 3 × 10⁻⁴ to 2 × 10⁻³ M across the campaign.

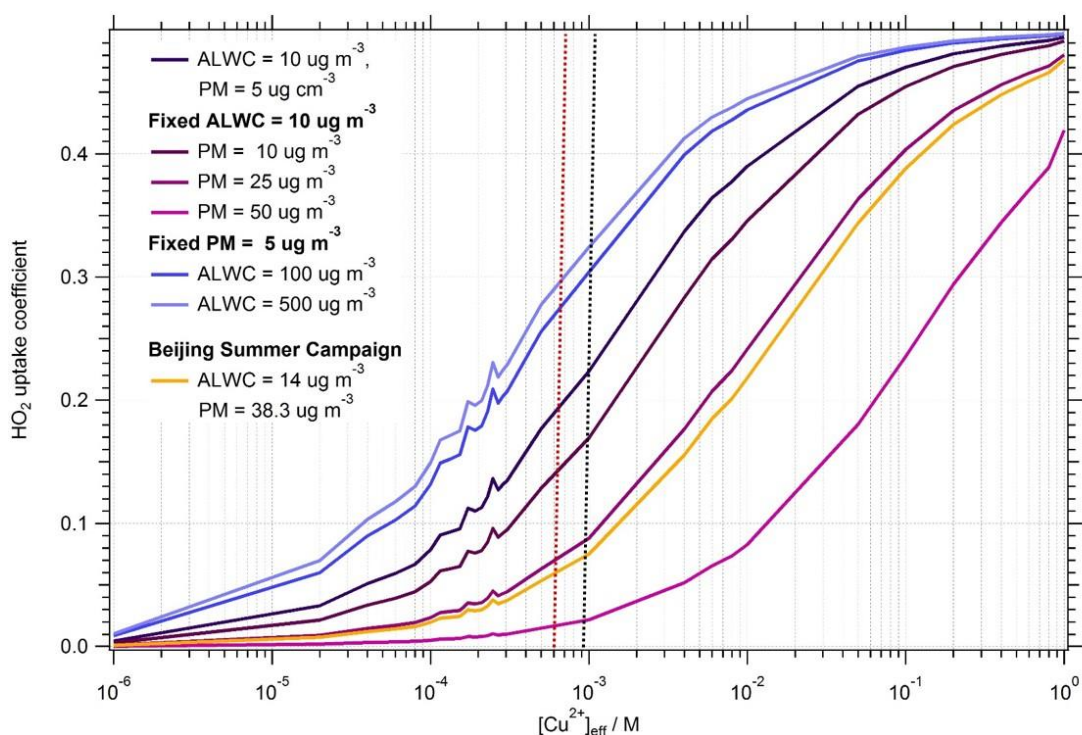


Figure 7.16. Dependence of uptake coefficient on aerosol copper concentration, $[\text{Cu}]^{2+}_{\text{eff}}$, focusing on the effect of varying $[\text{PM}]$ with fixed $[\text{ALWC}]$ and vice versa. Pink lines show the effect on uptake coefficient of varying $[\text{PM}]$ from 5-50 $\mu\text{g m}^{-3}$ with a fixed $[\text{ALWC}]$ of 10 g cm^{-3} . Blue lines show the effect on uptake coefficient of varying $[\text{ALWC}]$ from 10-500 $\mu\text{g m}^{-3}$ with a fixed $[\text{PM}]$ of 5 $\mu\text{g m}^{-3}$. The copper concentration range of 10^{-4} - 10^{-3} M is relevant for the Summer AIRPRO campaign. The yellow line shows the effect on the calculated uptake coefficient of varying Cu, with $[\text{ALWC}]$ and $[\text{PM}]$ taken as the averages from the Beijing campaign, i.e. $[\text{ALWC}] = 14 \mu\text{g m}^{-3}$ (fixed in parameterisation as such) and $[\text{PM}] = 38.8 \mu\text{g m}^{-3}$. Dashed black line indicates the average $[\text{Cu}]^{2+}_{\text{eff}}$ for Beijing summer campaign while the dashed red line indicates the average $[\text{Cu}]^{2+}_{\text{eff}}$ for the Wangdu campaign. Note that the $[\text{PM}]$ and $[\text{ALWC}]$ are both higher for Wangdu campaign compared to the Beijing campaign.

7.3.3.3 Effect of γ_{HO_2} on radical concentrations in Summer Beijing

To examine the effect of the HO_2 uptake on the concentration of OH , HO_2 and RO_2 in the Summer AIRPRO campaign, the uptake coefficient calculated using measured data from Summer AIRPRO campaign, as described in Section 7.3.3.1, was added to the MCM_apinene model to give the MCM_apinene_gamma model. All measured parameters were either given at a time resolution of 1 day or were averaged up to this time resolution. The average of the calculated γ_{HO_2} across the campaign was 0.070 ± 0.035 (1σ) with a minimum value of 0.002 on 27/05/2017 and a maximum value of 0.15 on 25/05/2017.

The comparison of modelled radical concentrations for MCM_αpinene, MCM_αpinene_SA (for which the uptake coefficient of HO₂ is taken as 0.2, fully described in Section 0) and MCM_αpinene_gamma is shown in Figure 7.17.

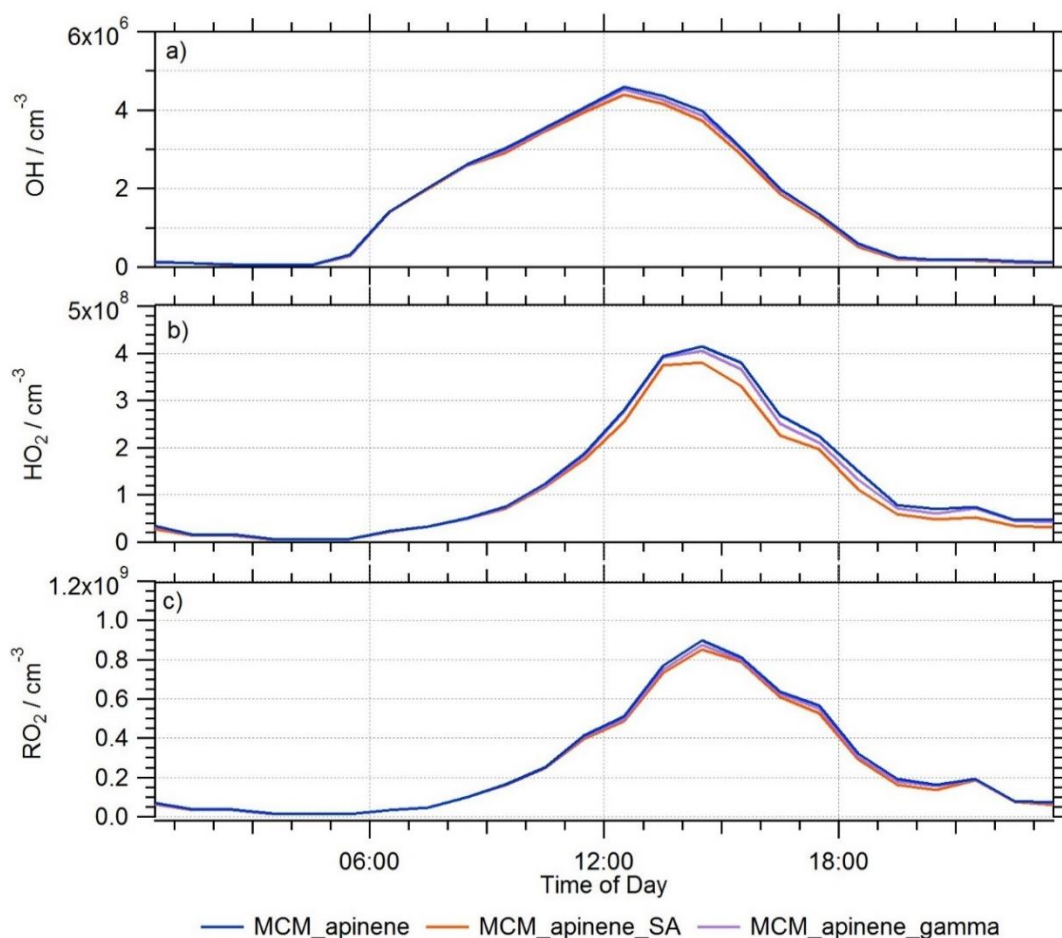


Figure 7.17. Average median diurnal comparison for modelled a) OH, b) HO₂ and c) RO₂ radicals from MCM_αpinene (blue), MCM_αpinene_SA (orange) and MCM_αpinene_SA (lilac) models. All diurnals are averaged at a time resolution of 60 minutes. 25th/75th percentile shown as dashed lines.

As expected, including the calculated uptake coefficient, varying from 0.002 to 0.15 (0.07 as an average across campaign) had only a small effect on the diurnal radical concentrations. The average median diurnal comparison shows that, on average, the OH and RO₂ concentrations were not significantly affected by the addition of HO₂ aerosol uptake across the Summer Beijing campaign. While the average median HO₂ concentration at the 14:30 peak still decreases with the addition of HO₂ uptake coefficient (average of ~0.07), the decrease was much less than seen in MCM_αpinene_SA where the uptake coefficient was taken as 0.2 across the entire campaign. To showcase this better, the measured to modelled ratios of OH, HO₂ and RO₂ for MCM_αpinene and MCM_αpinene_gamma were binned against NO as

shown in Figure 7.18. Very little difference between MCM_αpinene and MCM_αpinene_gamma is seen for OH, HO₂ or RO₂ in Figure 7.18, as expected for a small uptake coefficient.

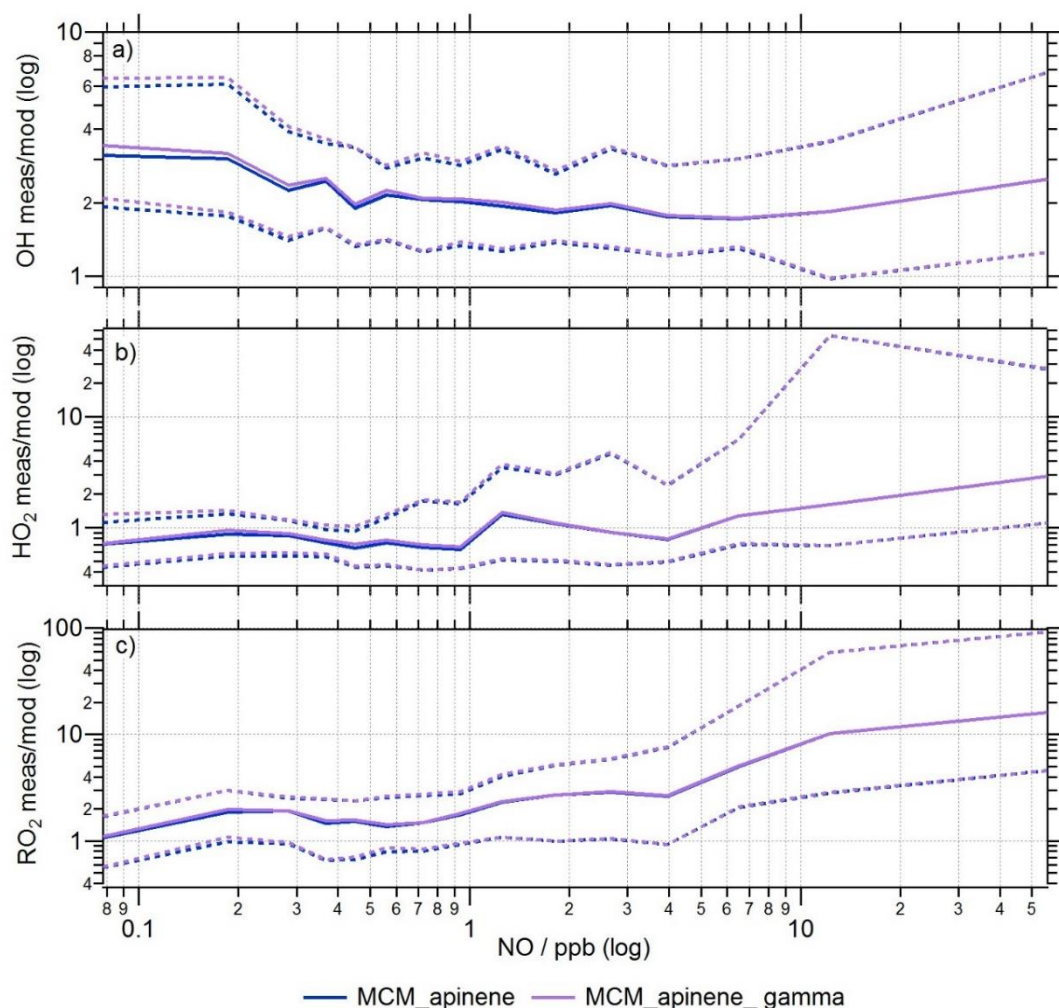


Figure 7.18. The ratio of measured/modelled OH, HO₂ and RO₂ for MCM_αpinene (blue) and MCM_αpinene_gamma (lilac) models binned over the range of NO concentrations for the Summer AIRPRO campaign for day-time values only ($j(\text{O}^1\text{D}) > 1 \times 10^6 \text{ s}^{-1}$). Solid lines show the median average radical concentrations while dashed lines show the 25th/75th percentile.

A rate of destruction analysis (RODA) was performed for MCM_αpinene_gamma to showcase the contribution of HO₂ uptake to the overall loss of HO₂. The RODA is shown in Figure 7.19. As for the MCM_αpinene and MCM_αpinene_SA models, the dominant loss pathway of HO₂ is HO₂ + NO across the entire campaign.

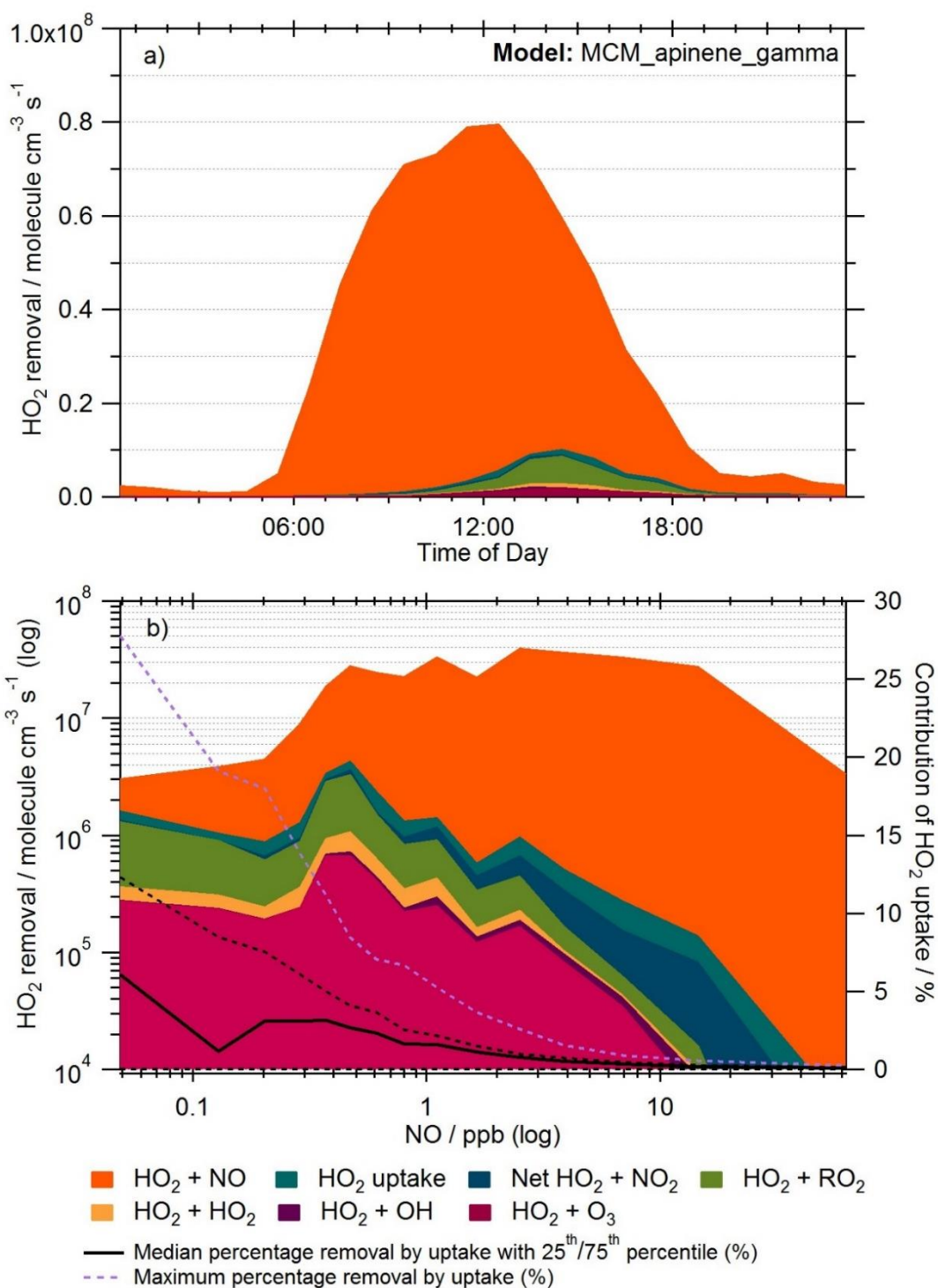


Figure 7.19. Rate of destruction analysis (RODA) showing the dominant loss pathways of HO₂ within MCM_αpinene_gamma shown as a) a diurnal variation and b) as a function of NO concentration. Median removal of HO₂ by uptake (%) as a function of NO / ppb is shown as solid black line, with 25th/75th percentile shown as the black dashed lines. Maximum percentage removal by uptake for a given NO mixing ratio is shown as a lilac dashed line.

As shown in Figure 7.19b, with decreasing NO concentration, the importance of other loss pathways, other than HO₂ + NO, increases. At the lowest NO concentration, i.e.

< 0.1 ppb NO, the most important loss pathways are on average HO₂ + NO (51 ± 19 %), HO₂ + RO₂ (29 ± 17 %), HO₂ + O₃ (8.5 ± 3.4 %) and HO₂ uptake (6.7 ± 6.7 %). At low NO concentrations, HO₂ uptake becomes more important as a removal pathway for HO₂ meaning that even with a smaller uptake coefficient, HO₂ uptake is still important to consider. To showcase this the percentage contribution to total HO₂ removal of HO₂ uptake for the Summer Campaign, as calculated using RODA, for MCM_αpinene, MCM_αpinene_SA and MCM_αpinene_gamma is compared for <0.1 ppb NO in Table 7.9 (contributions are compared for the lowest NO to show the maximum contribution of uptake, and the minimum contribution of HO₂ + NO in the model).

	HO ₂ +O ₃	HO ₂ +OH	HO ₂ +HO ₂	HO ₂ +RO ₂	Net HO ₂ +NO ₂	HO ₂ +NO	uptake
MCM_αpinene	9.1 ± 3.6	0.07 ± 0.05	2.7 ± 1.7	31 ± 19	2.6 ± 3.1	54 ± 19	-
MCM_αpinene_gamma (av. γ=0.07)	8.5 ± 3.4	0.07 ± 0.05	2.3 ± 1.6	29 ± 17	2.4 ± 2.8	51 ± 19	6.7 ± 6.7
MCM_αpinene_SA (γ=0.2)	6.6 ± 3.1	0.05 ± 0.05	1.4 ± 1.2	21 ± 14	1.6 ± 2.1	42 ± 23	28 ± 23

Table 7.9. Average contribution (%) of individual HO₂ loss pathways to total HO₂ loss in MCM_αpinene (shaded blue), MCM_αpinene_gamma (shaded lilac) and MCM_αpinene_SA (shaded orange) for <0.1 ppb NO

This comparison shows that while the modelled diurnal radical concentrations for OH, HO₂ and RO₂ are not significantly affected when using an average uptake coefficient of 0.07 (ranging from 0.002-0.15 across the campaign) due to the high (>0.1 ppb) concentrations of NO, on days where the NO concentration is very low, smaller uptake coefficients than just using γ=0.2 could still have a significant effect on total HO₂ loss. The contribution of HO₂ uptake to total HO₂ removal is binned against NO concentration for MCM_αpinene_SA and MCM_αpinene_gamma in Figure 7.20.

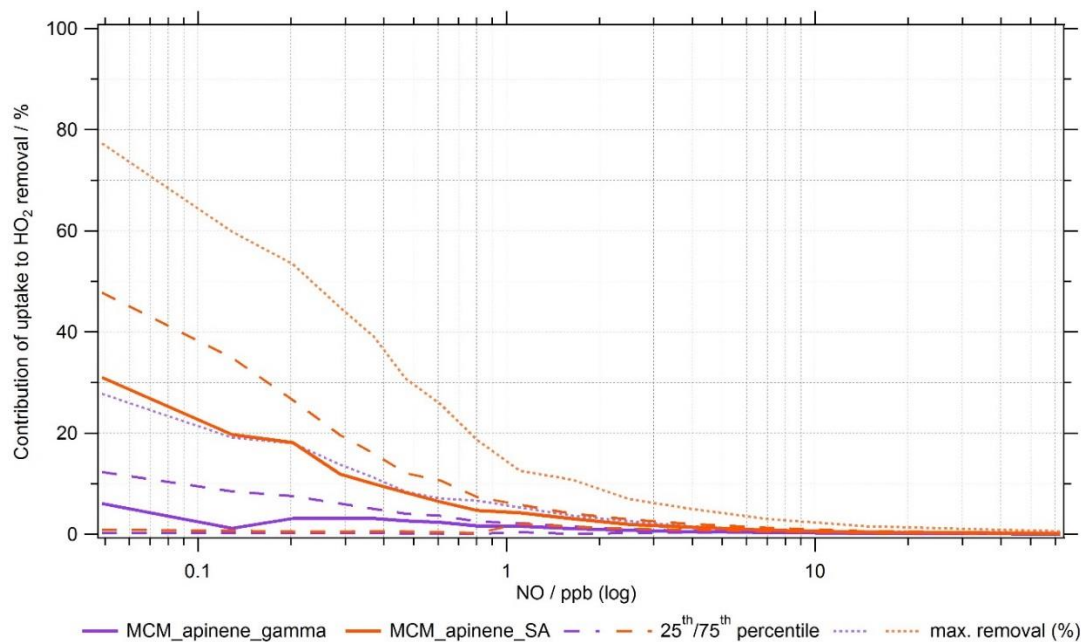


Figure 7.20. Percentage contribution of HO₂ uptake to HO₂ removal as seen in MCM_apinene_SA model (blue line, $\gamma_{HO_2} = 0.2$) and MCM_apinene_gamma model (purple line, $\gamma_{HO_2} = 0.070 \pm 0.035$) for Summer AIRPRO Beijing campaign plotted as a function of NO concentration / ppb. Dashed lines represent the 25th/75th percentiles.

Though there is not as much of a dependence on NO mixing ratio for an uptake coefficient of 0.07 ± 0.035 in MCM_apinene_gamma, compared to an uptake coefficient of 0.2 in MCM_apinene_SA, it can be seen that up to 28 % of total loss of HO₂ could still be due to heterogeneous uptake onto aerosol surfaces under low NO conditions, which is significant. For a higher uptake coefficient of 0.2, as recommended by Jacob, 2000, a maximum contribution of ~78 % can be seen <0.1 ppb. A time series of calculated uptake coefficient plotted with NO mixing ratio and aerosol surface area for the entire summer campaign is shown in Figure 7.21. There is not a strong correlation between aerosol surface area and NO_x for this campaign, as shown in Figure 7.11. However, on days where the NO mixing ratio is low and aerosol surface area is high, the uptake of HO₂ onto aerosols could be important. For the Beijing AIRPRO campaign, 27/05/2017-29/05/2017, 06/06/2017-07/06/2017 and 17/06/2017-18/06/2017 are examples of days when these conditions are met. For these days the calculated uptake coefficients are respectively: 0.002, 0.023, 0.028, 0.056, 0.054, 0.009 and 0.029.

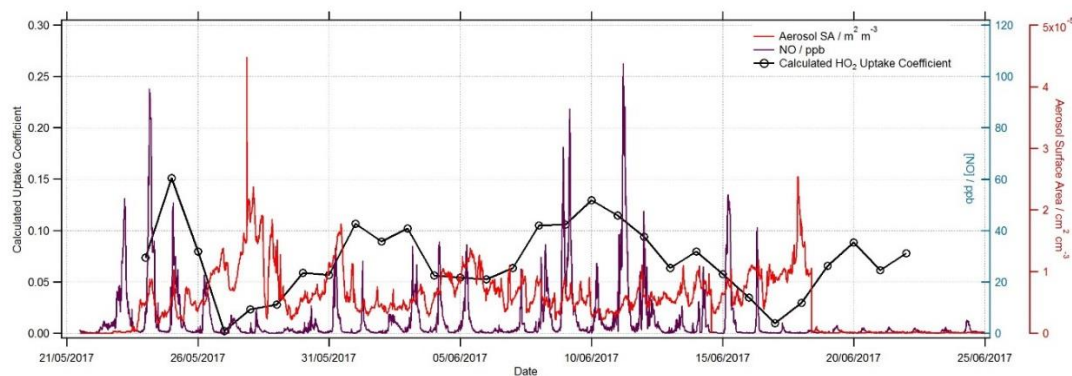


Figure 7.21. Time series of calculated HO₂ uptake coefficient (black line and markers), measured aerosol surface area/ m² m⁻³ (red line) and measured NO/ ppb (purple line) for the Summer AIRPRO campaign. Time resolution for uptake coefficient is 1 day while the time resolution for NO mixing ratio and aerosol surface area is 15 minutes.

7.4 Modelling Summary

In this chapter, the OH, HO₂ and RO₂ radical concentrations were modelled for the Summer AIRPRO campaign in Beijing using the Master Chemical Mechanism v.3.3.1 and compared to the measured concentrations. The effect of HO₂ uptake onto aerosols was then investigated using 2 models, MCM_αpinene_SA and MCM_αpinene_gamma. Using a new parameterisation given by Song et al., 2020, the HO₂ uptake coefficient was calculated for the Summer AIRPRO campaign as a function of [Cu²⁺]_{eff}, [ALWC] and [PM]. For the entire campaign the average HO₂ uptake coefficient calculated was 0.070 ± 0.035 , with values ranging from 0.002 to 0.15. The effect of calculated uptake coefficient on HO₂ concentration using MCM_αpinene_gamma, was then compared to the effect of inputting a fixed HO₂ uptake coefficient of 0.2 (commonly used within global and regional models) using MCM_αpinene_SA.

Rate of destruction analysis showed that for MCM_αpinene_SA, with $\gamma_{HO_2} = 0.2$, the main loss pathways of HO₂ at low NO (i.e. <0.1 ppb) were HO₂ + NO (42 ± 23 %), HO₂ uptake (28 ± 23 %), HO₂ + RO₂ (21 ± 14 %), and HO₂ + O₃ (6.6 ± 3.1 %). At higher NO (i.e. >10 ppb), the dominant loss pathway of HO₂ is HO₂ + NO (99 ± 0.3 %) showing that HO₂ uptake, even with a high uptake coefficient, is not a dominant loss of HO₂ in high NO environments such as Beijing. However during low NO conditions, up to 78 % of HO₂ loss was due to HO₂ uptake within MCM_αpinene_SA, which is a significant loss pathway.

The calculated uptake coefficients, using the parameterisation presented by Song et al., 2020, ranging from 0.002 to 0.15 had only a small effect on the overall radical concentration due to the usually high NO conditions across the campaign. However, at low NO conditions, i.e. <0.1 ppb, the rate of destruction analysis showed up to 28 % of HO₂ loss was by uptake to aerosols. As such, in clean environments, for conditions where NO is low but aerosol surface area is high such as forested regions where biogenics emissions are high away from urban centres or outflows from dust events over oceans, an $\gamma_{HO_2} < 0.2$ could still have a significant effect on the overall HO₂ concentration.

8 Conclusions and Future Work

8.1 Overview

The reactive uptake of NO₂ to form HONO onto single component TiO₂ aerosols in the presence of NO₂ and mixed TiO₂/NH₄NO₃ aerosols in the absence of NO₂ was measured using an aerosol flow reactor coupled to a highly sensitive photo-fragmentation laser induced fluorescence detector and an SMPS. The effect of RH on the uptake of NO₂ to form HONO onto TiO₂ was also investigated. A PAM chamber was characterised for the production of secondary organic aerosols from ozonolysis and OH-initiated reaction with VOCs. The uptake of HO₂ onto limonene-derived SOAs was then measured leading to discovery of two interferences, one from the reaction of residual limonene and OH from the injector and the second proposed to be due to RO₂ species desorbing from aerosol surfaces. Lastly, the effect of HO₂ uptake onto aerosol surfaces in summertime in Beijing was modelled using the Master Chemical Mechanism and a novel parameterisation by Song et al., 2020.

8.2 Production of HONO from Illuminated TiO₂ aerosols surfaces

The photo-fragmentation laser induced fluorescence instrument coupled to an aerosol flow-tube was validated for the measurement of HONO from aerosol surfaces. The PF-LIF instrument was successfully calibrated for both OH and HONO with calibration factors in N₂ determined to be $C_{OH} = (6.34 \pm 0.96) \times 10^8$ counts cm⁻³ molecule⁻¹ s⁻¹ mW⁻¹ and $C_{HONO} = (3.63 \pm 0.51) \times 10^9$ counts mW⁻¹. The limit of detection for HONO was then calculated to be 9 ppt for a 50 s averaging period and a SNR of 1.

The production of HONO from illuminated TiO₂ aerosol surfaces in the presence of NO₂ was investigated with the reactive uptake coefficient of NO₂ to form HONO for NO₂ mixing ratios of 34 - 400 ppb found to be in the range of $\gamma_{NO_2 \rightarrow HONO} = (9.97 \pm 3.51) \times 10^{-6}$ at 286 ppb to a maximum of $\gamma_{NO_2 \rightarrow HONO} = (1.26 \pm 0.17) \times 10^{-4}$ at 51 ppb NO₂ at 298 K. The photolysis rate coefficient of NO₂, $j(NO_2)$, was calculated using NO₂ chemical actinometry, and with this and the knowledge of the relationship between $j(NO_2)$, the absorption cross-section (σ_λ) for NO₂ and the spectral intensity of the lamp over the wavelength range of 290 -400 nm, the lamp photon flux could be calculated as

$(1.65 \pm 0.02) \times 10^{16}$ photons $\text{cm}^{-2} \text{s}^{-1}$ for 1 lamp and a $j(\text{NO}_2)$ of $(6.43 \pm 0.30) \times 10^{-3} \text{s}^{-1}$. This allows a HONO production rate to be calculated for a given light intensity.

The uptake coefficients measured varied with increasing NO_2 mixing ratio showing an increase followed by a decrease as a function of NO_2 , peaking at $51 \text{ ppb} \pm 5 \text{ ppb}$ NO_2 – the increase to 51 ppb being a trend contrary to previous literature which investigated HONO production on humic acid aerosols (Stemmler et al., 2007) and Arizona Test Dust (Dupart et al., 2014) as a function of $[\text{NO}_2]$. To investigate this, a kinetic scheme within a box model was created, with multiple mechanisms studied in order to explain the experimental observations. Modelling studies supported a mechanism involving two NO_2 molecules per HONO molecule generated, suggesting the formation of an NO_2 dimer intermediate, the exact mechanism of which is unclear. Previous studies on NO_2 dimer intermediates would suggest that the process occurs via the isomerisation of the symmetric N_2O_4 dimer on the aerosol surface to give *trans*-ONO- NO_2 , either via *cis*-ONO- NO_2 or directly, suggested to be more reactive with water than the symmetric dimer (Finlayson-Pitts et al., 2003; Ramazan et al., 2004b; Ramazan et al., 2006; de Jesus Madeiros and Pimentel, 2011; Liu and Goddard, 2012; Murdachaew et al., 2013; Varner et al., 2014).

Using the maximum experimental uptake coefficient of $\gamma_{\text{NO}_2 \rightarrow \text{HONO}} = (1.26 \pm 0.17) \times 10^{-4}$, scaled to ambient light levels in Beijing, a production rate of HONO was estimated using average daytime values from the AIRPRO Summer 2017 campaign ($[\text{NO}_2] = 50 \text{ ppb}$, $j(\text{NO}_2) = 1 \times 10^{-2} \text{s}^{-1}$ and aerosol surface area = $2.5 \times 10^{-3} \text{m}^2$ (of which 0.3 % was taken to be TiO_2)) to represent Summertime in Beijing. A HONO production rate of $1.70 \times 10^5 \text{ molecules cm}^{-3} \text{s}^{-1}$ ($\sim 24.8 \text{ ppt h}^{-1}$) was estimated: similar to the maximum production of HONO from urban humic acid aerosols in Europe, 17 ppt hr^{-1} , as reported by Stemmler et al., (2007). The net gas phase production of HONO was calculated under the same conditions in Beijing and found to be -3.8 ppb hr^{-1} , a net loss of HONO due to the large daytime HONO photolysis loss, suggesting that the production of HONO from TiO_2 aerosol surfaces in the presence of NO_2 would have little effect on the overall HONO budget for summertime in Beijing.

In addition to the uptake coefficient, the RH dependence of HONO production on TiO₂ surfaces at multiple NO₂ concentrations was investigated showing a peak in HONO production at ~ 30 % RH. At a higher NO₂ concentration the peak was slightly shifted to a lower RH, with more production at all RH's investigated. This shift in the peak is mostly likely due to the active sites filling faster with increasing RH if the concentration of NO₂ is higher, especially if NO₂ or the reaction of NO₂ with H₂O or other species poisons the surface of TiO₂, reducing the catalytic effect. It is also possible that increased NO₂ concentration decreases the effect light intensity which reaches the surface of the TiO₂ due to the NO₂ in gas phase adsorbing the light, thereby reducing the photolytic reactions which can occur to form HONO on the surface: this was not characterised in this work however. An increase in HONO production to a peak with RH can be attributed to the increased availability of water for the reaction with NO₂ to form HONO, though over a certain concentration, the water could competitively inhibit the adsorption of NO₂ to the surface thereby decreasing the production of HONO.

For non-urban environments, NO₂ concentrations is typically much lower and therefore the uptake of NO₂ to form HONO on aerosol surfaces would be expected to be much lower.

In the absence of NO₂, the production of HONO from ammonium nitrate aerosols was also investigated to determine if nitrate aerosols were a significant source of HONO via particulate nitrate photolysis or indeed if TiO₂ could catalyse the formation of HONO from nitrate. For pure deliquesced ammonium nitrate aerosols however, significant production of HONO was not seen for the range of conditions tested. With the addition of TiO₂ however, the production of HONO seen was significant with increasing aerosol surface area. Using experimental results for mixed TiO₂/ammonium nitrate experiment, a rate of HONO production from nitrate photolysis was calculated for ambient conditions in marine environments, taking the conditions in Cape Verde as an example of such environments. The rate of production was calculated to be 68 ppt hr⁻¹ which is similar in magnitude to the missing HONO production rate calculated previously for the RHaMBLe campaign, suggesting a significant production from particulate nitrate photolysis in the remote marine boundary layer.

8.2.1 Future Work

Future work would involve studying production of HONO from pure nitrate aerosols over a wider range of conditions for example RH, temperature and aerosol pH. It would be interesting to introduce a seed aerosol or other chemical species which commonly found in marine environments such as halogen species like Iodine or photosensitive organics to investigate the effect on particulate nitrate photolysis and the production of HONO. More investigations into the production of HONO from ambient aerosols should be done and compared to the results on TiO₂ aerosol surfaces to fully understand the effect a photocatalytic material has on the uptake of NO₂ to form HONO and what this could mean for haze or dust events in places such as Beijing.

8.3 Uptake of HO₂ onto Limonene-derived Secondary Organic Aerosols

A Potential Aerosol Mass chamber was built for the formation of secondary organic aerosols by the oxidation of volatile organic compounds. The PAM chamber was characterised for α -pinene and limonene derived SOAs. The effect of changing limonene and O₃ concentration on the size distributions of SOA was investigated. Size distributions for SOAs formed from both α -pinene and limonene with O₃ and OH were reported.

The HO₂ uptake system, as described in Section 2 and Lakey et al., 2016, was rebuilt and validated for the measurement of uptake onto aerosols surfaces. The uptake of HO₂ onto ammonium sulphate aerosols was done first, to allow sensitivity to be tested in comparison to previous measurements made by the instrument. The uptake coefficients of HO₂ onto ammonium sulphate salt aerosols were 0.04 ± 0.01 and 0.010 ± 0.002 for 65 and 73 % RH respectively: in agreement (taking into account standard deviation) with values measured previously by George et al., 2013. Following validation of the system, the uptake of HO₂ onto limonene-derived SOA was measured. Two interferences, A and B, were seen following the addition of limonene-derived SOA into the system, postulated to be due to OH and RO₂ species being present in flow tube: Interference A was observed as a production of peroxy radicals when the injector was pulled back from the FAGE cell, while interference B was observed as a signal seen when no HO₂ was present in the system but NO was flowing

into the cell. It was found that trace amounts of both limonene (after the charcoal denuders) and OH (from the injector) were present in the system leading to production of RO₂ and HO₂ species which caused an increase in signal as the injector was pulled back from the detector. The second interference, interference B, was proposed to be due to RO₂ species coming off aerosol surfaces due to the interference only being present when SOA were present. It is also possible OH could be released from the SOA surface, leading to an interference through reaction with trace limonene in the flow-tube. NO dependence testing of both interference B and the HO₂ signal without aerosols showed that the interference was caused by RO₂ rather than HO₂. It was shown that cleaning the walls of the PAM chamber by allowing O₃ to flow through the system and remove species absorbed to the walls through reaction significantly reduced interference B, suggesting the interference was due to aged aerosols. A GC hydrocarbon trap was added into the system directly in-line and after PAM chamber and the first charcoal denuder. This significantly reduced both interferences and allowed a decay of HO₂ to be seen in the presence of aerosols and an uptake coefficient to be measured: $\gamma_{HO_2} = 0.10 \pm 0.03$ at 22 % RH and $\gamma_{HO_2} = 0.15 \pm 0.03$ at 58 % RH.

8.3.1 Future Work

The extent to which the GC trap works to remove any interfering species must be further investigated. Additionally, the GC trap caused pressure to build up in the system and therefore a new trap which removes interferences in a similar manner without the associated risk must be found. Future work would also include further studies into the source of the interference before additional experiments into the RH dependency of limonene-derived SOA can be done. It would also be worth investigating whether other, less reactive, VOCs produce an interference in the system upon ozonolysis or whether using OH or NO₃ as an oxidant may remove said interference. The interference, postulated to be due to RO₂, shows that this system can measure RO₂ and suggests that RO₂ uptake experiments could be successful. Future work would therefore be investigating RO₂ uptake onto aerosol surfaces.

8.4 Modelling the Effect of HO₂ Uptake onto Aerosols Surfaces

During AIRPRO Summer Campaign

HO₂ is often over-predicted in models and this is believed to be due, in part, to a lack of understanding of HO₂ uptake onto tropospheric aerosols. In Chapter 7, the OH, HO₂

and RO₂ radical concentrations were modelled using the Master Chemical Mechanism for the Summer AIRPRO Beijing campaign in 2017 and compared to the measured concentrations, with and without the addition of aerosol uptake of HO₂ included. In 2020, a novel parameterisation giving the uptake coefficient of HO₂ onto aerosols as a function of aerosol liquid water content ([ALWC]), particulate matter concentration ([PM]) and effective aerosol condensed-phase soluble copper (II) ion concentration ([Cu²⁺]_{eff}), was introduced by Song et al., 2020. The uptake of HO₂ was calculated using measured values from the AIRPRO Beijing campaign and the Song parameterisation. The effect of HO₂ uptake onto aerosols was then investigated using 2 models: MCM_αpinene_SA which included $\gamma_{HO_2} = 0.2$ (fixed) as commonly used in global and regional models; and MCM_αpinene_gamma which included the γ_{HO_2} calculated from the Song parameterisation and the measured campaign values of temperature, RH, aerosol pH, [ALWC], [PM] and [Cu²⁺]_{eff}. For the entire campaign, the average HO₂ uptake coefficient calculated was 0.070 ± 0.035 (1σ) with values ranging from as low as 0.002 to as high as 0.15. Notably this maximum value is still significantly lower than $\gamma_{HO_2} = 0.2$, as recommended by Jacob (2000).

Rate of destruction analysis (RODA) showed that the dominant pathway of HO₂ loss for both models, was HO₂ + NO for all NO concentrations encountered during the campaign. The RODA for MCM_α-pinene_SA ($\gamma_{HO_2} = 0.2$), showed the main loss pathways of HO₂ at low NO (i.e. < 0.1 ppb when other loss pathways have more effect on overall HO₂ loss due to less HO₂ + NO) were HO₂ + NO (42 ± 23 %), HO₂ uptake (28 ± 23 %), HO₂ + RO₂ (21 ± 14 %) and HO₂ + O₃ (6.6 ± 3.1 %). This shows that at high NO, even with a higher γ_{HO_2} of 0.2, HO₂ uptake is not a dominant loss of HO₂. However, under low NO conditions, up to 78 % of HO₂ loss was due to HO₂ uptake (depending on conditions) within MCM_αpinene_SA, which is a significant loss pathway.

As would be expected, HO₂ uptake had a much smaller effect in MCM_αpinene_gamma where the γ_{HO_2} ranged from 0.002 – 0.15. As such, averaged across the whole campaign, the effect of HO₂ uptake was very small due to the high NO concentrations. However, at low NO (i.e. < 0.1 ppb) rate of destruction analysis showed that up to 28 % of HO₂ loss was by uptake onto aerosols (compared to 78 % for $\gamma_{HO_2} = 0.2$), which is still significant. In cleaner environments away from urban

centres, where NO is low and aerosol surface area is high, γ_{HO_2} of < 0.2 could still have a significant effect on the overall HO_2 concentration.

8.4.1 Future Work

Future work would include using this parameterisation for campaigns in different environments, ideally not in urban megacities, but in surrounding areas to investigate the significance of HO_2 uptake onto aerosols away from NO sources. Campaigns in forested regions with high biogenic emissions, or areas effected by dust outflows would also be good candidates. As the parameterisation fails at low [ALWC] due to it being designed only for a given range of [ALWC], further work should be done to improve on this allowing the parameterisation to be used to model in a wider variety of environments. Additionally, though simple chemical systems are most often investigated it is important to consider more complex systems to assess the potential coupling between reactive species in multi-component aerosols, such as how TiO_2 could catalyse the uptake of HO_2 on surfaces or the effect of transition metal redox coupling chemistry on the uptake of HO_2 .

Bibliography

Abramson, E., Imre, D., Beránek, J., Wilson, J., and Zelenyuk, A.: Experimental determination of chemical diffusion within secondary organic aerosol particles, *Phys. Chem. Chem. Phys.*, 15, 2983-2991, <https://doi.org/10.1039/C2CP44013J>, 2013.

Ammann, M., Poschl, U., and Rudich, Y.: Effects of reversible adsorption and Langmuir-Hinshelwood surface reactions on gas uptake by atmospheric particles, *Phys.Chem.Phys.Chem*, 5, 351-356, <https://doi.org/10.1039/B208708A>, 2003.

Ammann, M., Cox, R. A., Crowley, J., Jenkin, M. E., Mellouki, A., Rossi, M. J., Troe, J., and Wallington, T. J.: Evaluated kinetic and photochemical data for atmospheric chemistry: Volume VI—heterogeneous reactions with liquid substrates, *Atmos. Chem. Phys.*, 13, 8045-8228, <https://doi.org/10.5194/acp-13-8045-2013>, 2013.

Assaf, E., Song, B., Tomas, A., Schoemaeker, C., and Fittschen, C.: Rate Constant of the Reaction between CH_3O_2 Radicals and OH Radicals Revisited, *J. Phys. Chem. A*, 120, 8923-8932, <https://doi.org/10.1021/acs.jpca.6b07704>, 2016.

Assaf, E., Sheps, L., Whalley, L., Heard, D., Tomas, A., Schoemaeker, C., and Fittschen, C.: The Reaction between CH_3O_2 and OH Radicals: Product Yields and Atmospheric Implications, *Environ. Sci. Technol.*, 51, 2170-2177, <https://doi.org/10.1021/acs.est.6b06265>, 2017.

Atkins, P., and Paula, J. d.: *Elements of Physical Chemistry*, 4th ed., W. H. Freeman and Co., 2005.

Atkinson, R., Baulch, D. L., Cox, R. A., Crowley, J. N., Hampson, R. F., Hynes, R. G., Jenkin, M. E., Rossi, M. J., and Troe, J.: Evaluated kinetic and photochemical data for atmospheric chemistry: Volume I - gas phase reactions of O_x , HO_x , NO_x and SO_x species, *Atmos. Chem. Phys.*, 4, 1461-1738, <https://doi.org/10.5194/acp-4-1461-2004>, 2004.

Baardsen, E. L., and Terhune, R. W.: Detection of OH in the atmosphere using a dye laser, *Appl. Phys. Lett.*, 21, 209-211, <https://doi.org/10.1063/1.1654347>, 1972.

Baxter, R. J., and Hu, P.: Insight into why the Langmuir–Hinshelwood mechanism is generally preferred, *J. Chem. Phys.*, 116, 4379-4381, <https://doi.org/10.1063/1.1458938>, 2002.

Beckers, H., Zeng, X., and Willner, H.: Intermediates involved in the oxidation of nitrogen monoxide: Photochemistry of the $\text{cis-N}_2\text{O}_2\cdot\text{O}_2$ complex and of $\text{sym-N}_2\text{O}_4$ in Solid Ne Matrices, *Chemistry— A European Journal*, 16, 1506-1520, <https://doi.org/10.1002/chem.200902406>, 2010.

Bedjanian, Y., and El Zein, A.: Interaction of NO_2 with TiO_2 Surface Under UV Irradiation: Products Study, *J. Phys. Chem. A*, 116, 1758-1764, <https://doi.org/10.1021/jp210078b>, 2012.

Bejan, I., Abd-el-Aal, Y., Barnes, I., Benter, T., Bohn, B., Wiesen, P., and Kleffmann, J.: The photolysis of ortho-nitrophenols: A new gas phase source of HONO, *Physical chemistry chemical physics : PCCP*, 8, 2028-2035, <https://doi.org/10.1039/b516590c>, 2006.

Bianchi, F., Kurtén, T., Riva, M., Mohr, C., Rissanen, M. P., Roldin, P., Berndt, T., Crounse, J. D., Wennberg, P. O., Mentel, T. F., Wildt, J., Junninen, H., Jokinen, T., Kulmala, M., Worsnop, D. R., Thornton, J. A., Donahue, N., Kjaergaard, H. G., and

Ehn, M.: Highly Oxygenated Organic Molecules (HOM) from Gas-Phase Autoxidation Involving Peroxy Radicals: A Key Contributor to Atmospheric Aerosol, *Chem. Rev.*, 119, 3472-3509, <https://doi.org/10.1021/acs.chemrev.8b00395>, 2019.

Bohn, B., Heard, D. E., Mihalopoulos, N., Plass-Dülmer, C., Schmitt, R., and Whalley, L. K.: Characterisation and improvement of j(O¹D) filter radiometers, *Atmos. Meas. Tech.*, 9, 3455-3466, <https://doi.org/10.5194/amt-9-3455-2016>, 2016.

Bottorff, B., Reidy, E., Mielke, L., Dusanter, S., and Stevens, P. S.: Development of a laser-photofragmentation laser-induced fluorescence instrument for the detection of nitrous acid and hydroxyl radicals in the atmosphere, *Atmos. Meas. Tech.*, 14, 6039-6056, <https://doi.org/10.5194/amt-14-6039-2021>, 2021.

Boucher, O., Randall, D., Artaxo, P., Bretherton, C., Feingold, G., Forster, P., Kerminen, V. M., Kondo, Y., Liao, H., Lohmann, U., Rasch, P., Satheesh, S. K., Sherwood, S., Stevens, B., and Zhang, X. Y.: *Climate Change 2013: The Physical Science basis. Contribution of Working Group I to the Fifth Assessment Report of the Intergovernmental Panel on Climate Change*, Cambridge University Press, Cambridge, 2013.

Boustead, G. A.: Measurement of nitrous acid production from aerosol surfaces using Photo-Fragmentation Laser-Induced Fluorescence, School of Chemistry, University of Leeds, 2019.

Brauer, M., Freedman, G., Frostad, J., van Donkelaar, A., Martin, R. V., Dentener, F., Dingenen, R. v., Estep, K., Amini, H., Apte, J. S., Balakrishnan, K., Barregard, L., Broday, D., Feigin, V., Ghosh, S., Hopke, P. K., Knibbs, L. D., Kokubo, Y., Liu, Y., Ma, S., Morawska, L., Sangrador, J. L. T., Shaddick, G., Anderson, H. R., Vos, T., Forouzanfar, M. H., Burnett, R. T., and Cohen, A.: Ambient Air Pollution Exposure Estimation for the Global Burden of Disease 2013, *Environ. Sci. Technol.*, 50, 79-88, <https://doi.org/10.1021/acs.est.5b03709>, 2016.

Braure, T., Bedjanian, Y., Romanias, M. N., Morin, J., Riffault, V., Tomas, A., and Coddeville, P.: Experimental Study of the Reactions of Limonene with OH and OD Radicals: Kinetics and Products, *J. Phys. Chem. A*, 118, 9482-9490, <https://doi.org/10.1021/jp507180g>, 2014.

Bröske, R., Kleffmann, J., and Wiesen, P.: Heterogeneous conversion of NO₂ on secondary organic aerosol surfaces: A possible source of nitrous acid (HONO) in the atmosphere?, *Atmos. Chem. Phys.*, 3, 469-474, <https://doi.org/10.5194/acp-3-469-2003>, 2003.

Brown, J. M.: *Molecular Spectroscopy*, Oxford University Press, Oxford, 1998.

Brown, R. L.: Tubular flow reactors with 1st-order kinetics, *Journal of Research of the National Bureau of Standards*, 83, 1-8, <https://doi.org/10.6028/jres.083.001>, 1978.

Brust, A. S., Becker, K. H., Kleffmann, J., and Wiesen, P.: UV absorption cross sections of nitrous acid, *Atmos. Environ.*, 34, 13-19, [https://doi.org/10.1016/S1352-2310\(99\)00322-2](https://doi.org/10.1016/S1352-2310(99)00322-2), 2000.

Cantrell, C., Zimmer, A., and Tyndall, G. S.: Adsorption cross sections for water vapor from 183 to 193 nm, *Geophys. Res. Lett.*, 24, 2195-2198, <https://doi.org/10.1029/97GL02100>, 1997.

Cantrell, C. A., Shetter, R. E., Gilpin, T. M., and Calvert, J. G.: Peroxy radicals measured during Mauna Loa Observatory Photochemistry Experiment 2: The data and

first analysis, *J. Geophys. Res. Atmos.*, 101, 14643-14652, <https://doi.org/10.1029/95JD01698>, 1996.

Carpenter, L. J., Fleming, Z. L., Read, K. A., Lee, J. D., Moller, S. J., Hopkins, J. R., Purvis, R. M., Lewis, A. C., Müller, K., Heinold, B., Herrmann, H., Fomba, K. W., van Pinxteren, D., Müller, C., Tegen, I., Wiedensohler, A., Müller, T., Niedermeier, N., Achterberg, E. P., Patey, M. D., Kozlova, E. A., Heimann, M., Heard, D. E., Plane, J. M. C., Mahajan, A., Oetjen, H., Ingham, T., Stone, D., Whalley, L. K., Evans, M. J., Pilling, M. J., Leigh, R. J., Monks, P. S., Karunaharan, A., Vaughan, S., Arnold, S. R., Tschritter, J., Pöhler, D., Frieß, U., Holla, R., Mendes, L. M., Lopez, H., Faria, B., Manning, A. J., and Wallace, D. W. R.: Seasonal characteristics of tropical marine boundary layer air measured at the Cape Verde Atmospheric Observatory, *J. Atmos. Chem.*, 67, 87-140, <https://doi.org/10.1007/s10874-011-9206-1>, 2010.

Carslaw, N., Fletcher, L., Heard, D., Ingham, T., and Walker, H.: Significant OH production under surface cleaning and air cleaning conditions: Impact on indoor air quality, *Indoor Air*, 27, 1091-1100, <https://doi.org/10.1111/ina.12394>, 2017.

Carslaw, N., and Weschler, C. J.: Indoor Chemistry, *Environ. Sci. Technol.*, 2419-2428, <https://doi.org/10.1021/acs.est.7b06387>, 2018.

Champion, W. M., Rothfuss, N. E., Petters, M. D., and Grieshop, A. P.: Volatility and Viscosity Are Correlated in Terpene Secondary Organic Aerosol Formed in a Flow Reactor, *Environ. Sci. Tech. Letts.*, 6, 513-519, <https://doi.org/10.1021/acs.estlett.9b00412>, 2019.

Chen, H., Nanayakkara, C. E., and Grassian, V. H.: Titanium dioxide photocatalysis in atmospheric chemistry, *Chem. Rev.*, 112, 5919-5948, <https://doi.org/10.1021/cr3002092>, 2012.

Chen, S., Ren, X., Mao, J., Chen, Z., Brune, W. H., Lefer, B., Rappengluck, B., Flynn, J., Olson, J., and Crawford, J. H.: A comparison of chemical mechanisms based on TRAMP-2006 field data, *Atmospheric Environment*, 44, 4116-4125, <https://doi.org/10.1016/j.atmosenv.2009.05.027>, 2010.

Chen, S., Brune, W. H., Lambe, A. T., Davidovits, P., and Onasch, T. B.: Modeling organic aerosol from the oxidation of α -pinene in a Potential Aerosol Mass (PAM) chamber, *Atmos. Chem. Phys.*, 13, 5017-5031, <https://doi.org/10.5194/acp-13-5017-2013>, 2013.

Cheng, P., Cheng, Y., Lu, K., Su, H., Yang, Q., Zou, Y., Zhao, Y., Dong, H., Zeng, L., and Zhang, Y.: An online monitoring system for atmospheric nitrous acid (HONO) based on stripping coil and ion chromatography, *J. Environ. Sci.*, 25, 895-907, [https://doi.org/10.1016/S1001-0742\(12\)60251-4](https://doi.org/10.1016/S1001-0742(12)60251-4), 2013.

Clará, R. A., Marigliano, A. C. G., and Sólamo, H. N.: Density, Viscosity, and Refractive Index in the Range (283.15 to 353.15) K and Vapor Pressure of α -Pinene, d-Limonene, (\pm)-Linalool, and Citral Over the Pressure Range 1.0 kPa Atmospheric Pressure, *J. Chem. Eng. Data.*, 54, 1087-1090, <https://doi.org/10.1021/je8007414>, 2009.

Clegg, S. L., Brimblecombe, P., and Wexler, A. S.: Thermodynamic model of the system $H^+ - NH_4^+ - Na^+ - SO_4^{2-} - NO_3^- - Cl^- - H_2O$ at 298.15 K, *J. Phys. Chem. A*, 102, 2155-2171, <https://doi.org/10.1021/jp973043j>, 1998.

Comelli, F., Ottani, S., Francesconi, R., and Castellari, C.: Densities, Viscosities, and Refractive Indices of Binary Mixtures Containing n-Hexane + Components of Pine Resins and Essential Oils at 298.15 K, *J. Chem. Eng. Data.*, 47, 93-97, <https://doi.org/10.1021/je010216w>, 2002.

Conibear, L., Butt, E. W., Knote, C., Arnold, S. R., and Spracklen, D. V.: Residential energy use emissions dominate health impacts from exposure to ambient particulate matter in India, *Nat. Commun.*, 9, <https://doi.org/10.1038/s41467-018-02986-7>, 2018.

Creasey, D. J., Halford-Maw, P. A., Heard, D. E., Pilling, M. J., and Whitaker, B. J.: Implementation and initial deployment of a field instrument for the measurement of OH and HO₂ in the troposphere by laser-induced fluorescence, *Journal of Chemical Society, Faraday Transactions*, 93, 2907-2913, <https://doi.org/10.1039/A70149D>, 1997.

Crilley, L. R., Kramer, L., Pope, F. D., Whalley, L. K., Cryer, D. R., Heard, D. E., Lee, J. D., Reed, C., and Bloss, W. J.: On the interpretation of in situ HONO observations via photochemical steady state, *Faraday Discuss.*, 189, 191-212, <https://doi.org/10.1039/c5fd00224a>, 2016.

Crilley, L. R., Kramer, L. J., Ouyang, B., Duan, J., Zhang, W., Tong, S., Ge, M., Tang, K., Qin, M., Xie, P., Shaw, M. D., Lewis, A. C., Mehra, A., Bannan, T. J., Worrall, S. D., Priestley, M., Bacak, A., Coe, H., Allan, J., Percival, C. J., Popoola, O. A. M., Jones, R. L., and Bloss, W. J.: Intercomparison of nitrous acid (HONO) measurement techniques in a megacity (Beijing), *Atmos. Meas. Tech.*, 12, 6449-6463, <https://doi.org/10.5194/amt-12-6449-2019>, 2019.

de Jesus Madeiros, D., and Pimentel, A. S.: New insights in the atmospheric HONO formation: new pathways for N₂O₄ isomerisation and NO₂ dimerisation in the presence of water. , *J. Phys. Chem. A*, 115, 6357-6365, <https://doi.org/10.1021/jp1123585>, 2011.

de Reus, M., Fischer, H., Sander, R., Gros, V., Kormann, R., Salisbury, G., Dingenen, R. V., Williams, J., Zollner, M., and Levievel, J.: Observations and model calculations of trace gas scavenging in a dense Saharan dust plume during MINATROC, *Atmos. Chem. Phys.*, 5, 1787-1803, <https://doi.org/10.5194/acp-5-1787-2005>, 2005.

Dibb, J. E., L. Gregory Huey, Slusher, D. L., and Tanner, D. J.: Soluble reactive nitrogen oxides at South Pole during ISCAT 2000, *Atmos. Environ.*, 38, 5399-5409, <https://doi.org/10.1016/j.atmosenv.2003.01.001>, 2004.

Dinar, E., Taraniuk, I., Graber, E., Anttila, T., Mentel, T., and Rudich, Y.: Hygroscopic growth of model and atmospheric humic like substances (HULIS), *J. Geophys. Res.*, 112, <https://doi.org/10.1029/2006JD007442>, 2007.

Donahue, N. M., Epstein, S. A., Pandis, S. N., and Robinson, A. L.: A two-dimensional volatility basis set: 1. organic-aerosol mixing thermodynamics, *Atmos. Chem. Phys.*, 11, 3303-3318, <https://doi.org/10.5194/acp-11-3303-2011>, 2011.

Duan, J., Qin, M., Ouyang, B., Fang, W., Li, X., Lu, K., Tang, K., Liang, S., Meng, F., Hu, Z., Xie, P., Liu, W., and Häsler, R.: Development of an incoherent broadband cavity-enhanced absorption spectrometer for in situ measurements of HONO and NO₂, *Atmos. Meas. Tech.*, 11, 4531-4543, <https://doi.org/10.5194/amt-11-4531-2018>, 2018.

- Dunmore, R., Hopkins, J., Lidster, R., Lee, J., Evans, M., Rickard, A., Lewis, A., and Hamilton, J.: Diesel-related hydrocarbons can dominate gas phase reactive carbon in megacities, *Atmos. Chem. Phys.*, 15, 9983-9996, <https://doi.org/10.5194/acp-15-9983-2015>, 2015.
- Dupart, Y., Fine, L., D'Anna, B., and George, C.: Heterogeneous uptake of NO₂ on Arizona Test Dust under UV-A irradiation: an aerosol flow tube study, *Aeolian Res.*, 15, 45-51, <https://doi.org/10.1016/j.aeolia.2013.10.001>, 2014.
- Dusanter, S., Vimal, D., Stevens, P. S., Volkamer, R., Molina, L. T., Baker, A., Meinardi, S., Blake, D., Sheehy, P., Merten, A., Zhang, R., Zheng, J., Fortner, E. C., Junkermann, W., Dubey, M., Rahn, T., Eichinger, B., Lewandowski, P., Preuger, J., and Holder, H.: Measurements of OH and HO₂ concentrations during the MCMC-2006 field campaign - Part 2: Model comparison and radial budget, *Atmos. Chem. Phys.*, 9, 6655-6675, <https://doi.org/10.5194/acp-9-6655-2009>, 2009.
- Dyson, J. E., Boustead, G. A., Fleming, L. T., Blitz, M., Stone, D., Arnold, S. R., Whalley, L. K., and Heard, D. E.: Production of HONO from NO₂ uptake on illuminated TiO₂ aerosol particles and following the illumination of mixed TiO₂/ammonium nitrate particles, *Atmos. Chem. Phys.*, 21, 5755-5775, [10.5194/acp-21-5755-2021](https://doi.org/10.5194/acp-21-5755-2021), 2021.
- El Zein, A., Bedjanian, Y., and Romanias, M. N.: Kinetics and products of HONO interaction with TiO₂ surface under UV irradiation, *Atmos. Environ.*, 67, 203-210, <https://doi.org/10.1016/j.atmosenv.2012.11.016>, 2013.
- Emeline, A., Ryabchuk, V., and Serpone, N.: Dogmas and Misconceptions in Heterogeneous Photocatalysis. Some Enlightened Reflections, *The journal of physical chemistry. B*, 109, 18515-18521, <https://doi.org/10.1021/jp0523367>, 2005.
- Fan, X., Song, J., and Peng, P. a.: Comparison of isolation and quantification methods to measure humic-like substances (HULIS) in atmospheric particles, *Atmos. Environ.*, 60, 366-374, <https://doi.org/10.1016/j.atmosenv.2012.06.063>, 2012.
- Fateley, W. G., Bent, H. A., and Crawford Jr, B.: Infrared spectra of the frozen oxides of nitrogen, *J. Chem. Phys.*, 31, 204-217, <https://doi.org/10.1063/1.1730296>, 1959.
- Finlayson-Pitts, B. J., and Pitts, J. N.: *Chemistry of the upper and lower atmosphere: theory, experiments and applications*, Academic Press, 2000.
- Finlayson-Pitts, B. J., Wingen, L. M., Summer, A. L., Syomin, D., and Ramazan, K. A.: The heterogeneous hydrolysis of NO₂ in laboratory systems in outdoor and indoor atmospheres: An intergrated mechanism, *Phys.Chem.Phys.Chem*, 5, 223-242, <https://doi.org/10.1039/b208564j>, 2003.
- Fittschen, C., Al Ajami, M., Batut, S., Ferracci, V., Archer-Nicholls, S., Archibald, A. T., and Schoemaeker, C.: ROOOH: a missing piece of the puzzle for OH measurements in low-NO environments?, *Atmos. Chem. Phys.*, 19, 349-362, <https://doi.org/10.5194/acp-19-349-2019>, 2019.
- Flagan, R. C.: Differential mobility analysis of aerosols: a tutorial, *KONA Powder and Particle Journal*, 26, 254-268, <https://doi.org/10.14356/kona.2008023>, 2008.
- Forney, D., Thompson, W. E., and Jacox, M. E.: The vibrational spectra of molecular ions isolated in solid neon. XI. NO₂⁺, NO₂⁻, and NO₃⁻, *The Journal of Chemical Physics*, 99, 7393-7403, <https://doi.org/10.1063/1.465720>, 1993.

Forster, P., Ramaswamy, V., Artaxo, P., Berntsen, T., Betts, R., Fahey, D. W., Haywood, J., Lean, J., Lowe, D. C., Myhre, G., Nganga, J., Prinn, R., Raga, G., Schulz, M., and Dorland, R. V.: Chapter 2. Changes in atmospheric constituents and in radiative forcing. , *Climate Change 2007. The Physical Science Basis*, 2007.

Fountoukis, C., and Nenes, A.: ISORROPIA II: a computationally efficient thermodynamic equilibrium model for K^+ - Ca^{2+} - Mg^{2+} - NH_4^+ - Na^+ - SO_4^{2-} - NO_3^- - Cl^- - H_2O aerosols, *Atmos. Chem. Phys.*, 7, 4639-4659, <https://doi.org/10.5194/acp-7-4639-2007>, 2007.

Fuchs, H., Holland, F., and Hofzumahaus, A.: Measurement of tropospheric RO_2 and HO_2 radicals by a laser-induced fluorescence instrument, *The Review of scientific instruments*, 79, 084104, <https://doi.org/10.1063/1.2968712>, 2008.

Fuchs, N. A., and Sutugin, A. G.: *Highly dispersed aerosols*, 1970.

Gakidou, E., Afshin, A., Abajobir, A. A., Abate, K. H., Abbafati, C., Abbas, K. M., Abd-Allah, F., Abdulle, A. M., Abera, S. F., and Aboyans, V.: Global, regional, and national comparative risk assessment of 84 behavioural, environmental and occupational, and metabolic risks or clusters of risks, 1990–2016: a systematic analysis for the Global Burden of Disease Study 2016, *The Lancet*, 390, 1345-1422, [https://doi.org/10.1016/S0140-6736\(18\)32279-7](https://doi.org/10.1016/S0140-6736(18)32279-7), 2017.

GBD 2015 Risk Factors Collaborators: Global, regional, and national comparative risk assessment of 79 behavioural, environmental and occupational, and metabolic risks or clusters of risks, 1990–2015: a systematic analysis for the Global Burden of Disease Study 2015, *The Lancet*, 388, 1659-1724, [https://doi.org/10.1016/S0140-6736\(16\)31679-8](https://doi.org/10.1016/S0140-6736(16)31679-8), 2016.

George, C., Strekowski, R. S., Kleffmann, J., Stemmler, K., and Ammann, M.: Photoenhanced uptake of gaseous NO_2 on solid organic compounds: a photochemical source of $HONO$?, *Faraday Discuss.*, 130, 195-210, <https://doi.org/10.1039/b417888m>, 2005.

George, I. J., Matthews, P. S. J., Whalley, L. K., Brooks, B., Goddard, A., Baeza-Romero, M., and Heard, D. E.: Measurements of uptake coefficients for heterogeneous loss of HO_2 onto submicron inorganic salt aerosols., *Phys. Chem. Chem. Phys.*, 15, 12829-12845, <https://doi.org/10.1039/c3cp51831k>, 2013.

Ginoux, P., Chin, M., Tegen, I., Prospero, J. M., Holben, B., Dubovik, O., and Lin, S. J.: Sources and distributions of dust aerosols simulated with the GOCART model, *J. Geophys. Res. Atmos.*, 106, 20255-20273, <https://doi.org/10.1029/2000JD000053>, 2001.

Givan, A., and Loewenschuss, A.: On the intermolecularity or intramolecularity of nitrosonium nitrate formation in thin films of nitrogen dioxide: A Fourier transform infrared study, *The Journal of Chemical Physics*, 91, 5126-5127, <https://doi.org/10.1063/1.457609>, 1989a.

Givan, A., and Loewenschuss, A.: Fourier transform infrared and Raman studies on solid nitrogen dioxide: Temperature cycling of ordered, disordered, and multicomponent layers, *The Journal of Chemical Physics*, 90, 6135-6142, <https://doi.org/10.1063/1.456379>, 1989b.

Givan, A., and Loewenschuss, A.: Fourier transform infrared study of amorphous N₂O₄ solid: Destabilization with inert impurities, *The Journal of Chemical Physics*, 94, 7562-7563, <https://doi.org/10.1063/1.460192>, 1991.

Gong, Y., Chen, Z., and Li, H.: The oxidation regime and SOA composition in limonene ozonolysis: roles of different double bonds, radicals, and water, *Atmos. Chem. Phys.*, 18, 15105-15123, <https://doi.org/10.5194/acp-18-15105-2018>, 2018.

Goodman, A. L., Bernard, E. T., and Grassian, V. H.: Spectroscopic study of nitric acid and water adsorption on oxide particles: enhanced nitric acid uptake kinetics in the presence of adsorbed water, *J. Phys. Chem. A*, 105, 6443-6457, <https://doi.org/10.1021/jp0037221>, 2001.

Gustafsson, R. J., Orlov, A., Griffiths, P. T., Cox, R. A., and Lambert, R. M.: Reduction of NO₂ to nitrous acid on illuminated titanium dioxide aerosol surfaces: implications for photocatalysis and atmospheric chemistry, *Chem. Commun.*, 37, 3936-3938, <https://doi.org/10.1039/b609005b>, 2006.

Gysel, M., Weingartner, E., Nyeki, S., Paulsen, D., Baltensperger, U., Galambos, I., and Kiss, G.: Hygroscopic properties of water soluble matter and humic-like organics in atmospheric fine aerosol, *Atmos. Chem. Phys.*, 4, 35-50, <https://doi.org/10.5194/acp-4-35-2004>, 2004.

Hanisch, F., and Crowley, J. N.: Ozone decomposition on Saharan dust: an experimental investigation, *Atmos. Chem. Phys.*, 3, 119-130, <https://doi.org/10.5194/acp-3-119-2003>, 2003.

Hanson, D. R., Ravishankara, A. R., and Solomon, S.: Heterogeneous reactions in sulfuric acid aerosols: a framework for model calculations, *J. Geophys. Res.*, 99, 3615-3629, <https://doi.org/10.1029/93JD02932>, 1994.

Hanson, D. R., Ravishankara, A. R., and Lovejoy, E. R.: Reaction of BrONO₂ with H₂O on submicron sulfuric acid aerosol and the implications for the lower stratosphere, *J. Geophys. Res.*, 101, 9063-9069, <https://doi.org/10.1029/96JD00347>, 1996.

Hausmann, M., Brandenburger, U., Brauers, T., and Dorn, H. P.: Detection of tropospheric OH radicals by long-path differential-optical-absorption spectroscopy: Experimental setup, accuracy, and precision., *J. Geophys. Res.*, 102, 16011-16022, <https://doi.org/10.1029/97JD00931>, 1997.

He, H., Wang, Y., Ma, Q., Ma, J., Chu, B., Ji, D., Tang, G., Liu, C., Zhang, H., and Hao, J.: Mineral dust and NO_x promote the conversion of SO₂ to sulfate in heavy pollution days, *Scientific Reports*, 4, 4172, <https://doi.org/10.1038/srep04172>, 2014.

Heard, D. E.: Atmospheric field measurements of the hydroxyl radical using Laser-Induced Fluorescence spectroscopy, *Annu. Rev. Phys. Chem.*, 57, 191-216, <https://doi.org/10.1146/annurev.physchem.57.032905.104516>, 2006a.

Heard, D. E.: Analytical techniques for atmospheric measurement, Blackwell Publishing, Oxford, 2006b.

Heland, J., Kleffmann, J., Kurtenbach, R., and Wiesen, P.: A new instrument to measure gaseous nitrous acid (HONO) in atmosphere, *Environ. Sci. Technol.*, 35, 3207-3212, <https://doi.org/10.1021/es000303t>, 2001.

Hofzumahaus, A., Aschmutat, U., Heßling, M., Holland, F., and Ehhalt, D. E.: The measurement of tropospheric OH radicals by laser-induced fluorescence spectroscopy during the POPCORN Field Campaign, *Geophys. Res. Lett.*, 23, 2541-2544, <https://doi.org/10.1029/96GL02205>, 1996.

Holloway, A. M., and Wayne, R. P.: *Atmospheric Chemistry*, Royal Society of Chemistry, 2010.

Hopkins, J. R., Jones, C. E., and Lewis, A. C.: A dual channel gas chromatograph for atmospheric analysis of volatile organic compounds including oxygenated and monoterpene compounds., *J. Environ. Monit.*, 13, 2268-2276, <https://doi.org/10.1039/C1EM10050E>, 2011.

IPCC: *Climate Change 2014: Synthesis Report. Contribution of Working Groups I, II and III to the Fifth Assessment Report of the Intergovernmental Panel on Climate Change*, IPCC, Geneva, Switzerland, 2014.

Iyer, S., Rissanen, M. P., Valiev, R., Barua, S., Krechmer, J. E., Thornton, J., Ehn, M., and Kurtén, T.: Molecular mechanism for rapid autoxidation in α -pinene ozonolysis, *Nat. Commun.*, 12, 878, <https://doi.org/10.1038/s41467-021-21172-w>, 2021.

Jacob, D. J.: 11. Oxidizing Power of the Troposphere, in: *Introduction to Atmospheric Chemistry*, Princeton University Press, 200-230, 1999.

Jacob, D. J.: Heterogeneous chemistry and tropospheric ozone, *Atmos. Environ.*, 34, 2131-2159, [https://doi.org/10.1016/S1352-2310\(99\)00462-8](https://doi.org/10.1016/S1352-2310(99)00462-8), 2000.

Jin, Y., Andersson, H., and Zhang, S.: Air Pollution Control Policies in China: A Retrospective and Prospects, *Int. J. Environ. Res. Public Health*, 13, <https://doi.org/10.3390/ijerph13121219>, 2016.

Jokinen, T., Berndt, T., Makkonen, R., Kerminen, V.-M., Junninen, H., Paasonen, P., Stratmann, F., Herrmann, H., Guenther, A. B., Worsnop, D. R., Kulmala, M., Ehn, M., and Sipilä, M.: Production of extremely low volatile organic compounds from biogenic emissions: Measured yields and atmospheric implications, *Proceedings of the National Academy of Sciences*, 112, 7123, <https://doi.org/10.1073/pnas.1423977112>, 2015.

Kanakidou, M., Seinfeld, J. H., Pandis, S. N., Barnes, I., Dentener, F. J., Facchini, M. C., Van Dingenen, R., Ervens, B., Nenes, A., Nielsen, C. J., Swietlicki, E., Putaud, J. P., Balkanski, Y., Fuzzi, S., Horth, J., Moortgat, G. K., Winterhalter, R., Myhre, C. E. L., Tsigaridis, K., Vignati, E., Stephanou, E. G., and Wilson, J.: Organic aerosol and global climate modelling: a review, *Atmos. Chem. Phys.*, 5, 1053-1123, [10.5194/acp-5-1053-2005](https://doi.org/10.5194/acp-5-1053-2005), 2005.

Kanaya, Y. G., Cao, R. Q., Kato, S. G., Miyakawa, Y. K., Kajii, Y., Tanimoto, H., Yokouchi, Y., Mochida, M., Kawamura, K., and Akimoto, H.: Chemistry of OH and HO₂ radicals observed at Rishiri Island, Japan, in September 2003: Missing daytime sink of HO₂ and positive nighttime correlations with monoterpenes, *J. Geophys. Res. Atmos.*, 112, D11308, <https://doi.org/10.1029/2006JD007987>, 2007.

Kang, E., Root, M. J., Toohey, D. W., and Brune, W. H.: Introducing the concept of Potential Aerosol Mass (PAM), *Atmos. Chem. Phys.*, 7, 5727-5744, <https://doi.org/10.5194/acp-7-5727-2007>, 2007.

Kang, E., Lee, M., Brune, W. H., Lee, T., Park, T., Ahn, J., and Shang, X.: Photochemical aging of aerosol particles in different air masses arriving at

Baengnyeong Island, Korea, *Atmos. Chem. Phys.*, 18, 6661-6677, <https://doi.org/10.5194/acp-18-6661-2018>, 2018.

Khamaganov, V. G., and Hites, R. A.: Rate Constants for the Gas-Phase Reactions of Ozone with Isoprene, α - and β -Pinene, and Limonene as a Function of Temperature, *J. Phys. Chem. A*, 105, 815-822, <https://doi.org/10.1021/jp002730z>, 2001a.

Khamaganov, V. G., and Hites, R. A.: Rate constants for the gas-phase reactions of ozone with isoprene, α -pinene and β -pinene, and limonene as a function of temperature, *J. Phys. Chem. A*, 105, 815-822, 2001b.

Kim, S.-H., Jaques, P., Chang, O., Barone, T., Xiong, C., and Friedlander, S.: Versatile aerosol concentration enrichment system (VACES) for simultaneous in vivo and in vitro evaluation of toxic effects of ultrafine, fine and coarse ambient particles Part II: Field evaluation, *J. Aerosol Sci.*, 32, 1299-1314, [https://doi.org/10.1016/S0021-8502\(01\)00058-1](https://doi.org/10.1016/S0021-8502(01)00058-1), 2001.

Kinney, P. L.: Climate change, air quality, and human health, *Am. J. Prev. Med.*, 35, 459-467, Climate change, air quality, and human health, 2008.

Kiss, G., Tombácz, E., and Hansson, H.-C.: Surface Tension Effects of Humic-Like Substances in the Aqueous Extract of Tropospheric Fine Aerosol, *J. Atmos. Chem.*, 50, 279-294, <https://doi.org/10.1007/s10874-005-5079-5>, 2005.

Kleffmann, J., Lorzer, J. C., Wiesen, P., Kern, C., Trick, S., Volkamer, R., Rodenas, M., and Wirtz, K.: Intercomparison of the DOAS and LOPAP techniques for the detection of nitrous acid (HONO), *Atmos. Environ.*, 40, 3640-3652, <https://doi.org/10.1016/j.atmosenv.2006.03.027>, 2006.

Kleffmann, J.: Daytime sources of nitrous acid (HONO) in the atmospheric boundary layer, *Chem. Phys. Chem.*, 8, 1137-1144, <https://doi.org/10.1002/cphc.200700016>, 2007.

Krivácsy, Z., Kiss, G., Ceburnis, D., Jennings, G., Maenhaut, W., Salma, I., and Shooter, D.: Study of water-soluble atmospheric humic matter in urban and marine environments, *Atmos. Res.*, 87, 1-12, <https://doi.org/10.1016/j.atmosres.2007.04.005>, 2008.

Kroll, J., and Seinfeld, J.: Chemistry of secondary organic aerosol: Formation and evolution of low-volatility organics in the atmosphere, *Atmos. Environ.*, 42, 3593-3624, <https://doi.org/10.1016/j.atmosenv.2008.01.003>, 2008.

Krotkov, N. A., McLinden, C. A., Li, C., Lamsal, L. N., Celarier, E. A., Marchenko, S. V., Swartz, W. H., Bucsela, E. J., Joiner, J., Duncan, B. N., Boersma, K. F., Veefkind, J. P., Levelt, P. F., Fioletov, V. E., Dickerson, R. R., He, H., Lu, Z., and Streets, D. G.: Aura OMI observations of regional SO₂ and NO₂ pollution changes from 2005 to 2015, *Atmos. Chem. Phys.*, 16, 4605-4629, <https://doi.org/10.5194/acp-16-4605-2016>, 2016.

Kuang, B. Y., Lin, P., Huang, X. H. H., and Yu, J. Z.: Sources of humic-like substances in the Pearl River Delta, China: positive matrix factorization analysis of PM^{^{2.5}} major components and source markers, *Atmos. Chem. Phys.*, 15, 1995-2008, <https://doi.org/10.5194/acp-15-1995-2015>, 2015.

Kulkarni, P., Baron, P. A., and Willeke, K.: Aerosol measurement: principles, techniques, and applications, 3 ed., John Wiley & Sons, 2011.

Kurtenbach, R., Becker, K. H., Gomes, J. A. G., Kleffmann, J., Lörzer, J. C., Spittler, M., Wiesen, P., Ackermann, R., Geyer, A., and Platt, U.: Investigations of emissions and heterogeneous formation of HONO in road traffic tunnel, *Atmos. Environ.*, **35**, 3385-3394, [https://doi.org/10.1016/S1352-2310\(01\)00138-8](https://doi.org/10.1016/S1352-2310(01)00138-8), 2001.

Lakey, P. S. J., George, I. J., Whalley, L. K., Baeza-Romero, M., and Heard, D. E.: Measurements of HO₂ uptake coefficients onto single component organic aerosols., *Environmental Science Technology*, **49**, 4878-4885, <https://doi.org/10.1021/acs.est.5b00948>, 2015.

Lakey, P. S. J., Berkemeier, T., Krapf, M., Dommen, J., Steimer, S. S., Whalley, L. K., Ingham, T., Baeza-Romero, M., Pölsch, U., Shiraiwa, M., Ahmann, M., and Heard, D. E.: The effect of viscosity and diffusion on the HO₂ uptake by sucrose and secondary organic aerosol particles., *Atmos. Chem. Phys.*, **16**, 13035-13047, <https://doi.org/10.5194/acp-16-13035-2016>, 2016a.

Lakey, P. S. J., George, I. J., Baeza-Romero, M., Whalley, L. K., and Heard, D. E.: Organics substantially reduce HO₂ uptake onto aerosols containing transition metal ions. , *J. Phys. Chem. A*, **120**, 1421-1430, <https://doi.org/10.1021/acs.jpca.5b06316>, 2016b.

Lambe, A. T., Onasch, T. B., Croasdale, D. R., Wright, J. P., Martin, A. T., Franklin, J. P., Massoli, P., Kroll, J. H., Canagaratna, M. R., Brune, W. H., Worsnop, D. R., and Davidovits, P.: Transitions from Functionalization to Fragmentation Reactions of Laboratory Secondary Organic Aerosol (SOA) Generated from the OH Oxidation of Alkane Precursors, *Environ. Sci. Technol.*, **46**, 5430-5437, <https://doi.org/10.1021/es300274t>, 2012.

Lambe, A. T., Chhabra, P. S., Onasch, T. B., Brune, W. H., Hunter, J. F., Kroll, J. H., Cummings, M. J., Brogan, J. F., Parmar, Y., Worsnop, D. R., Kolb, C. E., and Davidovits, P.: Effect of oxidant concentration, exposure time, and seed particles on secondary organic aerosol chemical composition and yield, *Atmos. Chem. Phys.*, **15**, 3063-3075, <https://doi.org/10.5194/acp-15-3063-2015>, 2015.

Le Breton, M., Bacak, A., Muller, J. B. A., Bannan, T. J., Kennedy, O., Ouyang, B., Xiao, P., Bauguitte, S. J. B., Shallcross, D. E., Jones, R. L., Daniels, M. J. S., Ball, S. M., and Percival, C. J.: The first airborne comparison of N₂O₅ measurements over the UK using a CIMS and BBCEAS during the RONOCO campaign, *Analytical Methods*, **6**, 9731-9743, <https://doi.org/10.1039/C4AY02273D>, 2014.

Lee, J. D., Whalley, L. K., Heard, D. E., Stone, D., Dunmore, R. E., Hamilton, J. F., Young, D. E., Allan, J. D., Laufs, S., and Kleffmann, J.: Detailed budget analysis of HONO in central London reveals a missing daytime source, *Atmos. Chem. Phys.*, **16**, 2747-2764, <https://doi.org/10.5194/acp-16-2747-2016>, 2016.

Lelieveld, J., Gromov, S., Pozzer, A., and Taraborrelli, D.: Global tropospheric hydroxyl distribution, budget and reactivity, *Atmos. Chem. Phys.*, **16**, 12477-12493, <https://doi.org/10.5194/acp-16-12477-2016>, 2016.

Levy, H.: Normal atmosphere: large radical and formaldehyde concentrations predicted, *Science*, **173**, 141-143, <https://doi.org/10.1126/science.173.3992.141>, 1971.

Li, K., Jacob, D. J., Liao, H., Shen, L., Zhang, Q., and Bates, K.: Anthropogenic drivers of 2013-2017 trends in summer surface ozone in China, *Proceedings of the*

National Academy of Sciences, 116, 422-427, <https://doi.org/10.1073/pnas.1812168116>, 2018.

Li, S., Matthews, J., and Sinha, A.: Atmospheric hydroxyl radical production from electronically excited NO₂ and H₂O, *Science*, 319, 1657-1660, <https://doi.org/10.1126/science.1151443>, 2008.

Liao, W., Hecobian, A., Mastromarino, J., and Tan, D.: Development of a photo-fragmentation/laser-induced fluorescence measurement of atmospheric nitrous acid, *Atmos. Environ.*, 40, 17-26, <https://doi.org/10.1016/j.atmosenv.2005.07.001>, 2007.

Lin, C. Q., Liu, G., Lau, A. K. H., Li, Y., Li, C. C., Fung, J. C. H., and Lao, X. Q.: High-resolution satellite remote sensing of provincial PM_{2.5} trends in China from 2001 to 2015, *Atmos. Environ.*, 180, 110-116, <https://doi.org/10.1016/j.atmosenv.2018.02.045>, 2018.

Lin, J. S., and Tabazadch, A.: The effect of nitric acid uptake on the deliquescence and efflorescence of binary ammoniated salts in the upper troposphere, *Geophys. Res. Lett.*, 29, 126-121, <https://doi.org/10.1029/2002GL015251>, 2002.

Liu, F., Zhang, Q., van der A, R. J., Zheng, B., Tong, D., Yan, L., Zheng, Y., and He, K.: Recent reduction in NO_x emissions over China: synthesis of satellite observations and emission inventories, *Environ. Res. Lett.*, 11, 114002, <https://doi.org/10.1088/1748-9326/11/11/114002>, 2016.

Liu, W. G., and Goddard, W. A.: First-principle study of the role of interconversion between NO₂, N₂O₄, *cis*-ONO-NO₂, and *trans*-ONO-NO₂ in chemical processes, *J. Am. Chem. Soc.*, 134, 12970-12978, <https://doi.org/10.1021/ja300545e>, 2012.

Liu, Y.-H., Liao, W.-Y., Lin, X.-F., Li, L., and Zeng, X.-l.: Assessment of Co-benefits of vehicle emission reduction measures for 2015–2020 in the Pearl River Delta region, China, *Environ. Pollut.*, 223, 62-72, <https://doi.org/10.1016/j.envpol.2016.12.031>, 2017.

Loukhovitskaya, E., Bedjanian, Y., Morozov, I., and Le Bras, G.: Laboratory study of the interaction of HO₂ radicals with the NaCl, NaBr, MgCl₂·6H₂O and sea salt surfaces, *Phys. Chem. Chem. Phys.*, 11, 7896-7905, <https://doi.org/10.1039/b906300e>, 2009.

Loza, C. L., Craven, J. S., Yee, L. D., Coggon, M. M., Schwantes, R. H., Shiraiwa, M., Zhang, X., Schilling, K. A., Ng, N. L., Canagaratna, M. R., Ziemann, P. J., Flagan, R. C., and Seinfeld, J. H.: Secondary organic aerosol yields of 12-carbon alkanes, *Atmos. Chem. Phys.*, 14, 1423-1439, <https://doi.org/10.5194/acp-14-1423-2014>, 2014.

Lu, K. D., Rohrer, F., Holland, F., Fuchs, H., B.Bohn, Brauers, T., Chang, C. C., Häsel, R., Hu, M., Kita, K., Kondo, Y., Li, X., Loi, S. R., Nehr, S., Shao, M., Zeng, L. M., Wahner, A., Zhang, Y. H., and Hofzumahaus, A.: Observation and modelling of OH and HO₂ concentrations in the Pearl River Delta 2006: a missing OH source in a VOC rich atmosphere, *Atmos. Chem. Phys.*, 12, 1541-1569, <https://doi.org/10.5194/acp-12-1541-2012>, 2012.

Lu, X., Park, J., and Lin, M. C.: Gas phase reactions of HONO with NO₂, O₃ and HCl: Ab initio and TST study, *J. Phys. Chem. A*, 104, 8730-8738, <https://doi.org/10.1021/jp001610o>, 2000.

- Ma, X., Tan, Z., Lu, K., Yang, X., Liu, Y., Li, S., Li, X., Chen, S., Novelli, A., Cho, C., Zeng, L., Wahner, A., and Zhang, Y.: Winter photochemistry in Beijing: Observation and model simulation of OH and HO₂ radicals at an urban site, *Sci. Total Environ.*, 685, 85-95, <https://doi.org/10.1016/j.scitotenv.2019.05.329>, 2019.
- Ma, Z., Hu, X., Sayer, A. M., Levy, R., Zhang, Q., Xue, Y., Tong, S., Bi, J., Huang, L., and Liu, Y.: Satellite-Based Spatiotemporal Trends in PM_{2.5} Concentrations: China, 2004-2013, *Environ. Health Perspect.*, 124, 184-192, <https://doi.org/10.1289/ehp.1409481>, 2016a.
- Ma, Z., Xu, J., Quan, W., Zhang, Z., Lin, W., and Xu, X.: Significant increase of surface ozone at a rural site, north of eastern China, *Atmos. Chem. Phys.*, 16, 3969-3977, <https://doi.org/10.5194/acp-16-3969-2016>, 2016b.
- Macintyre, H. L., and Evans, M. J.: Parameterisation and impact of aerosol uptake of HO₂ on global tropospheric model, *Atmos. Chem. Phys.*, 11, 10965-10974, <https://doi.org/10.5194/acp-11-10965-2011>, 2011.
- Mao, J., Jacob, D. J., Evans, M. J., Olson, J. R., Ren, X., Brune, W. H., Chair, J. M. S., Crouse, J. D., Spencer, K. M., Beaver, M. R., Wennberg, P. O., Cubison, M. J., Jimenez, J. L., Fried, A., Weibring, P., Walega, J. G., Hall, S. R., Weinheimer, A. J., Cohen, R. C., Chen, G., Crawford, J. H., McHaughton, C., Clarke, A. D., Jaegle, L., Fisher, J. K., Yantosca, R. M., LeSager, P., and Carouge, C.: Chemistry of hydrogen oxide radicals (HO_x) in the arctic troposphere in spring, *Atmos. Chem. Phys.*, 10, 5823-5838, <https://doi.org/10.5194/acp-10-5823-2010>, 2010a.
- Mao, J., Fan, S., Jacob, D. J., and Travis, K. R.: Radical loss in the atmosphere from Cu-Fe redox coupling in aerosols, *Atmos. Chem. Phys.*, 13, 509-519, <https://doi.org/10.5194/acp-13-509-2013>, 2013.
- Matthews, P. S. J.: Heterogeneous uptake of HO₂ radicals onto atmospheric aerosols, School of Chemistry, University of Leeds, 2014.
- Matthews, P. S. J., Baeza-Romero, M., Whalley, L. K., and Heard, D. E.: Uptake of HO₂ radicals onto Arizona test dust particles using an aerosol flow tube, *Atmos. Chem. Phys.*, 14, 7397-7408, <https://doi.org/10.5194/acp-14-7397-2014>, 2014a.
- Matthews, P. S. J., Baeza-Romero, M. T., Whalley, L. K., and Heard, D. E.: Uptake of HO₂ radicals onto Arizona test dust particles using an aerosol flow tube, *Atmos. Chem. Phys.*, 14, 7397-7408, <https://doi.org/10.5194/acp-14-7397-2014>, 2014b.
- MCPA software Ltd.: Facsimile, 2020.
- Metts, T. A., and Batterman, S. A.: Effect of VOC loading on the ozone removal efficiency of activated carbon filters, *Chemosphere*, 62, 34-44, <https://doi.org/10.1016/j.chemosphere.2005.04.049>, 2006.
- Michoud, V., Colomb, A., Borbon, A., Miet, K., Beekmann, M., Camredon, M., Aumont, B., Perrier, S., Zapf, P., Siour, G., Ait-Helal, W., Afif, C., Kukui, A., Furger, M., Dupont, J. C., Haefelin, M., and Doussin, J. F.: Study of the unknown HONO daytime source at a European suburban site during the MEGAPOLI summer and winter field campaigns, *Atmos. Chem. Phys.*, 14, 2805-2822, <https://doi.org/10.5194/acp-14-2805-2014>, 2014.
- Miyazaki, K., Eskes, H., Sudo, K., Boersma, K. F., Bowman, K., and Kanaya, Y.: Decadal changes in global surface NO_x emissions from multi-constituent satellite data

assimilation, *Atmos. Chem. Phys.*, 17, 807-837, <https://doi.org/10.5194/acp-17-807-2017>, 2017.

Moon, D. R.: Heterogeneous reactions involving HO₂ radicals and atmospheric aerosols, University of Leeds, 2018.

Moon, D. R., Taverna, G. S., Anduix-Canto, C., Ingham, T., Chipperfield, M. P., Seakins, P. W., Baeza-Romero, M., and Heard, D. E.: Heterogeneous reaction of HO₂ with airborne TiO₂ particles and its implication for climate change mitigation strategies., *Atmos. Chem. Phys.*, 18, 327-338, <https://doi.org/10.5194/acp-18-327-2018>, 2018.

Moon, D. R., Ingham, T., Whalley, L. K., Seakins, P. W., Baeza-Romero, M. T., and Heard, D. E.: Production of OH and HO₂ radicals from near-UV irradiated airborne TiO₂ nanoparticles, *Phys.Chem.Phys.Chem*, 21, 2325-2336, <https://doi.org/10.1039/C8CP06889E>, 2019.

Morgenstern, O., Braesicke, P., O'Connor, F. M., Bushell, A. C., Johnson, C. E., Osprey, S. M., and Pyle, J. A.: Evaluation of the new UKCA climate-composition model - Part 1: The stratosphere, *Geoscientific Model Development*, 2, 43-57, <https://doi.org/10.5194/gmd-2-43-2009>, 2009.

Mozurkewich, M., McMurry, P. H., Gupta, A., and Calvert, J. G.: Mass accommodation coefficient for HO₂ radicals on aqueous particles, *J. Geophys. Res.*, 92, 4163-4170, <https://doi.org/10.1029/JD092iD04p04163>, 1987.

Murdachaw, G., Varner, M. E., Philips, L. F., Finlayson-Pitts, B. J., and Gerber, R. B.: Nitrogen dioxide at the air-water interface: trapping, adsorption, and solvation in the bulk and at the surface, *Phys. Chem. Chem. Phys.*, 15, 204-212, <https://doi.org/10.1039/c2cp42810e>, 2013.

Mutzel, A., Poulain, L., Berndt, T., Iinuma, Y., Rodigast, M., Böge, O., Richters, S., Spindler, G., Sipilä, M., and Jokinen, T.: Highly oxidized multifunctional organic compounds observed in tropospheric particles: A field and laboratory study, *Environ. Sci. Technol.*, 49, 7754-7761, <https://doi.org/acs.est.5b00885>, 2015.

Myhre, G., Shindell, D., Bréon, F. M., Collins, W., Fuglestedt, J., Huang, J., Koch, D., Lamarque, J. F., Lee, D., Mendoza, B., Nakajima, T., Robock, A., Stephens, G., Takemura, T., and Zhang, H.: Anthropogenic and Natural Radiative Forcing, in *Climate Change 2013: The Physical Science Basis. Contribution of Working Group I to the Fifth Assessment Report of the Intergovernmental Panel on Climate Change*, Cambridge University Press, Cambridge, 2013.

Nakamura, I., Sugihara, S., and Takeuchi, K.: Mechanism for NO photooxidation over the oxygen-deficient TiO₂ powder under visible light irradiation, *Chem. Lett.*, 29, 1276-1277, <https://doi.org/10.1246/cl.2000.1276>, 2000.

Ndour, M., D'Anna, B., George, C., Ka, O., Balkanski, Y., Kleffman, J., Stemmler, K., and Ammann, M.: Photoenhanced uptake of NO₂ on mineral dust: Laboratory experiments and model simulations, *Geophys. Res. Lett.*, 35, L05812, <https://doi.org/10.1029/2007GL032006>, 2008.

Ng, N. L., Kroll, J. H., Keywood, M. D., Bahreini, R., Varutbangkul, V., Flagan, R. C., Seinfeld, J. H., Lee, A., and Goldstein, A. H.: Contribution of First- versus Second-Generation Products to Secondary Organic Aerosols Formed in the Oxidation of

Biogenic Hydrocarbons, *Environ. Sci. Technol.*, 40, 2283-2297, <https://doi.org/10.1021/es052269u>, 2006.

Ng, N. L., Chhabra, P. S., Chan, A. W. H., Surratt, J. D., Kroll, J. H., Kwan, A. J., McCabe, D. C., Wennberg, P. O., Sorooshian, A., Murphy, S. M., Dalleska, N. F., Flagan, R. C., and Seinfeld, J. H.: Effect of NO_x level on secondary organic aerosol (SOA) formation from the photooxidation of terpenes, *Atmos. Chem. Phys.*, 7, 5159-5174, <https://doi.org/10.5194/acp-7-5159-2007>, 2007.

Ortega, A. M., Hayes, P. L., Peng, Z., Palm, B. B., Hu, W., Day, D. A., Li, R., Cubison, M. J., Brune, W. H., Graus, M., Warneke, C., Gilman, J. B., Kuster, W. C., de Gouw, J., Gutiérrez-Montes, C., and Jimenez, J. L.: Real-time measurements of secondary organic aerosol formation and aging from ambient air in an oxidation flow reactor in the Los Angeles area, *Atmos. Chem. Phys.*, 16, 7411-7433, <https://doi.org/10.5194/acp-16-7411-2016>, 2016.

Oswald, R., Behrendt, T., Ermel, M., Wu, D., Su, H., Cheng, Y., Breuninger, C., Moravek, A., Mougín, E., Delon, C., Loubet, B., Pommerening-Röser, A., Sörgel, M., Pöschl, U., Hoffmann, T., Andeae, M. O., Meixner, F. X., and Trebs, I.: HONO emissions from soil bacteria as a major source of atmospheric reactive nitrogen, *Science*, 341, 1233-1235, <https://doi.org/10.1126/science.1242266>, 2013.

Oswald, R., Ermel, M., Hens, K., Novelli, A., Ouwersloot, H. G., Paasonen, P., Petäjä, T., Sipilä, M., Kerónen, P., Bäck, J., Königstedt, R., Beygi, Z. H., Fischer, H., Bohn, B., Kubistin, D., Harder, H., Martinez, M., Williams, J., Hoffmann, T., Trebs, I., and Sörgel, M.: A comparison of HONO budgets for two measurement heights at a field station within the boreal forest in Finland, *Atmos. Chem. Phys.*, 15, 799-813, <https://doi.org/10.5194/acp-15-799-2015>, 2015.

Ots, R., Young, D. E., Vieno, M., Xu, L., Dunmore, R. E., Allan, J. D., Coe, H., Williams, L. R., Herndon, S. C., Ng, N. L., Hamilton, J. F., Bergström, R., Marco, C. D., Nemitz, E., Mackenzie, I. A., Kuenen, J. J. P., Green, D. C., Reis, S., and Heal, M. R.: Simulating secondary organic aerosol from missing diesel-related intermediate-volatility organic compound emissions during the Clean Air for London (ClearfLo) campaign, *Atmos. Chem. Phys.*, 16, 6453-6473, <https://doi.org/10.5194/acp-16-6453-2016>, 2016.

Palm, B. B., Campuzano-Jost, P., Day, D. A., Ortega, A. M., Fry, J. L., Brown, S. S., Zarzana, K. J., Dube, W., Wagner, N. L., Draper, D. C., Kaser, L., Jud, W., Karl, T., Hansel, A., Gutiérrez-Montes, C., and Jimenez, J. L.: Secondary organic aerosol formation from in situ OH, O₃, and NO₃ oxidation of ambient forest air in an oxidation flow reactor, *Atmos. Chem. Phys.*, 17, 5331-5354, <https://doi.org/10.5194/acp-17-5331-2017>, 2017.

Pankow, J. F.: Review and comparative analysis of the theories on partitioning between the gas and aerosol particulate phases in the atmosphere, *Atmospheric Environment* (1967), 21, 2275-2283, [https://doi.org/10.1016/0004-6981\(87\)90363-5](https://doi.org/10.1016/0004-6981(87)90363-5), 1987.

Peng, Z., Day, D. A., Stark, H., Li, R., Lee-Taylor, J., Palm, B. B., Brune, W. H., and Jimenez, J. L.: HO_x radical chemistry in oxidation flow reactors with low-pressure mercury lamps systematically examined by modeling, *Atmos. Meas. Tech.*, 8, 4863-4890, <https://doi.org/10.5194/amt-8-4863-2015>, 2015.

Peng, Z., Lee-Taylor, J., Orlando, J. J., Tyndall, G. S., and Jimenez, J. L.: Organic peroxy radical chemistry in oxidation flow reactors and environmental chambers and their atmospheric relevance, *Atmos. Chem. Phys.*, 19, 813-834, <https://doi.org/10.5194/acp-19-813-2019>, 2019.

Peng, Z., and Jimenez, J. L.: Radical chemistry in oxidation flow reactors for atmospheric chemistry research, *Chem. Soc. Rev.*, 49, 2570-2616, <https://doi.org/10.1039/C9CS00766K>, 2020.

Pieber, S. M., Kumar, N. K., Klein, F., Comte, P., Bhattu, D., Dommen, J., Bruns, E. A., Kılıç, D., El Haddad, I., Keller, A., Czerwinski, J., Heeb, N., Baltensperger, U., Slowik, J. G., and Prévôt, A. S. H.: Gas-phase composition and secondary organic aerosol formation from standard and particle filter-retrofitted gasoline direct injection vehicles investigated in a batch and flow reactor, *Atmos. Chem. Phys.*, 18, 9929-9954, <https://doi.org/10.5194/acp-18-9929-2018>, 2018.

Pimental, A. S., Lima, F. C. A., and A. B. F. da Silva: The isomerization of dinitrogen tetroxide: $O_2N-NO_2 \rightarrow ONO-NO_2$, *J. Phys. Chem. A*, 2007, 2913-2920, <https://doi.org/10.1021/jp067805z>, 2007.

Pinnick, D., Agnew, S., and Swanson, B.: Fluid dinitrogen tetroxide at very high pressure and high temperature: observation of the nitrite isomer, *The Journal of Physical Chemistry*, 96, 7092-7096, <https://doi.org/10.1021/j100196a046>, 1992.

Pinto, J. P., Dibb, J., Lee, B. H., Rappenglück, B., Wood, E. C., Levy, M., Zhang, R. Y., Lefer, B., Ren, X. R., Stutz, J., Tsai, C., Ackermann, L., Golovko, J., Herndon, S. C., Oakes, M., Meng, Q. Y., Munger, J. W., Zahniser, M., and Zheng, J.: Intercomparison of field measurements of nitrous acid (HONO) during the SHARP campaign, *J Geophys Res-Atmos*, 119, 5583-5601, <https://doi.org/10.1002/2013JD020287>, 2014.

Pitts, J. N., Sanhueza, E., Atkinson, R., Carter, W. P. L., Winer, A. M., Harris, G. W., and Plum, C. N.: An investigation of the dark formation of nitrous acid in environmental chambers, *Int. J. Chem. Kinet.*, 16, 919-939, <https://doi.org/10.1002/kin.550160712>, 1984.

Plane, J. M. C., and Nien, C. F.: Differential optical absorption spectrometer for measuring atmospheric trace gases, *Rev. Sci. Instrum.*, 63, 1867-1876, <https://doi.org/10.1063/1.1143296>, 1992.

Pöschl, U.: Atmospheric aerosols: composition, transformation, climate and health effects., *Angew. Chem. Int. Ed.*, 44, 7520-7540, <https://doi.org/10.1002/anie.200501122>, 2005.

Presto, A. A., and Donahue, N. M.: Investigation of α -Pinene + Ozone Secondary Organic Aerosol Formation at Low Total Aerosol Mass, *Environ. Sci. Technol.*, 40, 3536-3543, <https://doi.org/10.1021/es052203z>, 2006.

Price, H. C., Murray, B. J., Mattsson, J., O'Sullivan, D., Wilson, T. W., Baustian, K. J., and Benning, L. G.: Quantifying water diffusion in high viscosity and glassy aqueous solutions using a Raman isotope tracer method, *Atmos. Chem. Phys.*, 14, 3817-3830, <https://doi.org/10.5194/acp-14-3817-2014>, 2014.

Ramabhadran, T., Peterson, T., and Seinfeld, J.: Dynamics of aerosol coagulation and condensation, *AIChE J.*, 22, 840-851, <https://doi.org/10.1002/aic.690220505>, 1976.

Ramazan, K. A., Syomin, D., and Finlayson-Pitts, B. J.: The photochemical production of HONO during the heterogeneous hydrolysis of NO₂, *Physical Chemistry Chemical Physics*, 6, 3836-3843, 2004a.

Ramazan, K. A., Syomin, D., and Finlayson-Pitts, B. J.: The photochemical production of HONO and the heterogeneous hydrolysis of NO₂, *Phys. Chem. Chem. Phys.*, 6, 3836-3843, <https://doi.org/10.1039/b402195a>, 2004b.

Ramazan, K. A., Wingen, L. M., Miller, Y., Chaban, G. M., Gerber, R. B., Xantheas, S. S., and Finlayson-Pitts, B. J.: New experimental and theoretical approach to the heterogeneous hydrolysis of NO₂: key role of molecular nitric acid and its complexes, *J. Phys. Chem. A*, 110, 6886-6897, <https://doi.org/10.1021/jp056426n>, 2006.

Reed, C., Evans, M. J., Crilley, L. R., Bloss, W. J., Sherwen, T., Read, K. A., Lee, J. D., and Carpenter, L. J.: Evidence for renoxification in the tropical marine boundary layer, *Atmos. Chem. Phys.*, 17, 4081-4092, <https://doi.org/10.5194/acp-17-4081-2017>, 2017.

Remorov, R. G., Gerschenson, Y. M., Molina, L. T., and Molina, M. J.: Kinetics and mechanism of HO₂ uptake on solid NaCl, *J. Phys. Chem. A*, 106, 4558-4565, <https://doi.org/10.1021/jp013179o>, 2002.

Ren, X., Brune, W. H., Oliger, A., Metcalf, A. R., Simpas, J. B., Shirley, T., Schwab, J. J., Bai, C., Roychowdhury, U., Li, Y., and Cai, C.: OH, HO₂ and OH reactivity during the PMTACS-NY Whiteface Mountain 2002 campaign: Observations and model comparison, *J. Geophys. Res. Atmos.*, 111, <https://doi.org/10.1029/2005JD006126>, 2006.

Ren, X., Sanders, J. E., Rajendran, A., Weber, R. J., Goldstein, A. H., Pusede, S. E., Browne, E. C., Min, K. E., and Cohen, R. C.: A relaxed eddy accumulation system for measuring vertical fluxes of nitrous acid, *Atmos. Meas. Tech.*, 4, 2093-2103, <https://doi.org/10.5194/amt-4-2093-2011>, 2011.

Sakamaki, F., Hatakeyama, S., and Akimoto, H.: Formation of nitrous acid and nitric oxide in the heterogeneous dark reaction of nitrogen dioxide and water vapor in a smog chamber, *Int. J. Chem. Kinet.*, 15, 1013-1029, <https://doi.org/10.1002/kin.550151006>, 1983.

Saliba, N., Moussa, S., and Tayyar, G.: Contribution of airborne dust particles to HONO sources, *Atmos. Chem. Phys. Discuss.*, 14, <https://doi.org/10.5194/acpd-14-4827-2014>, 2014.

Salma, I., Mészáros, T., Maenhaut, W., Vass, E., and Majer, Z.: Chirality and the origin of atmospheric humic-like substances, *Atmos. Chem. Phys.*, 10, 1315-1327, <https://doi.org/10.5194/acp-10-1315-2010>, 2010.

Sander, S., Friedl, R., Barker, J., Golden, D., Kurylo, M., Wine, P., Abbatt, J., Burkholder, J., Kolb, C., and Moortgat, G.: Chemical kinetics and photochemical data for use in atmospheric studies, evaluation number 14, JPL Publ. 02-25, 2003.

Sander, S. P., Abbatt, J., Barker, J. R., Burkholder, J. B., Friedl, R. R., Golden, D. M., Huie, R. E., Kolb, C. E., Kurylo, M. J., Moortgat, G. K., Orkin, V. L., and Wine, P. H.: Chemical kinetics and photochemical data for use in atmospheric studies. Evaluation Number 17., JPL Publication 10-6, 2011.

Schleicher, N., Norra, S., Chai, F., Chen, Y., Wang, S., and Stüben, D.: Anthropogenic versus geogenic contribution to total suspended atmospheric particulate matter and its

variations during a two-year sampling period in Beijing, China, *J. Environ. Monit.*, 12, 434-441, <https://doi.org/10.1039/B914739J>, 2010.

Seinfeld, J. H., and Pandis, P. N.: Atmospheric chemistry and physics: From air pollution to climate change, John Wiley & Sons, New York, 2006.

Shan, J. H., Wategaonkar, S. J., and Vasudev, R.: Vibrational state dependence of the A state lifetime of HONO, *Chem. Phys. Lett.*, 158, 317-320, [https://doi.org/10.1016/0009-2614\(89\)87343-9](https://doi.org/10.1016/0009-2614(89)87343-9), 1989.

Shi, J. P., Harrison, R. M., and Brear, F.: Particle size distribution from a modern heavy duty diesel engine, *Sci. Total Environ.*, 235, 305-317, [https://doi.org/10.1016/S0048-9697\(99\)00214-4](https://doi.org/10.1016/S0048-9697(99)00214-4), 1999.

Shi, Z., Vu, T., Kotthaus, S., Harrison, R. M., Grimmond, S., Yue, S., Zhu, T., Lee, J., Han, Y., Demuzere, M., Dunmore, R. E., Ren, L., Liu, D., Wang, Y., Wild, O., Allan, J., Acton, W. J., Barlow, J., Barratt, B., Beddows, D., Bloss, W. J., Calzolari, G., Carruthers, D., Carslaw, D. C., Chan, Q., Chatzidiakou, L., Chen, Y., Crilley, L., Coe, H., Dai, T., Doherty, R., Duan, F., Fu, P., Ge, B., Ge, M., Guan, D., Hamilton, J. F., He, K., Heal, M., Heard, D., Hewitt, C. N., Hollaway, M., Hu, M., Ji, D., Jiang, X., Jones, R., Kalberer, M., Kelly, F. J., Kramer, L., Langford, B., Lin, C., Lewis, A. C., Li, J., Li, W., Liu, H., Liu, J., Loh, M., Lu, K., Lucarelli, F., Mann, G., McFiggans, G., Miller, M. R., Mills, G., Monk, P., Nemitz, E., O'Connor, F., Ouyang, B., Palmer, P. I., Percival, C., Popoola, O., Reeves, C., Rickard, A. R., Shao, L., Shi, G., Spracklen, D., Stevenson, D., Sun, Y., Sun, Z., Tao, S., Tong, S., Wang, Q., Wang, W., Wang, X., Wang, X., Wang, Z., Wei, L., Whalley, L., Wu, X., Wu, Z., Xie, P., Yang, F., Zhang, Q., Zhang, Y., Zhang, Y., and Zheng, M.: Introduction to the special issue "In-depth study of air pollution sources and processes within Beijing and its surrounding region (APHH-Beijing)", *Atmos. Chem. Phys.*, 19, 7519-7546, <https://doi.org/10.5194/acp-19-7519-2019>, 2019.

Silver, B., Reddington, C. L., Arnold, S. R., and Spracklen, D. V.: Substantial changes in air pollution across China during 2015–2017, *Environ. Res. Lett.*, 13, 114012, <https://doi.org/10.1088/1748-9326/aae718>, 2018.

Simoneit, B. R. T.: Eolian particulates from oceanic and rural areas—their lipids fulvic and humic acids and residual carbon, *Physics and Chemistry of the Earth*, 12, 343-352, [https://doi.org/10.1016/0079-1946\(79\)90117-4](https://doi.org/10.1016/0079-1946(79)90117-4), 1980.

Sindelarova, K., Granier, C., Bouarar, I., Guenther, A., Tilmes, S., Stavrou, T., Müller, J.-F., Kuhn, U., Stefani, P., and Knorr, W.: Global data set of biogenic VOC emissions calculated by the MEGAN model over the last 30 years, *Atmos. Chem. Phys.*, 14, 9317-9341, <https://doi.org/10.5194/acp-14-9317-2014>, 2014.

Slater, E. J.: Understanding radical chemistry in Beijing through observations and modelling, School of Chemistry, University of Leeds, 2020.

Slater, E. J., Whalley, L. K., Woodward-Massey, R., Ye, C., Lee, J. D., Squires, F., Hopkins, J. R., Dunmore, R. E., Shaw, M., Hamilton, J. F., Lewis, A. C., Crilley, L. R., Kramer, L., Bloss, W., Vu, T., Sun, Y., Xu, W., Yue, S., Ren, L., Acton, W. J. F., Hewitt, C. N., Wang, X., Fu, P., and Heard, D. E.: Elevated levels of OH observed in haze events during wintertime in central Beijing, *Atmos. Chem. Phys. Discuss.*, 2020, 1-43, <https://doi.org/10.5194/acp-2020-362>, 2020.

Smith, K. R., Edwards, P. M., Evans, M. J., Lee, J. D., Shaw, M. D., Squires, F., Wilde, S., and Lewis, A. C.: Clustering approaches to improve the performance of low cost

air pollution sensors, *Faraday Discuss.*, 200, 621-637, <https://doi.org/10.1039/C7FD00020K>, 2017.

Smith, S. C., Lee, J. D., Bloss, W. J., Johnson, G. P., Ingham, T., and Heard, D. E.: Concentrations of OH and HO₂ radicals during NAMBLEX measurements and steady state analysis, *Atmos. Chem. Phys.*, 6, 1435-1453, <https://doi.org/10.5194/acp-6-1435-2006>, 2006.

Smith, S. C.: Atmospheric measurements of OH and HO₂ using the FAGE technique: Instrument development and data analysis, School of Chemistry, University of Leeds, 2007.

Sommariva, R., Haggerstone, A. L., Carpenter, L. J., Carslaw, N., Creasey, D. J., Heard, D. E., Lee, J. D., Lewsi, A. C., Pilling, M. J., and Zador, J.: OH and HO₂ chemistry in clean marine air during SOAPEX-2, *Atmos. Chem. Phys.*, 4, 839-856, <https://doi.org/10.5194/acp-4-839-2004>, 2004.

Sommariva, R., Bloss, W. J., Brough, N., Carslaw, N., Flynn, M., Haggerstone, A. L., Heard, D. E., Hopkins, J. R., Lee, J. D., Lewis, A. C., McFiggans, G., Monks, P. S., Penket, S. A., Pilling, M. J., Plane, J. M. C., Read, K. A., Saiz-Lopez, A., Rickard, A. R., and William, P. I.: OH and HO₂ chemistry during NAMBLEX: roles of oxygenates, halogen oxides and heterogeneous uptake, *Atmos. Chem. Phys.*, 6, 1135-1153, <https://doi.org/10.5194/acp-6-1135-2006>, 2006.

Song, H., Chen, X., Lu, K., Zou, Q., Tan, Z., Fuchs, H., Wiedensohler, A., Moon, D. R., Heard, D. E., Baeza-Romero, M. T., Zheng, M., Wahner, A., Kiendler-Scharr, A., and Zhang, Y.: Influence of aerosol copper on HO₂ uptake: a novel parameterized equation, *Atmos. Chem. Phys.*, 20, 15835-15850, <https://doi.org/10.5194/acp-20-15835-2020>, 2020.

Sörgel, M., Trebs, I., Serafimovich, A., Moravek, A., Held, A., and Zetzsch, C.: Simultaneous HONO measurements in and above a forest canopy: influence of turbulent exchange on mixing ratio differences, *Atmos. Chem. Phys.*, 11, 841-855, <https://doi.org/10.5194/acp-11-841-2011>, 2011a.

Sörgel, M., Trebs, I., Wu, D., and Held, A.: A comparison of measured HONO uptake and release with calculated source strengths in a heterogeneous forest environment, *Atmos. Chem. Phys.*, 15, 9237-9251, <https://doi.org/10.5194/acp-15-9237-2015>, 2015.

Spataro, F., and Ianniello, A.: Sources of atmospheric nitrous acid: State of the science, current research needs, and future prospects, *J. Air Waste Manage. Assoc.*, 64, 1232-1250, <https://doi.org/10.1080/10962247.2014.952846>, 2014.

Stemmler, K., Ndour, M., Elshorbany, Y., Kleffmann, J., D'Anna, B., George, C., Bohn, B., and Ammann, M.: Light induced conversion of nitrogen dioxide into nitrous acid on submicron humic acid aerosol, *Atmos. Chem. Phys.*, 7, 4237-4248, <https://doi.org/10.5194/acp-7-4237-2007>, 2007.

Stone, D., Whalley, L. K., and Heard, D. E.: Tropospheric OH and HO₂ radicals: field measurements and model comparisons, *Chem. Soc. Rev.*, 41, 6348-6404, <https://doi.org/10.1039/C2CS35140D>, 2012.

Stone, D., Whalley, L. K., Ingham, T., Edwards, P. M., Cryer, D. R., Brumby, C. A., Seakins, P. W., and Heard, D. E.: Measurement of OH reactivity by laser flash

photolysis coupled with laser-induced fluorescence spectroscopy, *Atmos. Meas. Tech.*, 9, 2827-2844, <https://doi.org/10.5194/amt-9-2827-2016>, 2016.

Su, H., Cheng, Y., Oswald, R., Behrendt, T., Trebs, I., Meixner, F. C., Andreae, M. O., Cheng, P., Zhang, Y., and Pöschl, U.: Soil nitrate as a source of atmospheric HONO and OH radicals, *Science*, 333, 1616-1618, <https://doi.org/10.1126/science.1207687>, 2011.

Syomin, D. A., and Finlayson-Pitts, B. J.: HONO decomposition on borosilicate glass surfaces: implications for environmental chamber studies and field experiments, *Phys. Chem. Chem. Phys.*, 5, 5236-5242, <https://doi.org/10.1039/b309851f>, 2003.

Taketani, F., Kanaya, Y., and Akimoto, H.: Kinetics of heterogeneous reactions of HO₂ radical at ambient concentration levels with (NH₄)₂SO₄ and NaCl aerosol particles., *J. Phys. Chem. A*, 112, 2370-2377, <https://doi.org/10.1021/jp0769936>, 2008.

Taketani, F., Kanaya, Y., and Akimoto, H.: Kinetics of HO₂ uptake in levoglucosan and polystyrene latex particles. , *The Journal of Physical Chemistry Letters*, 1, 1701-1704, <https://doi.org/10.1021/jz100478s>, 2010.

Taketani, F., Kanaya, Y., Pocharnart, P., Liu, Y., Li, J., Okuzawa, K., Kawamura, K., Wang, Z., and Akimoto, H.: Measurement of overall uptake coefficients for HO₂ radicals by aerosol particles sampled from ambient air at Mts. Tai and Mang (China). *Atmos. Chem. Phys.*, 12, 11907-11916, <https://doi.org/10.5194/acp-12-11907-2012>, 2012.

Takeuchi, M., Sakamoto, K., Martra, G., Coluccia, S., and Anpo, M.: Mechanism of photoinduced superhydrophilicity on the TiO₂ photocatalyst surface, *J. Phys. Chem. B*, 109, 15422-15428, <https://doi.org/10.1021/jp058075i>, 2005.

Tan, J., Xiang, P., Zhou, X., Duan, J., Ma, Y., He, K., Cheng, Y., Yu, J., and Querol, X.: Chemical characterization of humic-like substances (HULIS) in PM_{2.5} in Lanzhou, China, *Sci. Total Environ.*, 573, 1481-1490, <https://doi.org/10.1016/j.scitotenv.2016.08.025>, 2016.

Tan, Z., Fuchs, H., Lu, K., Hofzumahaus, A., Bohn, B., Broch, S., Dong, H., Gomm, S., Häsel, R., He, L., Holland, F., Li, X., Liu, Y., Lu, S., Rohrer, F., Shao, M., Wang, B., Wang, M., Wu, Y., Zeng, L., Zhang, Y., Wahner, A., and Zhang, Y.: Radical chemistry at a rural site (Wangdu) in the North China Plain: observation and model calculations of OH, HO₂ and RO₂ radicals, *Atmos. Chem. Phys.*, 17, 663-690, <https://doi.org/10.5195/acp-17-663-2017>, 2017.

Tan, Z., Rohrer, F., Lu, K., Ma, X., Bohn, B., Broch, S., Dong, H., Fuchs, H., Gkatzelis, G. I., Hofzumahaus, A., Holland, F., Li, X., Liu, Y., Liu, Y., Novelli, A., Shao, M., Wang, H., Wu, Y., Zeng, L., Hu, M., Kiendler-Scharr, A., Wahner, A., and Zhang, Y.: Wintertime photochemistry in Beijing: Observations of RO_x radical concentrations in the North China Plain during the BEST-ONE campaign, *Atmos. Chem. Phys. Discuss.*, 18, 12391-12411, <https://doi.org/10.5194/acp-18-12391-2018>, 2018.

Tan, Z., Hofzumahaus, A., Lu, K., Brown, S. S., Holland, F., Huey, L. G., Kiendler-Scharr, A., Li, X., Liu, X., Ma, N., Min, K.-E., Rohrer, F., Shao, M., Wahner, A., Wang, Y., Wiedensohler, A., Wu, Y., Wu, Z., Zeng, L., Zhang, Y., and Fuchs, H.: No Evidence for a Significant Impact of Heterogeneous Chemistry on Radical

Concentrations in the North China Plain in Summer 2014, *Environ. Sci. Technol.*, 54, 5973-5979, <https://doi.org/10.1021/acs.est.0c00525>, 2020.

Tang, M. J., Thieser, J., Schuster, G., and Crowley, J. N.: Kinetics and mechanism of the heterogeneous reaction of N₂O₅ with mineral dust particles, *Phys. Chem. Chem. Phys.*, 14, 8551-8561, <https://doi.org/10.1039/C2CP40805H>, 2012.

Tang, M. J., Cox, R. A., and Kalberer, M.: Compilation and evaluation of gas phase diffusion coefficients of reactive trace gases in the atmosphere: volume 1. Inorganic compounds, *Atmos. Chem. Phys.*, 14, 9233-9247, <https://doi.org/10.5194/acp-14-9233-2014>, 2014a.

Tang, M. J., Schuster, G., and Crowley, J. N.: Heterogeneous reaction of N₂O₅ with illite and Arizona test dust particles, *Atmos. Chem. Phys.*, 14, 245-254, <https://doi.org/10.5194/acp-14-245-2014>, 2014b.

Thornton, J. A., and Abbatt, J. P. D.: Measurements of HO₂ uptake of aqueous aerosol: Mass accommodation coefficients and net reactive loss., *J. Geophys. Res.*, 110, <https://doi.org/10.1029/2004JD005402>, 2005.

Thornton, J. A., Jaegle, L., and McNeill, V. F.: Assessing known pathways for HO₂ loss in aqueous atmospheric aerosols: Regional and global impacts on tropospheric oxidants. , *J. Geophys. Res.*, 113, <https://doi.org/10.1029/2007JD009236>, 2008.

Tong, H., Arangio, A. M., Lakey, P. S. J., Berkemeier, T., Liu, F., Kampf, C. J., Brune, W. H., Pöschl, U., and Shiraiwa, M.: Hydroxyl radicals from secondary organic aerosol decomposition in water, *Atmos. Chem. Phys.*, 16, 1761-1771, <https://doi.org/10.5194/acp-16-1761-2016>, 2016.

TSI: Model 3076 Constant Output Atomiser Instruction Manual, 2005.

TSI: Model 3775 Condensation Particle Counter: Operation and Service Manual, 2007.

TSI: Model 3936 Scanning Mobility Particle Sizer (SMPS) Spectrometer Operation and Service Manual, 2008a.

TSI: Model 3074B Filtered Air Supply: Operation and Service Manual, 2008b.

Tu, P., Hall, W. A., and Johnston, M. V.: Characterization of Highly Oxidized Molecules in Fresh and Aged Biogenic Secondary Organic Aerosol, *Anal. Chem.*, 88, 4495-4501, <https://doi.org/10.1021/acs.analchem.6b00378>, 2016.

van der A, R. J., Mijling, B., Ding, J., Koukouli, M. E., Liu, F., Li, Q., Mao, H., and Theys, N.: Cleaning up the air: effectiveness of air quality policy for SO₂ and NO_x emissions in China, *Atmos. Chem. Phys.*, 17, 1775-1789, <https://doi.org/10.5194/acp-17-1775-2017>, 2017.

Varner, M. E., Finlayson-Pitts, B. J., and Gerber, R. B.: Reaction of a charge-separated ONONO₂ species with water in the formation of HONO: an MP2 molecular dynamics study, *Phys. Chem. Chem. Phys.*, 16, 4483-4487, <https://doi.org/10.1039/c3cp55024a>, 2014.

Veres, P. R., Roberts, J. M., Wild, R. J., Edwards, P. M., Brown, S. S., Bates, T. S., Quinn, P. K., Johnson, J. E., Zamora, R. J., and de Gouw, J.: Peroxynitric acid (HO₂NO₂) measurements during the UBWOS 2013 and 2014 studies using iodide ion chemical ionization mass spectrometry, *Atmos. Chem. Phys.*, 15, 8101-8114, <https://doi.org/10.5194/acp-15-8101-2015>, 2015.

- Verstraeten, W. W., Neu, J. L., Williams, J. E., Bowman, K. W., Worden, J. R., and Boersma, K. F.: Rapid increases in tropospheric ozone production and export from China, *Nat. Geosci.*, 8, 690-695, <https://doi.org/10.1038/ngeo2493>, 2015.
- Villena, G., Bejan, I., Kurtenbach, R., and Kleffmann, J.: Interferences of commercial NO₂ instruments in the urban atmosphere and in a smog chamber, *Atmos. Meas. Tech.*, 5, 149-159, <https://doi.org/10.5195/amt-5-149-2012>, 2012.
- Vogel, B., Vogel, H., Kleffmann, J., and Kurtenbach, R.: Measured and simulated vertical profiles of nitrous acid - Part II. Model simulations and indications for a photolytic source, *Atmos. Environ.*, 37, 2957-2966, [https://doi.org/10.1016/S1352-2310\(03\)00243-7](https://doi.org/10.1016/S1352-2310(03)00243-7), 2003.
- Wang, J., and Koel, B. E.: IRAS studies of NO₂, N₂O₃, and N₂O₄ adsorbed on Au (111) surfaces and reactions with coadsorbed H₂O, *J. Phys. Chem. A*, 102, 8573-8579, <https://doi.org/10.1021/jp982061d>, 1998.
- Wang, J., and Koel, B. E.: Reactions of N₂O₄ with ice at low temperatures on the Au (111) surface, *Surf. Sci.*, 436, 15-28, [https://doi.org/10.1016/S0039-6028\(99\)00457-4](https://doi.org/10.1016/S0039-6028(99)00457-4), 1999.
- Washida, N., Nori, Y., and Tanaka, I.: Quantum yield of ozone formation from the photolysis of the oxygen molecule at 184.9 and 193.1A, *The Journal of Chemical Physics*, 54, 1119-1122, <https://doi.org/10.1063/1.1674946>, 1971.
- Wayne, R. P.: *Chemistry of Atmospheres*, Oxford University Press, 2000.
- Weast, R. C., and Astle, M. J.: *CRC Handbook of Chemistry and Physics...: 1983-1984*, CRC press, 1983.
- Wexler, A. S., and Clegg, S. L.: Atmospheric aerosol models for systems including the ions H⁺, NH₄⁺, Na⁺, SO₄²⁻, NO₃⁻, Cl⁻, Br⁻, and H₂O, *J. Geophys. Res. Atmos.*, 107, ACH 14-11-ACH 14-14, <https://doi.org/10.1029/2001JD000451>, 2002.
- Whalley, L. K., Furneaux, K. L., Goddard, A., Lee, J. D., Mahajan, A., Oetjen, H., Read, K. A., Kaaden, N., Carpenter, L. J., Lewis, A. C., Plane, J. M. C., Saltzman, E. S., Wiedensohler, A., and Heard, D. E.: The chemistry of OH and HO₂ radicals in the boundary layer over the tropical Atlantic Ocean, *Atmos. Chem. Phys.*, 10, 1555-1576, <https://doi.org/10.5194/acp-10-1555-2010>, 2010.
- Whalley, L. K., Blitz, M. A., Desservattez, M., Seakins, P. W., and Heard, D. E.: Reporting the sensitivity of laser-induced fluorescence instruments used for HO₂ detection to an interference from RO₂ radicals and introducing a novel approach that enables HO₂ and certain RO₂ types to be selectively measured, *Atmos. Meas. Tech.*, 6, 3425-3440, <https://doi.org/10.5194/amt-6-3425-2013>, 2013.
- Whalley, L. K., Stone, D., Dunmore, R., Hamilton, J., Hopkins, J. R., Lee, J. D., Lewis, A. C., Williams, P., Kleffmann, J., Laufs, S., Woodward-Massey, R., and Heard, D. E.: Understanding in situ ozone production in the summertime through radical observations and modelling studies during the Clean air for London project (ClearfLo), *Atmos. Chem. Phys.*, 18, 2547-2571, <https://doi.org/10.5194/acp-18-2547-2018>, 2018.
- Whalley, L. K., Slater, E. J., Woodward-Massey, R., Ye, C., Lee, J. D., Squires, F., Hopkins, J. R., Dunmore, R. E., Shaw, M., Hamilton, J. F., Lewis, A. C., Mehra, A., Worrall, S. D., Bacak, A., Bannan, T. J., Coe, H., Ouyang, B., Jones, R. L., Crilley, L. R., Kramer, L. J., Bloss, W. J., Vu, T., Kotthaus, S., Grimmond, S., Sun, Y., Xu, W.,

- Yue, S., Ren, L., Acton, W. J. F., Hewitt, C. N., Wang, X., Fu, P., and Heard, D. E.: Evaluating the sensitivity of radical chemistry and ozone formation to ambient VOCs and NO_x in Beijing, *Atmos. Chem. Phys. Discuss.*, 21, 2125-2147, <https://doi.org/10.5194/acp-2020-785>, 2021.
- Wong, K., Tsai, C., Lefer, B., Haman, C., Grossberg, N., Brune, W. H., Ren, X., Luke, W., and Stutz, J.: Daytime HONO vertical gradients during SHARP 2009 in Houston, TX., *Atmos. Chem. Phys.*, 12, 635-652, <https://doi.org/10.5194/acp-12-635-2012>, 2012.
- Wu, L., Li, X., and Ro, C.: Hygroscopic behavior of ammonium sulfate, ammonium nitrate, and their mixture particles, *Asian J. Atmos. Environ.*, 13.3, 196-211, <https://doi.org/10.5572/ajae.2019.13.3.196>, 2019.
- Xu, W., Ovadnevaite, J., Fossum, K. N., Lin, C., Huang, R. J., O'Dowd, C., and Ceburnis, D.: Aerosol hygroscopicity and its link to chemical composition in the coastal atmosphere of Mace Head: marine and continental air masses, *Atmos. Chem. Phys.*, 20, 3777-3791, <https://doi.org/10.5194/acp-20-3777-2020>, 2020.
- Xue, L. K., Wang, T., Gao, J., Ding, A. J., Zhou, X. H., Blake, D. R., Wang, X. F., Saunders, S. M., Fan, S. J., Zuo, H. C., Zhang, Q. Z., and Wang, W. X.: Ground-level ozone in four Chinese cities: precursors, regional transport and heterogeneous processes, *Atmos. Chem. Phys.*, 14, 13175-13188, <https://doi.org/10.5194/acp-14-13175-2014>, 2014.
- Yamanokoshi, E., Okochi, H., Ogata, H., and Kobayashi, Y.: Behavior and origin of water-soluble humic-like substances in particulate matter in central Tokyo, *Journal of Japan Society for Atmospheric Environment*, 49, 43-52, <https://doi.org/10.11298/taiki.49.43>, 2014.
- Ye, C., Gao, H., Zhang, N., and Zhou, X.: Photolysis of nitric acid and nitrate on natural and artificial surfaces, *Environ. Sci. Technol.*, 50, 3530-3536, <https://doi.org/10.1021/acs.est.5b05032>, 2016a.
- Ye, C., Zhou, X., Pu, D., Stutz, J., Festa, J., Spolaor, M., Tsai, C., Cantrell, C., Mauldin, R. L., Campos, T., Weinheimer, A., Hornbrook, R. S., Apel, E. C., Guenther, A., Kaser, L., Yuan, B., Karl, T., Haggerty, J., Hall, S., Ullmann, K., Smith, J. N., Ortega, J., and Knote, C.: Rapid cycling of reactive nitrogen in the marine boundary layer, *Nature*, 532, 489-491, <https://doi.org/10.1038/nature17195>, 2016b.
- Ye, C., Heard, D. E., and Whalley, L. K.: Evaluation of novel routes for NO_x formation in remote regions, *Environ. Sci. Technol.*, 51, 7442-7449, <https://doi.org/acs.est.6b06441>, 2017a.
- Ye, C., Zhang, N., Gao, H., and Zhou, X.: Photolysis of particulate nitrate as a source of HONO and NO_x, *Environ. Sci. Technol.*, 51, 6849-6856, <https://doi.org/10.1021/acs.est.7b00387>, 2017b.
- Young, C. J., Washenfelder, R. A., Roberts, J. M., Mielke, L. H., Osthoff, H. D., Tsai, C., Pikelnaya, O., Stutz, J., Veres, P. R., Cochran, A. K., Vandenboer, T. C., Flynn, J., Grossberg, N., Haman, C. L., Lefer, B., Stark, H., Graus, M., Gouw, J. D., Gilman, J. B., Kuster, W. C., and Brown, S. S.: Vertically resolved measurements of nighttime radical reservoirs in Los Angeles and their contribution to the urban radical budget, *Environ. Sci. Technol.*, 46, 10965-10973, <https://doi.org/10.1021/es302206a>, 2012.

- Yu, K.-P., Lin, C.-C., Yang, S.-C., and Zhao, P.: Enhancement effect of relative humidity on the formation and regional respiratory deposition of secondary organic aerosol, *J. Hazard. Mater.*, 191, 94-102, <https://doi.org/10.1016/j.jhazmat.2011.04.042>, 2011.
- Zhang, D., and Zhang, R.: Ozonolysis of α -pinene and β -pinene: Kinetics and mechanism, *J. Chem. Phys.*, 112, 114308, <https://doi.org/10.1063/1.1862616>, 2005.
- Zhang, J. K., Sun, Y., Liu, Z. R., Ji, D. S., Hu, B., Liu, Q., and Wang, Y. S.: Characterisation of submicron aerosols during a month of serious pollution in Beijing, 2013, *Atmos. Chem. Phys.*, 14, 2887-2903, <https://doi.org/10.5194/acp-14-2887-2014>, 2014.
- Zhang, N., Zhou, X., Shepson, P. B., Gao, H., Alaghmand, M., and Stirm, B.: Aircraft measurement of HONO vertical profiles over a forested region, *Geophys. Res. Lett.*, 36, L15820, <https://doi.org/10.1029/2009GL038999>, 2009.
- Zhang, N., Zhou, X., Bertman, S., Tang, D., Alaghmand, M., Shepson, P. B., and Carol, M. A.: Measurements of ambient HONO concentrations and vertical HONO flux above a northern Michigan forest canopy, *Atmos. Chem. Phys.*, 12, 8285-8296, <https://doi.org/10.5194/acp-12-8285-2012>, 2012.
- Zhao, Y., Lambe, A. T., Saleh, R., Saliba, G., and Robinson, A. L.: Secondary Organic Aerosol Production from Gasoline Vehicle Exhaust: Effects of Engine Technology, Cold Start, and Emission Certification Standard, *Environ. Sci. Technol.*, 52, 1253-1261, <https://doi.org/10.1021/acs.est.7b05045>, 2018.
- Zhao, Z., Zhang, W., Alexander, T., Zhang, X., Martin, D. B. C., and Zhang, H.: Isolating α -Pinene Ozonolysis Pathways Reveals New Insights into Peroxy Radical Chemistry and Secondary Organic Aerosol Formation, *Environ. Sci. Technol.*, 55, 6700-6709, <https://doi.org/10.1021/acs.est.1c02107>, 2021.
- Zheng, G., He, K., Duan, F., Cheng, Y., and Ma, Y.: Measurement of humic-like substances in aerosols: A review, *Environ. Pollut.*, 181, 301-314, <https://doi.org/10.1016/j.envpol.2013.05.055>, 2013.
- Zhou, J., Murano, K., Kohno, N., Sakamoto, Y., and Kajii, Y.: Real-time quantification of the total HO₂ reactivity of ambient air and HO₂ uptake kinetics onto ambient aerosols in Kyoto (Japan), *Atmos. Environ.*, 223, 117189, <https://doi.org/10.1016/j.atmosenv.2019.117189>, 2020.
- Zhou, X., Gao, H., He, Y., Huang, G., Bertman, S. B., Civerolo, K., and Schwab, J.: Nitric acid photolysis on surfaces in low NO_x environments: Significant atmospheric implications, *Geophys. Res. Lett.*, 30, 2217, <https://doi.org/10.1029/2003GL018620>, 2003.
- Zhou, X., Zhang, N., TerAvest, M., Tang, D., Hou, J., Bertman, S., Alaghmand, M., Shepson, P. B., Carroll, M. A., and Griffith, S.: Nitric acid photolysis on forest canopy surface as a source for tropospheric nitrous acid, *Nat. Geosci.*, 4, 440-443, <https://doi.org/10.1038/ngeo1164>, 2011.
- Zieger, P., Väisänen, O., Corbin, J. C., Partridge, D. G., Bastelberger, S., Mousavi-Fard, M., Rosati, B., Gysel, M., Krieger, U. K., Leck, C., Nenes, A., Riipinen, I., Virtanen, A., and Salter, M. E.: Revising the hygroscopicity of inorganic sea salt particles, *Nat. Commun.*, 8, 15883, <https://doi.org/10.1038/ncomms15883>, 2017.

Zobrist, B., Soonsin, V., Luo, B. P., Krieger, U. K., Marolli, C., Peter, T., and Koop, T.: Ultra-slow water diffusion in aqueous sucrose glasses, *Phys.Chem.Phys.Chem*, 13, <https://doi.org/10.1039/C0CP01273D>, 2011.